Mixed-matrix membranes for the separation of higher hydrocarbons from permanent gas

Vom Promotionsausschuss der

Technischen Universität Hamburg

zur Erlangung des akademischen Grades

Doktor-Ingenieurin (Dr.-Ing.)

genehmigte Dissertation

von

Heike Mushardt

aus

Geesthacht

2022

1. Gutachterin: Prof. Dr.-Ing. Irina Smirnova
2. Gutachter: Prof. Dr.-Ing. Matthias Kraume
3. Gutachter: Dr. Torsten Brinkmann

Vorsitzender des Prüfungsausschusses: Prof. Dr. Raimund Horn

Datum der mündlichen Prüfung: 13.01.2022

DOI: https://doi.org/10.15480/882.4646

ACKNOWLEDGEMENTS

This work is based on the results that have been received during my time as a Ph.D. student at the former Helmholtz Zentrum Geesthacht, known today as Hereon. For me, it was a time of learning and growing, which I will always keep in good memory.

At first I would like to give my special thanks to my supervisor Dr. Torsten Brinkmann, who gave me the opportunity to work in his group and introduced me to the fascinating world of membranes. His knowledge, support and encouragement were of invaluable help at any time.
I would like to express my gratitude to Prof. Dr.-Ing. Irina Smirnova for being my doctoral supervisor at the TUHH and the confidence given, for all her advise through valuable discussions and the time and energy to review my dissertation. I would also like to thank Prof. Dr.-Ing. Matthias Kraume, for being my co-supervisor and for his great support and guidance throughout the whole project. And also my thanks to Prof. Dr. Raimund Horn for taking over the lead of the examination committee.

The work was part of the BMBF project "Mixed Matrix Membranes for gas separation" which was a co-operation between the Hereon, the TU Berlin and the two industrial companies Blücher GmbH and Sterling SIHI GmbH. It was a great pleasure to be part of the project team and I thank all participants for the excellent cooperation: Prof. Matthias Kraume, Verena Kramer, Deniz Hülagü, Henning Scheel, Stefan Kämper and all participants at the Hereon.
I want to express great thanks to all my former colleagues at the Hereon who were always of great support in all professional and technical challenges. In particular, Sergey Shishatskiy, Jan Wind, Jan Pohlmann, Carsten Scholles, Holger Pingel, Jelena Lillepärg, Torsten Wolf, Kristian Buhr, Anne Schröder, Sofia Dami and Clarissa Abetz. My student co-workers, Markus Müller and Florian Metzler, for their contribution. And also my warm thanks to Maria, Wiebke and Svenja, for being my companions in sharing of failures and celebrating successes.

My special thanks to all my friends, in particular my "Hamburg family", for all the distractions through all the years and the support in good and bad times.
Last but not least, many cordial thanks to my dear parents, sisters and my husband. You have always been there for me with love, confidence, encouragement and patience.

Abstract

The separation of hydrocarbon mixtures is part of many industrial processes. Being still dominated by conventional energy-intensive techniques such as distillation, they make a substantial contribution to the total energy consumption and the release of greenhouse gas emissions. While the use of membrane-based separation processes allows for a better energy-efficiency, their application is often not competitive or even feasible for separations dealing with hydrocarbon mixtures. Many attempts have been made to improve the materials but they still suffer from the harsh operating conditions limiting their performance. Therefore, in this work a thin film composite membrane material for the selective separation of higher hydrocarbons was developed based on the concept of mixed matrix membranes. The performance was investigated and evaluated with respect to an industrial application. Key aspects are an improved separation performance *n*-C_4H_{10} / CH_4 compared to state-of-art membrane materials, a reproducible production even on technical scale and the stability of performance under varying operating conditions, in presence of multi-component mixtures and under long-term exposure.

A promising membrane material is identified by the combination of a polymeric matrix based on poly(octyl)methylsiloxane POMS with activated carbon as inorganic filler material. The selectivity of the *n*-C_4H_{10} / CH_4 separation is increased up to 32 % compared to the state-of-art membrane material POMS, allowing for a reduction of energy up to 42 %. The mixed-matrix membrane could be prepared successfully on a technical scale. A detailed study of the separation performance under varying operating conditions reveals the optimum range of application. The improved performance is also proven for multi-component hydrocarbon mixtures and under long-term exposure. The detailed permeation data obtained in this work are the basis for the technical design of the process. This work demonstrates the benefits of the mixed matrix membrane concept to promote the application of energy-efficient membrane based separation processes.

TABLE OF CONTENTS

List of Figures

List of Tables

Symbols and Abbreviations

Latin symbols

A_f	Factor for size and shape of gas molecules in equation (3.3-7)	-
$A_{M,eff}$	Effective membrane area for permeation	m^2
a	Activity	-
B_d	Free volume parameter	-
b	Adsorption affinity constant	1/bar
bp	Boiling point	°C
C_{corr}	Gas conversion factor	-
c	Concentration	mol/cm^3
c_p	Heat capacity	J/(g K)
D_{0i}	Diffusion coefficient	m^2/s
D_m	Binary diffusion coefficient	m^2/s
d_p	Pore diameter	nm or Å
d_{50}	Average particle diameter	µm
∂	Partial derivative	-
E_P	Energy of activation for permeation	kJ/mol
f	Fugacity of component i	bar
H	Enthalpy	J
H_i	Henry coefficient of component i	bar
Kn	Knudsen Number	-
L	Permeance	$m^3_N/(m^2\ h\ bar)$
Mw	Molecular weight	g/mol
m	Free Volume Model Parameter for concentration dependency	
m	Sample weight	g
n	Number	-
$\dot{n}''$	Molar flux	$mol/(cm^2\ s)$
P_i	Permeability of component i	Barrer

p	Pressure	bar
q	Loading with adsorbed species	mmol/g
R	Universal gas constant	J/(K mol)
Rf	Response factor	-
s	Standard deviation	-
S_i	Solubility Coefficient of component i	1/bar
T	Temperature	°C
T_g	Glass transition temperature	°C
t	Tóth parameter for surface heterogeneity	-
$\dot{V}$	Volume Flow Rate	ml/min
$\overline{V}$	Molar volume	cm³/mol
y	Volume fraction	vol-%

Greek letters

α	Selectivity	-
β_K^*	Compressibility Factor	-
δ	Thickness	µm
ε	Porosity	-
θ	Time-lag	s
λ_m	Mean free path	Nm
μ_i	Chemical potential of component i	J/mol
ϱ	Density	g/cm³
σ	Lennard-Jones potential	Å
τ	Tortuosity	-
Φ, φ	Volume fraction	-
χ	Flory-Huggins interaction parameter	-
ω	Acentric factor	-

Subscripts

A	Air
ads	Adsorbed
B	Auxiliary liquid in density measurement
c	Continuous polymeric matrix phase

crit	Critical point
cond	Condensation
d	Dispersed filler phase
eff	Effective
F	Feed
FV	Free volume
I	Non-ideal interfacial layer in MMM
i,j	Components i,j
M	Membrane
m	Molar; arithmetic average
max	Maximum
mix	Mixing
P	Permeate
p	Pore
s	Solution
T	Operating temperature
0	Reference temperature

Abbreviations

AC	Activated Carbon
ACM	Aspen Custom Modeler ®
AS	AEROSIL ® R8200 (Evonik, formerly Degussa)
BET	Surface area determined acc. to method of Brunauer, Emmett & Teller
BMBF	German Federal Ministry of Education and Research
BTX	Mixture of aromatics benzene, toluene, xylene
CB	Carbon Black
CEM	Controlled Evaporation and Mixing Unit
CMS	Carbon Molecular Sieves
CNT	Carbon Nanotube
DEA	Diethanolamine
DSC	Differential Scanning Calorimetry
FV	Free Volume
GC	Gas Chromatography
GL	Gutter layer

GS	Gas Separation
IUPAC	International Union of Pure and Applied Chemistry
LPG	Liquefied petroleum gas
MEA	Monoethanolamine
MG	Mixed gas
MMM	Mixed-Matrix Membrane
MOF	Metal Organic Frameworks
PAN	Polyacrylonitrile
PE	Polyethylene
PES	Polyethersulfone
PDMS	Poly(dimethylsiloxane)
PMP	Poly(4-methyl-2-pentyne)
POMS	Poly(octylmethylsiloxane)
POSS	Polyhedral Oligomeric Silsesquioxane
PP	Polypropylene
PS	Polystryrol
PSA	Pressure Swing Adsorption
PTMSP	Poly(1-(trimethylsilyl)-1-propyne)
PVC	Polyvinylchloride
SEM	Scanning Electron Microscopy
S	Standard Polymeric Precursor Solution
SG	Single gas
SSF	Selective Surface Flow
TCD	Thermal Conductivity Detector
TFC	Thin Film Composite Membrane
TGA	Thermogravimetric Analysis
TL	Top layer
VOC	Volatile Organic Components
XL	Modified polymeric precursor solution
Z	Zeolite (type CBV-780, Zeolyst)
ZIF	Zeolitic Imidazolate Framework
ZSM-5	Zeolite Socony Mobil-5

1 INTRODUCTION

The increased awareness of the impacts of climate change has led to more responsibility and sustainability in the use of resources and energy. This is not only reflected in today's innovation strategies of chemical industry but also defined in certain political objectives, e.g., the "Strategy Europe 2020" that demands a 40 % reduction of greenhouse gas emissions by 2020 compared to 1990, following the "Roadmap 2050" with its aspired 80 % reduction by 2050 [25, 46, 47]. Currently, even a net-zero target with respect to CO_2 emissions for the year 2050 is being discussed. Almost 60-80 % of the total energy consumption in the chemical industry is used for separation processes [137]. They play a vital role in nearly all chemical and petrochemical processes ranging from bulk separations to purifications. The objectives of separation are governed by both economical and environmental reasons, that is, to yield high purity products, minimize the product loss in waste or purge gas streams or meet regulations for waste air, energy consumption and CO_2 emissions.

An important field of application is the separation of hydrocarbon mixtures. Around 95 % of all industrial separations deal with the refinery and processing of fossil fuels like crude oil or natural gas and the treatment of associated effluent gas [58]. With a worldwide annual production of around 3.5 billion m³ (data for 2013 by the U.S. Energy Information Association [157]), natural gas is by far the largest market for industrial gas separations [14]. It is a gaseous hydrocarbon mixture with mainly CH_4 and significantly varying amounts of C_2-C_6 alkanes, carbon dioxide (CO_2), hydrogen sulfide (H_2S), water (H_2O) and inerts (He, N_2) [18]. The separation of C_{2+} hydrocarbons is essential to achieve a consumer grade product with an appropriate heating value. Further, the hydrocarbon dew point has to be adjusted in order to avoid damage of the pipeline system and prevent coking or pre-detonation problems [43]. According to the Intergovernmental Panel on Climate Change (IPCC), CH_4 has a 28 times higher global warming potential than CO_2 [64] and as a result, 1.6 billion tons of CO_2 equivalents were estimated to be released during the processing of natural gas and crude oil in Germany in 2010 [141]. Crude oil, a liquid hydrocarbon mixture of mainly $C_{5\text{-}15}$ alkanes (paraffins), cycloalkanes and aromatic hydrocarbons, is by far the most important raw material accounting for 77 % of all chemical

industry as illustrated in Figure 1-1 [125, 10]. Particularly ethylene, propylene and the BTX aromatics are important building blocks for the synthesis of a great variety of products, for example, plastics, synthetic fibers, detergents, dyes, adhesives, plasticizers, insecticides or pharmaceuticals [10]. The recovery of volatile organic compounds (VOCs) released during their petrochemical processing are a further important field of application [62]. The United States emitted in 1995 around 30 million tons of VOCs, of which 13 million tons were released during the industrial processing [158].

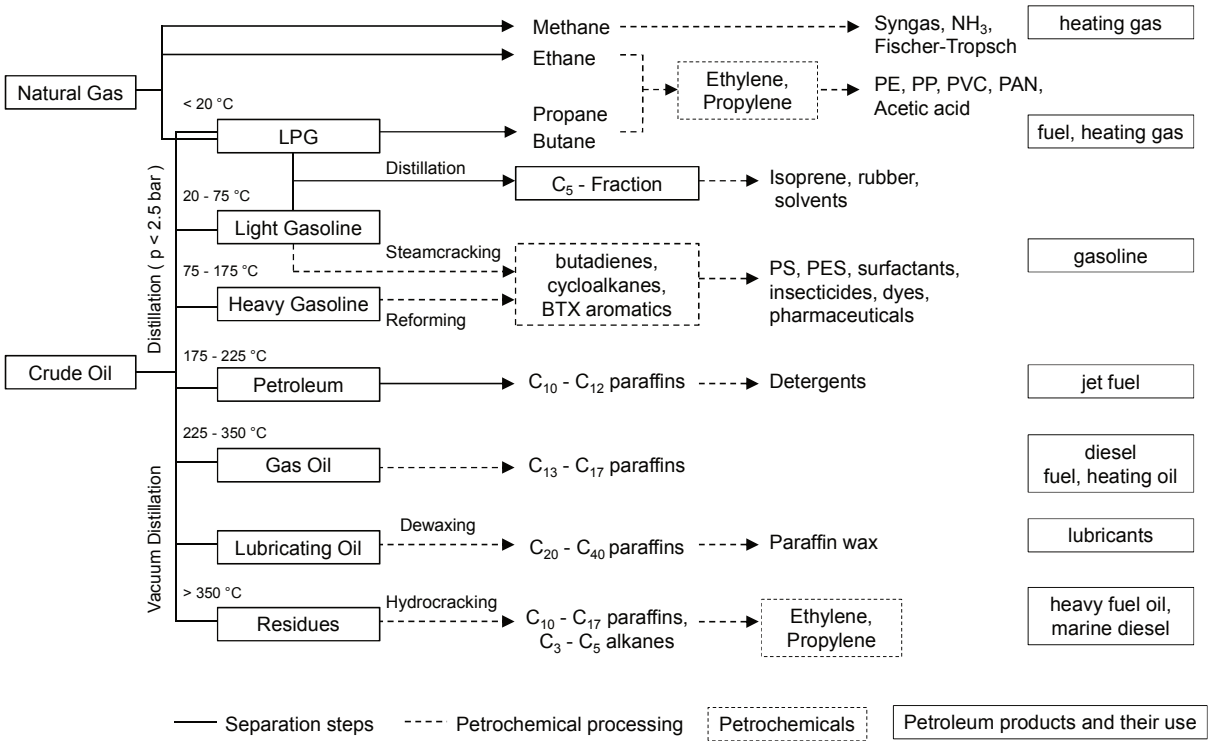

Figure 1-1: Products from crude oil and natural gas via refinery and petrochemical processing, adapted from [10] with supplemented information [18]

The diverse separation tasks related to hydrocarbon mixtures are still dominated by conventional processes, i.e., cryogenic distillation or condensation, absorption and adsorption [139]. Distillations are widely favored and the common benchmark process to compare efficiency of newly developed techniques [120]. In the processing of the light gasoline fraction for conditioning of natural gas, i.e., the separation of low boiling components methane, ethane or propane, distillation processes require high operating pressures (up to 20 bar), cryogenic temperatures (below -30 °C), a large number of trays (up to 200) and a high reflux ratio, rendering them the most energy-intensive process [44, 120]. Despite the enormous expenditure of energy and expensive operation, distillations cover 90-95 % of all separation processes in

chemical industry, thereby causing an energy consumption of approximately 40 % of the total energy consumption [62]. Only few technologies have reached competitiveness today [44].

The application of membrane-based processes has gained much interest in the last years due to their low energy consumption, simple and continuous operation, flexibility, low costs and space requirements and the avoidance of additional solvents [58]. While they are one of the major basic unit operations in liquid separations, e.g., water treatment by micro- and ultrafiltration or reverse osmosis, research is still necessary and on-going for gas separation and pervaporation processes [11]. Today's state-of-art materials for higher hydrocarbon separation, poly(dimethylsiloxane) PDMS and poly(octylmethylsiloxane) POMS, are industrially successful but with their limited selectivity and stability not competitive for all applications [139]. Particularly, the challenging fields of natural gas processing and olefin / paraffin separations are currently not feasible due to the lack of suitable materials for such harsh conditions [12].

This work was carried out in the framework of the project "Mixed-matrix membranes for gas separation" which is part of the funding activity "Technologies for Sustainability and Climate Protection – Chemical Processes and Use of CO_2" supported by the German Federal Ministry of Education and Research (BMBF). It contributes to the environmental objectives by proposing an energy-efficient membrane-based alternative to major energy-intensive processes dealing with the separation of higher hydrocarbons. The key demands for an improved separation efficiency and performance stability are addressed by the combination of different materials to form the membrane separation layer. These so-called mixed-matrix membranes (MMM) composed of a polymeric matrix with embedded inorganic fillers shall overcome drawbacks of previous membrane materials and in this respect open up new opportunities for the application of energy-efficient membrane separation technologies.

The aim of this work is the development of a MMM to be used for the selective separation of higher hydrocarbons. The work is focused on POMS as state-of-the-art polymeric matrix with binary mixtures of *n*-C_4H_{10} and CH_4 serving as model mixtures to identify suitable filler materials. Special importance is given to the applicability on an industrial scale including the development of a reliable method for a defect-free industrial production, the separation performance under varying operating conditions and the long-term stability of performance. For comparison, the use of PDMS based MMMs was investigated by D. Hülagü at the Technical University of Berlin [61]. As a supplement, a mathematical mass transfer model for the description of MMMs was

developed by V. Kramer [77]. The fitting of the model is based on the experimental results presented in this work as well as the work by D. Hülagü.

This work starts with a general overview of the conventional as well as membrane-based state-of-the-art technologies for the separation of higher hydrocarbons in Chapter 2. The fundamental basics of membrane technology for gas separations are explained in Chapter 3. The concept of MMMs will be introduced in more detail in Chapter 4 including an overview of previous works and findings. Chapter 5 describes the applied materials and methods for the production and characterisation of MMMs. Chapter 6 includes the material development steps to achieve a reproducible preparation of an appropriate thin film composite MMM material with an improved *n*-C_4H_{10}/CH_4 separation efficiency (Chapter 6.1), the characterisation of MMMs separation performance under process-related single, binary and multi-component mixed gas conditions to identify major influencing parameters (Chapter 6.2) and the evaluation of separation performance with respect to an industrial application (Chapter 6.3). Finally, the main findings are summarised in Chapter 7 and completed by an outline to future work required.

2 SEPARATION OF HIGHER HYDROCARBONS

The state-of-art technologies for the separation of higher hydrocarbons are shortly presented in this chapter. They include the conventional energy-intensive techniques, i.e., condensation, distillation, lean oil absorption and adsorption techniques, described in chapter 2.1. Environmentally friendly state-of-art membrane-based processes are illustrated in chapter 2.2. Examples for hybrid processes based on both conventional and membrane-based technologies will be given in chapter 2.4.

2.1 Conventional Separation Techniques

Conventional techniques are based on the introduction of energy to create a liquid (condensation) or vapour phase (distillation) or the addition of separating agents in form of a solid (adsorption), liquid (absorption) or vapour (stripping). Their principles, advantages and disadvantages and common applications with respect to hydrocarbon separations are summarised in Table 2-1. The selection of an appropriate process is governed by the investment and operating costs, the demand for energy, the sensitivity of components to be separated and of course the separation efficiency and attainable purities [106]. The combination of various techniques can be the most economical option to achieve high purity products. Such hybrid processes will be described in section 2.4.

Table 2-1: Overview of conventional separation technologies for hydrocarbon separations

Method	Separation Principle	Ad- / Disadvantages	Application
Distillation / Condensation	Addition of energy or flash expansion; differences in boiling points (volatility) or saturation pressure (dew point)	Widely used and studied, simple design and operation, easy to stage and scale-up, high purities; Highest energy consumption, low production rate, thermal stability of products required	Fractionation of crude oil, separation of bulk chemicals, e.g., propylene / propane or other olefins / paraffins, recovery and purification of solvents [31, 62]
Absorption	Addition of a liquid phase (absorbent); specific uptake of molecules via physi-/ chemisorption	Suitable for high feed volume rates, low (chemisorption) to high (physisorption) feed concentrations, fluctuating feed concentrations; Moderate purities (90-98%), regeneration steps, waste disposal for irreversible absorption	Removal of lower amounts of impurities or valuable products, e.g., dehydration and sweetening of natural gas, recovery of polymer resins from reactor effluent gas, removal of benzene from natural or refinery gas [62, 137]
Adsorption	Addition of a solid phase (adsorbent); specific interactions of molecules with solid surfaces allow for a steric, equilibrium or kinetic selectivity	High product purity (> 99%), high flexibility due to a variety of adsorbent materials; Complex process design, higher capital costs, regeneration steps, only for minor feed concentrations and moderate feed volume rates	Bulk gas separations, drying and product purifications, e.g., VOC removal, solvent recovery in polymer production, separation *n-*/*iso*-paraffins and light hydrocarbons [37, 69]

2.2 Membrane-based Separations

Today, the market for membrane-based gas separations is still small but shows a promising annual growth rate up to 15 % [19]. They gain increased attention due to their simple operation, low energy consumption and capital costs. In contrast to conventional techniques, no phase change or additional solvents are required. The membrane acts as a selective barrier that separates the feed mixture into permeate and retentate streams which are either depleted of or enriched in certain components. Key element is the membrane material whose affinity and specific properties determine the selectivity and thus the separation principle in terms of differences in penetrant size (porous membranes) or solubility and diffusion (dense membranes) [106]. Basic fundamentals to membrane-based gas separations are given in Chapter 3.

In most applications higher hydrocarbons are minor components and their preferential permeation and separation as permeate is desired to reduce the membrane area and recompression costs [123]. Industrial state-of-art polymers for the selective separation of higher hydrocarbons are poly(dimethylsiloxane) PDMS and poly(octylmethylsiloxane) POMS. They are widely applied for the recovery of gasoline, solvents or monomers during polymer production and the removal of VOC from vent gas or air [13]. Further materials will be discussed in more detail in chapter 2.3.

Especially at high feed concentrations and moderate purity requirements (90 – 95 %), membrane separations are often the most economic process [131]. An example is the resin degassing vent in polymer production which usually contains 15-20 % of hydrocarbon monomers. A multi-stage membrane process allows the purification up to 99 % nitrogen and the enrichment of up to 95 % propylene in the permeate. A promising but still developing market is the natural gas treatment. Basically, all drying and sweetening steps in natural gas processing can be performed with membranes but the separation of higher hydrocarbons is the most challenging [14]. It is depicted in Figure 2-1. The feed is separated by a hydrocarbon-selective membrane into a depleted retentate with required pipeline specifications, namely a hydrocarbon dew point below -2 °C and a heating value in the range of 30.2 – 47.2 MJ/m³ [43]. The permeate stream, enriched with higher hydrocarbons C_{3+}, is recompressed and the hydrocarbons removed via condensation to be used as feedstock for example for LPG production.

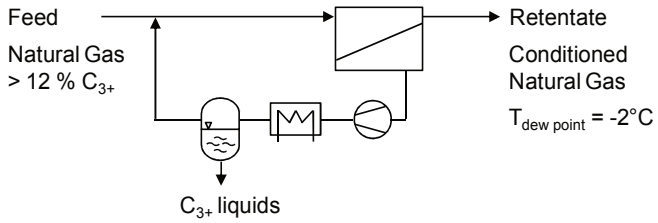

Figure 2-1: Membrane-based separation of higher hydrocarbons from natural gas

Further examples of such membrane separations are the production of fuel gas for gas engines directly on natural gas sites, in remote or off-shore applications and for operations on ship, for which the low energy demand, low space requirement and ease of operation of membrane-based processes are particularly advantageous [13]. Nevertheless, only 1% of the worldwide natural gas processing with its annual production of around 35 billion m³ is so far realized by membranes [99]. For further applications, materials with higher selectivity and stability under the harsh conditions are urgently required. An overview of the various polymeric and inorganic membrane

materials for the separation of hydrocarbon mixtures studied up to now is given in the following section.

2.3 Membrane Materials for Hydrocarbon Separations

State-of-art membrane materials PDMS and POMS are both highly rubbery polymers characterised by a solubility-selective permeation [13]. High permeability and moderate *n*-C_4H_{10}/CH_4 selectivity are reported in literature [140, 151]. The rubbery, liquid like structure allows an easy processing, low costs and a high permeability facilitating low area requirements and capital costs. However, the moderate *n*-C_4H_{10} / CH_4 mixed gas selectivity of around 14 for PDMS (25 °C) [127] often demands several membrane stages and recycle streams to achieve an adequate separation. In addition, they suffer from low stability under harsh conditions, for example, high temperature (above 100 °C) or aggressive chemicals (e.g., aprotic solvents or acids), and their susceptibility to dissolution of gas molecules into the polymeric phase [14]. Dissolved molecules act as plasticisers, decrease chain interactions and lead to swelling and softening of the polymeric structure, causing a strong impairment of selectivity and mechanical stability [94, 114, 131]. A decrease of *n*-C_4H_{10} / CH_4 selectivity from 17 to 4.5 has been reported for PDMS in consequence of swelling by dissolved hydrocarbons [139]. Glassy polymeric materials exhibit in general low permeability coefficients and a size-selective separation in favour of smaller components. Nevertheless, promising results were found for membranes based on poly(acetylenes) such as poly(1-trimethylsilyl-1-propyne) PTMSP [96] or poly(4-methyl-2-pentyne) PMP [57] or poly(cycloolefins) [53]. Especially for PTMSP, whose exceptional high free volume resembles a porous network that allows a selective surface diffusion mechanism (see section 3.3.2), a promising *n*-C_4H_{10} / CH_4 mixed gas selectivity of 35 (25 °C) accompanied by high permeability coefficients is reported in literature [57]. However, an industrial application is unlikely due to the high fabrication costs and severe problems arising from ageing phenomena, low solvent resistance, plasticization and degradation in presence of organic vapours [96].

Inorganic membranes based on carbon [130], zeolites [8, 28, 41, 110, 167], ceramic [160] or metal [66] have also been extensively studied in the last years. These materials show a superior stability under harsh conditions and a high selectivity due to a selective-surface-flow (SSF) mechanism as presented by Rao and Sircar for thin microporous carbon layers on support structures [149]. Due to the small pore diameters, the adsorption of gas molecules can block the pores for non-condensable components [149, 165]. These mechanisms are also present in

mesoporous glass [152] and zeolite materials based on MFI structures like silicalite or ZSM-5 [28]. Wohlrab *et al.* investigated the *n*-C_4H_{10}/CH_4 separation performance of a MFI membrane on α-Al_2O_3 support and found as best a separation factor of around 11.3 (defined as molar ratio *n*-C_4H_{10} / CH_4 in permeate vs. retentate) at an elevated temperature, low pressure difference and in the presence of a sweep gas [167]. However, inorganic materials are much more expensive, often with manufacturing costs up to 10 times higher compared to polymeric materials [11]. Their brittleness causes severe problems to process them into thin films and transfer into defect-free industrial scale modules. Besides, the superior temperature stability can often not be utilized due to inappropriate sealing materials [131, 142]. The industrial application of inorganic membranes is so far limited to ceramic materials in filtration processes and niche applications such as the enrichment of uranium [106].

To overcome the limitations of polymeric and inorganic materials, a new approach is followed by hybrid mixed-matrix materials (MMM) combining both polymeric and inorganic phases. Among the investigated MMMs for the separation of higher hydrocarbons are glassy polymers PTMSP, PMP or Teflon® AF2400 in combination with silica [57, 96] or TiO_2 [170] and rubbery PDMS with various fillers, i.e., zeolites [29, 154, 155], silica [52, 74, 112] or activated carbon [61, 87]. Very different, sometimes even contradictory effects have been reported. While improvements are generally expected at high filler loadings surpassing the percolation threshold, this often results in brittle, unstable films and the formation of non-selective voids [39, 50, 175]. Lower contents of inorganic particles are reported to positively affect the stability. For instance, the addition of fumed silica resulted in a reduced ageing of PMP [170] and a reduced plasticization of PTMSP [96]. A lower tendency to swelling was found by Nunes *et al.* for PDMS filled with silica nanoparticles from a sol-gel reaction of TEOS but the *n*-C_4H_{10}/CH_4 mixed gas selectivity of 10 at 30 °C (mixture composed of 83.3 vol% CH_4, 11.1 vol% C_3H_8 and 5.6 vol% *n*-C_4H_{10}; 1 bar feed pressure) was still far below the state-of-art. [112]. Promising results were reported for the addition of fumed silica to PMP showing a simultaneous increase of both permeability and *n*-C_4H_{10} / CH_4 mixed gas selectivity up to 26 at 25 °C (2 vol% *n*-C_4H_{10} in CH_4, 10 bar feed pressure) [57]. The potential of MMMs composed of PDMS and activated carbon for the separation *n*-C_4H_{10}/CH_4 has been investigated by Kramer and Hülagü on a lab-scale, yet no successful improvement was reported [61, 87]. Almost all research has been focused on the lab-scale formation of films to investigate effects of filler addition, mainly under ideal conditions. The performance under real operating conditions thus has to be carefully revised. Especially the transfer of lab-scale production into technical scale thin-film composite membranes is considered

highly problematic. A successful application of industrial scale membrane modules based on mixed-matrix materials has not been reported yet.

Despite all research, almost all industrial processes applied today for the separation of higher hydrocarbons and organic vapours are based on rubbery PDMS and POMS [13]. All processes would benefit from a higher selectivity of the membrane material as this allows the reduction of the required membrane area, the costs for compression or vacuum and the energy which, in turn, would increase the competitiveness against conventional processes. Besides, an improved stability to withstand the challenging operating conditions is often required.

2.4 Hybrid Processes

For many applications, particularly the removal of VOCs and olefin/paraffin separations, a vivid competition between the various techniques exists [44, 62, 120]. Their combination to hybrid processes is highly advantageous as it allows each unit to operate at its preferred conditions and thus to improve on both, energy efficiency and product purity. In particular, membrane-based separations do not perform a separation into two pure product streams and often several stages are necessary to achieve an appropriate purity. The combination of membrane and conventional separation units is thus widely established in industry, e.g., the combination with distillation for olefin/paraffin separation [120] or the combination with condensation for recovery of hydrocarbons in the natural gas treatment (see Figure 2-1) [13, 131]. In the recovery of monomers during polymer production, only feasible under cryogenic conditions, the addition of a membrane unit reduces the cooling demand while the condensation simultaneously yields optimum feed conditions (cold, saturated gas) for a solubility selective membrane allowing a higher recovery of polypropylene (> 99.8 %) and a higher purity of nitrogen (> 99 %) in the residual vent-gas [114]. A further widely applied hybrid process is the combination of absorption and membrane separation units with a pressure swing adsorption (PSA) unit as final polishing step for the recovery of gasoline or other organic vapours at tank storage sites or refineries [13, 115]. The organic vapour / air mixture is compressed and saturated in an absorption unit with hydrocarbon vapour to surpass the flammable range of 3 - 15 % hydrocarbon in air. The saturated vapour is fed into the membrane unit equipped with a hydrocarbon selective membrane. It enriches the hydrocarbons on the permeate side leaving a stripped retentate below the flammable range with around 0.5 – 2 % hydrocarbons. A further purification step is necessary to achieve the hydrocarbon concentration below 50 mg/m³ as demanded by the German TI Air

[24, 113]. Most economical is a PSA unit using the high pressure of the membrane unit for adsorption and the vacuum on permeate side generated by a liquid ring vacuum pump for desorption. Around 60 % of all gasoline vapour recovery units in Germany apply such an economical and safe hybrid process design presented in Figure 2-2 [114].

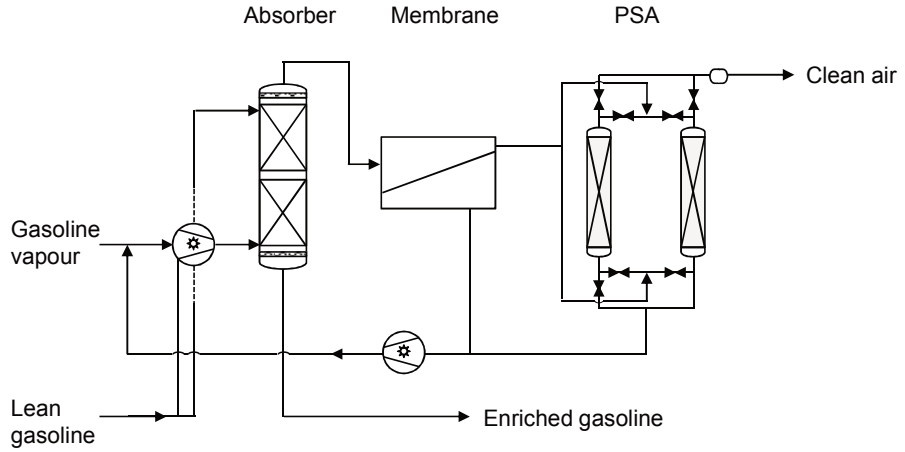

Figure 2-2: Hybrid process design for gasoline recovery according to Ohlrogge *et al.* [114]

3 MEMBRANE-BASED GAS SEPARATION

This chapter presents the basic fundamentals and principles for membrane-based separations. After a brief definition and classification in section 3.1, membrane materials and corresponding transport phenomena will be described in section 3.2 and 3.3. Basic criteria for module and process design are given in section 3.4.

3.1 Classification of Membranes

Membranes are defined as thin interfaces which act as selective barriers and allow the preferential permeation of specific components. There are several criteria for their classification [131]. An overview is given in Table 3-1. Besides the material, the membrane structure strongly impacts the separation mechanism. Typical structures are schematically shown in Figure 3-1 [11]. Symmetrical membranes are characterised by a homogeneous cross-section which can be either porous or dense. Asymmetrical membranes show a non-uniform cross-section with a finer porous structure towards the membrane surface. They can be composed of one (integral asymmetrical) or more (thin-film composite) materials. In thin film composite (TFC) membranes, a very thin active separation layer is deposited on porous and non-woven support structures providing the necessary mechanical stability. The layers of different material and porosity allow for the independent optimisation of each layers' function and thus the economic industrial application in membrane separations.

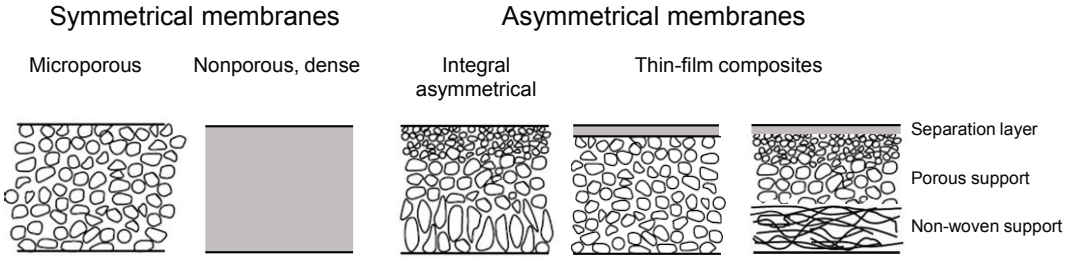

Figure 3-1: Typical symmetrical and asymmetrical membrane structures (adapted from [11])

Table 3-1: Classification of membrane-based separation processes [131]

Classification criteria	Category	Description
Membrane material	Natural / synthetic	Biological (e.g., cell walls) / artificial
	Organic / inorganic	Polymers / metal, ceramic, carbon, glass
	Homogeneous / heterogeneous	Pure materials / hybrid MMM
	Polar / non-polar	Hydrophilic / hydrophobic
Membrane surface	Porous	Surface pores > molecular dimension
	Dense	Surface pores < molecular dimension
Membrane structure	Symmetrical	Uniform composition and structure
	Asymmetrical (integral, composite)	Layers with different porosity
Membrane geometry	Flat	Planar sheets
	Tubular	Cylindrical hollow fibers or capillaries
Driving force	Pressure difference	Filtration, reverse osmosis
	Partial pressure or fugacity difference	Gas permeation, pervaporation
	Concentration difference	Dialysis
	Electric potential difference	Electrodialysis
Separation task	Gas / gas	Gas and vapour permeation
	Gas / liquid	Pervaporation
	Liquid / liquid	Micro-, ultra-, nanofiltration, dialysis

3.2 Membrane Materials and Preparation

Basically, all materials can be used as membrane material as long as they can be processed into thin layers and exhibit a selective permeation. The choice strongly depends on the application. Membranes based on polymeric films are by far the most important and key element for a variety of applications including water purification, gas and vapour separation, food packaging, fuel cells, microelectronics, protective clothing or medical applications [117]. Besides the diversity of materials, less than 10 polymers account for 90% of all industrial membrane gas separation applications today [12]. The selection is based on specific properties, i.e., chemical structure, molecular weight, spatial arrangement and interactions [131]. An important parameter is the state of polymer under operating conditions which determines its physical properties and permeation behaviour. For detailed information regarding polymer chemistry please refer to literature [45, 94, 106, 121]. Depending on the desired membrane structure (see Figure 3-1) different preparation

techniques can be applied [106]. Dense symmetric membranes are prepared via solution casting or thermal melt-pressing forming films down to 20 μm thickness. These are only important for lab-scale characterisations. Microporous symmetric membranes for microfiltration can be prepared via track-etching, template-leaching or film expansion techniques. Various techniques are available for asymmetric membranes. Most important is the phase inversion mechanism developed by Loeb and Sourirajan. The precipitation of a polymeric casting solution into a non-solvent bath yields integral asymmetric membranes used for micro- and ultrafiltration, reverse osmosis, gas separation or as support structures, e.g., for gas separation membranes. Thin film composite membranes are prepared via solution coating or interfacial polymerisation of the active separation layer on microporous support structures [11].

Common inorganic materials are ceramics, zeolites, carbon, glass, aluminium, metals or metal oxides. They allow for a high selectivity and superior resistance against chemical, thermal and mechanical conditions and thus are suitable for aggressive feed media or corrosive conditions and high temperature applications. Inorganic membranes are usually prepared via extrusion, pressing or suspension coating and sintering, chemical vapour deposition or a sol-gel process to achieve nanoporous structures [66, 142]. Carbon membranes are further prepared via compression of carbon powder or pyrolysis of polymeric precursor membranes. Often additional treatments for a further densification or surface modification are necessary [106]. Both, polymeric and inorganic, materials have been combined in the concept of hybrid mixed-matrix materials illustrated in Figure 3-2 and discussed in chapter 4.

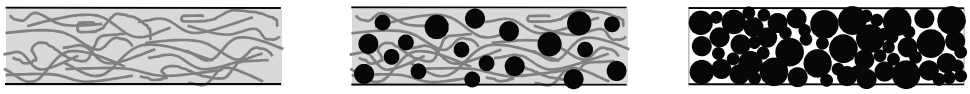

Figure 3-2: Membrane morphologies based on polymeric, inorganic and hybrid mixed matrix materials

3.3 Transport Phenomena

Gas separation by membranes depends on the different permeation rates of components resulting from a different mobility, concentration or external driving forces. According to the main separation principles, membranes are roughly distinguished into porous, dense and facilitated carrier membranes as illustrated in Figure 3-3. Facilitated membranes based on an

active transport by specific carrier molecules will not be discussed in this work. Fundamental equations for dense and porous membranes are given in section 3.3.1 and 3.3.2, respectively. These are also the basis for the later discussed hybrid MMM in chapter 4.3. Additional phenomena affecting the overall separation performance are briefly discussed in section 3.3.3.

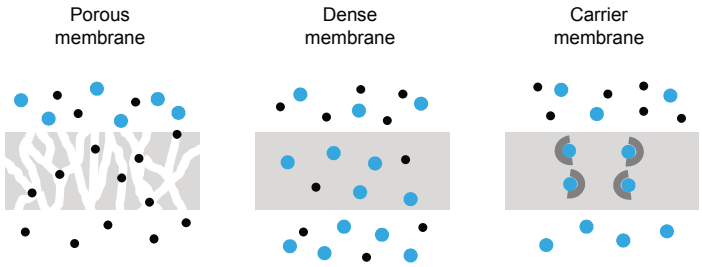

Figure 3-3: Membrane structures and gas transport mechanisms

3.3.1 Transport in Dense Membranes

Membranes with openings in the range of the thermal motion of polymeric chains are termed dense membranes [168]. The permeation strongly depends on the material itself and the specific interactions between gas molecules and the polymeric matrix [106].

3.3.1.1 Ideal solution-diffusion model

According to the ideal solution-diffusion model illustrated in Figure 3-4, the transport is composed of three main steps: 1) solution in the polymeric material at the high pressure side of the membrane, 2) diffusion of gas molecules to the low pressure side and 3) desorption into the permeate stream at the low pressure side.

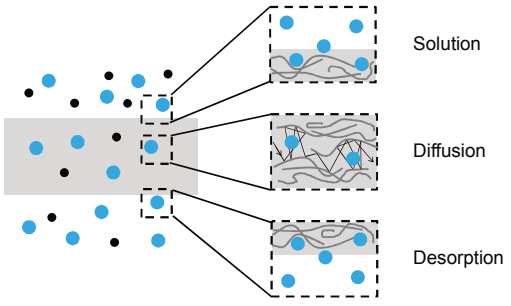

Figure 3-4: Transport steps in dense membranes according to the solution-diffusion model

The membrane is assumed to be in a thermodynamic equilibrium with the adjacent, ideally mixed fluid phases. Further, solution and desorption are assumed to be much faster than diffusion rates

[4, 131]. In similarity to Fick's first law, a general description of flux is given by the product of concentration $c_{i,M}$ of component i inside the membrane, its mobility and driving force as stated below in equation (3.3-1) [131].

$$\dot{n}_i'' = -c_{i,M} \cdot \frac{D_{0i,M}}{RT} \cdot \frac{\partial \mu_{i,M}}{\partial z} \qquad \textbf{(3.3-1)}$$

The rate of transport depends on the concentration $c_{i,M}$ of diffusing molecules inside the polymer given by the thermodynamic equilibrium of sorption. The mobility, characterised by the thermodynamic diffusion coefficient $D_{0i,M}$, depends on characteristic properties of the membrane material and dimensions of the gas molecules. The mechanisms of sorption and diffusion will be discussed in more detail below. The driving force results from differences in operating conditions between the two membrane surfaces, particularly pressure, temperature and concentration, or, more general, the gradient of the chemical potential $\mu_{i,M}$. For low concentrations of gas inside the membrane within the limit of Henry's law (see section 3.3.1.2) and constant solubility and diffusion coefficients, integration of (3.3-1) gives the basic equation for permeation in a dense gas separation membrane of thickness δ in (3.3-2). The fugacity difference between feed ($f_{i,F}$) and permeate ($f_{i,P}$) side corresponds to the driving force.

$$\dot{n}_i'' = \frac{D_{0i,M} \cdot S_i}{\delta} \cdot \left(f_{i,F} - f_{i,P}\right) = \frac{P_i}{\delta} \cdot \left(f_{i,F} - f_{i,P}\right) = L_i \cdot \left(f_{i,F} - f_{i,P}\right) \qquad \textbf{(3.3-2)}$$

The product of the diffusion coefficient $D_{0i,M}$ and the solubility coefficient S_i is termed permeability P_i. Technically applied thin film composite membranes have very thin separation layers with a thickness difficult to accurately determine. The permeability coefficient is thus related to the membrane thickness as expressed by the permeance L_i. While the permeability describes the intrinsic property of the polymeric material, the permeance corresponds to a characteristic property of the membrane describing its productivity. The ratio of permeances $L_{i,j}$ or permeability coefficients $P_{i,j}$ of components i and j gives the membranes' selectivity, equation (3.3-3). It characterises the effectiveness or the capability of a membrane to separate two gases [11]. With respect to equation (3.3-2), the selectivity can be divided into the product of diffusivity selectivity and solubility selectivity.

$$\alpha_{i/j} = \frac{L_i}{L_j} = \frac{P_i}{P_j} = \frac{D_i}{D_j} \cdot \frac{S_i}{S_j} \qquad \textbf{(3.3-3)}$$

The equations above are derived for ideal conditions, that is, constant diffusion and solubility coefficients independent of changes in the concentration of a component and the lack of

interactions or coupling effects between mixture components [131]. These assumptions might be valid for permanent gases but strong deviations are observed in presence of condensable gases or vapors. Especially in rubbery polymers, diffusion and solubility coefficients are highly dependent on the concentration of condensable components inside the membrane and swelling affects the diffusion of all components [162].

3.3.1.2 Sorption in Polymers

The sorption of gas molecules into polymers results from a condensation of gas followed by mixing of the condensed gas with polymer chain segments. It depends on specific interactions between the gas molecules and the polymer and usually increases with the condensability of components, represented for example by the critical volume or the boiling point (see Table A–1 in Appendix A) [162]. The equilibrium concentration of component i inside the polymer can be expressed by the sorption isotherm. Depending on the specific interactions between the dissolved gas and the polymer, different shapes of isotherms are possible.

The simplest relation is given by Henry's law in equation (3.3-4) stating a linear increase of the concentration of a component with its activity. The proportionality is expressed by the Henry coefficient H_i or by its reciprocal, the solubility S_i.

$$c_{i,M} = \frac{a_i}{H_i(T)} = S_i(T) \cdot f_i \qquad \textbf{(3.3-4)}$$

Such a linear correlation is only valid for low activities or low concentrations of the component inside the polymer. Significant deviations occur for condensable components in rubbery polymers. The isotherm shows an increasing curvature with increasing activity of the component. It can be described by the thermodynamic model for mixing proposed by Flory & Huggins, equation (3.3-5), with ϕ as volume fractions, $\overline{V}$ as partial molar volumes of the gas component i and polymer m, respectively, and χ_i as interaction parameter [118].

$$\ln a_i = \ln \phi_i + \left(1 - \frac{\overline{V}_i}{\overline{V}_m}\right) \cdot \phi_m + \chi_i \cdot \phi_m^2 \qquad \textbf{(3.3-5)}$$

A curvature opposite to the Flory-Huggins type isotherm is observed for the sorption in glassy polymers. It is expressed by the dual-sorption model combining a Henry type solution and a Langmuir type adsorption in the micro cavities present in the rigid glassy state.

$$c_i = S_i \cdot f_i + \frac{c_{i,max}^{L} \cdot b_i \cdot f_i}{1 + b_i \cdot f_i} \qquad \textbf{(3.3-6)}$$

3.3.1.3 Diffusion in Polymers

Diffusion in polymers can be explained by the presence of free volume and the probability of forming a free volume element large enough to accommodate the specific gas molecule [168]. The highly flexible chain segments in rubbery polymers facilitate the formation of free volume elements while the rigid structure in glassy polymers inhibits this. The rate of diffusion depends on the state of polymer or rather the mobility of polymeric chain segments, the dimensions of diffusing gas molecules, the concentration of gas molecules inside the polymer and the operating temperature and pressure [162]. Equation (3.3-7) correlates the thermodynamic diffusion coefficient D_i to the fraction of free volume ϕ_{FV} with A_f depending on the size and the shape of gas molecules and $B_{d,i}$ relating to the minimum free volume necessary to allow a diffusional jump of the gas molecule [106]. The mobility of a gas molecule is thus depending on the probability that a free volume large enough to accommodate the gas molecule is formed in its vicinity. A higher fraction of free volume enhances this probability as expressed by the exponential term in equation (3.3-7).

$$D_i\left(T, p, \varphi_{1\ldots n}\right) = A_f \cdot RT \cdot \exp\left(-\frac{B_{d,i}}{\varphi_{FV}}\right) \qquad \textbf{(3.3-7)}$$

The diffusion coefficient decreases with increasing size of gas molecules, often expressed by the critical volume or the collision diameter, as larger gas molecules require larger free volume elements to perform jumps [162].

3.3.1.4 Free Volume Model

An extension of the solution-diffusion model has been expressed in the free volume model by Fang & Stern which accounts for the concentration dependency of diffusion coefficients [49]. The free volume element is assumed to result from the thermal movements of polymeric chain segments as a function of temperature, pressure and concentration of the gas components. The model has been extended by Alpers to multi-component mixtures and impacts of the real gas behaviour and high pressure [4]. The free volume model for a multi-component mixture is given in equation (3.3-8). Parameter L_{i0}^{∞} corresponds to the permeance at indefinite dilution, more

precise, the pressure approaching zero and the temperature approaching infinity. The other parameters will be explained below in more detail.

$$L_i(T,p,y_i) = L_{i0}^{\infty} \cdot \exp\left[\left(\frac{-E_{P,i}}{RT}\right) + \sum_{j=1}^{n}\left(\left(\frac{\sigma_i}{\sigma_i}\right)^2 \cdot m_{j0} \cdot \exp\left(m_{jT} \cdot T\right) \cdot f_{i,m}\right)\right] \cdot \exp\left[\left(\frac{\sigma_i}{\sigma_k}\right)^2 \cdot \beta_k^* \cdot \left(p_F - p_P\right)\right] \quad \textbf{(3.3-8)}$$

Influence of temperature — Influence of concentration — Influence of high pressure

Influence of Temperature

Temperature has a strong influence on permeation as both, diffusion and solubility, are affected. It can be described by an exponential trend following the equation of Arrhenius. The activation energy for permeation $E_{P,i}$ is the sum of the activation energy for diffusion $E_{D,i}$ and the enthalpy of solution $\Delta H_{s,i}$.

$$E_{P,i} = E_{D,i} + \Delta H_{s,i} \quad \textbf{(3.3-9)}$$

While $E_{D,i}$ is always positive and diffusion increases with temperature due to the increased chain mobility, $\Delta H_{s,i}$ depends on the specific gas component and the membrane material. It is composed of the molar heat of condensation ΔH_{cond} and the molar heat of mixing ΔH_{mix}. For non condensable gases, the value of $E_{D,i}$ is generally much larger than ΔH_s and permeation increases with temperature. For condensable components, permeation decreases with increasing temperature as their exothermic condensation yields a highly negative $\Delta H_{s,i}$.

Influence of Concentration

The swelling of a polymeric matrix in consequence of the solution of gas molecules leads to the increase of free volume. The parameter m describes the dependency of permeation on the concentration of dissolved gas molecules within the polymeric matrix. The concentration is related to the effective average fugacity $f_{i,m}$ (see 3.3.1.2). The parameter m is temperature dependent following an exponential relation. Subscripts 0 and T refer to the temperatures at reference state (T = 0 K) and under operating conditions (T). For multi-component mixtures, the coupling of driving forces and fluxes is expressed by the summand and the influences of the different molecule sizes is accounted for by the Lennard-Jones molecule diameters σ of all n components present in the gas mixture.

Influence of High Pressure

High pressure conditions can impair the membrane structure via compaction causing the decrease of free volume and thus diffusivity [49]. The compression is described in the last term in equation (3.3-8) in relation to a reference gas k with β_k^* as the compressibility factor, p_F as the feed pressure and p_P as the permeate pressure. Besides the impact of compaction, high pressure conditions cause significant deviations from the ideal gas behaviour for condensable components that influence the driving force of permeation [114].

3.3.2 Transport in Porous Membranes

Porous membranes are characterised by a fixed structure with holes on the surface and over the whole thickness. A common classification by IUPAC distinguishes into macropores (d_p > 50 nm), mesopores (d_p = 2 - 50 nm) and micropores (d_p = < 2 nm) [135]. The transport depends on the pore size and geometry as well as the molecular size of gas mixture components. Different transport regimes can be identified according to the Knudsen number Kn, defined as the ratio of mean free path λ_m of a gas molecule without collisions and the pore diameter d_p [26]. The main mechanisms are illustrated in Figure 3-5 and briefly described below.

Molecular Diffusion

At very low Knudsen numbers (Kn « 1) or elevated pressure gas molecules predominantly collide with other gas molecules resulting in molecular or bulk diffusion mechanisms (see Figure 3-5 (a)). According to Fick's first law, the molar flow in binary mixtures is proportional to the negative concentration gradient over the length of the pore with the binary molecular diffusion coefficient $D_{i,m}$ as proportionality constant. Additional parameters such as porosity ε and tortuosity τ account for relative pore volume and non-straight cylindrical pores.

Viscous Flow

The presence of a pressure gradient induces a non-selective viscous or convective flow that overlaps the mechanisms of diffusion (Figure 3-5 (b)). A viscous flow can be described as function of structural parameters (porosity, tortuosity, pore diameter), viscosity, temperature and pressure, i.e., by correlations of Hagen-Poiseuille [131].

Knudsen Diffusion

At very high Knudsen numbers (Kn » 1) or low pressures, collisions with the pore wall are dominant and molecules are transported according to their thermal mobility via Knudsen diffusion (Figure 3-5 (c)). Equations are based on the kinetic gas theory. Knudsen diffusion is slightly selective with the separation factor estimated by the square root of the inverse ratio of molecular weights [131]. The mechanism is important for the description of porous support structures applied for thin film composite membranes.

Surface Diffusion

A strong interaction of gas molecules with solid surfaces can result in their adsorption and a transport along the pore wall due to a surface concentration gradient. This is illustrated in Figure 3-5 (d). The molecules are assumed to jump along adsorption sites. Separation results from different adsorption energies and different diffusion velocities, represented by the surface diffusion coefficient $D_{i,s}$.[66]. Detailed studies have been performed by Seidel-Morgenstern and co-workers [152].

Capillary Condensation

The presence of condensable gases and strong adsorption energies can cause the formation of multi-layers and a progressively filling of pores with condensed liquid, particularly present in small pores (diameter < 15 Å) [37]. As illustrated in Figure 3-5 (e), the liquid adsorption layer can block the transport for other gas molecules allowing a high selectivity [66]. Capillary condensation can be described by the Kelvin equation [26].

Activated Diffusion and Molecular Sieving

In micropores in the range of the molecular dimensions, transport is controlled by the interactions of gas molecules with the pore walls. As every motion requires energy for activation, this mechanism is termed activated diffusion. It is highly temperature dependent and allows a selective transport based on the shape and size of gas molecules and their interactions with pore walls [26]. If the size of pores is in between the sizes of gas molecules, a sieving or size exclusion mechanism allows a very sharp separation, see Figure 3-5 (f).

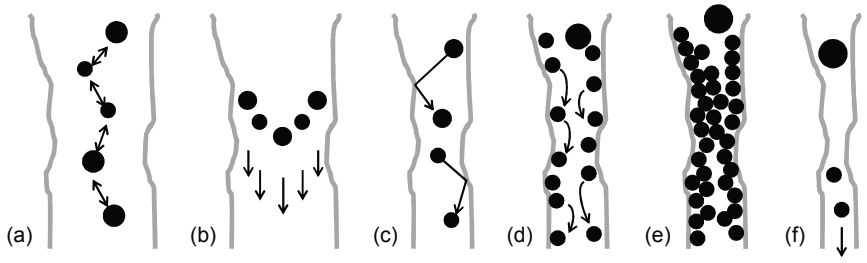

Figure 3-5: Transport mechanisms in porous membranes: (a) molecular diffusion, (b) viscous flow, (c) Knudsen diffusion, (d) selective surface diffusion, (e) capillary condensation and (f) molecular sieving (adapted from Burganos [26])

3.3.3 Additional Transport Phenomena

The actual performance of a membrane is often not ideal and constant over time as additional transport resistances impact the overall trans-membrane driving force and the permeation. Some important phenomena are described below.

Concentration Polarisation

The selective permeation causes a depletion of the more permeable component on the feed side and its enrichment in the permeate stream. This results in the formation of a concentration gradient and a boundary layer that decreases the actual driving force and overall flux [88]. The impact can be minimized by high feed flow velocities to ensure a sufficient mixing, low stage-cuts or the choice of a less permeable membrane material [131].

Joule-Thomson Effect

Gas permeation through a membrane resembles an isenthalpic expansion. It can induce a large temperature change in presence of real gases known as the Joule-Thomson effect. The extent is characterised by the Joule-Thomson coefficient with a negative coefficient corresponding to a decrease of temperature [131]. As permeation is highly temperature dependent, the Joule-Thomson effect can strongly impact the separation performance and has to be taken into account in the process design for industrial applications.

Permeate Pressure Drop

Pressure drops are the result of friction and dissipation during the diffusion through porous substructures. They cause a decrease of the driving force and thus the overall permeation. This phenomenon can normally be neglected at a high feed pressure, but applications with low permeate pressure down to vacuum are highly sensitive [131].

3.4 Membrane Module and Process Design

The industrial application of membrane-based separations requires configurations which allow the easy handling and integration of large membrane areas into the process design [1]. This is realized by modules in which the membrane is either applied as flat sheets or tubular hollow fibres [106]. General requirements are a high packing density, uniform flow distribution, low pressure drops, minimization of boundary layer formation, mechanical, thermal and chemical stability, ease of maintenance and cleaning, possibility to replace the membrane material and low manufacturing costs [1, 131]. Most common for hydrocarbon separations are envelope type and spiral wound modules, both based on flat sheet membranes [21]. The design and flow pattern of the GS envelope type module is exemplary depicted in Figure 3-6.

The material is fabricated into envelopes composed of two membrane sheets with the active layers facing the outside and a porous spacer in between to ensure channels for the permeate flow. The sheets and spacer are glued or welded along the edges. The module is composed of a pressure vessel equipped with a stack of membrane envelopes and feed spacers around a perforated permeate pipe. Baffle plates divide the stack into compartments with a flexible number of envelopes to ensure a constant flow velocity and thus enabling the minimization of boundary layer and polarisation effects [21].

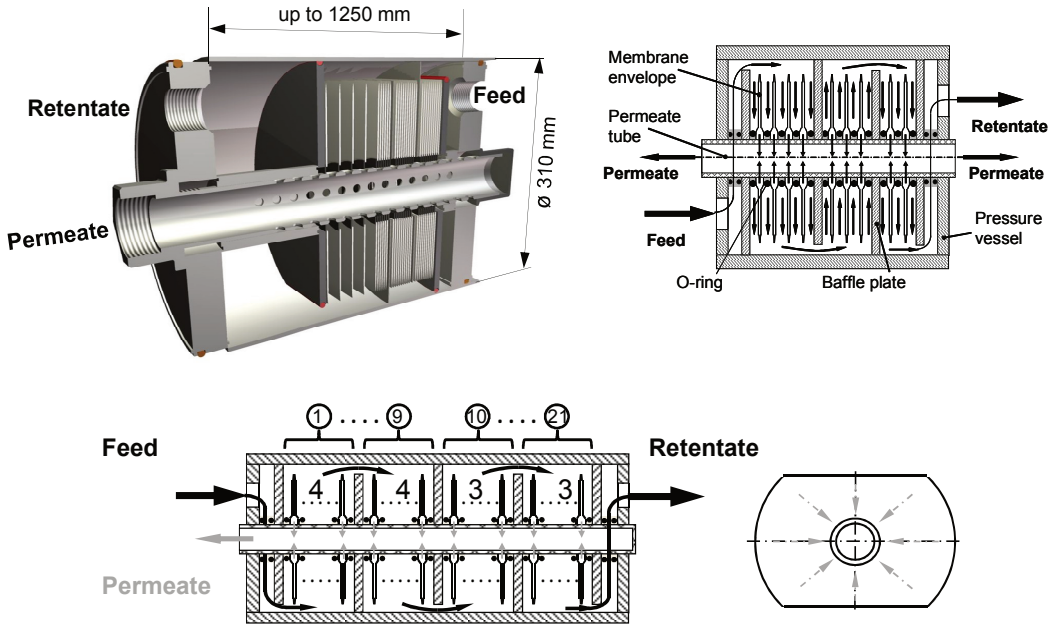

Figure 3-6: Design of the HZG envelope type membrane module for gas separation with schematic representation of the flow directions within the module and the membrane envelopes [21]

A suitable process design is nearly as important for an economic operation as the membrane material itself. The simplest set-up is a one-stage system with the membrane module separating the feed into permeate and retentate. A feed compressor, permeate vacuum pump or both generate the driving force. Most industrial separations require more complex designs to achieve sufficient separation. Modules are arranged in series or parallel to multi-stage and multi-step systems. More information regarding the membrane module and process design can be found in literature [11, 106, 113, 131].

4 MIXED-MATRIX MEMBRANES

The keen competition among separation technologies evokes an ongoing challenge to improve or develop new membrane materials with outstanding and stable separation performance. A new concept of material research is followed by the concept of hybrid mixed-matrix membranes (MMM) introduced in this chapter. The potentials and challenges are presented in 4.1, followed by materials and methods of preparation in 4.2. The permeation behaviour and predictive models for the separation behaviour are described in 4.3.

4.1 Potentials and Challenges

MMMs are composed of a polymeric matrix in which solids, liquids or fillers of both types are embedded [85]. In this work, only MMMs based on solid filler particles will be discussed. The concept, illustrated in Figure 4-1, aims to exploit advantages of both polymeric and inorganic materials via synergistic effects. As stated in 2.3, promising inorganic materials are unlikely to achieve industrial application due to their comparatively high costs and severe fabrication problems while polymeric materials are often not sufficiently selective and stable under harsh conditions [11].

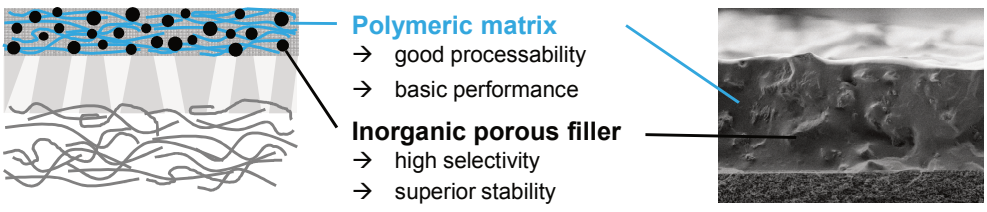

Figure 4-1: Potential of mixed-matrix membranes

In general, the addition of filler materials aims to maintain, extend or modify bulk or surface properties of the polymer, to stabilize during processing and under operating conditions and induce application-oriented properties. As a result, an improved separation performance in terms of permeability and selectivity, mechanical, thermal and chemical stability or even newly gained

properties such as conductivity or coloring can be evoked. The concept may sound simple and highly promising but represents a great challenge. Not only has the selection of materials to be carefully addressed, but also their merging into defect-free structures realized to achieve the transfer of pure material properties into the assembled MMM.

Different MMM morphologies can result from the incorporation of inorganic phases as illustrated in Figure 4-2. Most research is focused on a homogeneous dispersion of spherical (a), non-spherical (b) or flake-like (c) particles. Further, particles of different shape or size can be combined (d), particles can be concentrated to form surface layers (e) or electrochemically aligned in case of flake-like fillers (f).

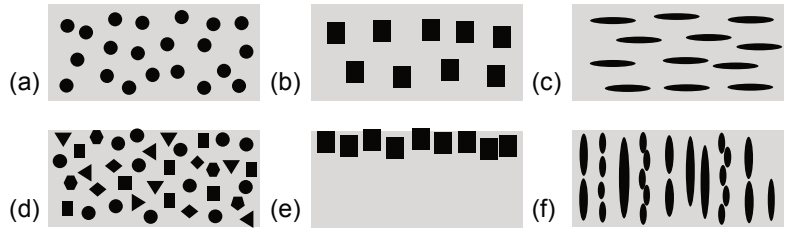

Figure 4-2: Structures and morphologies of MMM separation layers

The most important key factor for a successful MMM formation is the interface between the continuous polymeric matrix and the dispersed filler phase [85]. Possible interfacial morphologies are presented in Figure 4-3. Ideally, a good compatibility between both materials exists that allows a simultaneous increase of selectivity and permeability with an increasing filler content. Poor wetting of the filler surface by polymeric chains due to weak interactions results in the formation of non-selective voids. Voids larger than gas molecules, a "sieve-in-a-cage" morphology, cause a by-passing of filler particles. Voids on the molecular range result in a "leaky interface" with an increased permeability and a decreased selectivity. The presence of particles can induce strong interactions with the polymeric chains. As a result, a rigidified layer in the vicinity of filler particles is formed, characterized by a higher selectivity but decreased permeability. Finally, polymeric chains, especially highly flexible rubbery chains, can penetrate into the porous structure and block the transport through the porous system or the access to sorption sites resulting in a decreased permeability.

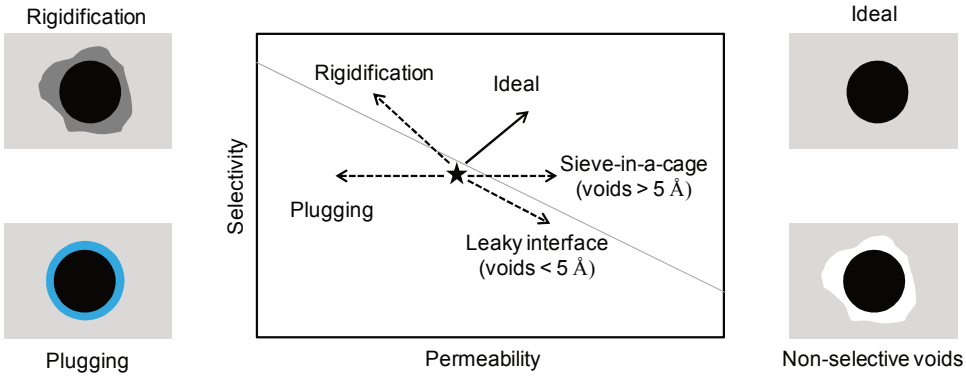

Figure 4-3: Influence of MMM interface morphology on separation performance (adapted from Moore [102])

To summarise, the main challenges besides a proper material selection are the formation of an ideal interface structure without non-selective voids or rigidified polymer layers, a good adhesion but no plugging of pores or adsorptive surface sites, a good dispersion of particles without agglomeration or sedimentation and the realization of high filler loadings to exceed the percolation threshold, preferably in ultrathin separation layers. The latter is especially important with regard to the technical scale applications based on thin film composite membranes. A successful realization of all these demands has not yet been reported in literature, especially no transfer and application into industrial scale.

4.2 Materials and Production

A great variety of MMM material combinations is presented in numerous research studies. The appropriate selection of the polymeric and filler phase is crucial for a successful enhancement of the separation performance [79]. The polymeric matrix determines the minimum performance in absence of defects. Its performance should be close to the upper bound limit in order to ensure the best improvement [174]. The matrix should allow a good compatibility with the filler material to minimize interfacial defects, facilitate and maintain the dispersion and restrain costs [85]. The permeability has to be carefully adapted to prevent a starving or by-passing of filler particles [99]. Best results are often found for similar ranges of the matrix and filler permeability. Both, rubbery or glassy polymeric materials can be applied. The flexibility of rubbery polymers usually facilitates a good contact and processability but simultaneously can cause a blockage of pores or the adsorption sites of filler particles [73, 9]. The most studied rubbery matrix polymer is PDMS, for which the addition of filler particles mainly aims to improve the selectivity and the stability

against swelling. Investigations mostly deal with separations O_2/N_2 [67, 154], CO_2/N_2 [9], CO_2/CH_4 [42] or pervaporation [2, 68, 163]. Among studied glassy polymers are Ultem® [111, 174], Matrimid® [91, 164], other polyimides [38, 59, 82, 84], cellulose acetate [78], PTMSP [35, 72, 96], PMP [57, 169], Teflon™ [97], polycarbonates [144] and polysulfones [16, 81, 104]. Their good selectivity is highly promising but their rigid character even more challenging. The polymeric chains are often not able to fully surround the filler particles resulting in defective interfaces (see Figure 4-3). The addition of filler particles to glassy polymers usually aims to affect chain packing to improve permeability.

Among the investigated inorganic filler materials are zeolites, colloidal or fumed silica, carbon based materials like carbon molecular sieves (CMS), carbon black, activated carbon, graphene or carbon nanotubes (CNTs), layered silicate, metal-oxides or new classes based on well-defined nanostructured frameworks such as metal-organic frameworks (MOF) or zeolitic-imidazolate frameworks (ZIF) [51, 119]. Table 4-1 gives an overview of inorganic filler materials studied for MMM preparations so far. Non-porous particles usually affect the chain packing density, provide additional sites for cross-linking or induce coloring effects, electrical conductivity or catalytic properties [35]. Often, a decrease in permeability is reported due to longer, more tortuous pathways, in particular for fillers with high aspect ratios [15, 33, 34]. The addition of active porous particles aims to evoke additional transport mechanisms to improve the overall separation performance. Most common are microporous zeolites or CMS that facilitate a sieving via steric or kinetic effects. In contrast, mesoporous adsorbent particles are able to induce a highly selective surface flow (SSF) mechanism in favour of large, condensable penetrants [39, 102]. Adsorbent particles act as adsorptive reservoirs that increase the sorption selectivity, however, they can immobilize gas molecules in case of strong adsorption energies. This has been investigated for various zeolite types in silicone rubber with respect to the sorption of CO_2 [42, 63, 73], chlorinated hydrocarbons [40] or VOC [29].

The possibility of synergistic effects by the addition of different filler types has also been investigated [118, 161]. It was shown by Valero *et al.* that the presence of silica reduces the aggregation of MOF particles in Matrimid® and Ultem®. The microporous MOF improved the H_2/CH_4 selectivity while the mesoporous silica enhanced the permeability. Further investigations by Majeed *et al.* showed an improved dispersion of multi-walled CNT in PDMS in presence of POSS particles [92].

Table 4-1: Overview of inorganic filler materials applied in MMMs

Filler type	Description and Common Application	Application in MMM
Zeolite	Crystalline aluminosilicates with cage-like channels and apertures between 3-10 Å. Separation according to steric (molecular sieving), kinetic or equilibrium effects. Common adsorbent, e.g., for natural gas drying and separation olefin / paraffin [71, 79, 134].	Well-studied as filler in various glassy [89, 90, 91, 103, 144, 171] and rubbery polymers [42, 63, 68, 73, 154, 163] to induce molecular sieving and increase the adsorption capacity for separations, e.g., O_2/N_2, CO_2/H_2 or CO_2/CH_4.
Silica colloidal / fumed	Amorphous structures of SiO_2 or tetrahedral $(SiO_4)^{4-}$ with high surface areas. Colloidal silica is mesoporous, fumed silica is non-porous. Good mechanical and thermal stability. Common dehydrating agent, adsorbent for hydrocarbons $C_5 – C_{10}$ from petroleum fractions and flow additive in food and powder industry [58, 62, 166].	Well-studied as filler in various glassy [3, 5, 33, 35, 54, 57, 96, 111] and rubbery polymers [29, 42, 74, 84, 101, 112, 143] for separation CO_2/CH_4, H_2/CH_4, *n*-C_4H_{10}/CH_4 or VOC removal. Mostly increase of free volume, cross-linking density, thermal stability and stability against plasticization.
Carbon Molecular Sieves (CMS)	Carbonaceous materials produced via pyrolysis. Very narrow pore size distributions (2 – 10 Å). Separation according to molecular sieving and differences in diffusion rates. Adsorbent material for gas separations and purifications [62, 71].	Well-studied for MMM applications to improve the separation performance for O_2/N_2 and CO_2/CH_4 but seldom successful improvement achieved [91, 100, 136, 174].
Carbon Black	Non-porous particles produced via combustion of carbon based materials with graphitic and amorphous regions. Antistatic, conductive, high tendency to agglomerate. Most important reinforcing additive in tire industry and black colorant [45, 94].	Application in MMM to modify chain packing, improve mechanical stability or induce electrical conductivity [118].
Activated Carbon	Highly porous structures with amorphous and graphite-like regions produced by partial oxidation, e.g., of wood, nut shells or polymeric resins. Large surface areas and pore volumes, bimodal pore size distributions, mainly hydrophobic surfaces. Versatile adsorbent, mainly applied in purification processes, filtration or odour control [142].	Rarely studied as MMM filler for gas separations [50, 61, 81, 93, 108]. Investigations of AC as filler for single gas studies [164] or *n*-C_4H_{10}/CH_4 separation by Loeffler *et al.* [87] and Buhr [23].
Carbon Nanotube (CNT)	Graphitic sheets forming single or multi-walled bundles of tubes. Very good electrical, mechanical, thermal and optical properties, small channel diameters for size discrimination. Applied in research, e.g., for H_2 storage, nanoelectronics or artificial muscles [51, 94, 107].	Rarely studied as filler for MMM. Mostly added to induce conductivity or ion exchange capacity and improve the thermal stability but expensive and difficult to disperse [60, 65, 92].

Table 4–1 (continued): Overview of inorganic filler materials applied in MMMs

Filler type	Description and Common Application	Application in MMM
Metal Oxide (e.g., TiO_2, MgO, ZnO)	Non-porous nanosized particles with high surface areas. Similar effects as fumed silica but less difficult to disperse. Applied as white pigment (TiO_2), catalysts, electrodes for electrochemical cells, chemical sensors and optical devices [45, 51, 107].	Act as additional cross-linking sites, disrupt chain packing, enlarge free volume and thermal stability [51, 104, 105, 169, 170].
Metal Organic Framework (MOF) / Zeolitic Imidazolate Framework (ZIF)	Metal ions bridged by organic molecules (MOFs) or imidazolate linkers (ZIFs). Well-defined materials characterized by high surface areas, unimodal micropores, superior chemical and thermal stability, adsorptive selectivity and molecular sieving [30]. Promising materials for gas storage, catalysts, sensors and drug delivery [109].	Application of both MOF [133, 175] and ZIF [30, 36, 86, 173] rarely studied up to now, mainly ZIF-8 as filler for separation of H_2, CO_2 and lower hydrocarbons. No successful defect free formation reported so far.
Layered Silicate	Hydrophobic, non-porous materials with high aspect ratio up to 1000. Naturally occurring as clay. Inexpensive, good mechanical and thermal properties. Application as barrier material in food packaging [51].	Rarely studied as filler for MMM. Shows a reduced permeability and increase of the diffusive selectivity. Hydrophobic character requires modification to be compatible [51, 176].

Common production methods are solution-blending, in-situ polymerisation and sol-gel routes [33]. As illustrated in Figure 4-4, these methods differ in the resulting structure and are suitable for different materials. While solution blending usually results in van-der-Waals forces or hydrogen bonds between polymer and filler, in-situ polymerisation and sol-gel methods allow the integration of inorganic particles into the polymeric matrix via covalent bonds [52]. The preparation process and arising stresses strongly affect the MMM morphology and performance [32, 54, 171]. Critical issues are a sufficient dispersion of particles to minimize agglomeration and sedimentation, the prevention of pore blockage and defect formation, the formation of thin separation layers and the reproducibility of production [32, 39, 109, 163]. A good dispersion requires an appropriate polymer viscosity [103], filler particle size and shape [68, 175], strong mechanical forces, ultrasonic power or UV irradiation [144, 153]. A preparation above T_g is recommended to reduce the formation of defects [103]. Often pre- or post-treatment steps are necessary, e.g., the pre-dispersion or priming of filler particles, thermal annealing or surface modifications to adjust the hydrophobicity, roughness or presence of active groups [51]. Additives can be used to improve the adhesion, e.g., silane coupling agents or plasticizers to increase the flexibility of polymeric chains [59, 163]. The selection of the type of solvent and the

drying conditions are also important for a successful preparation. An inappropriate choice can result in the formation of voids due to a clustering of particles and repulsive forces [29], a blockage of pores by polymeric chains [61] or, with regard to drying conditions, interfacial stress and the formation of irregular surface patterns [52, 54, 103, 173]. So far, only lab-scale formations of thick MMM films are reported in literature [79, 173]. Results of such have to be treated with caution as the transfer into industrial relevant thin film composite membranes represents a great challenge [32, 175].

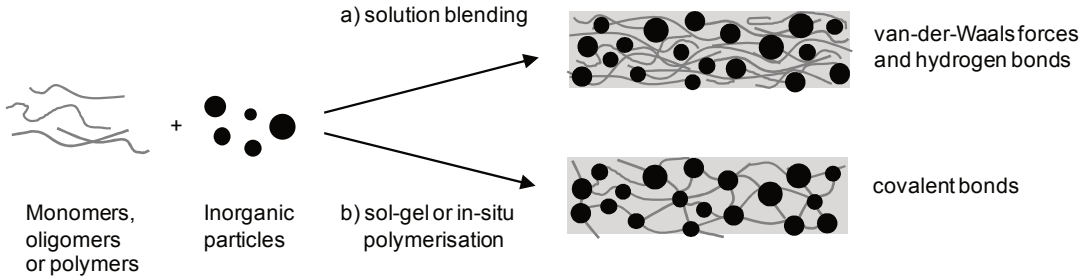

Figure 4-4: Production of MMM materials via a) solution blending and b) sol-gel or in-situ polymerisation with covalent bond formation (adapted from [33])

4.3 Permeation Behaviour and Predictive Models

The understanding of the permeation is necessary for a successful adaptation of composition and operating conditions. Due to their heterogeneity, the transport in MMMs is more complex than in pure polymeric or inorganic membranes. While transport through the bulk polymeric matrix can still be assumed to follow the solution-diffusion mechanisms (see section 3.3.1), the presence of filler particles affects both solubility and diffusion. Impermeable particles usually prolong diffusion pathways and modify the chain packing thus diffusion through polymeric matrix. Porous filler particles further allow additional mechanisms, e.g., molecular sieving, capillary condensation or a selective surface flow (see section 3.3.2). The overall performance results from the interplay of diffusion and solution in the polymeric matrix, transport mechanisms through the porous filler particles and transport through the interfacial layer. The interplay of mechanisms is illustrated in Figure 4-5.

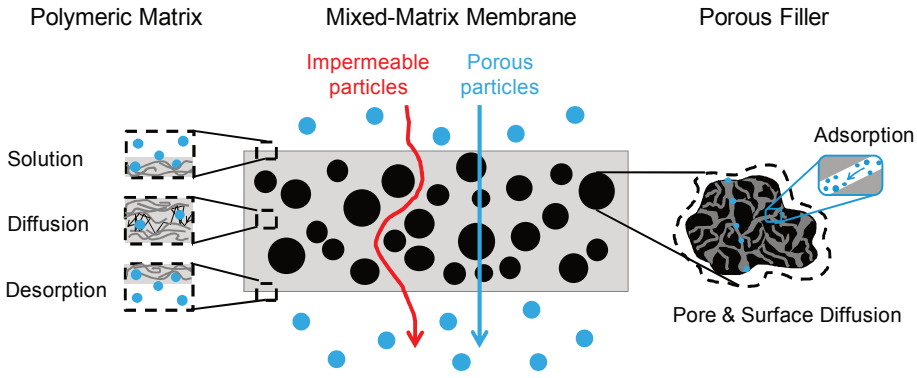

Figure 4-5: Transport mechanisms in MMMs filled with impermeable and porous filler particles

The properties of the interfacial layer are crucial for the description and prediction of the transport in MMMs. The possible interfacial morphologies and their influence on the permeation have been illustrated in Figure 4-3. A common, simplified approach to describe the permeation of filled membranes is to superpose the transport through the polymeric matrix and the filler phase weighted according to their volume fractions. For such an approach, independent diffusion and solubility in both phases is assumed [17]. Ideal two-phase models describe the effective steady-state permeability P_{eff} as a function of the continuous polymer permeability P_c, the dispersed filler permeability P_d and the volume fraction of filler φ_d [7]. The limiting cases correspond to transport in series or parallel through both phases [174]. Various models have been proposed in literature. Most popular is the Maxwell model in equation (4-1), originally developed for dielectric constants of composite materials. It allows the prediction of permeabilities for diluted suspensions of spherical particles in a polymeric matrix up to moderate volume fractions ($\varphi_d < 0.2$) of the dispersed filler. A simplified version can be used for impermeable and non-interacting filler particles.

$$P_{eff} = P_c \cdot \left[\frac{2 \cdot (1 - \varphi_d) + (1 + 2\varphi_d) \cdot (P_d / P_c)}{(2 + \varphi_d) + (1 - \varphi_d) \cdot (P_d / P_c)} \right] \qquad \textbf{(4-1)}$$

Further models have been proposed, for example, by Bruggeman, Lewis-Nielsen or Pal [116]. The latter are more precise for higher filler loadings and are even sensitive for structural effects and the morphology of filler particles. Cussler developed a model for filler particles with high aspect ratios used as barrier materials [34]. As based on simplified assumptions, the models often do not reflect the experimental results. Non-ideal interfaces formed in the vicinity of filler particles (see Figure 4-3) and a non-homogeneous dispersion of particles cause strong deviations of the experimental results. They are addressed in extended permeation models with the interface forming an additional third phase, for example by Mahajan and Koros [89, 90], Felske *et al.* and

Pal *et al.* [116]. The most important permeation models are briefly summarised in Table A−4 in Appendix A. Detailed descriptions can be found in literature [116, 147]. Serious drawbacks of the permeation models are the availability of raw material data, in particular, permeability or diffusion coefficients of the filler phase, and the knowledge about the extent of an interphase formation [103]. Further, the models were developed for thick MMM layers and are not appropriate to describe the industrial relevant thin film composite structures developed in this work. A different approach for the description of transport in sorption-selective MMMs based on mass transfer mechanisms has been proposed by Kramer [77].

5 MATERIALS AND METHODS

5.1 Membrane Materials

5.1.1 Polymeric Matrix

Poly(octylmethylsiloxane) (POMS) was used as the polymeric matrix in this work. It is a derivative of the industrial state-of-art poly(dimethylsiloxane) (PDMS) with one methyl group replaced by an octyl methyl group [140]. Chemical structures of repeat units are shown in Figure 5-1. Glass transition temperatures of -110 °C for POMS and -123°C for PDMS [151] indicate their highly rubbery character and a solubility selective separation.

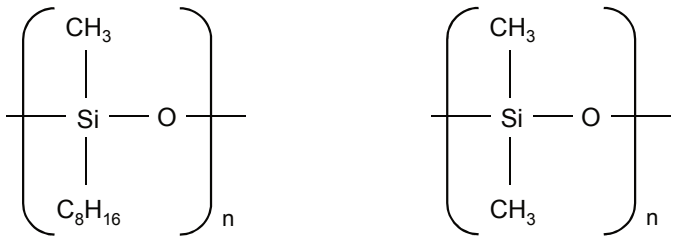

Figure 5-1: Chemical structures of repeat units of POMS and PDMS

Polymeric components were purchased at Gelest Inc., USA and Wacker Chemicals, Germany. The cross-linking is a hydrosilylation reaction between siloxane oligomers and cross-linkers forming Si-CH_2-CH_2-Si linkages and a three-dimensional network structure [27]. A simplified scheme is shown in Figure 5-2**.**

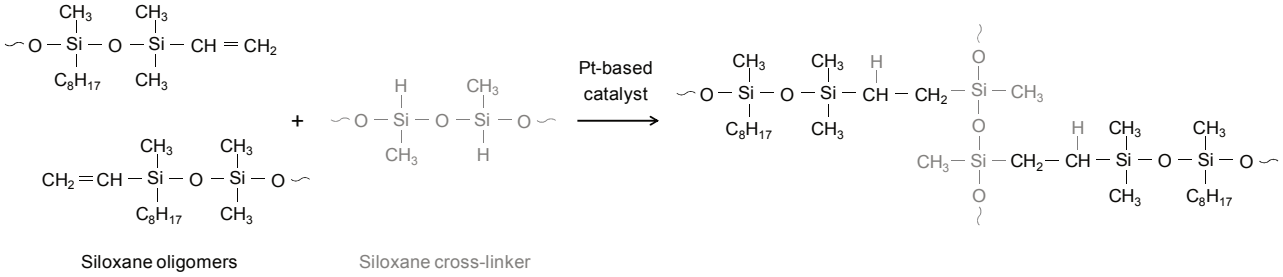

Figure 5-2: Chemical cross-linking of POMS via hydrosilylation addition

5.1.2 Inorganic Fillers

Different inorganic fillers including porous and non-porous materials were applied: activated carbons, zeolite, carbon black and AEROSIL®. The activated carbons (AC) were kindly provided by Blücher GmbH (Germany). Following types were available: AC 100050, AC 100942 and AC 100085. The AC type 100050 was milled to two different fractions with mean particle sizes of 3.5 µm and 1.5 µm (see Figure B-1 in Appendix). The Y-type zeolite CBV-780 was purchased at Zeolyst International (USA). The SiO_2/Al_2O_3 ratio was specified as 80, giving a hydrophobic surface. Carbon black was delivered by abcr GmbH (Germany) as a pigment concentrate dispersed in silicone (vinyl terminated PDMS) with 45 wt% carbon. The stated Hegman Grind of 6 corresponds to a particle size smaller than 25 µm (ASTM D1210-05) [76]. AEROSIL® R8200, a pyrogenic silicon dioxide ($SiO_2 \geq 99.8\%$) with a hexamethyldisilazane treated hydrophobic surface of 160 m^2/g, was purchased at Evonik (formerly Degussa, Germany). Table 5-1 summarises characteristic properties of the applied inorganic filler materials. All inorganic materials were dried at 150 °C and 7 mbar in a vacuum oven for 2 days to remove residual moisture prior to use.

Table 5-1: Inorganic materials used as filler phase and specifications according to manufacturer

Inorganic Filler	Type	Symbol	Manufacturer	S_{BET} m^2/g	d_{pore} Å	v_{pore} cm^3/g	d_{50} µm
Activated Carbon	100050	AC050	Blücher GmbH	1361	18.68	0.636	3.5 / 1.5
Activated Carbon	100942	AC942	Blücher GmbH	1477	19.01	0.702	n.s.
Activated Carbon	100085	AC085	Blücher GmbH	2113	22.23	1.174	n.s.
Zeolite	CBV-780	Z	Zeolyst Int.	780	24.24	n.s.	n.s.
Carbon Black	AB127744	CB	abcr GmbH	n.s.	non porous		25 [1]
AEROSIL®	R8200	AS	Evonik AG	160 ± 25	non porous		0.05-0.005 [2]

[1] present in dispersed form as smooth paste with maximum particle size defined by Hegman grind of 6
[2] average particle size of primary particles [80]

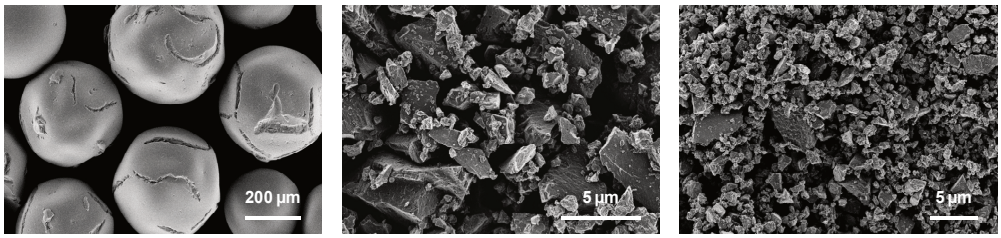

Figure 5-3: SEM images of AC050 pellets (a) and sieving fractions with d_{50} = 3.5 µm (b) or d_{50} = 1.5 µm (c)

5.1.3 Solvents

All polymeric precursor and coating solutions were prepared with iso-octane (Merck KGaA, purity > 99.5%) as solvent. To facilitate the dispersion, inorganic filler particles were pre-saturated with solvent for at least 40 min. For this purpose, iso-octane (Merck KGaA, purity > 99.5%), ethanol (Merck KGaA, purity > 99.9 %), toluene (Merck KGaA, purity > 99.9 %) or iso-propanol (Merck KGaA, purity > 99.9 %) were used.

5.2 Membrane Preparation

5.2.1 Production of TFC membranes

Membranes were prepared as thin film composite (TFC) membranes via successively coating on a support structure. The production steps and a schematic structure of the final thin film composite membranes are shown in Figure 5-4. The support structure was composed of microporous poly(acrylonitrile) (PAN) (average pore size 20 nm, surface porosity 13-15 %) on non-woven polyester. Partially, the support structure was coated with an additional PDMS gutter layer (GL). A final PDMS top layer (TL) was applied to seal eventually formed surface defects. The precursor and coating solutions were prepared according to the procedures described below. The rotational rheometer MCR 502 (Anton Paar GmbH, Germany) equipped with a Couette geometry (DG26.7) was used to measure the viscosity of coating solutions at a constant temperature of 27 °C and varying shear rates.

POMS Precursor Solutions

POMS precursor solutions were prepared by combining siloxane-based oligomers, cross-linking and reinforcement agents with a platinum based catalyst in iso-octane (purity > 99.5 %, Merck

KGaA, Germany) as solvent followed by extensive mixing. The exact disclosure of the composition is not possible due to the commercial production of POMS membranes. Two types of precursor solution were used: a standard solution with viscosity of 4 mPa·s (indicated by S) and a modified solution with an increased viscosity of 14 mPa·s (indicated by XL). The precursor solutions were stored in a fridge to prevent a further cross-linking and mixed for at least 30 min prior to use.

POMS Coating Solutions

Membranes with pure POMS separation layers were produced as reference material. Precursor solutions were diluted with appropriate amounts of catalyst and iso-octane, mechanically mixed with a dissolver (Dispermat®, VMA Getzmann GmbH) for 5 minutes at 9500 rpm, degassed for 2 min and directly used for coating. The final concentrations of POMS were 20 or 30 wt% for the standard precursor solution (S) and 20 wt% for the modified precursor solution (XL).

MMM Coating Solutions

The MMM coating solutions were prepared by a stepwise addition of the polymer precursor solution and catalyst to the solvent saturated inorganic particles and thoroughly mixing with a dissolver (Dispermat®, VMA Getzmann GmbH) for at least 15 min at 10000 – 12000 rpm. The solution was placed in an ultrasonic bath (Elmasonic S30H) for 2 min to assure a homogeneous dispersion and degassing and was directly used for coating. The final concentration of the polymer was determined by the mass of all polymeric components divided by the total mass of solution. The filler content is referred to the dry polymeric mass and given as mass fraction (wt%). The final concentration of POMS was adjusted to 20 or 30 wt% (standard precursor solution) or varied from 7.5 to 20 wt% (modified precursor solution). Filler contents of 10 – 40 wt% for activated carbon type 100050 and 20 wt% for all other filler types were used.

Coating Solutions for Top Layer (TL) and Gutter Layer (GL)

The coating solutions for the top layer (TL) and gutter layer (GL) were both based on PDMS. Due to licensing restrictions, the exact composition cannot be disclosed. The cross-linking mechanism is similar to the hydrosilylation reaction in Figure 5−2. Coating solutions with a final concentration of 0.5 wt% PDMS in iso-octane (purity > 99.5 %, Merck KGaA, Germany) were prepared by a successive addition and mixing of all components with a magnetic stirrer.

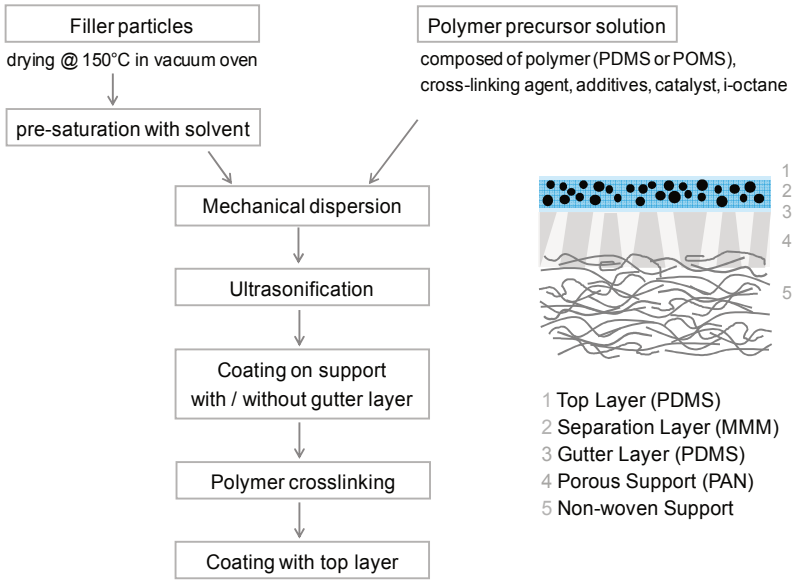

Figure 5-4: Production steps and scheme of cross-section of TFC MMM

The membranes were produced on the roll coating machine depicted in Figure 5-5. The coating solutions were added manually or by pump. Coating parameters are listed in Table B–2 in Appendix B. The coating was followed by a thermal treatment (100°C, 5 min) to induce the removal of solvent and cross-linking. An overview of realized membrane configurations is given in Table B–3 in Appendix B. TFC membrane samples were used for single and mixed gas permeation experiments, SEM analysis and sorption analysis.

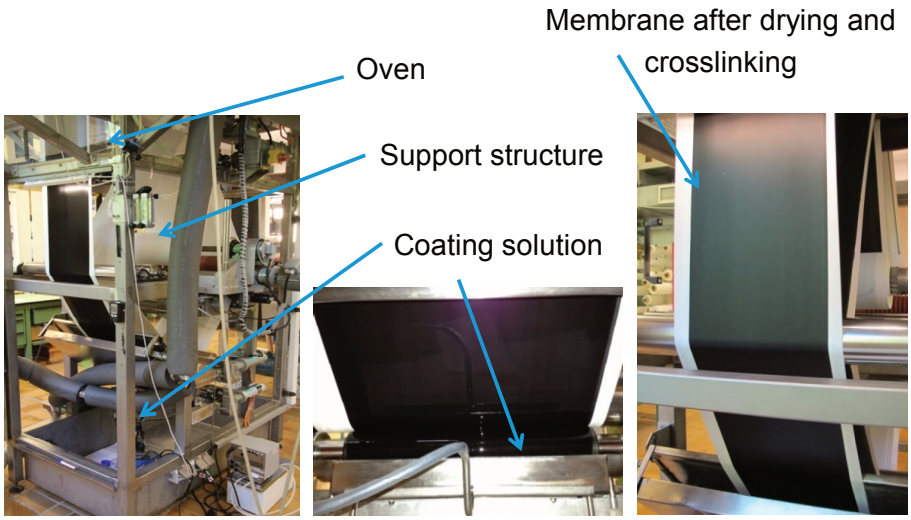

Figure 5-5: Production of TFC MMM with a roll-coating machine

5.2.2 Preparation of Thick Films

Thick films of pure POMS and MMMs were prepared via solution casting. Casting solutions were prepared with a 30 wt% POMS precursor solution. AC050 particles were pre-dispersed in a solvent (iso-octane, ethanol or toluene; ratio 1:2) for at least 2 h. POMS precursor solution and catalyst were stepwise added and mixed with a magnetic stirrer for 2 h min or 30 min, respectively. After mixing and degassing in an ultrasonic bath for 2 min the solutions were directly poured into a horizontally aligned Teflon™ bowl (diameter 80 mm) placed on a heating plate. Samples were covered with glass and the solvent was evaporated for 5 days at 22 – 25 °C in nitrogen or pressurized air atmosphere followed by drying at 150 °C and 5 mbar for at least 17 h. The final film thickness was determined with the coating thickness measurement device Deltascope® FMP10 (Helmut Fisher GmbH) allowing a non-destructive measurement via magnetic conduction. An overview of prepared samples is given in Table B–4 in Appendix B. The samples of thick films were used for sorption analysis, density and permeability measurements.

5.3 Membrane Characterisation

5.3.1 Gases and Liquids

For single gas characterisation, chemical-grade O_2 (99.5 % purity), N_2, CO_2, CH_4, C_2H_6, C_3H_8 and *n*-C_4H_{10} (> 99.95% purity) were purchased at Linde AG or Air Liquide. Higher hydrocarbons *n*-C_5H_{12} (> 99%, purchased at Merck KGaA, Carl Roth GmbH or AppliChem GmbH), *n*-C_7H_{16} (> 99%, AlfaAesar), C_7H_8 (> 99.9 %, Merck KgaA) and C_2H_6O (> 99.9 %, Merck KgaA) were applied in liquid state. Selected properties of applied gases and liquids are listed in Table A–1 in Appendix A. Binary mixtures composed of 1.0, 2.1, 4.3 or 4.8 vol- % *n*-C_4H_{10} in CH_4 and a multi-component mixture of various hydrocarbons C_1 – C_5 and CO_2 with the composition given in Table 5-2 were used to study the mixed gas separation performance. The mixtures were prepared by filling an evacuated gas cylinder with the respective components according to their desired partial pressure. The total pressure was controlled with a highly sensitive pressure controller. To ensure a homogeneous mixture, the gas cylinder was placed on a rolling mixing device and equalized for at least 24 h prior to use. The final composition was detected by a GC (Varian 3400, column chromosorb 107).

Table 5-2: Composition of the investigated multi-component gas mixture

Component	Chemical formula	Concentration in vol- %
Carbondioxide	CO_2	2.0
Methane	CH_4	78.6
Ethane	C_2H_6	10.4
Propane	C_3H_8	5.6
n-Butane	*n*-C_4H_{10}	2.4
n-Pentane	*n*-C_5H_{12}	1.0

5.3.2 Sample Pre-treatment

All samples were dried in a vacuum oven at 80 °C and 7 mbar for at least 15 h unless otherwise noted to ensure the complete removal of residual solvent or moisture and allow the activation of filler particles. The suitability of pre-treatment conditions, more precisely temperature and time, was investigated in preliminary tests. Temperatures above 100 °C should be avoided as a change of PAN support structure (T_g = 87 °C [138]) and significant reduction of permeability might occur.

5.3.3 Single Gas Permeation Measurements

Pressure Increase Set-Up

Single gas measurements were performed with an automated pressure increase set-up. The set-up was composed of a membrane test cell (diameter 75 mm, effective area was adjusted with reduction plates), a vacuum pump, feed and permeate vessels, pressure sensors on feed and permeate side and a water bath for temperature control. A flow-sheet is given in Figure C−1 in Appendix C. After insertion of the sample into the test cell the system was evacuated and the feed vessel filled with the gas component up to the desired pressure. After equilibration, the valves connecting to the test cell were opened allowing the permeation of gas through the membrane into the permeate vessel. Measurements were performed at feed pressures of 0.2 – 1 bar, permeate pressures up to 0.12 bar and temperatures ranging from 20 to 120 °C. Permeances were calculated from the time dependent change of pressure in feed and permeate vessels, the volumes of the vessels, permeate flow rate $\dot{V}_P$, effective membrane area $A_{M,eff}$ and temperature T (see equation (C-1)). Free volume parameters L_{i0}^{∞}, E_P, m_0 and m_T were determined

by means of varying operating conditions. A detailed description of the procedure and derivation of equations can be found elsewhere [23, 75].

Manual Set-Up for Single Gas Measurements N_2 / O_2

A manual set-up (see Figure C−2 in Appendix C) was used for quality control measurements with N_2 and O_2 at room temperature. The set-up was composed of a membrane test cell (diameter 75 mm, $A_{M,eff}$ = 0.003632 m²) and measuring devices for feed pressure and permeate flow rate (Bios DryCal Definer 220 (L), Mesa Labs Inc., USA). After insertion of the sample and sealing of the test cell the system was flushed with the respective gas and equilibrated. Measurements were performed at room temperature in the range of 16 – 23 °C and constant feed pressure of 5 bar. Permeances were calculated according to equation (C-2) by means of the permeate volume flow rate $\dot{V}_P$, the effective membrane area $A_{M,eff}$, feed p_F and permeate p_P pressure (see Appendix C).

Manual Set-Up for Single Gas Measurements n-C_4H_{10} / CH_4

A similar manual set-up as described above was used for the investigation of single gases *n*-C_4H_{10} and CH_4. The set-up (see Figure C−3 in Appendix C) was composed of a membrane test cell (diameter 47 mm, $A_{M,eff}$ = 0.001384 m²), pressure valves and measuring devices for feed pressure (LEO 3, Keller AG, Switzerland) and permeate flow rate (Bios DryCal Definer 220, Mesa Labs Inc., USA). A vacuum pump (Vacuubrand GmbH & Co., Germany) on the permeate side was used to control the permeate pressure. After insertion and sealing of the sample into the test cell, the system was flushed with the respective gas and equilibrated. Experiments were performed at room temperatures in the range of 22 – 27 °C, varying feed pressure from 1 – 3 bar and permeate pressure from 0 – 1 bar. Permeances were calculated according to equation (C-2) in Appendix C.

Time-Lag Apparatus

The permeability of films with known thickness was determined with a so-called time-lag apparatus which applies the method of using a constant volume but variable pressure. The time-lag is defined as the time between the first contact of gas molecules with the feed side of a membrane film and the measurable change of pressure on the permeate side in consequence of the diffusion of gas molecules through the film. The set-up was composed of a membrane test cell (diameter 80 mm, the effective membrane area was adjusted with reduction plates to $A_{M,eff}$ = 0.000345 m²), a vacuum pump, feed and permeate reservoirs and devices for pressure control on feed and permeate side. A flow sheet is given in Figure C−4 in Appendix C. After insertion of the

sample into the test cell, the whole system was evacuated before the feed valve of the respective gas was opened. The change of the permeate pressure in consequence of permeation was recorded until the permeate volume of either 45.8 or 224 cm³ was completely filled. Measurements were performed at a constant temperature of 30 °C and feed pressures between 0.18 – 0.75 bar. The diffusion coefficient and permeability were calculated by means of equation (C-3) and equation (C-4), respectively (see Appendix C). A detailed description of the time-lag apparatus and measurement procedure can be found elsewhere [148].

5.3.4 Binary and Multi-component Permeation Measurements

Mixed gas measurements were performed with the experimental set-up presented in Figure 5-6. A detailed flow sheet and specifications of the components are given in Appendix C. Membrane samples with a diameter of 47 mm ($A_{M,eff}$ = 0.001204 m²) were inserted into the test cell (M1). After evacuation for at least 30 min the preliminary prepared gas mixture (see 5.3.1) was filled into the feed vessel up to 1.5 bar. The desired feed pressure between 10 to 40 bar was generated by a compressor (C1). A gas circulator (C2) was used to ensure a sufficient mixing and a flow velocity to avoid concentration polarisation. A filter cell equipped with non-woven polyester was used to minimize the deposition of graphite on membrane sample caused by the attrition of the rotary vanes. Before entering the test cell the temperature of the feed mixture was adjusted with a water bath (HX1). Measurements have been performed at constant temperatures between 15 to 35 °C. Permeate and retentate streams were partly recycled to the feed vessel. A stage-cut below 1 % ensured that results are not affected by back-mixing or changing concentrations on the feed side. The permeate pressure was either not regulated or adjusted using a vacuum pump. The system was equilibrated for at least 30 min before measuring flow rates on feed, permeate and retentate side, feed and permeate pressure and feed temperature. Gas composition was analysed using a gas chromatograph (GC Varian 3400, column Chromosorb 107). Details to GC analysis are given in Appendix C. Measurements were performed with either a varied feed pressure (10 to 40 bar), permeate pressure (0.05 to 1.6 bar) or temperature (15 to 35 °C). Meanwhile, all other parameters were kept constant as best as possible. Operating conditions are summarised in Table 5-3. Permeances were calculated by means of the permeate volume flow rate $\dot{V}_P$, the volume fraction y_i, the effective membrane area $A_{M,eff}$, the feed and the permeate pressure (see equation (C-5) in Appendix C). Due to the presence of condensable gases and high pressure conditions, significant gas phase non-idealities can be expected [4]. The real gas behaviour was taken into

account by the use of fugacities f_i with fugacity coefficients φ_i estimated according to the equation of state by Soave-Redlich-Kwong (see Appendix A).

Table 5-3: Operating conditions for permeation measurements with binary and multi-component mixtures (values in brackets indicate fixed values during parameter variation)

Parameter		Binary	Multi-component mixture
$y_{F,n\text{-}C4H10}$	vol %	1 – 5 (5)	2.4
Feed pressure	bar	10 – 40 (10 / 30)	10 – 40
Permeate pressure	bar	0.05 – 1.6 (1.2 – 1.6)	1.2 – 1.6
Temperature	°C	15 – 35 (20)	20
Eff. Membrane area	m²	0.001205	0.001205

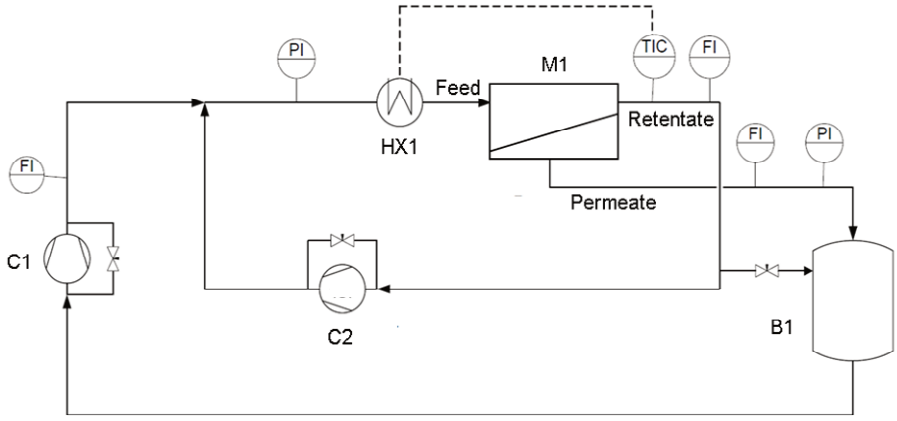

Figure 5-6: Schematic diagram of the experimental set-up for binary and multi-component permeation measurements with feed vessel (B1), gas compressor (C1), gas circulator (C2), heat exchanger (HX 1) and membrane test cell (M1) [23]

5.3.5 Long-term Permeation Measurements

The experimental set-up for long-term studies of the separation performance is depicted in Figure 5-7. A detailed flow sheet is given in Figure C–6 in Appendix C. Samples with a diameter of 47 mm ($A_{M,eff}$ = 0.001134 m²) were inserted into the test cell (D). Liquid *n*-C_5H_{12} (> 99%, various suppliers) was filled in a feed vessel (A), evaporated and mixed with N_2 (99.99%, Linde or

Air Liquide) in a controlled evaporation and mixing unit (B) at 50 °C. The feed gas entered the open gas cycle via a gas circulator (E). The gas circulator was adjusted to a frequency of 20 Hz to ensure a sufficiently high flow rate on the feed side to avoid concentration polarisation. The stage-cut was kept below 1 %. A filter cell (diameter 62 mm) equipped with non-woven polyester was used to collect graphite abrasion. Before entering the test cell the temperature of the feed mixture was adjusted in a water bath (F) to remove heat generated by the gas circulator. The set-up was equipped with measuring devices for pressure, flow rate and temperature in feed, permeate and retentate that were monitored and controlled by a control program (G) designed in LabVIEW (National Instruments). The gas composition was analysed with a GC (C) (MTI Refinery Analyzer). Details to GC analysis are given in Appendix C. The system was calibrated prior to use with N_2 (99.996 %, Linde AG) and *n*-C_5H_{12} (> 99%, Roth GmbH). Measurements were performed at constant temperature and pressure of 20 °C, 30 bar feed side and 1.1 bar permeate side with a feed gas mixture of 1.3 to 1.5 vol% *n*-C_5H_{12} in N_2. In addition, the influence of the feed composition on the separation performance was investigated in the range of 0.05 to 1.5 vol% *n*-C_5H_{12}. Permeances were calculated according to Equation (C-6) by means of the permeate volume flow rate $\dot{V}_P$, feed and permeate concentrations $y_{F,i}$ and $y_{P,i}$, the effective membrane area $A_{M,eff}$ and the fugacity coefficients φ_i according to Soave-Redlich-Kwong (see Appendix C).

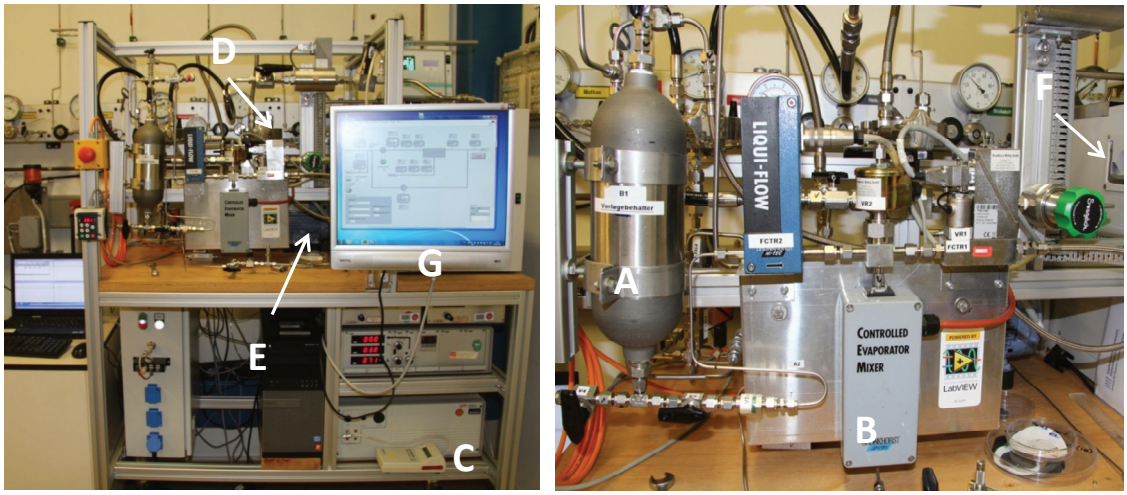

Figure 5-7: Testing facility for long-term studies with feed vessel for liquid component (A), CEM system (B), GC analysis (C), membrane test cell (D), gas circulator (E), heat exchanger (F) and control system (G)

5.3.6 Scanning Electron Microscopy (SEM)

The morphology of membranes was analysed by SEM images of surfaces and cross sections. The samples were dried in a vacuum oven for at least 24 h to ensure the removal of solvent. Afterwards they have been immersed in iso-propanol, freeze-fractured in liquid N_2 and sputter-coated with a 2 nm layer of platinum. Images were obtained with the SEM system LEO Gemini 1550 VP (Zeiss, Germany) equipped with two detectors, an in-lens detector and a conventional secondary electron detector. SEM images of cross sections were used to determine the thicknesses of the active separation layers. SEM analysis was also used to study the morphology of inorganic filler materials. Particles were stuck on a conductive carbon tab and coated with 2 nm layer of platinum.

5.3.7 Sorption Analysis

The gravimetric determination of the gas uptake by POMS, MMMs and powdered inorganic samples was performed with a magnetic suspension balance (Rubotherm GmbH, Germany). The set-up was composed of a metal measuring chamber magnetically coupled to a highly sensitive mass balance allowing the determination of gas uptake with high accuracy at large pressure and temperature ranges. The measuring system was thermally insulated and equipped with a water bath for temperature control. Samples with a minimum of 10 mg were dried over night at 80 °C in vacuum oven prior to insertion into the sample container. Buoyancy measurements to determine the correct sample weight and volume were performed with N_2 followed by the uptake

of single gases CH_4 and *n*-C_4H_{10}. The whole system was evacuated in between runs at elevated temperatures. A step-wise increase of pressure was performed and the sample weight determined and monitored at specified intervals until equilibrium. Measurements were performed up to 2.5 bar for *n*-C_4H_{10} and up to 30 bar for CH_4. The temperature was adjusted to 20, 30 or 50 °C. For the determination either thick isotropic films or detached separation layers of TFC MMMs were applied. The detached layers were obtained after immersion of TFC samples into N,N-dimethylformamide followed by rinsing and drying in a vacuum oven.

5.3.8 Thermal Analysis

Thermal gravimetric analysis (TGA) was performed with a thermo-microbalance (TG209F1 Iris, Netzsch, Germany). A temperature range of 20 to 1000 °C with 10 K/min in argon atmosphere was applied. Differential scanning calorimetry (DSC) was performed with a DSC 1 (Mettler-Toledo AG, Switzerland) in the range of -160 to 130 °C. The glass transition temperatures were determined as the midpoint of the heat capacity transition of repeated cycles. Samples of approximately 10 mg in Al_2O_3 sample containers were used.

5.3.9 Density Analysis

The density of thick films was determined from the weight difference of the samples in air (m_A) or in an auxiliary liquid (m_B) measured with the high-precision analytical balance Excellence XS/XP equipped with a density kit (Mettler-Toledo Int. Inc, USA). Fluorinert™ FC-77 was applied as auxiliary liquid (Sigma-Aldrich GmbH, Germany). The density can be calculated according to equation (5-1) with the corresponding densities ρ_A = 0.0012 g/cm³ for air and ρ_B = 1.7749 g/cm³ for the auxiliary liquid Fluorinert™ FC-77.

$$\rho = \frac{m_A}{m_A - m_B} \cdot (\rho_B - \rho_A) - \rho_A \qquad \textbf{(5-1)}$$

6 RESULTS AND DISCUSSION

In this chapter the results of the MMM material development and characterisation are presented and discussed according to the structure shown in Figure 6-1. First, investigations with the objective to develop a suitable MMM material with a high selectivity, flux and stability are described in chapter 6.1. A detailed study under varying single and mixed-gas operating conditions of the most promising MMM is then presented in chapter 6.2 to identify the optimal range of application. Based on the experimental results, the potential of MMMs is evaluated and highlighted in chapter 6.3 with respect to the industrial application.

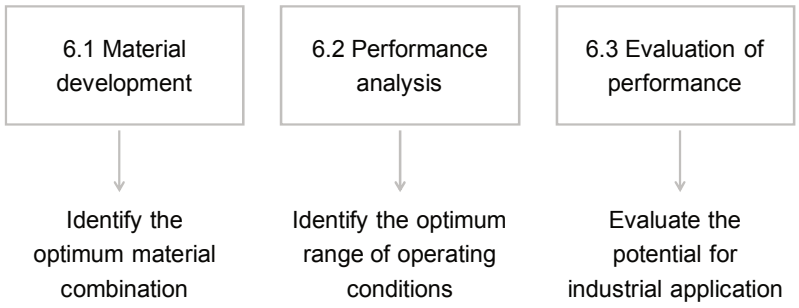

Figure 6-1: Structure of the results section

6.1 Material Development

A competitive membrane material for an industrial application requires a high selectivity as well as a high flux, a good mechanical, thermal and chemical stability to withstand the operating conditions, a low tendency to ageing, fouling or plasticization to assure a long lifetime, a reproducible production, low manufacturing costs and the ability to be transferred into high surface area modules [58]. Particularly for the application in the petrochemical industry or natural gas processing, a pressure stability to endure common pipeline pressures in the range of 40 to

80 bar, a tolerance to corrosive media such as H_2S, CO_2 or organic vapours and a high selectivity to minimize the methane loss are of great importance [131, 14]. As presented in Chapter 4, there are several parameters influencing the performance and stability of MMMs, including compositional, structural and operational parameters. A crucial part is the choice of the polymeric and inorganic MMM components and how to exploit the advantages of both materials. The parameters investigated in this work to achieve an efficient, defect-free MMM with an improved selectivity, high flux and a reproducible production are summarised in Figure 6-2.

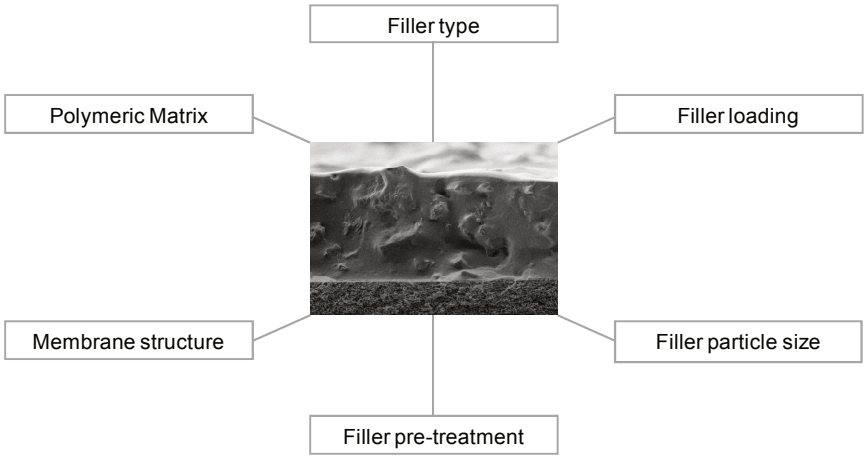

Figure 6-2: Overview of parameters influencing the performance and stability of the thin film composite MMMs investigated in this work

6.1.1 Selection of Polymeric Matrix

The choice of the polymeric matrix determines the minimum performance of a MMM and should exhibit an economical attractive selectivity and permeability [174]. Poly(octylmethylsiloxane) was chosen as polymeric matrix as it is one of the industrial state-of-the-art materials for the separation of higher hydrocarbons. Its highly rubbery character (T_g = -110 °C) allows a good compatibility to the filler particles thus minimizing the defect formation or sieve-in-a-cage morphologies often found for glassy polymeric matrixes [103, 89].

Sorption Behaviour

According to the solution-diffusion model, the separation performance of dense polymeric membranes is determined by the interplay of solution and diffusion [131]. The rubbery state of POMS provides a favourable environment for gas transport governed by the sorption of

condensable hydrocarbons. This is presented in Figure 6-3 (a) in terms of the sorption isotherms of *n*-C_4H_{10} and CH_4 at 20 °C in dense POMS. The significant difference in the sorption behaviour of the two gases is of vital importance for the separation performance since the overall permeation is determined by both diffusion and solution. For the permanent gas CH_4 the solution follows a linear trend which can be described by a Henry type sorption isotherm. In contrast, the high condensability of *n*-C_4H_{10} leads to an exponential increase of the concentration with pressure which can be attributed to a Flory-Huggins type of solution. A change of temperature strongly affects the sorption behaviour. An increase of temperature leads to a decreased amount of dissolved gas in the polymer. POMS exhibits even a higher sorption selectivity for the higher hydrocarbons than state-of-the-art membrane material PDMS as illustrated in Figure 6-3 (b) for different temperatures. The grey circles represent data for PDMS by Raharjo *et al.* [126]. The superiority of POMS is reflected especially at low temperatures.

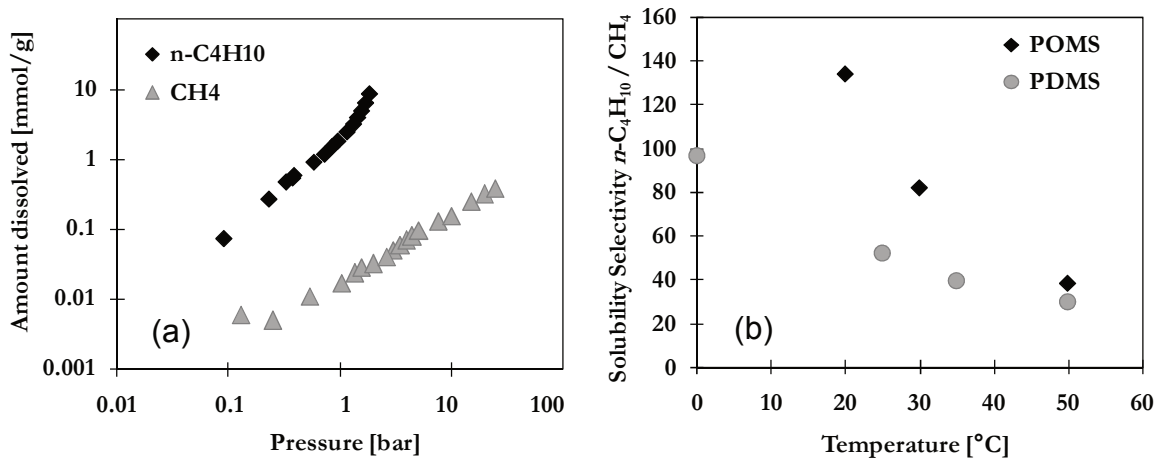

Figure 6-3: (a) Sorption of *n*-C_4H_{10} (black) and CH_4 (grey) in POMS at 20 °C and different pressure and (b) solubility selectivity *n*-C_4H_{10}/CH_4 of POMS (black) and PDMS (grey, data by Raharjo *et al.* [128]) at different temperatures

Permeability

An important parameter for a successful MMM formation is the permeability of the polymeric matrix. If the polymer is too permeable it dominates the permeation and does not allow the participation of particles dispersed in the polymeric matrix in the gas transport. In contrast, a low permeability causes a starving of filler particles. For best results, the matching of the permeability of polymeric and inorganic filler phase with respect to the gas mixture components to be separated is recommended [103, 99]. The determination of permeability was done with a time-lag apparatus by means of samples of thick isotropic films.

The permeability of pure POMS was estimated to 5330 (± 440) Barrer for *n*-C_4H_{10} and 690 (± 20) Barrer for CH_4 at 30 °C. Values are averaged for CH_4 and in case of *n*-C_4H_{10} extrapolated to zero pressure according to the equation of the free volume theory. The corresponding diffusion coefficients are 3.8 (± 0.23) for *n*-C_4H_{10} and 10.0 (± 0.34) cm^2/s for CH_4, respectively. According to literature, PDMS shows much higher values of 16000 (± 800) and 1200 (± 60) Barrer for the permeabilities of *n*-C_4H_{10} and CH_4 at 25 °C, respectively. The diffusion coefficients for PDMS are stated as 4.4 (± 0.3) and 18 (± 1) cm^2/s for *n*-C_4H_{10} and CH_4, respectively [126]. In general, PDMS is the most permeable silicone based polymer known [151]. The lower permeability of POMS stems from the larger octyl group in the side chain which affects the rigidity and the free volume of the polymer. It has to be noted, that the polymer permeability can differ in the vicinity of filler surfaces, especially when the concentration of higher hydrocarbons is expected to be higher than in the surrounding bulk polymeric matrix [116].

Polymer Concentration and Viscosity

The concentration of the polymer in the coating solution affects the viscosity and hence the thickness of the separation layer. A lower concentration usually results in thinner layers. To achieve a stable film formation a critical concentration has to be exceeded. The polymer concentration is even more important in the formation of MMMs where a high concentration or rather high viscosity is necessary to facilitate the dispersion and prevent a sedimentation of filler particles [144]. No improvement can be expected if particles are not homogeneously dispersed [68]. The influence of the polymer concentration on viscosity is presented in Figure 6-4 (a) for pure POMS solutions prepared via the standard (black symbols) and modified (grey symbols) routes described in section 5.2.1. The modified preparation route results in higher viscosities for the same amount of polymer in the precursor solution. The addition of filler particles leads to an increase of the viscosity with increasing particle content as shown in Figure 6-4 (b) for 30 wt% POMS filled with AC050 (d_{50} = 1.5 μm). Similar correlations are reported in literature [104, 159]. The increase of viscosity can be attributed to the presence of high-energetic surfaces, particle-particle interactions and an increased cross-linking density [98, 83, 84].

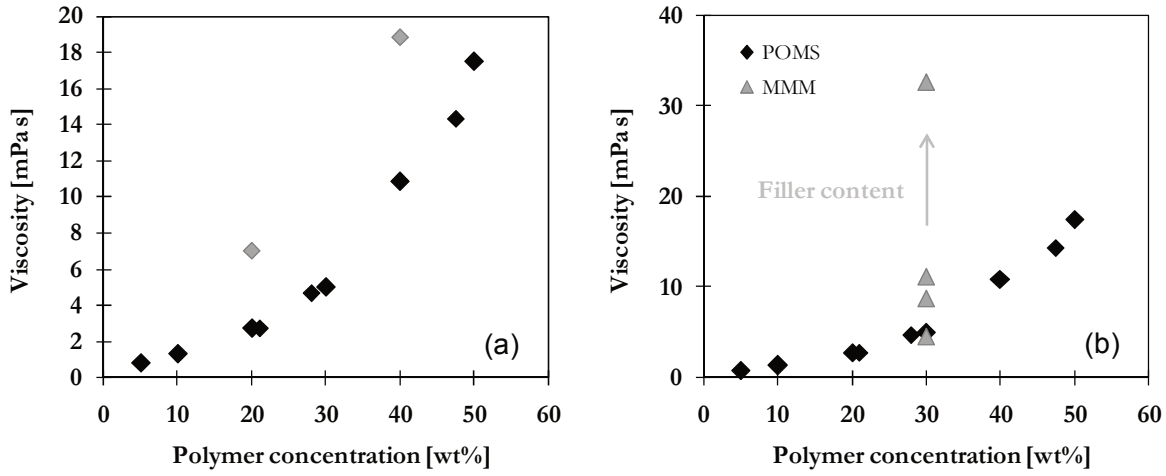

Figure 6-4: (a) Influence of polymer concentration on viscosity of standard (black) and modified (grey) POMS coating solution and (b) influence of increasing amount of AC050 (grey triangles) at 27 °C

Coating solutions with different POMS concentrations, respectively viscosity, have been applied for the preparation of MMMs. As can be seen in Figure 6-5 (a), the application of a 20 wt% standard POMS solution did not result in a homogeneous MMM separation layer. SEM images show a good contact between polymer and filler particles but great variations in the thickness render a reproducible production and thus steady separation performance impossible. The uniformity of the selective layer could be improved by increasing the polymer concentration to 30 wt, see Figure 6-5 (b), or by using a 20 wt% modified POMS solution, see Figure 6-7 (a).

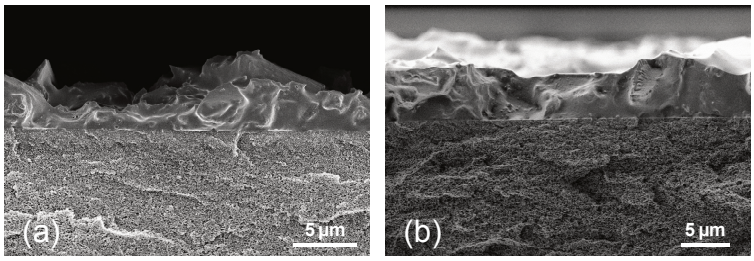

Figure 6-5: SEM cross-section images of MMMs composed of (a) 20 wt% or (b) 30 wt% POMS and 20 wt% AC050 (d50 = 3.5 µm) casted on non-woven/PAN support structure

The impact of the polymer concentration was further investigated with respect to the thickness of the selective separation layer and the *n*-C_4H_{10}/CH_4 separation performance of MMMs composed of 7.5 to 20 wt% POMS (modified) and 20 wt% AC050 (d_{50} = 1.5 µm). In Figure 6−6 (a), the influence of the polymer concentration on the separation layer thickness is presented. The corresponding SEM images MMM of cross-sections used for the evaluation of the separation layer thickness are given in Figure 6-7. The separation layer thickness decreases

with decreasing polymer concentration. As previously stated, the modified POMS pre-cursor solution exhibits a higher viscosity which facilitates the dispersion of particles. This ensures the stability of the casting solution during membrane production and thus the homogeneity of the selective layer. Even at low polymer concentrations of only 7.5 wt%, a quite uniform separation layer could be achieved with an average thickness of approximately 2 µm. A further decrease of the thickness would be at the expense of uniformity as filler particles might protrude.

The influence of the polymer concentration on the separation performance is illustrated in Figure 6-6 (b). Results were obtained with a binary gas mixture containing 5 vol% *n*-C_4H_{10} at 20 °C and 30 bar. Opposing trends for the *n*-C_4H_{10} permeance and the *n*-C_4H_{10} / CH_4 selectivity with respect to the polymer concentration are observed. Although the thin but uniform layers at POMS concentrations of 7.5 or 10 wt% allow a high flux, the selectivity is relatively low. The trade-off between selectivity and flux has long been dominating material research. Assessing the two targets, selectivity and flux, is often to the detriment of the latter. Generally, a low flux or permeance is easier to compensate by increasing the membrane area whereas a low selectivity would require additional membrane stages. For this reason, despite their lower permeances, final concentrations of 15 or 20 wt% of modified POMS in coating solutions have been selected for further MMM production.

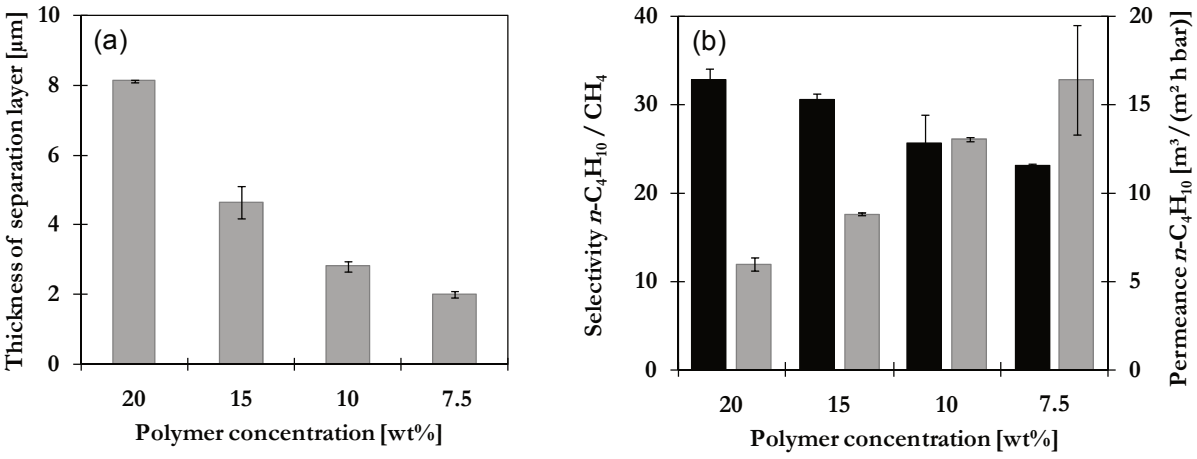

Figure 6-6: Influence of the polymer concentration on (a) the thickness of the separation layer and (b) the separation performance in terms of selectivity *n*-C_4H_{10}/CH_4 (black) and permeance *n*-C_4H_{10} (grey) of MMMs composed of POMS-XL and 20 wt% AC050 (d50 = 1.5 µm) casted on a non-woven/PAN support with GL at 20°C, 30 bar and $y_{F,n\text{-}C4H10}$ = 0.05

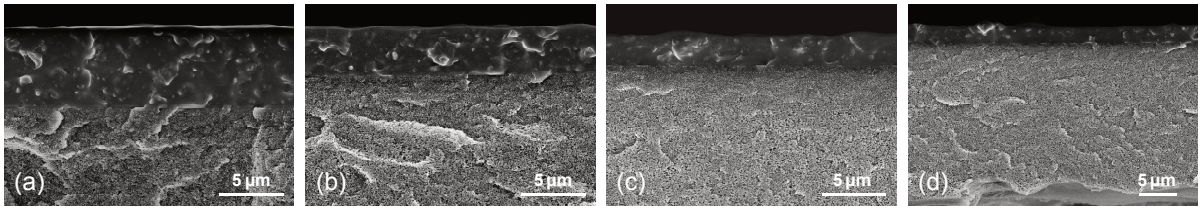

Figure 6-7: SEM cross-section images of MMM composed of (a) 20 wt%, (b) 15 wt%, (c) 10 wt% and (d) 7.5 wt% POMS-XL and 20 wt% AC050 (d_{50} = 1.5 µm) casted on a non-woven/PAN support with GL

6.1.2 Selection of Inorganic Filler Phase

The choice of the filler material, it's shape and inner structure determine the final membrane performance [51]. As described in Chapter 4, a variety of effects can be pursued with the addition of filler particles. The aim of this work was to improve the membrane's selectivity for higher hydrocarbons being in mixture with permanent gases. This can be achieved by the incorporation of filler materials with a superior adsorption selectivity for the higher hydrocarbons or by affecting the chain packing density in the right way. For this purpose, different inorganic materials have been applied, including porous activated carbons and zeolite as well as non-porous silica and carbon black. The activated carbons (type AC050, AC942, AC085) were chosen due to the high adsorption capacity of *n*-C_4H_{10} provided by their highly developed microporous structure. These activated carbons are based on polymeric resins that undergo a conversion and activation during a very reproducible production process and are highly resistant against chemical and mechanical impacts [20]. The hydrophobic Y-type zeolite CBV-780 is commonly applied as adsorbent for the removal of water or organic vapours, as catalyst in petroleum refining or as ion exchange material in detergents [172]. The non-porous AEROSIL® R8200 is commonly used as an additive to silicone rubber, sealants or adhesives, as anti-foaming agent or as flowing agent for powders [48]. Silica is usually present in form of spherical primary particles in the range of 10 – 20 nm clustered to aggregates and agglomerates via physical forces [6]. Carbon black, likewise present in aggregated form, is a common reinforcing additive in the rubber industry to enhance the hardness and abrasion resistance of tires. Besides, it is the most commonly used black pigment for the production of ink, paint or the colouring of plastics, tires and food [107].

For the selection of the optimum filler material, the different filler types were analysed with respect to their adsorptive properties and their impact on the morphology and separation performance of produced MMM samples.

Adsorptive Properties

The adsorptive properties of the different inorganic filler types were evaluated by means of sorption measurements with CH_4 and *n*-C_4H_{10} at 25 or 28 °C. Measurements were performed with AEROSIL® R8200 (AS) and activated carbon type AC050. Data for zeolite CBV-780 (Z) was provided by the Institut für Nicht-klassische Chemie (INC, University of Leipzig, Germany). Measurements with carbon black (CB) were not possible as only present in dispersed form. The adsorption isotherms are presented in Figure 6-8.

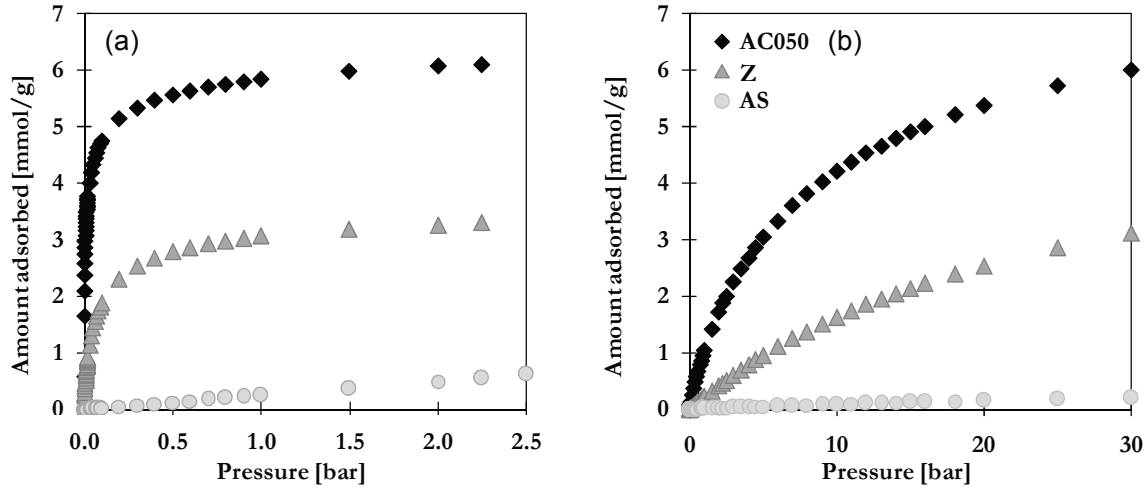

Figure 6-8: Sorption isotherms of (a) *n*-C_4H_{10} and (b) CH_4 for inorganic filler materials AC050 (diamonds), zeolite CBV-780 (Z, triangles) and AEROSIL® R8200 (AS, circles) at 25 °C or 30 °C (AS)

In contrast to pure POMS (Flory-Huggins type solution, see Figure 6-3), the adsorption isotherms of porous inorganic fillers follow a Langmuir type behaviour. This is observed for both CH_4 and *n*-C_4H_{10} in the porous materials activated carbon AC050 and zeolite CBV-780. It can accurately be described by the equation of Toth (see Table A−3 in Appendix A). A similar curve is expected for the activated carbon type AC942 as characterised by a similar porous system than AC050 whereas the greater pore volume of AC085 (see Table 5-1) might allow an even higher adsorption capacity (no results available). For *n*-C_4H_{10}, a fast saturation of adsorption sites occurs up to 1 bar. The maximum amounts adsorbed are 6 and 3 mmol/g for AC050 and zeolite, respectively. While both gases are adsorbed up to the same amount, a much slower adsorption rate is observed for CH_4. The maximum amount adsorbed is reached at pressures higher than 30 bar. AEROSIL® shows nearly no adsorption, neither of CH_4 nor *n*-C_4H_{10}. Similar behaviour can be expected for CB. Both are non-porous materials and thus no typical adsorbents.

The adsorption data allows the determination of the limiting thermodynamic selectivity by interpolating the values to zero coverage ($p \rightarrow 0$). Results for single and mixed gas selectivities of different filler materials at 25 - 28 °C are given in Table 6-1. Results for gas mixtures were kindly provided by INC Leipzig, Germany. By far the highest thermodynamic selectivity was found for AC050 showing its suitability as filler material for higher hydrocarbon selective MMMs. Nevertheless, both porous materials, activated carbon AC050 and zeolite, exhibit a superior selectivity than pure POMS which is characterised by a solubility selectivity n-C_4H_{10}/CH_4 of 134 or 82 at 20 or 30 °C, respectively (see Figure 6-3). Being not a typical adsorbent, the selectivity of non-porous AS is, as expected, far below the values of AC and zeolite. Comparing the single and mixed gas selectivity, great differences are noted for AC050 while differences are neglegible for zeolite. A lower mixed gas selectivity can indicate a strong competition between mixture components for sorption sites. Such competitive or coupling effects will affect the overall separation performance.

Table 6-1: Thermodynamic selectivity of different filler types for zero coverage ($p \rightarrow 0$) determined with single or mixed gas (data provided by INC, Leipzig) sorption measurements

Filler Type	Temperature [°C]	Single Gas α n-C_4H_{10} / CH_4	Mixed Gas [1] α n-C_4H_{10} / CH_4
AC050	25	26864	14160
Z	25	496	493,5
AS	28	17	n.s.

MMM Morphology

The permeation in MMMs strongly depends on the established structure visible on macroscale, i.e., the separation layer thickness and the dispersion of particles [68], as well as on the interfacial microscale [103]. While research published on MMMs is often focused on thick films, industrial scale applications for separating higher hydrocarbons are mainly based on TFC structures with ultrathin active separation layers [12]. The defect-free and reproducible production of such is an even greater challenge to realize in MMM structures. The morphology of TFC MMM separation layers prepared in this work is studied by SEM analysis. SEM images of cross-sections for MMMs filled with 20 wt% of different filler materials are presented in Figure 6-9. They were used to determine the final thickness of the active separation layers.

All membranes show separation layers with quite uniform thicknesses and a good contact between the filler particles and the polymeric matrix. No visible defects caused by an improper

material selection are revealed. The highest uniformity of the separation layer is found for AEROSIL®, Figure 6-9 (a). It also results in the highest thickness of 8.60 (± 0.62) µm. Specifications regarding the particle size were not provided by the manufacturer but reported data for similar types AEROSIL® 812 and AEROSIL® A300 describe spherical primary particles with diameter of 7 nm [80]. This seems to be in good agreement with observed SEM images of MMMs filled with AEROSIL® R8200. Spherical particle shapes are often reported as beneficial for the MMM production [175]. A similar selective layer morphology is observed for CB as filler, Figure 6-9 (b). The layer thickness is 5.19 (± 1.09) µm. The zeolite containing membranes, Figure 6-9 (c), have an average thickness of the selective layer of 6.18 (± 1.14) µm. Particles seem to be agglomerated and not homogeneously dispersed. MMMs filled with AC050 have an average thickness of 5.80 (± 0.92) µm. The average particle size is specified as 3.5 µm and thus not a limiting parameter itself, but the broad particle size distribution allows the presence of larger, disruptive particles (see Figure B-1). This seems also the case for MMMs containing AC942 and AC085 which show the strongest scattering in the separation layer thickness. Thicknesses of MMM separation layers and standard deviations are 7.71 (± 2.24) µm for AC942 and 7.90 (± 2.03) in case of AC085.

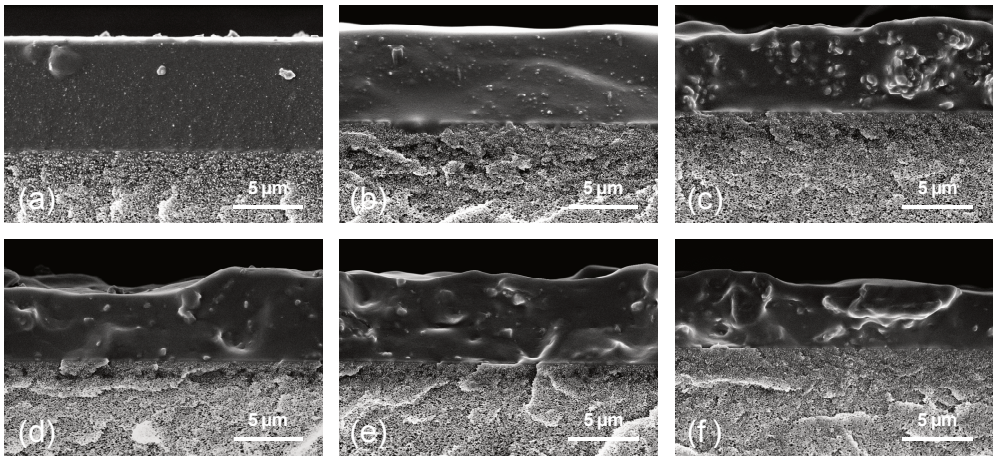

Figure 6-9: SEM images of MMM cross-sections with 20 wt% POMS (type XL) and a) AEROSIL® R8200, b) Carbon Black, c), zeolite CBV-780, d) AC942, e) AC085 or f) AC050 as inorganic filler particles casted on non-woven/PAN supports with GL

Separation Performance n-C_4H_{10} / CH_4

The suitability of filler materials has been investigated in terms of the *n*-C_4H_{10} / CH_4 separation performance of MMMs composed of 20 wt% POMS (type XL) and 20 wt% of the different filler

materials. Measurements were performed with single gases *n*-C_4H_{10} and CH_4 at 20°C up to 1 bar as well as with binary mixtures with 5 vol% *n*-C_4H_{10} in CH_4 at 20°C and 30 bar.

The single and mixed gas selectivities *n*-C_4H_{10}/CH_4 are summarised in Table 6-2. Values for single gas selectivities correspond to non-swollen membranes extrapolated to zero pressure. Mixed gas selectivities are given for a feed pressure of 30 bar. It has to be noted that a direct comparison of results would be misleading due to the different operating conditions.

The results of single gas investigations imply that no significant improvement can be achieved by the addition of filler particles. The ideal selectivity *n*-C_4H_{10}/CH_4 of POMS is 15.9 and only slighlty influenced by the addition of filler materials. Only small deviations are found for CB, AS and Z giving values of 15.9, 16.0 and 16.2, respectively. The high thermodynamic selectivity found for activated carbon (see Table 6-1) is not reflected by MMMs in single gas permeation. On the contrary, addition of activated carbon AC050, AC942 or AC085 causes a slight decrease of the ideal POMS selectivity. In particular, MMMs with AC050 show the lowest selectivity of 13.9. The formation of defects can be excluded with regard to the single gas *n*-C_4H_{10} permeability, which is much lower for MMM-AC050 (3109 Barrer) than for pure POMS (4070 Barrer). It is more likely that the permeation is reduced in consequence of the immobilization of gas molecules by adsorption forces as described by Paul & Kemp [73]. This would especially be observed for AC as having the highest affinity for *n*-C_4H_{10} adsorption (see Figure 6-10).

The mixed gas permeation measurements reveal very different impacts of the filler materials. A clear improvement of mixed gas separation performance is observed for all filler types except for CB. By far the highest selectivity is found for AC050. The results of the *n*-C_4H_{10}/CH_4 mixed gas selectivity are further illustrated in Figure 6-10 and supplemented by results for the *n*-C_4H_{10} permeability. According to the Maxwell model (see section 4.3), the addition of non-porous filler particles such as CB is reported to reduce the permeability. An opposed trend was observed in this case for the non-porous materials CB and AEROSIL® which give *n*-C_4H_{10} permeabilities slightly higher than POMS. CB does not provide an adsorptive porous system and is assumed to affect only the chain packing density and the free volume. The low selectivity seems reasonable as in absence of further interactions an increase in free volume and thus diffusivity would be in favour for smaller CH_4 molecules. However, this MMM also exhibits the highest error of measurement.

Table 6-2: Single and mixed gas selectivity *n*-C_4H_{10}/CH_4 for MMMs composed of 20 wt% POMS (type XL) and 20 wt% of various filler types at 20 °C (single gas: experimental values for non-swollen membranes at zero pressure, mixed gas: experimental values at 30 bar feed pressure, $y_{F,n\text{-}C4H10} = 0.05$)

Filler Type	α *n*-C_4H_{10}/CH_4	
	Single Gas	Mixed Gas
none (POMS-XL)	15.9	26.0
CB	15.9	24.6
AS	16.0	28.4
Z	16.2	27.8
AC942	15.3	27.0
AC085	15.5	27.6
AC050 (type 1)	13.9	31.7

The high selectivity of 28.4 for MMMs filled with AEROSIL® (AS) seems quite surprising at first glance as it is a non-porous material either and showed a poor thermodynamic selectivity (see Figure 6-8). It is assumed that the highly hydrophobic character of AS creates a less favorable environment for CH_4 and that surface groups interact with the polymeric chains forming an additionally cross-linked network which is less prone to swelling. A particle induced network formation in PDMS has been ascribed by Şerbescu *et al.* to hydrogen bonds between silica surfaces and PDMS [145]. MMMs filled with zeolite, AC942 or AC085 show moderate improvements in *n*-C_4H_{10}/CH_4 selectivity of 27.8, 27.0 and 27.6, respectively. MMMs with AC942 and AC085 are accompanied with the highest (type AC942) and lowest *n*-C_4H_{10} permeability (AC085) of all MMMs. In accordance with the thermodynamic selectivity (see Table 6-1), the highest improvement is clearly found for AC050 with a *n*-C_4H_{10}/CH_4 selectivity of 32. This is 20 % higher than the selectivity of pure POMS. Despite the only moderate improvments in membrane permeability, AC050 is identified as the most promising filler type and thus choosen for further investigations.

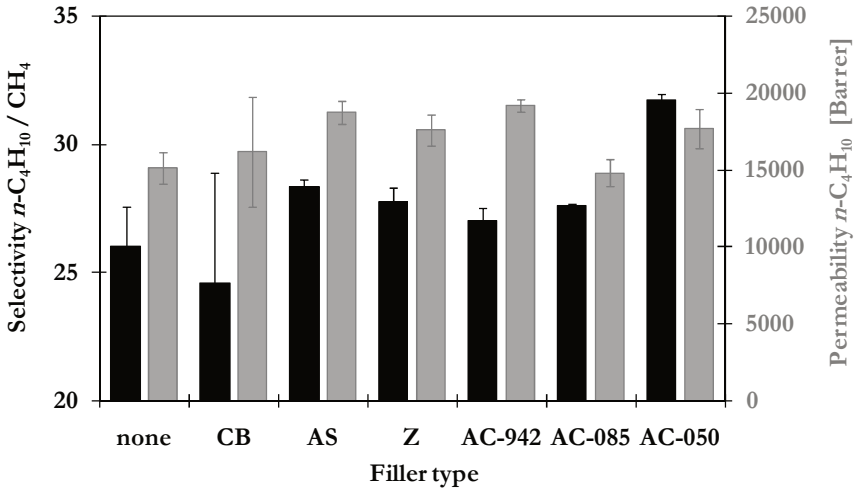

Figure 6-10: Mixed gas selectivity *n*-C_4H_{10}/CH_4 (black) and permeability *n*-C_4H_{10} (grey) for MMMs composed of POMS and 20 wt% different inorganic filler materials at 20 °C, 30 bar and 5 vol% *n*-C_4H_{10} in feed mixture (CB = carbon black, AS = AEROSIL®, Z = zeolite, AC = activated carbon)

6.1.3 Optimisation of Filler Content and Particle Size

Besides the type of inorganic material, the filler content incorporated into the polymeric matrix and the filler particle size are of great importance. While classical spherical particles usually require high contents, stronger effects are expected for fillers with high aspect ratios [34, 176]. However, high contents and irregular particle shapes often evoke brittleness and fabrication problems due to a severe change in polymer viscosity, non-uniform distribution of particles and the formation of non-selective voids [90, 50, 81]. The impacts of the filler content and particle size on the MMM morphology and separation performance will be discussed in this section.

6.1.3.1 Influence of Filler Content

The influence of the filler content on the membranes' gas transport properties was investigated on the basis of MMMs filled with 10 to 40 wt% AC050 (pre-saturated with ethanol) as proofed in 6.1.2 to be the most promising filler type. A multitude of measurements has been performed to characterize the impacts of the filler content, for example, on the membrane morphology, the single gas O_2/N_2 and mixed gas *n*-C_4H_{10}/CH_4 permeation and separation performance, the sorption behaviour and the flexibility of polymeric matrix. Impacts and improvements are generally expected to be more pronounced with an increasing filler content which should thus be maximized to surpass the specific percolation threshold [175].

MMM Morphology

Figure 6-11 shows SEM images of cross-sections of MMM separation layers filled with different contents of AC050-1 with d_{50} = 3.5 µm (a-c) and AC050-2 with d_{50} = 1.5 µm (d-f). The thicknesses of the separation layer are given in Figure 6-13 (a). An increase of the filler content leads to thicker separation layers. Besides the volume of particles itself, the increase in thickness is caused by the change of the viscosity of the coating solution (see Figure 6-4). While the separation layer of pure POMS is about 3.4 µm, the MMM layers are nearly doubled in thickness for AC050-1 (d_{50} = 3.5 µm). Thicknesses of 6.1, 7.8 and 15.2 µm for contents of 10, 20 or 40 wt% of AC050-1 were found. The smaller fraction AC050-2 (d_{50} = 1.5 µm) resulted in even thicker layers with 11.1, 12.5 and 48.5 µm for contents of 10, 20 or 40 wt% AC050-2, respectively. The filler content was adjusted as mass fraction with respect to the dry polymeric mass. A larger number of particles are thus present in case of AC050-2 which might affect the arrangement of polymer chain. At a filler content of 40 wt%, the layers show severe non-uniformity and agglomeration of particles. Especially for the smaller fraction AC050-2, the separation layer seems more like packed particles with only small amounts of polymer in between and is suspected to show defects.

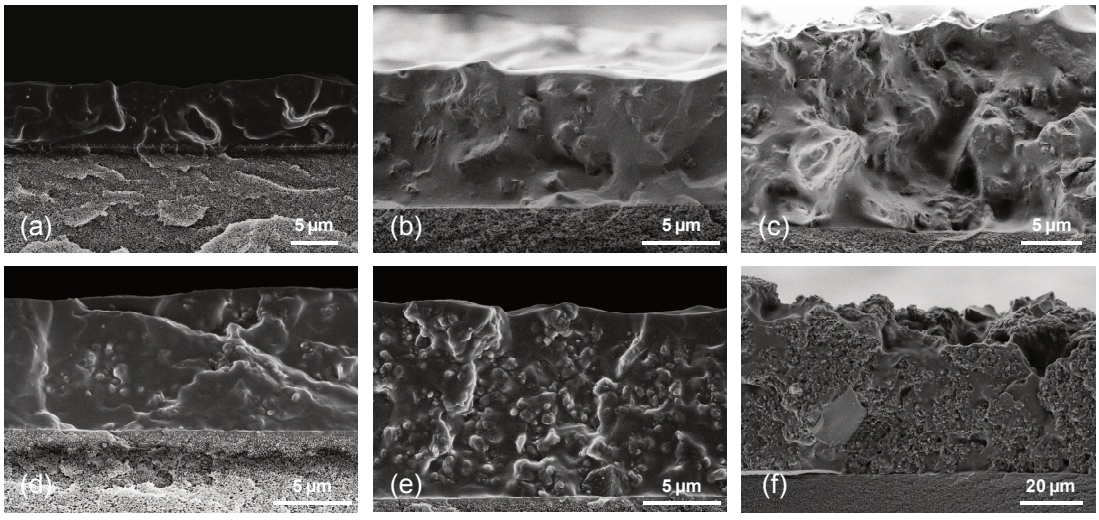

Figure 6-11: Influence of the filler content on the morphology of MMMs composed of POMS and 10, 20 or 40 wt% (left to right) AC050 type 1 with d_{50} = 3.5 µm (a-c) and AC050 type 2 with d_{50} = 1.5 µm (d-f)

Single Gas Permeation and Separation of O_2/N_2

The investigation of the transport of N_2 and O_2 through the membrane allows a quick screening of the prepared MMMs with respect to a defect formation. Both gases are relatively small and not

significantly interacting with the polymeric matrix or the filler phase. The addition of AC050 is therefore not expected to change the O_2/N_2 selectivity. In contrast, a major drop would indicate the presence of defects offering and selective pathways. The results of O_2/N_2 single gas measurements of MMMs filled with 10 – 40 wt% of AC050 type 1 (d_{50} = 3.5 µm) and type 2 (d_{50} = 1.5 µm) are given in Figure 6-12.

The O_2/N_2 selectivity of MMMs filled with AC050-1 is hardly influenced by the filler content. Values of 2.3 to 2.4 were found that are within the range of pure POMS with its' selectivity of 2.3. N_2 permeability shows a clear optimum of 95 Barrer for 10 wt% AC050-1. An increasing filler decreases the permeability below 50 Barrer. For comparison, POMS shows a N_2 permeability of 76 Barrer at 20 °C. At high filler contents, the additional transport resistances and high tortuosity often negatively impair the permeation [96, 82]. The polymer might get rigidified due to the impacts of the filler particles on the chain mobility [103] or the filler particles additional cross-linking sites [84]. Both effects reduce the free volume and permeability and increase the selectivity (see Figure 4-3). An opposing trend was found for MMMs filled with AC050-2 (Figure 6-12 b). An increasing content leads to a continuous increase of permeability up to 20 wt% and a sharp increase to more than 650 Barrer for 40 wt% AC050-2. The sharp increase is accompanied by a large drop of selectivity down to 1.1 which corresponds to the value of Knudsen selectivity. It indicates the presence of non-selective defects (see Figure 4-3) which has been confirmed by SEM images (Figure 6-11).

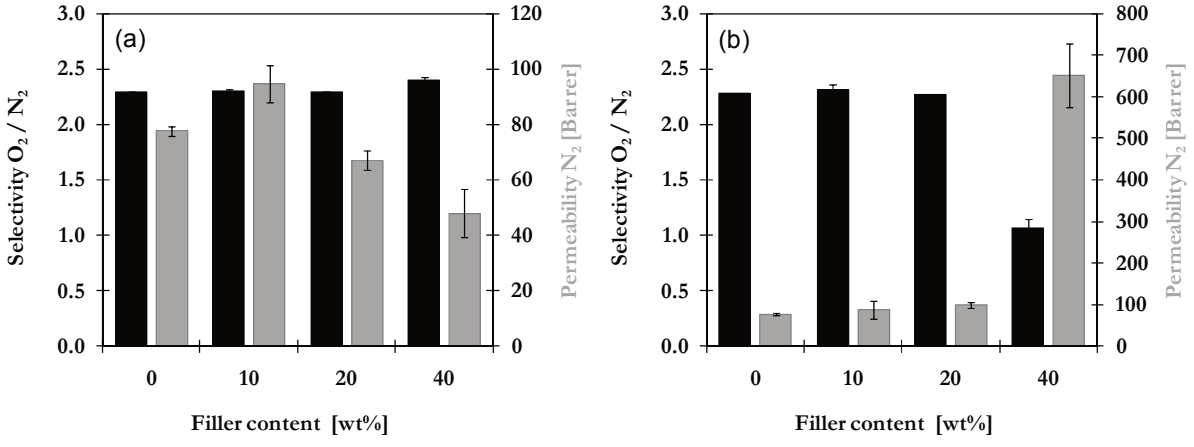

Figure 6-12: Influence of the filler content on O_2/N_2 selectivity and N_2 permeability for MMM composed of POMS and (a) AC050 type 1 (d_{50} = 3.5 µm) or (b) AC050 type 2 (d_{50} = 1.5 µm) at 20 °C

Mixed Gas Permeation and Separation of n-C_4H_{10}/CH_4

The influence of the filler content shall further be discussed based on the mixed gas permeation of *n*-C_4H_{10} and CH_4. Results for *n*-C_4H_{10} permeability and *n*-C_4H_{10}/CH_4 selectivity of MMMs composed of POMS and different amounts of AC050-1 at 30 °C and 30 bar are presented in Figure 6-13 b. For pure POMS, the *n*-C_4H_{10} permeability was found to be approximately 10700 Barrer. It continuously declines with increasing filler content giving values of 10600, 7700 and 5100 Barrer at 10, 20 and 40 wt% of AC050, respectively. The *n*-C_4H_{10}/CH_4 selectivity for pure POMS is found to be 18 at 30 °C. The addition of 10 wt% AC050 leads to a slight reduction of selectivity which is followed by an increase up to 21.6 at 20 wt%. At higher contents the selectivity drops below the value of pure POMS.

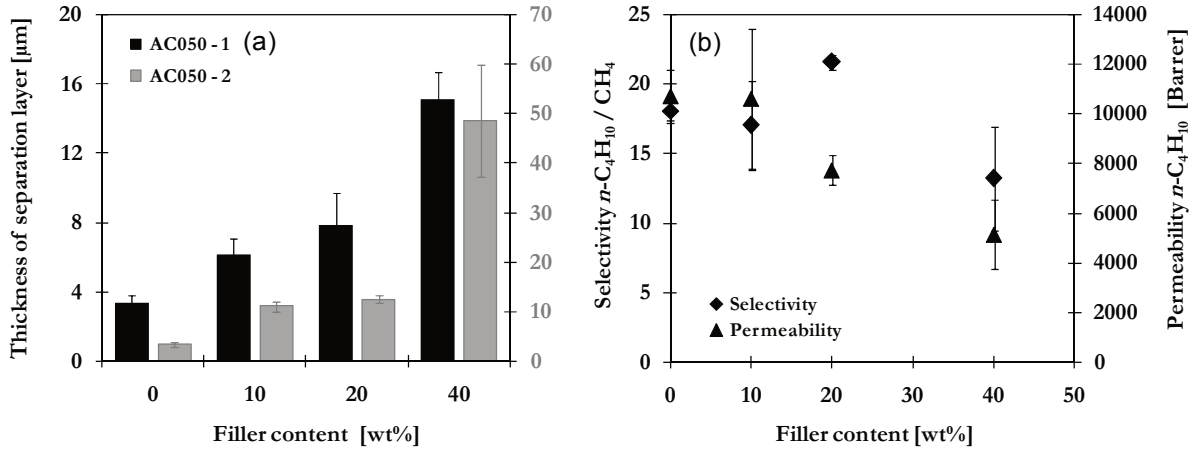

Figure 6-13: Influence of the filler content on (a) the thickness of separation layer of MMMs composed of POMS and 10 – 40 wt% AC050-1 or AC050-2 and (b) separation performance *n*-C_4H_{10}/CH_4 and permeability *n*-C_4H_{10} in binary mixtures with 5 vol% *n*-C_4H_{10} at 30°C and 30 bar

The presence of an optimum for MMM separation performance in dependency on filler content has been reported manifold in literature for various filler types [90, 50, 175]. Below the percolation threshold, the transport through the membrane is governed by the polymeric matrix and the addition of filler particles has little, sometimes even negative effect. In this work, filler contents below 20 wt% are too small to exceed the percolation threshold. The polymeric matrix is still dominant and gas molecules are rather retarded or trapped by tortuosity. At 20 wt% AC the inorganic particles are exploited to their best advantage allowing an improved separation efficiency. Even if the respective percolation threshold has to be defined for each MMM and separation task individually, this value is in good accordance with other studies [155, 90, 86]. At higher filler contents, the agglomeration of particles can lead to the formation of non-selective

channels as particles might not be fully surrounded by the polymeric phase. As will be shown later, density measurements can provide additional information about the formation of voids. MMMs in the form of isotropic films are often reported to be brittle and mechanically unstable at high filler contents above 30 wt% [3]. In addition, high transport resistances, immobilization by adsorption, intermolecular interactions or rigidified polymer layers close to the filler surfaces might impede the exploitation of the filler particles (see Figure 4-3). Some aspects will be discussed below to identify occurring effects.

Activation Energy for Permeation

An interesting point to discuss is the influence of the filler content on the activation energy for permeation E_P. The activation energies calculated from *n*-C_4H_{10} and CH_4 single gas permeation data of POMS and MMMs at different temperatures are presented in Table 6-3.

The E_P values for *n*-C_4H_{10} and CH_4 permeation in POMS are -2.93 kJ/mol and 11.44 kJ/mol, respectively. In comparison, E_P values of -7.0 kJ/mol and 6.8 kJ/mol are reported for *n*-C_4H_{10} and CH_4 in PDMS [127]. The positive values for CH_4 indicate an increasing permeability coefficient with increasing temperature and, vice versa, the negative values for *n*-C_4H_{10} a decreasing permeability coefficient. The addition of AC050 leads to a slight increase of E_P with an increasing filler content up to 20 wt%. The permeation of CH_4 seems to be hindered. At 40 wt% AC050 the E_p shows a strong decline for both components.

As previously described, E_P is composed of the activation energy for diffusion E_D and the enthalpy of solution ΔH_s (see equation (3.3-9)) which both are affected by the presence of filler particles. Diffusion through a polymer is an activated process based on the thermal motion of polymeric chains, the formation of free volume elements and jumps between them. Opposing effects of the addition of filler particles on the E_D can be expected. An increased rigidity of the polymeric matrix would impede diffusive jumps and result in a larger E_D [9, 101, 144]. On the other hand, the presence of particles might disrupt the polymeric chain packing and increase the free volume or even cause the formation of defects which would reduce energy barriers and facilitate diffusion, in particular for the smaller CH_4 molecules [29, 57]. In addition, the porous system of AC050 allows further transport following pore diffusion and surface diffusion mechanisms (see Figure 3-5) which both are characterized by higher diffusion coefficients than the diffusion through POMS [108]. The enthalpy of solution ΔH_s in a polymeric matrix is composed of the enthalpy of condensation ΔH_{cond} and the enthalpy of mixing ΔH_{mix}. In case of

MMMs, the additional heat for adsorption on AC particles has to be considered. These values were estimated from the parameters of the Toth adsorption isotherm to -55.3 and -16.8 kJ/mol for *n*-C_4H_{10} and CH_4 in AC050, respectively.

Regarding the observed values for E_P in Table 6-3, different impacts of the described trends are reflected. The initially higher E_P shows the influence of a larger E_D due to a restricted chain mobility. This would particularly affect CH_4. In case of the highly soluble *n*-C_4H_{10}, this initial domination of E_D is overlaid at 20 wt% by changes of ΔH_s. The low E_p for both *n*-C_4H_{10} and CH_4 at 40 wt% could either reflect the highly negative heat of solution of adsorbing carbon particles or suggest the formation of defects that provide pathways with non-activated diffusion. For 20 wt% AC050, the highest activation energy for CH_4 along with a minor influence on *n*-C_4H_{10} is found. These are beneficial conditions for an improved *n*-C_4H_{10} / CH_4 selectivity. Indeed, it perfectly fits to the optimum in MMM mixed gas selectivity shown in Figure 6-13 (b). However, a direct transfer of single gas results might be misleading as coupling effects in case of gas mixtures can imply further effects on the activation energies [126].

Table 6-3: Energy of activation for *n*-C_4H_{10} and CH_4 permeation in POMS and MMM filled with 10 – 40 wt% AC050 (d_{50} = 3.5 µm)

Filler content	Activation Energy of Permeation	
	n-C_4H_{10}	CH_4
[wt%]	[kJ/mol]	[kJ/mol]
0	-2.93	11.4
10	-2.58	12.4
20	-2.66	12.7
40	-3.43	10.0

Density and Void Formation

The density of thick MMM films can be estimated from the densities and volume fractions of the pure polymer and filler phase according to equation (6-1). Deviations between calculated and measured values are often observed and related to an increased free volume or void volume at the interface polymer – particle or in between aggregated filler particles [169, 3, 55]. The void volume fraction is given by equation (6-2).

$$\rho_{MMM} = (1 - \varphi_F) \cdot \rho_P + \varphi_F \cdot \rho_F \qquad \textbf{(6-1)}$$

$$\varphi_{void} = 1 - \frac{\rho_{MMM,exp}}{\rho_{MMM,calc}} \quad \textbf{(6-2)}$$

The predicted and measured densities of thick MMM films as well as the estimated void volume fractions are presented in Table 6-4 as function of AC050 (d_{50} = 3.5 µm) content. The densities increase with an increasing filler content, reflecting the significantly higher density of AC050 (2.1 g/cm³) compared to pure POMS (0.962 g/cm³). Stronger deviations between measured and calculated values are observed for higher filler contents giving a linear increase of the void volume. As shown in Table 6-4, the presence of voids reduces the actual volume fraction (φ_F^T) of filler particles present in the MMM sample.

Table 6-4: Measured (ϱ_{exp}) and calculated (ϱ_{calc}) density of thick MMM films based on POMS and AC050 (d_{50} = 3.5 µm), estimated void volume fraction (φ_{void}) and true filler fraction (φ_F^T)

Filler content [wt%]	φ_F [vol%]	ϱ_{exp} [g/cm³]	ϱ_{calc} [g/cm³]	φ_{void} [vol%]	φ_F^T [vol%]
0	0.0	0.9615	-	-	-
10	10.7	1.0018	1.0834	7.5	9.9
24	25.4	1.0657	1.2509	14.8	21.7
42	43.9	1.1189	1.4609	23.4	33.6

Thermal Behaviour and Flexibility of Polymeric Matrix

As previously mentioned, a reduced permeability of MMMs at high filler loadings (see Figure 6-12 and Figure 6-13) can be evoked by a restricted chain mobility in vicinity of solid filler particles forming a rigidified polymeric matrix. The chain flexibility or rigidity of a polymeric matrix can be described by the glass transition temperature T_g. Even slight changes can have major impacts on the mechanical and thermal behaviour [117]. While a decrease of T_g can be attributed to a higher free volume due to the disruption of cross-links by filler particles, the presence of a rigidified layer at the interface polymer – filler can be evidenced by an increase of T_g [103, 33]. Results of DSC analysis of thick POMS and MMM films with varying amounts of AC050 are presented in Table 6-5.

A T_g of -110.0 °C was found for pure POMS. A clear impact of the addition of AC050 on T_g could not be observed. A slightly higher T_g of -108.3 °C was observed merely for 24 wt% AC050, while other filler contents resulted in slightly lower T_g. It has to be noted that differences are

mostly in the range of the typical error range of DSC measurements. Similar ambiguous results were found by Liu *et al.* for polyether-block-amide (PEBA) filled with ZIF-71 [86]. As usually only small volumes of the rigidified interfacial layers are present, the changes in T_g are difficult to determine [101]. A more sensitive parameter is the specific heat capacity at glass transition temperature. It shows a continuous decrease with increasing filler content. The decrease results from the thermal properties of the activated carbon that hints at rigidified polymeric layers. Similar results are reported by Tavman *et al.* for a high density PE filled with expanded graphite [156].

Table 6-5: Influence of the filler content on the glass transition temperature T_g and corresponding specific heat capacity Δc_p of MMM films filled with varying amounts of AC050-1 (d_{50} = 3.5 µm)

Filler content [wt%]	T_g [1] [°C]	Δc_p [J/(g K)]
0	-110.0	0.240
11 [2]	- 110.8	0.201
18	- 110.3	0.195
24	- 108.3	0.165
42	- 110.6	0.130

[1] Typical error in DSC results ranges from ± 0.5 – 1 °C [146]
[2] Ethanol as solvent for pre-saturation

Sorption Behaviour

The adsorptive properties of inorganic filler materials have already been discussed in 6.1.2 and it was shown that AC050 preferentially interacts with condensable *n*-C_4H_{10} (see Figure 6-8). The influence of the AC050 content on the sorption behaviour of POMS based MMMs (see Figure 6-3) will be described in this section. Sorption measurements of *n*-C_4H_{10} and CH_4 were performed with MMM separation layers filled with 10 – 40 wt% AC050 (type 1) at 30 °C. Experimental results are compared with values calculated by means of an additive model for sorption in filled systems.

The additive model is given in equation (6-3). It superposes the dissolution in the polymer q_{diss} and the adsorption q_{ads} in the inorganic filler according to the volume fractions of filler φ_F and polymer φ_P [17].

$$q_{total} = q_{ads} \cdot \varphi_F + q_{diss} \cdot \varphi_P \qquad \textbf{(6-3)}$$

As described in 6.1.2, the adsorption of both gases on pure AC can be described by the equation of Toth [37]. For the rubbery polymeric matrix, a polynomial 2nd order equation was used to describe the Flory-Huggins type dissolution of *n*-C_4H_{10} and a linear Henry type isotherm for CH_4 [126]. The suitability of both equations has previously been verified (see 6.1.1) [108, 77]. Results for 20 wt% and 40 wt% filler contents are illustrated in Figure 6-14 with symbols representing the experimental values and lines the calculated values.

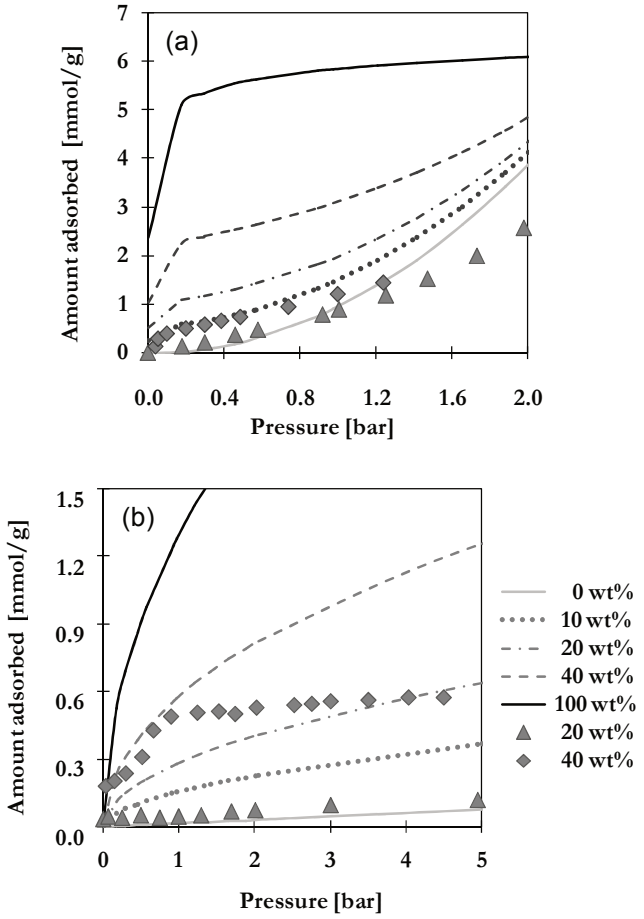

Figure 6-14: Sorption of (a) *n*-C_4H_{10} and (b) CH_4 in POMS filled with AC050 calculated according to the additive model (lines) at 30 °C and corresponding experimental results (filled symbols) for samples of detached MMM separation layers with 20 and 40 wt% AC050 (d_{50} = 3.5 µm, ethanol saturated)

As expected, the model predicts an increase of the sorption capacity by addition of adsorptive filler AC050. Similar results have been reported in literature, e.g., the sorption of chlorinated hydrocarbons in PDMS filled with zeolite silicalite by Dotremeont *et al.* [40]. The increasing AC content changes the exponential or linear curve shapes of pure POMS sorption towards the Langmuir type adsorption isotherm with a finite saturation limit characteristic for adsorbents. However, this could not be confirmed by the experimental results of sorption analysis. Nearly no

effect of AC content on the sorption behaviour was observed for 10 or 20 wt% (experimental results for 10 wt% are not shown for reasons of clarity). The sorption isotherm still follows the characteristic shapes for pure POMS. In case of *n*-C_4H_{10}, experimental values are even below values for pure POMS at a pressure greater 1 bar. This might be ascribed to the lower amount of polymer available for sorption in presence of filler particles and the additionally reduced flexibility of polymeric chains. Minor effects occur at high filler contents of 40 wt% AC, but still strong deviations between expected and measured values are observed. The results for *n*-C_4H_{10}, Figure 6-14 (a), clearly demonstrate the dominating influence of the Flory-Huggins type dissolution, especially at a pressure greater than 0.4 bar. Whereas the Langmuir type shape of curve could be observed for CH_4 in samples with 40 wt% AC, the amounts adsorbed are far below the expected values. As shown in Table 6-4, the actual filler volume fraction is slightly lower due to the presence of void spaces. While this would lower the impact of filler on sorption, it alone does not explain the large deviations. The high sorption of bulk AC particles is clearly not revealed when being embedded into the polymeric matrix. Results suggest that active sites are not fully accessible, e.g., due to an agglomeration of particles, adsorbed impurities or a coverage by polymeric chains. This renders the approach of the additive model, which is based on independent sorption and solubility, to be invalid and oversimplified. A comparison of experimental and calculated values reveals that only 5 - 15 % of active sites seem to be available in MMMs. Similar results have been reported by Barrer [17] and Bae [9]. A further model proposed by Barrer limits the additive model to the polymer phase to describe the sorption in case of wetted filler surfaces [17].

$$q_{total} = q_{diss} \cdot \varphi_P \qquad \textbf{(6-4)}$$

Results of the additive model and the reduced model by Barrer are compared in Figure 6-15 by means of the sorption of *n*-C_4H_{10} in MMM filled with 20 or 40 wt% AC050 at 30 °C.

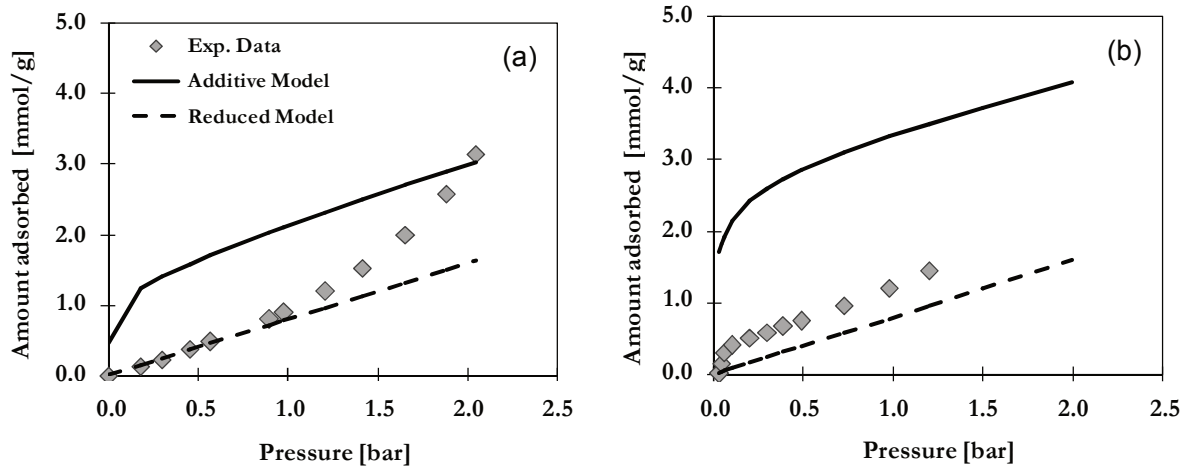

Figure 6-15: Sorption of *n*-C_4H_{10} in MMM separation layers at 30 °C with (a) 20 wt% or (b) 40 wt% AC050 (d_{50} = 3.5 µm, ethanol saturated) calculated according to the additive model (solid lines) or the reduced model by Barrer (dotted line) and corresponding experimental results (filled symbols)

The reduced Barrer model yields a good fit to the experimental data up to 1 bar in case of MMMs filled with 20 wt% AC (Figure 6-15 (a)). At a higher pressure, a Flory-Huggins curve is observed indicating the dominance of the polymeric matrix. MMMs filled with 40 wt% AC clearly show the shape of a Langmuir type adsorption according to the additive model but the total amount is better described by the reduced model (Figure 6-15 (b)). A partial inactivation of the filler particles in MMM with respect to adsorption is thus likely preventing the full exploitation of superior properties of AC. However, it has to be noted that these conclusions are based on experimental results performed with very small sample sizes. The influence of filler might be hard to determine in this case and prone to error. Residual solvent used to detach the separation layers from the composite structure might still be adsorbed despite of an extensive evacuation and block adsorption sites. Further, the beneficial effect of AC is expected to be more pronounced in case of gas mixtures.

6.1.3.2 Influence of Filler Particle Size

Two different fractions of AC050 were available to investigate the influence of the filler particle size. The fraction AC050-1 is obtained after 26 h of crushing bulk particles in a porcelain tumbling mill followed by air classifying. It is characterised by a broad particle size distribution with a mean particle size d_{50} = 3.5 µm. The fraction AC050-2 is additionally milled in an attritor for 300 min resulting in a narrower distribution with a mean particle size d_{50} = 1.5 µm and about 90 % of particles smaller than 3.2 µm. The particle size distributions of AC050 fractions are given

in Table B−1 in Appendix. The application of smaller particles was not possible as a further milling only caused an agglomeration an no further decrease of the particle size. Based on analytical investigations of the manufacturer, it is assumed that the milling process did not change the pore characteristics. TFC MMMs with POMS (type S) and 20 wt% of each filler fraction were prepared and characterised on the basis of SEM images and binary mixture permeation *n*-C_4H_{10}/CH_4 ($y_{F,n\text{-}C4H10}$ = 5 vol%).

For MMMs, the filler particle size is often the limiting parameter regarding the thickness of the separation layer [173]. It is thus particularly challenging to achieve the industrially demanded high flux TFC membrane structures with separation layers as thin as possible. While small particles would be beneficial to reduce the thickness, their high tendency to agglomerate makes them more difficult to disperse homogeneously [7, 103, 109]. This has also been observed for the MMMs prepared in this work. As previously shown in Figure 6-11 and Figure 6-13 (a), the addition of AC050 particles leads to a dramatic increase of the thickness of the separation layer, especially in the case of the smaller AC050-2 particles. MMMs with 40 wt% of the smaller AC050-2 showed a thickness of approximately 49 µm which is far off from an efficient TFC membrane. A smaller particle size allows the introduction of a higher number of particles at the same weight percentage resulting in a larger interfacial area and enhanced interactions with the polymeric matrix [104]. These intense interactions influence the viscosity of the coating solution giving thicker, reinforced separation layers. Besides a higher thickness, MMMs with AC050-2 show more inhomogeneous separation layers. It can be assumed that the narrower fraction with d_{50} = 1.5 µm is more affected by agglomeration and by the presence of residual large particles. Surfaces with protruding particles will be prone to defect formation during further coating, handling and processing steps.

Results of binary gas mixture permeation measurements for MMMs filled with 20 wt% AC050 with an average particle size of either 3.5 µm or 1.5 µm are presented in Figure 6-16. The *n*-C_4H_{10} permeability and *n*-C_4H_{10}/CH_4 selectivity are shown as a function of the feed pressure. Measurements were performed at 30 °C. While the permeability is often reported to decrease with decreasing particle size due to a higher tortuosity, an enhanced interfacial area and thus a higher mass transfer resistance [32, 35], a higher permeability was found in this work for MMMs filled with smaller AC050-2 particles. In this case the smaller particles seem to be more effective for a flux improvement by loosening the polymeric chain packing and facilitating diffusion pathways. A more effective increase of free volume without defect formation in case of smaller particles has been stated in literature [97, 52]. Further, Moore *et al.* reported a less pronounced

formation of rigidified interface layers in consequence of an inhibited contradiction [102]. Apart from the large scattering of results due to the non-uniformity of the separation layers, no effect of the filler particle size on selectivity was observed. Results are confirmed with findings in literature, e.g., by Tantekin-Ersolmaz for PDMS filled with zeolites [154] or by Petsi *et al.* demonstrating in theoretical investigations that particle size only affects the permeability [122].

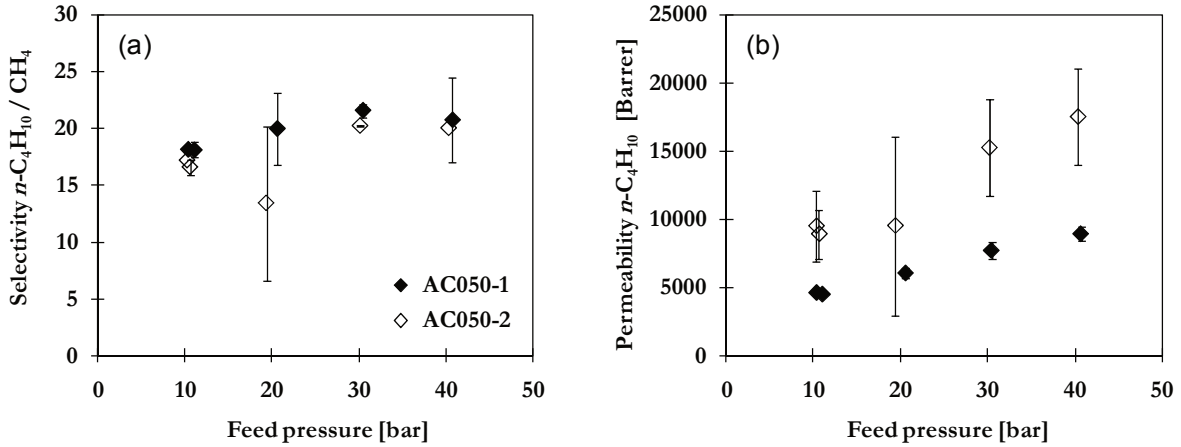

Figure 6-16: Influence of the filler particle size on (a) n-C_4H_{10}/CH_4 selectivity and (b) n-C_4H_{10} permeability of MMMs filled with AC050-1 (d_{50} = 3.5) or AC050-2 (d_{50} = 1.5 µm) determined with binary feed mixture with 5 vol% n-C_4H_{10} at 30 °C

6.1.4 Solvent for Filler Pre-treatment

The participation of AC particles in MMM separation performance is mainly determined by its porous structure thus it is essential to allow gas molecules a free access to it. During MMM preparation, polymeric chains might penetrate into the pores of the AC particles rendering the filler particles inactive in terms of the separation efficiency. Such a penetration and blockage of pores by polymeric chains is especially reported for flexible rubbery polymers [9]. The extent of pore penetration can be influenced by the use of a solvent for filler pre-treatment. An appropriate solvent should be compatible to both phases, allowing for interactions between the polymeric precursor and the inorganic filler, do not inhibit cross-linking reactions while preventing filler aggregation, pore blockage and the formation of interfacial or surface defects due to repulsive forces [29]. A number of organic solvents (iso-octane, ethanol, toluene, iso-propanol) has been tested as agents for pre-blocking of AC micropores in order to prevent the penetration of polymeric chains into the porous structure during the preparation.

The compatibility between solvent and polymer can be described by the Hildebrand solubility parameter, a numerical estimation of interaction derived from the cohesive energy density or the heat of vaporization. Materials with a similar solubility parameter are likely to have a good compatibility and miscibility [56]. No reference data was found for POMS but one can expect values similar to the well-studied PDMS. The Hildebrandt solubility parameter for PDMS and solvents investigated in this work are specified in Table 6-6.

Table 6-6: Hildebrand Solubility Parameter of PDMS [a] [94] and investigated solvents [b] [56]

Solvent	Hildebrand Solubility Parameter $(cal/cm^3)^{1/2}$
PDMS	7.28
Iso-octane	6.99
Toluene	8.91
Iso-propanol	11.5
Ethanol	12.92

[a] data from J.Mark, *Physical Properties of Polymers*, 2nd edition, Springer, 2006 [94]

[b] data from A. Barton, *Handbook of Solubility Parameters*, CRC Press, 1983 [56]

According to the idea of the similarity of solubility parameters, the highest compatibility to POMS is expected for iso-octane and toluene. Both are commonly applied as solvent for the preparation of POMS or PDMS membranes [126]. While they ensure a good compatibility of components, one can expect a certain penetration of polymeric chains into the porous structure of the filler particles. The lack of improvement of first MMMs prepared in this work with iso-octane saturated activated carbon particles in POMS (type S) (results not shown) was ascribed to a blocked pore system in consequence of the use of iso-octane. Alcohols such as iso-propanol and ethanol show only a low compatibility and are thus good candidates to prevent the access of polymeric chains into the pores. This was confirmed by results of Hülagü *et al.* who investigated the penetration of a PDMS solution into saturated activated carbon particles (type AC050, not milled spherical pellets with d_{50} = 450 - 500 µm) via EDX line scan analysis [61]. A maximum penetration depth was found for iso-octane which could be successfully reduced by using ethanol for filler pre-saturation instead.

In a first approach, the use of iso-octane for pre-saturation was replaced by ethanol in order to prevent a blockage of pores. MMMs based on standard POMS-S and 20 wt% AC050 showed a

higher selectivity in case of ethanol pre-saturation as shown in Figure 6−17 (a). This was ascribed to a better accessibility of the porous structure for the penetrants. However, samples prepared with the high viscosity precursor solution POMS-XL showed an aggregation of filler particles (see Figure 6−17 (c)) and a segregation of the coating suspension, leaving a fair amount of sedimented filler particles in the tub after coating. The addition of a non-solvent always holds the risk of a void formation at the interface polymer – filler due to repulsive forces or the provocation of a phase separation in consequence of the diffusion of non-solvent from filler pores into the polymeric solution [29].

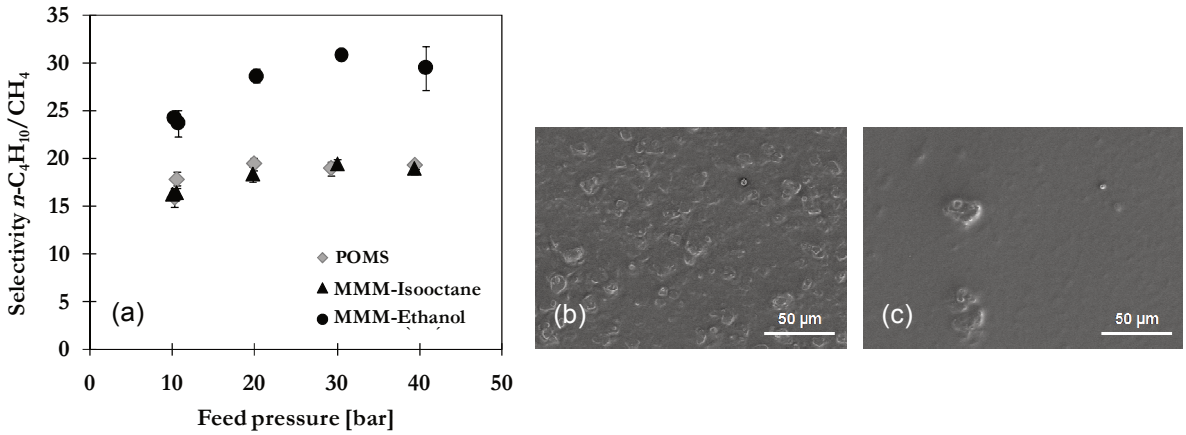

Figure 6-17: Influence of the solvent type for pre-saturation on (a) mixed gas selectivity *n*-C_4H_{10} / CH_4 for MMMs composed of POMS-S and 20 wt% AC050 (d_{50} = 3.5 µm) at 25 - 30 °C and dispersion of (b) iso-octane or (c) ethanol saturated AC050 (d_{50} = 3.5 µm; 13 wt%) in POMS-XL

A further screening of a suitable solvent for the preparation of MMMs based on a modified POMS-XL precursor solution was performed and extended to toluene and iso-propanol. The corresponding Hildebrand-solubility coefficients are in between iso-octane and ethanol. In addition, the mixing procedure has been slightly adjusted in terms of the time and intensity of stirring. SEM images of MMM surfaces presented in Figure 6-18 show no significant difference in MMMs surface morphology. Provided that the dispersion forces are sufficiently high to achieve a stable coating suspension, the preparation of MMMs based on a high viscosity POMS-XL precursor solution seems to be successful even with ethanol saturated filler particles. The solvent also affects the morphology of MMMs in terms of the thickness of the separation layer. The application of ethanol and iso-propanol as pore filling agents results in thicker separation layers of approximately 6.1 µm. For iso-octane, a separation layer with thickness of 5.8 µm and for toluene only 5.2 µm were obtained. The separation performance of MMMs prepared with different solvents is presented in Figure 6-19. All MMMs show a higher selectivity than pure

POMS and, furthermore, no great difference in n-C_4H_{10}/CH_4 selectivity with regard to the different solvents.

The high viscosity POMS-XL is equal to a pre-polymerised solution with a denser network and bulkier chains. A lower risk of penetration can be expected, allowing an improved separation performance even for iso-octane saturated particles. Similar benefits of an additionally cross-linked polymeric matrix with regard to pore penetration and particle precipitation have been reported by Jia *et al.* [68].

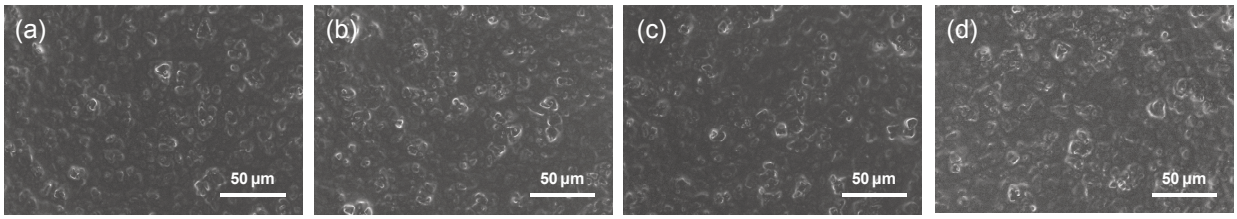

Figure 6-18: SEM images of MMM surfaces composed of POMS-XL and 20 wt% AC050 (d_{50} = 3.5 µm) saturated with (a) iso-octane, (b) toluene, (c) iso-propanol and (d) ethanol

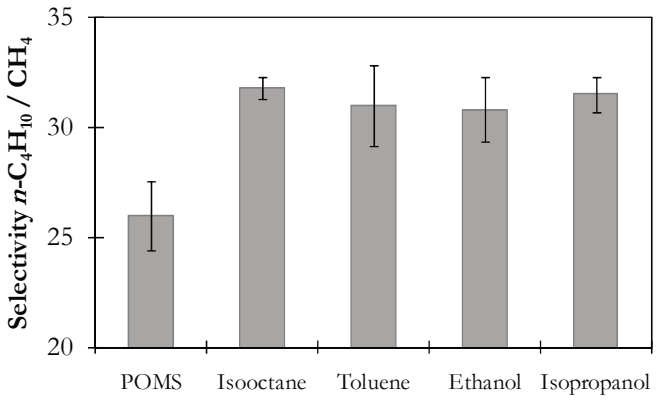

Figure 6-19: Influence of different solvents for pre-saturation on selectivity n-C_4H_{10}/CH_4 of MMMs composed of POMS-XL and AC050 (d_{50} = 3.5 µm) at 20°C, 30 bar and $y_{F,n\text{-}C4H10}$ = 0.05

6.1.5 Optimisation of Composite Structure

Modifications of the membrane composite structure have been performed with the aim to improve the separation performance, the stability during handling as well as the reproducibility of production. These modifications include the application of additional coating layers, a top layer (TL) and a gutter layer (GL). The former is used to seal small pinholes or defects formed at the

membrane surface during coating or drying which impair the separation performance. A common material is PDMS due to its easy handling and sufficient selectivity [142]. A 0.5 wt% PDMS solution has been applied in this work as a final coating layer. The influence of a gutter layer on the membrane morphology and separation performance will be described in more detail below. As already discussed, the addition of filler particles has a strong impact on the uniformity of the separation layer (see Figure 6-5). In order to improve the uniformity, the polymer concentration, respectively viscosity, can be adjusted as described in section 6.1.1. A further possibility is given by the introduction of an additional thin polymeric layer between the porous support structure and the selective separation layer, a so-called gutter layer [12]. In this work, a thin layer made from a 0.5 wt% PDMS solution has been used. PDMS is highly permeable for *n*-C_4H_{10} and ensures a negligible transport resistance. Figure 6-20 shows SEM images of MMM separation layers casted either directly on a porous non-woven/PAN support (a) or a non-woven/PAN support with an additional gutter layer (b). The coating solution was composed of 30 wt% POMS (type S) and 20 wt% AC050 (d_{50} = 3.5 µm, pre-saturated with ethanol) as filler.

The advantage of the modified support structure is clearly reflected in the much more uniform separation layers, see Figure 6-20. The gutter layer serves as a barrier that prevents penetration of coating solution into porous support and provides a smoother surface so that following layers can be applied with higher uniformity. It thus enables a reproducible production. The smoother surfaces further improve the abrasion resistance, a great benefit during handling and module preparation.

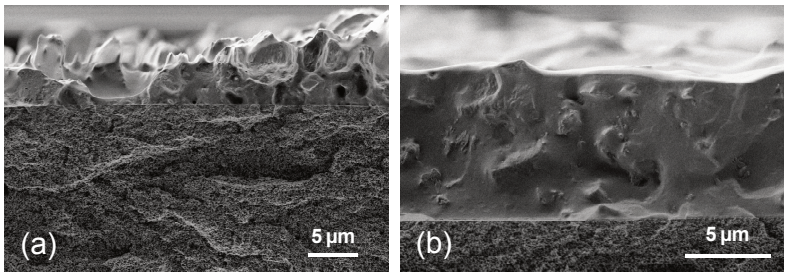

Figure 6-20: SEM cross-sections of MMM separation layers composed of 30 wt% POMS and 20 wt% AC050 (d_{50} = 3.5 µm) casted on (a) pure non-woven/PAN support and (b) non-woven/PAN with additional GL

The influence of the gutter layer on the separation performance is presented in Figure 6-21 in terms of *n*-C_4H_{10} permeance (a) and *n*-C_4H_{10}/CH_4 selectivity (b). The more uniform MMMs casted on a gutter layer show much higher permeances over the whole pressure range and an improved performance at feed pressures greater 20 bar. The highly permeable gutter layer prevents the accumulation of *n*-C_4H_{10} on the permeate side, responsible among others, for the

drop of performance at higher feed pressure. The improved control of the permeate flux in presence of the gutter layer facilitates the permeate withdrawal by directing the flux to the pores of the support structure and shortening the diffusion path length so that the overall permeation is less influenced by surface or pore geometry of the support structure [70].

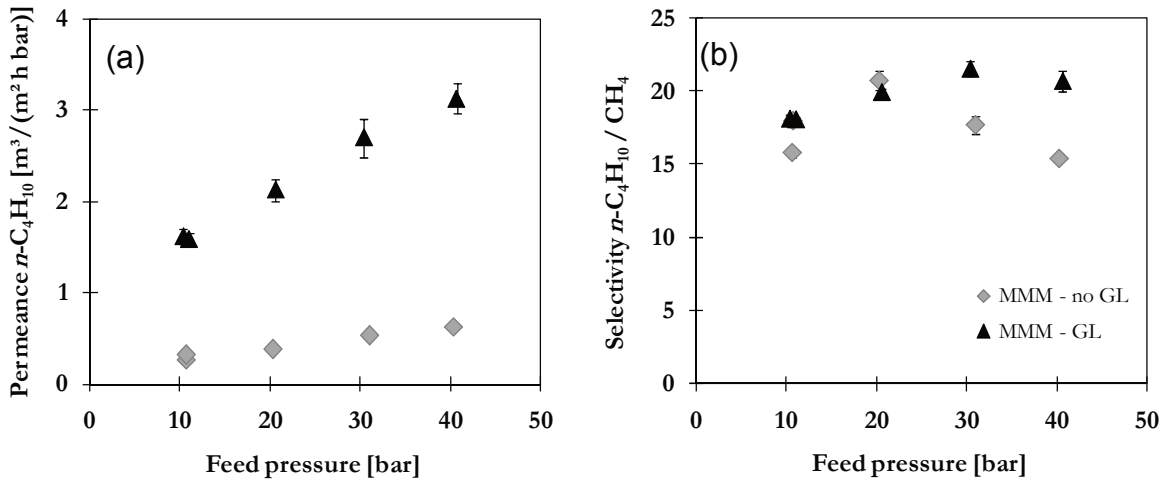

Figure 6-21: Influence of a gutter layer (GL) on (a) *n*-C_4H_{10} permeance and (b) *n*-C_4H_{10} / CH_4 selectivity of MMMs composed of POMS (30 wt%, type S) and 20 wt% AC050-1 (d_{50} = 3.5 µm) casted on non-woven/PAN support structures with (triangles) or without (diamonds) additional GL (0.5 wt% PDMS) determined with a binary mixture of 5 vol% *n*-C_4H_{10} in CH_4 at 30 °C

6.1.6 Summary of Results of Material Development

The most important conclusions of the material development steps to achieve an appropriate defect-free MMM with an improved separation performance and a reproducible production are briefly summarised in Table 6-7. The parameters investigated in this work include the type and properties of the polymeric matrix, the selection of filler material, the filler content and particle size, the solvent for pre-saturation and the properties of the support structure. By optimizing these parameters, it was possible to improve the *n*-C_4H_{10}/CH_4 mixed gas selectivity compared to pure polymeric POMS membranes. A uniform and reproducible MMM production up to technical scale could be achieved. Two promising MMMs structures with an improved *n*-C_4H_{10}/CH_4 selectivity were identified. Best results were achieved with MMMs composed of 20 wt% AC050-1 (d_{50} = 3.5 µm) or AC050-2 (d_{50} = 1.5 µm), pre-saturated in iso-octane, and 15 or 20 wt% POMS-XL casted on a non-woven/PAN with an additional gutter layer. The most

selective MMM with 20 wt% AC050-1 and 20 wt% POMS-XL has a *n*-C_4H_{10}/CH_4 mixed gas selectivity of 31.8 ± 0.25 at 20 °C, 30 bar and 5 vol% *n*-C_4H_{10} in mixture. This corresponds to an improvement of 20 % compared to the pure POMS membrane. The *n*-C_4H_{10} permeability and permeance are 17629 ± 1281 Barrer and 7.69 ± 0.53 $m_N^3/(m^2\ h\ bar)$, respectively. A similar selectivity of 30.5 ± 0.76 but slightly higher permeances (8.81 ± 0.08 $m_N^3/(m^2\ h\ bar)$) were found for MMMs with AC050-2 (d_{50} = 1.5 µm) and 15 wt% POMS-XL. MMM samples of the latter such composition were used for further analysis of operating conditions.

Table 6-7: Conclusions of MMM material development

Parameter	Impact and Results
Type of polymer	POMS provides a good sorption selectivity and appropriate permeability; rubbery state allows a good contact to particles
Polymer concentration	Determines the viscosity of the coating solution and the thickness of separation layer; more stable dispersions at higher concentration; uniform coating requires at least 30 wt% POMS-S;
	POMS-XL allows better dispersion and less polymer penetration into pores; decrease in concentration gives a lower selectivity and higher flux; best performance for 15 wt% POMS-XL
Type of filler	Improved mixed-gas selectivity for all filler types except for CB; highest *n*-C_4H_{10}/CH_4 mixed gas selectivity found for AC050; good selectivity for AS assumed to result from enhanced cross-linking
Filler content (AC050)	Addition of filler particles increases the thickness and non-uniformity; rigidification (T_g) and void formation (density) at high filler contents of 40 wt%; filler particles affect the activation energy for permeation; optimum in *n*-C_4H_{10}/CH_4 mixed gas selectivity at 20 wt% AC050; sorption measurements indicate that the adsorptive capacity is not fully exploited
Filler size & shape (AC050)	No impact on selectivity but higher permeability for smaller particles; smaller particles seem to be more effective to facilitate permeation; stronger increase of the thickness of the separation layer for smaller particles; spherical nanosized particles allow a higher uniformity of the separation layer; minimum size is limited by agglomeration of particles
Solvent for pre-saturation	Non-solvent ethanol prevents pore blockage but bears risks of particle aggregation and void formation; solvent type is less important for POMS-XL based MMMs
Gutter layer (GL)	GL allows more uniform coating layers and smoother surfaces, higher flux and stable performance at high feed pressure; improved permeate withdrawal

6.2 Investigation of the MMM Separation Performance

In addition to the material and the composition of the membrane, the operating conditions have a significant influence on the separation performance. Main parameters are summarised in Figure 6-22. Based on the results of the material development described in section 6.1, the investigations were performed with MMMs composed of 15 wt% POMS (type XL) and 20 wt% AC050 (d_{50} = 1.5 µm, iso-octane saturated). A POMS membrane composed of 30 wt% POMS (type S) was investigated as a reference. Both membranes were casted on porous structures of non-woven/PAN with an additional gutter layer. Samples were dried in a vacuum oven for 15 h at 80 °C and initially screened to assure that only defect-free samples with an O_2/N_2 selectivity of at least 2.27 at 20 °C are analysed. The *n*-C_4H_{10}/CH_4 separation performance is investigated as an exemplary model system for the separation of higher hydrocarbons from permanent gas streams. After a brief introduction of the general differences between the permeation of *n*-C_4H_{10} and CH_4 in section 6.2.1, this work focuses on binary and multi-component hydrocarbon mixtures. Results for the separation of binary mixtures of *n*-C_4H_{10}/CH_4 under varying operating conditions (feed and permeate pressure, temperature, feed composition) are presented in section 6.2.2. The performance of MMMs regarding the separation of a multi-component mixture of various hydrocarbons C_1 – C_5 and CO_2 simulating a real natural gas composition is described in section 6.2.3 followed by a long-term permeation study with a binary mixture of *n*-C_5H_{12}/N_2 in 6.2.4.

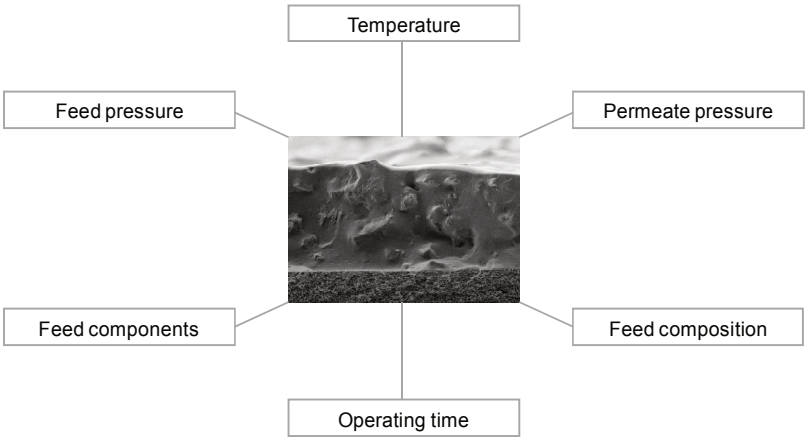

Figure 6-22: Overview of studied operating conditions influencing the membrane separation performance

6.2.1 Permeation of Single Gases *n*-C_4H_{10} and CH_4

As a first step in membrane characterisation usually measurements with single gases are performed. While they only describe an idealized performance as no coupling or competitive effects between mixture components are taken into account, their investigation is necessary to fundamentally understand the differences between gas components and assign effects to the filler or to interactive effects of the gas mixtures. Thus, the single gas permeation of *n*-C_4H_{10} and CH_4 is briefly highlighted before the performance regarding the separation of binary mixtures is discussed. Measurements with single gases were performed with a pressure-increase set-up at pressures up to 1 bar and temperatures in the range of 20 to 70 °C.

The driving force for gas permeation is usually provided by a pressure difference across the membrane. It is evoked by an elevated pressure on the feed side and a preferably low pressure on the permeate side. To describe the state within the membrane associated to the prevalent feed and permeate pressure, the resulting average value of the pressure is used. In case of the marked non-ideal gas phase behaviour expected for higher hydrocarbons such as *n*-C_4H_{10}, the average pressure is replaced by the fugacity [4, 114]. Results for *n*-C_4H_{10} and CH_4 permeances are thus presented in Figure 6−23 in dependency of the average fugacity at constant temperatures of 20 and 70 °C. The *n*-C_4H_{10} permeance in POMS increases with the average fugacity. This is caused by the solution of condensable *n*-C_4H_{10} into the polymeric matrix and the higher diffusive flux through the expanded swollen polymer. The average fugacity serves as reference for the resulting degree of swelling [114, 4]. The relation between permeance and average fugacity can be described by an exponential equation according to the free volume model presented in 3.3.1.4, with L_0 as the permeance at zero pressure or rather for a non-swollen membrane and m as the slope parameter reflecting the influence of operating conditions, i.e., the concentration of dissolved gas molecules. The exponential trend curves are represented in the following figures by solid lines. At higher temperatures, a lower *n*-C_4H_{10} permeance is observed. The permeation is controlled by solution. For condensable gases like *n*-C_4H_{10}, the solution is dominated by the exothermic condensation and gives negative ΔH_s and a decreasing solubility with increasing temperature [94]. Less *n*-C_4H_{10} can be dissolved at higher temperatures rendering the polymer less swollen. In comparison, the permanent gas CH_4 shows no pressure dependency of the permeance (see Figure 6−23 (b)) and a contrary effect of temperature. The permeation is controlled by diffusion. As the heat of condensation is negligibly small, the solution is dominated by the endothermic mixing resulting in small and positive ΔH_s and an increasing solubility with

temperature. An increase of temperature enhances the mobility of gas molecules and facilitates the diffusion.

Similar trends as found for the permeation of single gases *n*-C_4H_{10} and CH_4 in POMS are revealed by MMMs. The presence of activated carbon does not lead to a qualitative change of pressure or temperature dependencies but leads to lower overall values due to a higher thickness and an increased tortuosity. By comparing the parameters of exponential trend curves summarised in Table 6-8, higher slope parameters can be observed for MMMs. The difference declines with rising temperature. Higher slope parameters usually indicate an increased tendency to swelling but in case of MMMs might rather be ascribed to the beneficial effects of the adsorption on the activated carbon. The ideal selectivity was estimated by extrapolating the permeances to zero pressure in order to represent the unswollen state. No great difference was found between POMS and MMM. The selectiviy follows the same trend with respect to temperature with values calculated to 15.6 (POMS) and 14.6 (MMM) at 20 °C and 6.6 (POMS) and 6.5 (MMM) at 70 °C.

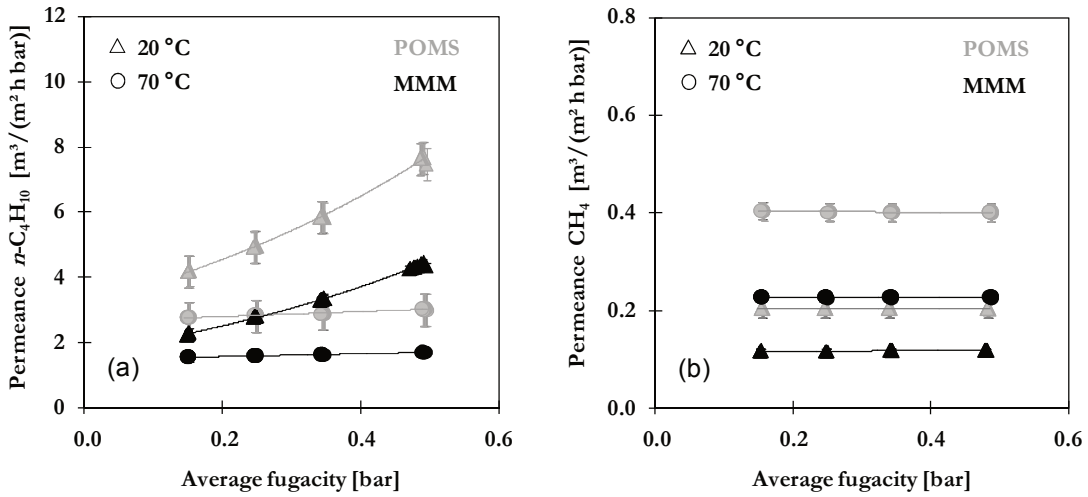

Figure 6-23: Single gas permeation of (a) *n*-C_4H_{10} and (b) CH_4 in POMS (grey) and MMM filled with 20 wt% AC050-2 (black) as function of the average fugacity at different temperatures (lines represent exponential trend curves; error bars are based on results for binary mixture permeation at 20 °C and 30 bar)

Table 6-8: Single gas permeation data for CH_4 (average values) and *n*-C_4H_{10} (extrapolated values) in POMS and MMM filled with 20 wt% AC050-2 at different temperatures

	POMS			MMM		
ϑ	L CH_4	L_0 *n*-C_4H_{10}	m *n*-C_4H_{10}	L CH_4	L_0 *n*-C_4H_{10}	m *n*-C_4H_{10}
[°C]	[$m_N^3/(m^2$ h bar)]		[-]	[$m_N^3/(m^2$ h bar)]		[-]
20	0.203	3.161	1.780	0.117	1.709	1.929
30	0.241	3.120	1.161	0.134	1.654	1.267
50	0.319	2.911	0.511	0.178	1.565	0.595
70	0.402	2.640	0.261	0.226	1.462	0.313

6.2.2 Permeation of Binary Mixtures *n*-C_4H_{10} / CH_4

As previously described, the permeation of single gases is not sufficient to correctly evaluate the separation performance due to the neglecting of interaction or coupling effects between gas mixture components usually present in real applications. The separation performance of MMMs has thus been investigated with binary gas mixtures *n*-C_4H_{10} / CH_4 under varying operating conditions to identify such coupling effects. The influence of various operating conditions, in particular, feed pressure, permeate pressure, temperature and mixture composition, will be first discussed individually in the following sections 6.2.2.1 to 6.2.2.4 and then summarised and evaluated in section 6.2.2.5.

6.2.2.1 Influence of Feed Pressure

A significant influence of the feed pressure on the separation performance is expected as it is directly affecting the pressure difference and thus the driving force for permeation. Measurements have been performed at feed pressures ranging from 10 to 40 bar at a constant temperature of 20 °C and permeate pressures of 1.2 – 1.6 bar. Results will be presented as functions of the average fugacity to account for the state of swelling within the membrane.

The change of the average *n*-C_4H_{10} fugacity with feed pressure is illustrated in Figure 6-25 (a). For both membranes, an increase of the average fugacity with feed pressure is calculated. A higher feed pressure promotes the dissolution into the polymeric matrix and the adsorption on activated carbon, causing a slightly higher concentration and thus a higher fugacity of *n*-C_4H_{10} inside the MMM. The *n*-C_4H_{10} and CH_4 permeances are presented in Figure 6-24 as functions of the average *n*-C_4H_{10} fugacity. Similar to the results for single gas permeation in Figure 6−23 (a), both

membranes show an increase of the *n*-C_4H_{10} permeance with an increasing average *n*-C_4H_{10} fugacity. For POMS, the *n*-C_4H_{10} permeance increases from 6.8 to 14.8 $m_N^3/(m^2\ h\ bar)$ and for the MMM from 4.1 to 10.9 $m_N^3/(m^2\ h\ bar)$, respectively. Again, this can be attributed to the higher diffusive flux in consequence of the dissolution of *n*-C_4H_{10} and a loosening of the polymeric structure. No significant differences between trends in POMS and MMM are found, but the overall permeances of the MMM are on a lower level. While *n*-C_4H_{10} retains its single gas behaviour in case of a binary mixture separation, a significant difference is observed for CH_4. No pressure dependency of permeation was found for single gas CH_4 (see Figure 6−23 (b)) but the CH_4 permeance increases from 0.3 to 0.6 $m_N^3/(m^2\ h\ bar)$ in POMS and from 0.16 to 0.36 $m_N^3/(m^2\ h\ bar)$ in MMM under binary mixture conditions. This reveals the coupling of CH_4 permeation to the amount of dissolved *n*-C_4H_{10} and the associated degree of swelling. The high concentration of *n*-C_4H_{10} within the membrane creates a more favourable environment for the transport of CH_4. The increased flux of all mixture components due to such coupling effects can be accurately described by the extended free volume model described in section 3.3.1.4 for dense polymeric membranes. The lines in Figure 6-24 do not represent calculations according to the free volume model but exponential trend curves fitted to the experimental results.

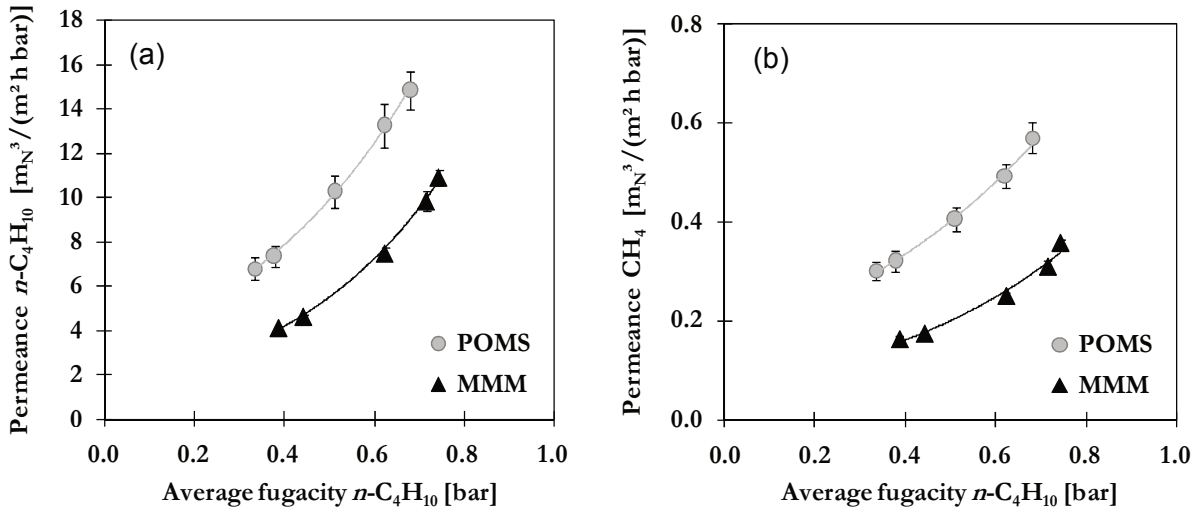

Figure 6-24: Influence of the average *n*-C_4H_{10} fugacity on the permeance of (a) *n*-C_4H_{10} and (b) CH_4 in POMS (grey) and MMMs filled with 20 wt% AC050-2 (black) for a binary feed mixture with 5 mol% *n*-C_4H_{10} at 20 °C (lines represent exponential trend curves)

The *n*-C_4H_{10} / CH_4 selectivity is presented in Figure 6-25 (b) as function of the feed pressure. Both membranes show initially an increase of the selectivity with feed pressure but the selectivity starts to level off at a feed pressure greater 30 bar. At 30 bar, *n*-C_4H_{10} / CH_4 mixed gas

selectivities of 26.8 and 31.6 were found for POMS and MMM. Under ideal high pressure conditions in absence of co-permeation, a much higher selectivity of 55.7 and 58.1 could be expected for POMS and MMM (values were extrapolated based on the single gas parameters L_0 and m to an average *n*-C_4H_{10} fugacity of 0.72 bar that corresponds to the experimental mixed gas conditions of 30 bar, 20 °C and 5 vol% *n*-C_4H_{10} in feed gas). The observed behaviour is often reported in literature when changing ideal single to mixed gas conditions. It reflects the enhanced diffusive fluxes of all mixture components in case of a highly swollen membrane. As diffusion is usually in favour for small molecules, such co-permeation reduces the selectivity. In short, a swollen membrane allows a high diffusion whereas this flux is less selective. A similar behaviour is reported for PDMS, showing a decrease of *n*-C_4H_{10} / CH_4 selectivity from 17 in single gas to 4.5 in mixed gas [139].

Besides the impacts of co-permeation, a stronger competition for adsorption sites at a higher pressure is likely for MMMs as disclosed by the adsorption isotherms in Figure 6-8. Such co-adsorption further enhances the flattening of the selectivity curve. Further effects are reported in literature to decrease the separation performance at high feed pressure conditions, e.g., polarisation or compaction effects. Concentration polarisation results from the formation of an additional boundary layer in consequence of the enrichment of the less permeable component on the feed side of the membrane. Stronger impacts are reported for high flux membrane materials with low feed flow velocities [88]. Its occurrence has been evaluated in preliminary studies for POMS membranes by comparing experimental results and values calculated according to the free volume model at varying feed flow rates and hence feed flow velocities. The presence of concentration polarisation was excluded under the chosen experimental conditions. As the MMMs in this work exhibit an even lower flux, impacts of a concentration polarisation are even less likely. A compaction of the separation layer under high pressure, known to reduce the free volume and thus diffusive flux [150], is likewise excluded.

Comparing both membrane types, a higher selectivity is found for the MMM over the whole investigated pressure range. Selectivities are in the range of 25.1 to 31.6 for MMM and 22.6 to 26.8 for POMS, respectively. In both cases the optimum in selectivity occurs at 30 bar. The improvement can be ascribed to the beneficial effect of the activated carbon and its high affinity towards *n*-C_4H_{10}. In consequence of adsorption on AC, less *n*-C_4H_{10} is available to swell the polymeric matrix. The presence of particles might further reduce the mobility of polymeric chains and its ability to loosen up. For these reasons, a lower degree of swelling can be expected for the MMM. Similar findings have been reported in literature, for example by Nunes *et al.* [112] or

Merkel *et al.* [96]. Both investigated MMMs filled with silica for the separation of *n*-C_4H_{10} / CH_4. Nunes *et al.* used PDMS as polymeric matrix, Merkel *et al.* glassy PTMSP. A high amount of *n*-C_4H_{10} adsorbed inside the pores might not only reduce the swelling of the surrounding polymeric matrix and minimize an undesired co-permeation but also evokes a blocking of CH_4 diffusion via the formation of a condensed layer and a selective surface flow [129].

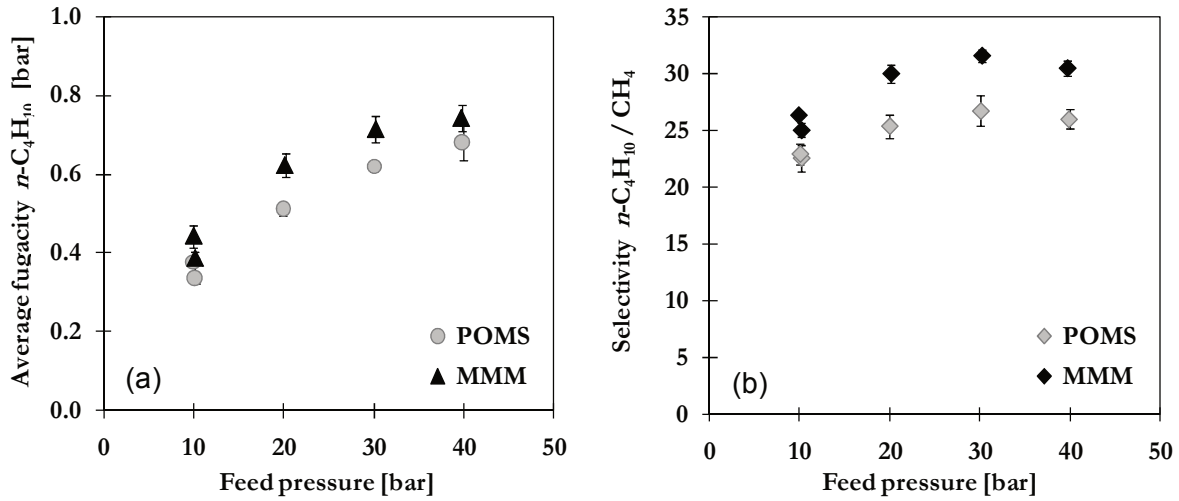

Figure 6-25: Influence of the feed pressure on (a) average *n*-C_4H_{10} fugacity and (b) *n*-C_4H_{10} / CH_4 selectivity for POMS (grey) and MMMs (black) filled with 20 wt% AC050-2 in binary feed mixtures with 5 mol% *n*-C_4H_{10} at 20 °C

The successfully improved *n*-C_4H_{10} / CH_4 selectivity found for the MMMs in this work shall further be compared to common industrial state-of-art reference materials, namely POMS and PDMS. A lower ideal and mixed gas selectivity *n*-C_4H_{10} / CH_4 of 14.1 and 14.8, respectively, is presented for example by Raharjo *et al.* for PDMS at 25 °C (p_F = 4.5 bar, $y_{F,n\text{-}C4H10}$ = 0.06, Helium sweep) [127]. Pinnau reported a mixed gas selectivity of 11.5 for PDMS at 25 °C (p_F = 11 bar, p_P = 1 bar, $y_{F,n\text{-}C4H10}$ = 0.06) [123]. Scholes *et al.* summarised data for the *n*-C_4H_{10} / CH_4 binary separation performance of various polymers including PDMS and POMS [139] and gives selectivity values of 5, 7.5 and 10 for PDMS, radiation cross-linked PDMS and POMS, respectively at 30 °C (p_F = 10 bar, $y_{F,n\text{-}C4H10}$ = 0.03). For similar conditions stated in literature, namely a feed pressure of 10 bar and a temperature of 30 °C, the membranes investigated in this work show a considerably higher selectivity of 16.6 for POMS and 18.4 for MMM, respectively. It was thus not only possible to improve the selectivity by 11% compared to the pure POMS membranes but even stronger compared to the industrial benchmark membrane material PDMS.

6.2.2.2 Influence of Permeate Pressure

The pressure difference across the membrane can be evoked by variation of either feed or permeate pressure. Often the separation is performed with vacuum on the permeate side in order to enhance the driving force and pressure ratio [95]. To investigate the influence of the permeate pressure, a vacuum pump was installed on the permeate side and the pressure was adjusted to values between 0.05 and 1.5 bar at a constant feed pressure of 30 bar and a temperature of 20 °C.

The permeances of *n*-C_4H_{10} and CH_4 as function of the permeate pressure are presented in Figure 6-26 for POMS and MMMs. A reduction of the permeate pressure causes a decrease of both *n*-C_4H_{10} and CH_4 permeance. Values are in the range of 9.25 to 5.95 $m_N^3/(m^2\ h\ bar)$ for *n*-C_4H_{10} in MMM and 0.27 to 0.24 $m_N^3/(m^2\ h\ bar)$ for CH_4, respectively. The variation of the permeate pressure seems to have stronger effects for POMS as indicated by the higher slopes of the exponential trend curves shown in Figure 6-26. Slopes were estimated to 0.36 and 0.29 for *n*-C_4H_{10} or 0.14 and 0.09 for CH_4 in POMS and MMM, respectively.

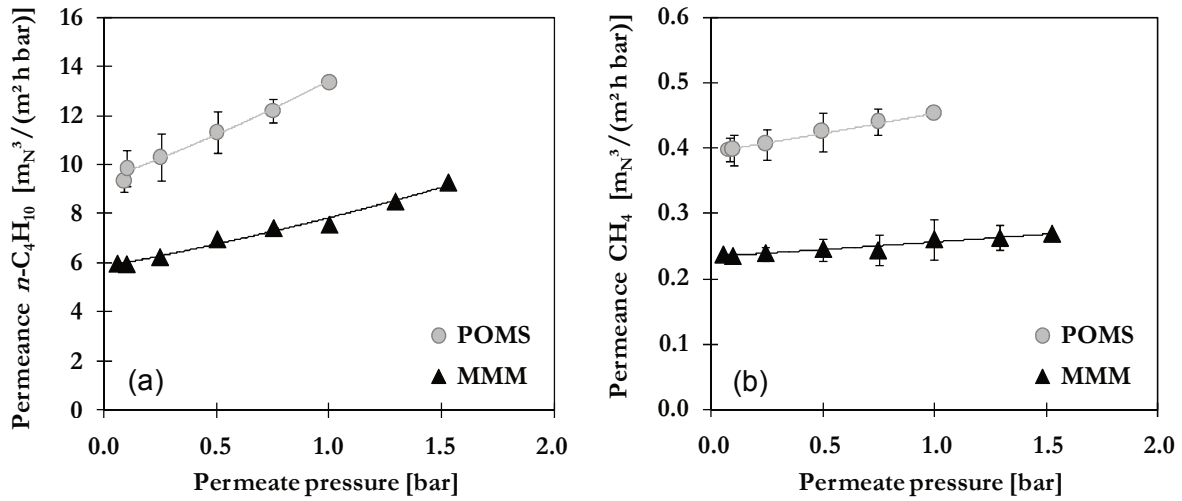

Figure 6-26: Influence of the permeate pressure on the permeance (a) *n*-C_4H_{10} and (b) CH_4 of POMS (grey) and MMM filled with 20 wt% AC050-2 (black) for a binary feed mixture with 5 mol% *n*-C_4H_{10} at 30 bar feed pressure and 20 °C (lines represent exponential trend curves)

The variation of the permeate pressure leads to opposing effects. Decreasing the permeate pressure at a constant feed pressure gives a higher pressure ratio, which is defined as the ratio of the operating feed to permeate pressure. This provides a higher driving force for diffusion and facilitates particularly the permeation of small gas components. Further, the change of the permeate pressure creates different swelling conditions and pressure or concentration profiles [88]. The higher diffusive flux is opposed by a reduced degree of swelling due to an enhanced

removal of *n*-C_4H_{10} as the lower pressure supports desorption from both polymeric matrix and activated carbon. The *n*-C_4H_{10} / CH_4 selectivity shows the same downward trend with respect to the variation of the permeate pressure. It is presented in Figure 6-27 (a). The best performance was achieved at the highest permeate pressure of 1.5 bar yielding a selectivity of 34.4 for MMM. For very low permeate pressures, the pressure loss caused by the support structure represents an additional transport resistance impeding further improvements [88]. The better separation at a higher permeate pressure is beneficial as the application of an energy- and cost intensive vacuum on the permeate side is not necessarily useful. This is underlined by Figure 6-27 (b) showing the selectivity as a function of the pressure ratio and a constant performance for a pressure ratio greater than 120. Baker *et al.* stated that the separation performance of a membrane is either determined by the pressure ratio or by the membrane selectivity [12]. The relation has been illustrated for a vapour selective membrane and clearly demonstrates that the efforts to increase either the selectivity by an intensive material research or the pressure ratio by an energy intensive application of high vacuum on the permeate side should be carefully revised as not expedient in all cases. As stated by Ohlrogge *et al.* the best performance is often achieved for a pressure ratio in the same range as the selectivity [114].

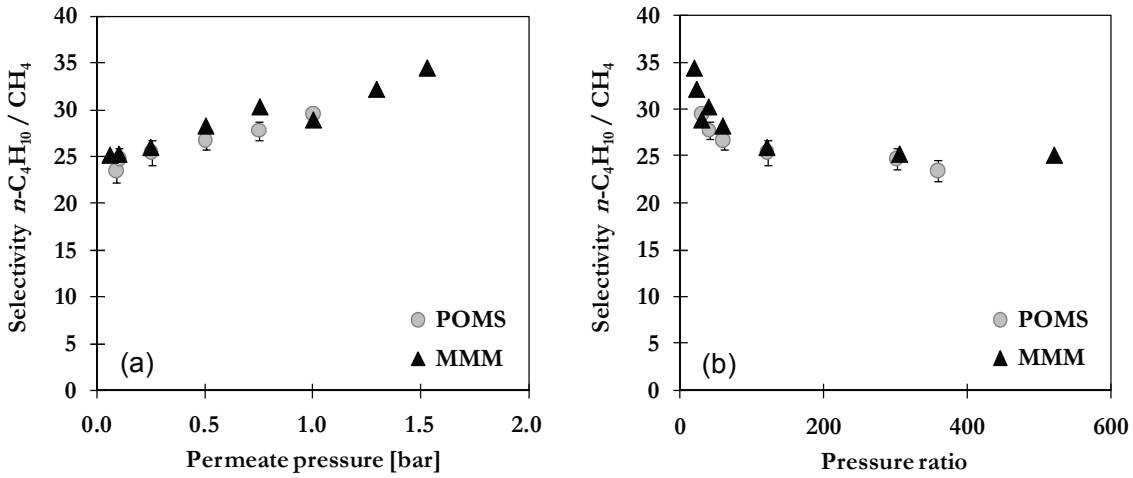

Figure 6-27: Influence of (a) permeate pressure and (b) pressure ratio on the selectivity *n*-C_4H_{10} / CH_4 of POMS (grey) and MMM filled with 20 wt% AC050-2 (black) for a binary mixture with 5 mol% *n*-C_4H_{10} at 30 bar and 20 °C as feed

6.2.2.3 Influence of Temperature

The operating temperature has a strong impact on the separation performance as sorption by the polymeric matrix, adsorption on activated carbon and diffusion are all temperature dependent mechanisms. To quantify the influence, mixed gas permeation experiments were performed at

temperatures varying from 15 to 35 °C with a binary feed mixture of 5 mol% *n*-C_4H_{10} in CH_4 at constant feed pressures of 10 or 30 bar. The investigated application range was limited by the cooling capacity of the water bath as well as the highest temperature suitable for the gas compressor.

The influence of temperature on the permeance of *n*-C_4H_{10} and CH_4 is depicted in Figure 6-28 for POMS (grey) and MMM (black) for feed pressures of 10 (unfilled symbols) or 30 bar (filled symbols). By increasing the temperature from 20 °C to 35 °C at a feed pressure of 30 bar, the permeance *n*-C_4H_{10} shows a strong decrease up to 49 % from 9.2 to 4.7 $m_N^3/(m^2\ h\ bar)$ for MMM and of 43 % from 14.8 to 8.1 $m_N^3/(m^2\ h\ bar)$ for POMS, similar to the trends observed for single gases (see Figure 6−23 (a)). This reflects the sorption controlled permeation present in both cases. The temperature dependency is less pronounced for CH_4 as presented in Figure 6-28 (b). At a feed pressure of 10 bar hardly any influence of temperature on the CH_4 permeance is observed, at the utmost a slight increase. At 30 bar, both membranes show a decrease of permeance when changing the temperature from 20 °C to 35 °C. Comparing to single gas results, this is a reversal of the temperature dependency. For single gases, the higher CH_4 permeance at higher temperature reflected the enhanced mobility and facilitated diffusion (see Figure 6−23 (b)). This behaviour seems to be offset in binary mixtures by the effects of swelling in presence of *n*-C_4H_{10}. Higher hydrocarbons such as *n*-C_4H_{10} exhibit a higher affinity to sorption into the polymeric matrix as they are easier to condensate. The boiling point is -0.5 °C for *n*-C_4H_{10} compared to -161.5 °C for the non-condensable CH_4 at atmospheric pressure [132]). Temperature affects the concentration of a component inside a non-ideal mixture or rather its activity. The activity is estimated as the ratio of fugacity to the fugacity at saturation pressure for the corresponding temperature. As the point of saturation depends on the temperature, the saturation fugacity of *n*-C_4H_{10} increases from 1.6 bar at 15 °C to 4.3 bar at 50 °C. Thus, at higher temperatures *n*-C_4H_{10} exhibits a lower activity in the gas phase which in turn affects its readiness to condensate and thus its solubility [126]. The same impact of temperature described for the sorption into a polymeric matrix is valid for the adsorption on activated carbon. As the adsorption resembles a surface condensation of gas components, lower temperatures are beneficial and enhance the concentration or activity of *n*-C_4H_{10} inside the membrane. The estimated activity of *n*-C_4H_{10} inside the membrane is presented in Figure 6-29 (a) as function of the temperature. The diffusive transport of CH_4 through the pore system of AC is assumed to be hindered by adsorbed *n*-C_4H_{10}, resulting in the constant permeance at 10 bar for the MMM (see Figure 6-28 (b)).

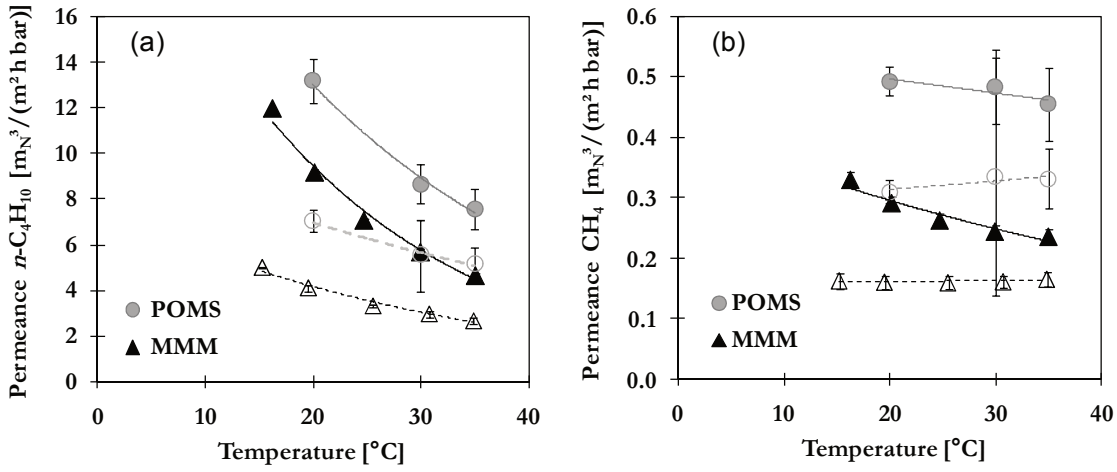

Figure 6-28: Influence of temperature on the permeance n-C_4H_{10} (a) and CH_4 (b) in POMS (grey) and MMM filled with 20 wt% AC050-2 (black) for a binary feed mixture with 5 mol% n-C_4H_{10} at 30 bar (filled symbols, solid lines) or 10 bar (unfilled symbols, dotted lines; lines represent exponential trend curves)

The strong temperature dependency of the n-C_4H_{10} permeance and only minor impacts of temperature on the CH_4 permeance result in a significant temperature dependency of the selectivity. This is illustrated in Figure 6-29 (b). Both membranes show a decrease of selectivity with increasing temperature. The selectivity of the MMM is hereby at each temperature the highest. As previously described, the transport through the polymeric matrix and the activated carbon inside the MMM are both affected by temperature. Similar to conventional separation processes, best performance is achieved at low temperatures.

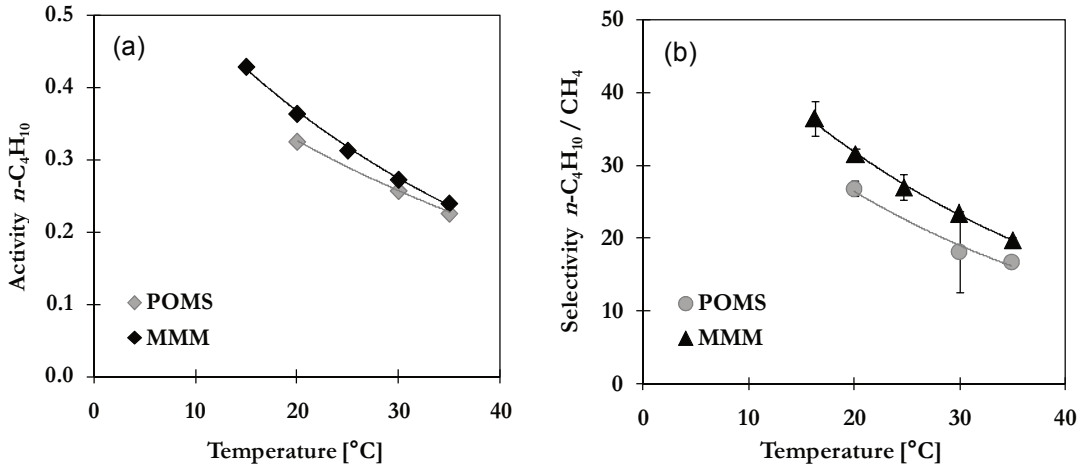

Figure 6-29: Influence of temperature on the (a) n-C_4H_{10} activity and (b) n-C_4H_{10}/CH_4 selectivity of POMS (grey) and MMM with 20 wt% AC050 (black) for a binary feed mixture with 5 mol% n-C_4H_{10} at 30 bar (filled symbols; lines represent exponential trend)

6.2.2.4 Influence of Binary Mixture Composition *n*-C_4H_{10} / CH_4

Often, substantial changes in the mixture compositions are present in industrial separations, e.g., integrally changing concentrations between the feed and retentate side of a membrane module. As directly related to the driving force, the performance is influenced by such variations in the feed compositions [114]. For the aspired field of application, namely the separation of higher hydrocarbons, only minor feed concentrations of the component to be separated are present. For example, the feed concentration of higher hydrocarbons in natural gas is in the range of 1 – 3 % [14]. In order to ensure a sufficient separation performance under these fluctuating conditions, measurements with different concentrations of *n*-C_4H_{10} in binary mixtures with CH_4 were performed. The concentration of *n*-C_4H_{10} was 1, 2 or 5 mol%. Experiments were performed at a constant temperature of 20 °C and a feed pressure of 30 bar.

Results for permeances *n*-C_4H_{10} and CH_4 for POMS and MMM as function of the *n*-C_4H_{10} concentration in the feed mixture are presented in Figure 6-30. For both membranes and feed components, an increase of the permeance with increasing feed concentration of *n*-C_4H_{10} is shown. The permeance of *n*-C_4H_{10} increases from 6.8 to 14.8 $m_N^3/(m^2\ h\ bar)$ in POMS and from 3.8 to 9.8 in MMM, respectively. Corresponding values for the permeances of CH_4 range from 0.30 to 0.57 $m_N^3/(m^2\ h\ bar)$ in POMS and from 0.17 to 0.31 $m_N^3/(m^2\ h\ bar)$ in MMM, respectively. A low concentration of the desired component in the feed mixture usually results in a lower driving force and a more difficult separation. A high feed concentration is of course beneficial for both the swelling of the polymeric matrix as well as the adsorption in the filler phase. High concentrations of condensable components can further induce an excessive swelling, degrade the polymeric matrix in case of corrosive components or saturate filler particles. The change of the average *n*-C_4H_{10} fugacity with its feed concentration is the same for POMS and MMM as depicted in Figure 6-31 (b). However, the permeance of CH_4 seems to be less dependent on the *n*-C_4H_{10} feed concentration in case of the MMM. This is indicated by the slope parameters of the exponential trend curves, which match for *n*-C_4H_{10} in POMS (0.22) and MMM (0.23) but show a lower increase for CH_4 in MMM (0.14) compared to POMS (0.17).

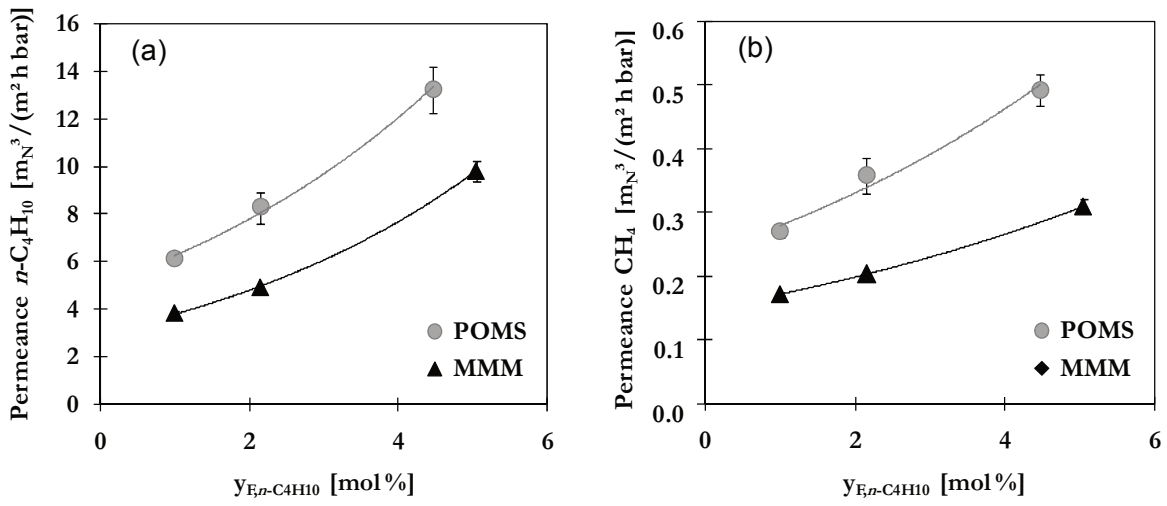

Figure 6-30: Influence of the binary mixture composition on the (a) permeance *n*-C_4H_{10} and (b) permeance CH_4 of POMS (grey) and MMM filled with 20 wt% AC050-2 (black) at 20 °C and 30 bar

The selectivity as a function of the feed composition is given in Figure 6-31 (a). It shows an increase of the selectivity with an increasing concentration of *n*-C_4H_{10} in the feed mixture. For POMS, the selectivity ranges from 22.6 to 26.8 and for MMM from 22.2 and 31.6. While nearly the same selectivity is achieved at low feed concentrations of 1 – 2 vol% *n*-C_4H_{10}, the effects of the AC are particularly disclosed at high feed concentrations at which a higher selectivity of the MMM is observed. It was concluded that in the case of the MMM the permeation of CH_4 is affected by a reduced swelling in presence of particles as well as an inherent *n*-C_4H_{10} phase occupying the pore system and blocking the diffusive path. The less selective diffusion through a swollen polymeric matrix is surpassed by the enhanced adsorption on AC. At low *n*-C_4H_{10} concentrations, the number of adsorption sites in AC is large enough to accommodate both *n*-C_4H_{10} and CH_4. The sorption affinity is getting more important at higher *n*-C_4H_{10} concentrations. High concentrations of the component to be separated in the feed mixture are thus advantageous. In the specific case investigated here, at least more than 2 vol% are required to give a better separation performance.

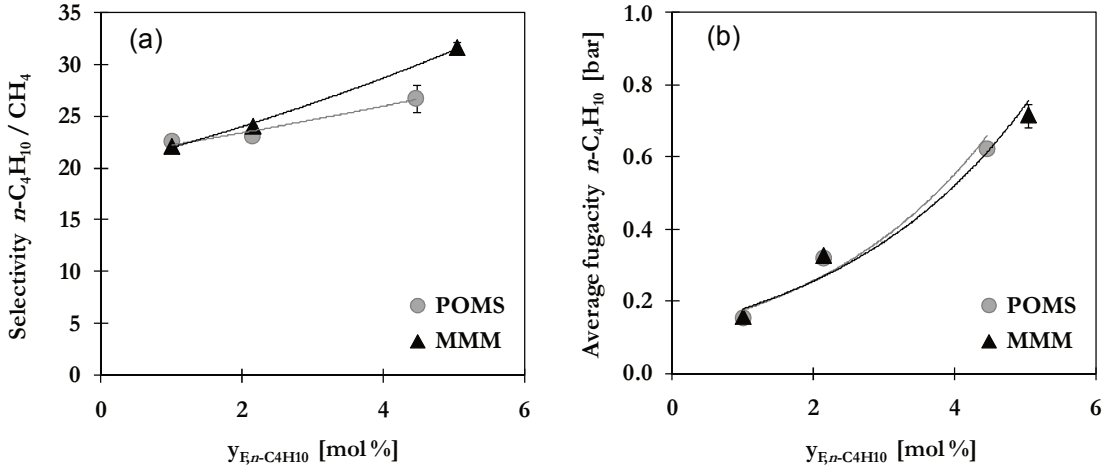

Figure 6-31: Influence of the binary mixture composition on the (a) selectivity *n*-C_4H_{10}/CH_4 and (b) average fugacity *n*-C_4H_{10} POMS (grey) and MMM filled with 20 wt% AC050-2 (black) at 20 °C and 30 bar (lines represent exponential trend curves)

6.2.2.5 Summary of Binary Separation Performance *n*-C_4H_{10} / CH_4

This chapter summarises and evaluates the separation performance of MMMs regarding binary mixtures of *n*-C_4H_{10} / CH_4 as described in the previous sections 6.2.2.1 to 6.2.2.4. First, the investigated operating parameters and their effect on separation performance are again listed in Table 6-9.

Almost all operating parameters have a direct or indirect influence on the concentration of the condensable component inside the membrane and thus the degree of swelling. In Figure 6-32, all results for permeances of *n*-C_4H_{10} (a) and CH_4 (b) obtained in the various series of experiments with a MMM composed of 15 wt% POMS and 20 wt% AC050-2 are thus presented as function of the average *n*-C_4H_{10} fugacity. Despite the variations as a result of individual impacts of operating conditions, an overall exponential trend can be observed. As temperature does not affect the average fugacity but the activity of the components, the change in permeance occurs at the same average fugacity.

Table 6-9: Summary of the impacts of operating conditions on the separation performance based on the binary mixed gas separation experiments performed in this work

Parameter	Impacts	Best performance
Feed pressure	Pressure gradient, driving force, solution in the polymeric matrix, adsorption in filler particles, degree of swelling, real gas behaviour (including Joule-Thomson effect)	High feed pressure (up to 30 bar)
Permeate pressure	Driving force, permeate withdrawal, desorption, degree of swelling, influence of pressure drop	Ambient permeate pressure
Temperature	Activity of gas molecules, mobility of polymeric chains and gas molecules, solution in the polymeric matrix, adsorption in filler particles, degree of swelling	Low temperatures
Mixture composition	Concentration of condensable components, degree of swelling, coupling of permeation, competitive adsorption or blocking of permeation	High concentration of condensable component

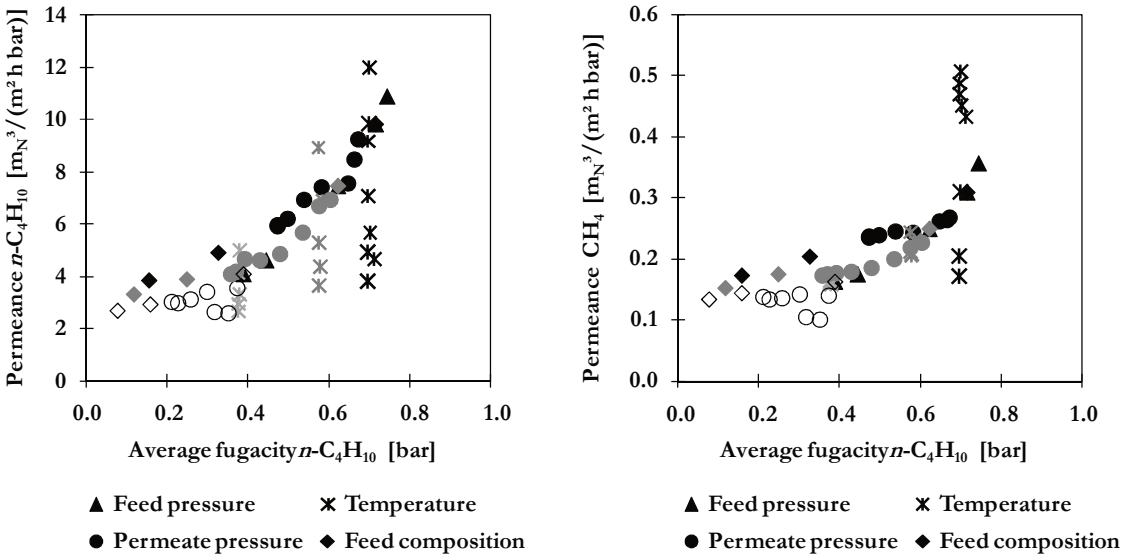

Figure 6-32: Permeances of (a) *n*-C_4H_{10} and (b) CH_4 as function of the average *n*-C_4H_{10} fugacity for MMM composed of 15 wt% POMS and 20 wt% AC050-2 (d_{50} = 1.5 µm, iso-octane saturated) under varying operating conditions of feed pressure (10 – 40 bar, triangles), permeate pressure (0.05 – 1.6 bar, circles), temperatures (15 – 35 °C, crosses) and *n*-C_4H_{10} feed concentration (1 – 5 vol%, diamonds); colour indicates variations at different constant feed pressures of 10 bar (open symbols or light grey crosses), 20 bar (grey) or 30 bar (black)

A good prediction of the mixed gas permeation of pure polymeric membranes is given by the free volume model described in 3.3.1.4 [4]. A similar relation can be derived for the permeation of MMMs. Based on the results depicted in Figure 6-32, the dependency of the permeance (L_i) on

the average *n*-C_4H_{10} fugacity ($f_{m,n\text{-}C4H10}$) and temperature can be described by the exponential model given in Equation (6-5).

$$L_i = L_{i,0}^{\infty} \cdot \exp\left(\frac{-E_{P,i}}{RT} + m_{i0} \cdot f_{m,n-C4H10} \cdot \exp(m_{iT} \cdot T)\right) \qquad \textbf{(6-5)}$$

The model resembles the free volume model derived for the permeation inside dense polymeric membranes. Originally, L_i denotes the permeance of component i, $L^{\infty}_{i,0}$ the permeance at zero pressure and infinite temperature, $E_{A,i}$ the apparent activation energy for permeation, R the universal gas constant, T the operating temperature and $m_{i,0}$ or $m_{i,T}$ parameters that describe the influence of the concentration on the membrane material (swelling and adsorption). The coefficients found for the investigated MMM are summarised in Table 6-10. It has to be noted that parameters given for the 'pseudo free volume model' for the MMMs are only empirical and do not have a physical meaning.

Table 6-10: Model parameters to describe the binary permeation of mixtures *n*-C_4H_{10} / CH_4 in MMMs composed of 15 wt% POMS and 20 wt% AC050 according to Equation (6-5)

Parameter		CH_4	*n*-C_4H_{10}
$L^{\infty}_{i,0}$	[$m_N^3/(m^2\ h\ bar)$]	0.0092	0.0053
$E_{A,i}$	[kJ/kmol]	- 5910.9	- 14447.8
$m_{i,0}$	[bar^{-1}]	0.75	5895.01
$m_{i,T}$	[K^{-1}]	0.0025	- 0.0268

In Figure 6-33, the experimental results at varying operating conditions are shown in comparison to calculated permeances of *n*-C_4H_{10} (a) and CH_4 (b) as a function of the average *n*-C_4H_{10} fugacity. A good agreement is obtained for variations at either 20 or 30 °C. The influence of temperature is shown for a feed pressure of 30 bar. It can also be estimated with good agreement. The MMM permeation behaviour for *n*-C_4H_{10} and CH_4 can thus successfully be described with calculations according to the equation (6-5) using the parameters given in Table 6-10. This enables further estimations of the performance which are necessary, for example, for the design of membrane modules used in industrial applications.

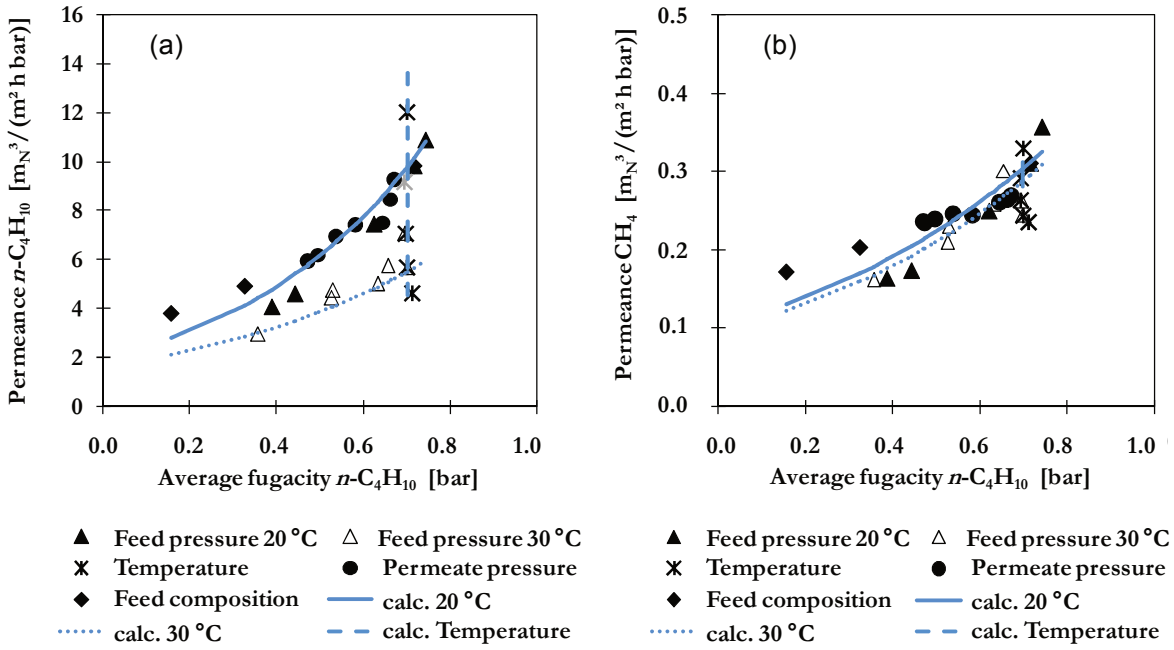

Figure 6-33: Comparison of experimental (symbols) and calculated (lines) results for MMM permeances of (a) n-C_4H_{10} and (b) CH_4 as function of the average fugacity n-C_4H_{10} at 20 °C (black symbols, solid line) and 30 °C (grey symbols, dotted line)

6.2.3 Permeation of Multi-component Mixtures

The separation of binary feed mixtures is already more meaningful than single gas investigations, but still does not reflect the reality of industrial separations. Multi-component mixtures reveal significant interactions, e.g., frictional drags between components that cause an even stronger coupling of transport via co-solution or co-diffusion, a slowing down or accelerating of one component's permeation or a high competition for adsorption sites [175, 86]. The performance of MMMs shall further be discussed for a multi-component mixture composed of n-C_5H_{12}, n-C_4H_{10}, C_3H_8, C_2H_6, CH_4 and CO_2. The mixture composition is given in Table 6-11. The measurements were performed at feed pressures of 10 – 40 bar, permeate pressures of 1.4 – 1.8 bar and a temperature of 20 °C.

As presented in Figure 6-34, all components show the expected increase of the permeance with feed pressure caused by an increasing degree of swelling. As mentioned above, the condensability of a component, indicated by its critical temperature or boiling point, is related to the ability to dissolve into the polymeric matrix or adsorb on the activated carbon filler particles. The boiling points of mixture components increase with increasing number of carbon atoms (see Table 6-11). As reflected by the high boiling points of -0.5 and 36 °C, the highest condensability is thus given

for *n*-C_4H_{10} and *n*-C_5H_{12}. It can be assumed that the swelling of the polymeric matrix is mainly induced by these components. With the mixed gas permeances following the same order as the boiling points, the lowest permeance of 0.41 $m_N^3/(m^2\ h\ bar)$ is found for CH_4 and by far the highest permeance of approximately 61 $m_N^3/(m^2\ h\ bar)$ for *n*-C_5H_{12}. An exception is found for CO_2 for which the presence of polar groups induces different interactions. The permeance of selected hydrocarbon components in MMMs as function of the feed pressure at 20 °C is depicted in Figure 6-34 (a). For the sake of clarity, a logarithmic scale was chosen. The relation of the boiling point to the permeance is illustrated in Figure 6-34 (b).

Table 6-11: Boiling point T_b [132], feed concentration, mixed gas permeance L and mixed gas selectivity vs. CH_4 for mixture components determined at 30 bar feed pressure, 1.4 - 1.8 bar permeate pressure and 20 °C for MMM composed of 15 wt% POMS filled with 20 wt% AC050-2

Component	CH_4	CO_2	C_2H_6	C_3H_8	*n*-C_4H_{10}	*n*-C_5H_{12}
T_b [°C]	- 161.5	- 78.5	- 88.7	- 42.1	-0.5	36.0
Feed concentration [vol%]	79.0	2.0	10.0	6.0	2.0	1.0
L $[m_N^3/(m^2\ h\ bar)]$	0.41	1.20	1.64	4.14	12.95	60.97
Selectivity	-	2.92	3.98	10.06	31.46	148.12

For MMMs, the permeance is influenced by swelling effects and by the adsorption affinity of the AC. Both increase with the condensability of the component. This is reflected by the declining differences between permeances of components in POMS and MMM with increasing condensability, i.e., for CH_4 the permeance is up to 52 % lower in MMM compared to POMS while for the condensable components *n*-C_4H_{10} and *n*-C_5H_{12} the differences are only 34 % and 6.5 %, respectively. The selectivity of mixture components towards CH_4 is given in Table 6-11. It reflects the same trend as found for the permeances, namely an increase with increasing number of carbon atoms. By far the highest selectivity of approximately 148 is found for *n*-C_5H_{12} followed by 31.5 for *n*-C_4H_{10}. For all other components, the selectivity lies at or below 10. With a selectivity of only 2.9 or 2.8, no promising separation performance CO_2 / CH_4 was achieved neither with MMM nor POMS. These membrane types are thus not suitable for applications relating to the upgrading of biogas or sour natural gas, often dealing with large CO_2 concentrations in the feed mixture.

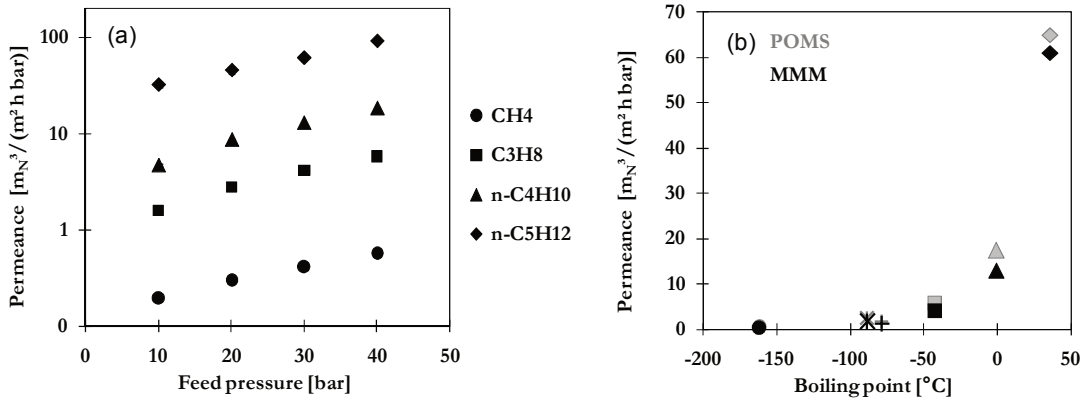

Figure 6-34: Permeances of selected components of a multi-component mixture in MMM composed of 15 wt% POMS and 20 wt% AC at 20 °C and 30 bar as function of (a) feed pressure or (b) the components' boiling point (mixture composition: 1 vol% *n*-C_5H_{12}, 2 vol% *n*-C_4H_{10}, 6 vol% C_3H_8, 10 vol% C_2H_6, 79 vol% CH_4, 2 vol% CO_2)

By comparing the results to the binary separation performance, both, higher permeances and higher *n*-C_4H_{10} / CH_4 selectivity are achieved for the multi-component mixture at 20 °C. The comparison is shown in Figure 6-35 for the multi-component mixture (2 vol% *n*-C_4H_{10} in feed) as well as the binary mixtures (1 – 5 vol% *n*-C_4H_{10} in feed). The total concentration of approximately 9 vol% higher hydrocarbons (C_{3+}) and especially the presence of *n*-C_5H_{12} lead to a much higher degree of swelling of the polymeric matrix as suggested by the much steeper curve shapes shown in Figure 6-35 (a). The *n*-C_4H_{10} permeance in the multi-component mixture increases from 4.7 to 18.3 $m_N^3/(m^2$ h bar) with a slope of 7.6 (solid line). For comparison, the results of binary mixtures can be summarised in a joined trend curve with a slope of 1.7 (dashed line). Similar trends are also predicted by the free volume model presented in 6.2.2.5. Despite the high degree of swelling, no negative impacts on the selectivity for example by co-diffusion of the less permeable components are found. In contrast, the even higher selectivity can be attributed to the enhanced effect of the activated carbon. The selectivity *n*-C_4H_{10} / CH_4 for the multi-component mixture is between 24.4 and 32.4, which corresponds to the results found for a binary mixture with a feed concentration of 5 vol% *n*-C_4H_{10}.

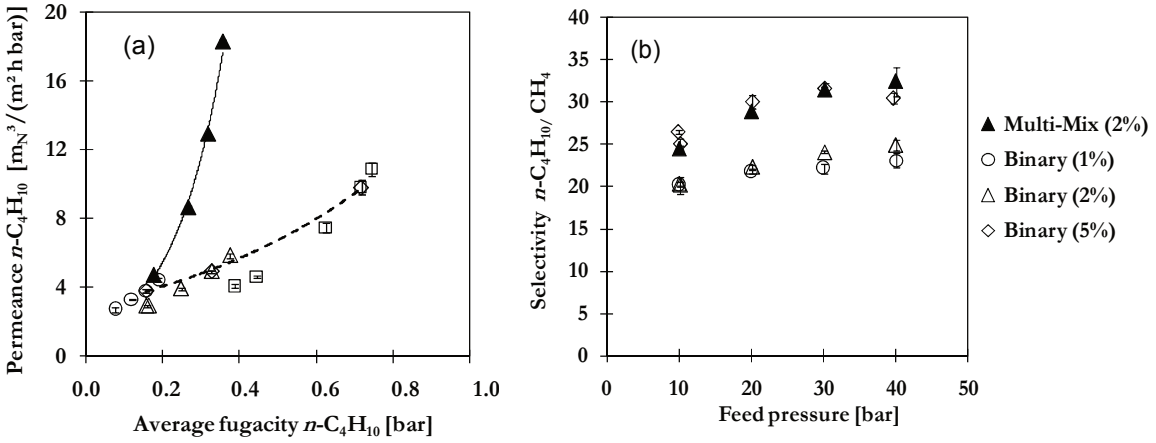

Figure 6-35: Comparison of the n-C_4H_{10} / CH_4 separation performance of a multi-component mixture (2 vol% n-C_4H_{10}; filled symbols, solid line) and binary mixtures (1, 2 or 5 vol% n-C_4H_{10}; unfilled symbols, dashed line) at 20 °C in terms of the (a) permeance n-C_4H_{10} as function of average fugacity n-C_4H_{10} and (b) selectivity n-C_4H_{10} / CH_4 as function of feed pressure for a MMM composed of 15 wt% POMS and 20 wt% AC (lines represent exponential trend curves)

The n-C_4H_{10} / CH_4 selectivity for POMS and MMM with 20 wt% AC at single, binary or multi-component mixed gas conditions at 30 bar feed pressure and 20 °C are summarised in Table 6-12. The selectivity for single gases is given as extrapolated values to either zero pressure (α_0) or to an average fugacity of n-C_4H_{10} of 0.33 bar (α_p) which corresponds to the mixed gas conditions with 2 vol% n-C_4H_{10} in the feed. Similar trends are found for POMS and MMM up to 2 vol% n-C_4H_{10} in the binary mixture. The occurring effects, namely a decrease of the separation performance due to the swelling of the polymeric matrix and an enhanced adsorption and permeation due to the addition of AC, seem relatively balanced. At a feed concentration greater than 2 vol% of n-C_4H_{10} (binary mixture) or in presence of further condensable components (multi-component mixture), a significant improvement can be achieved by the application of a MMM. The higher selectivity not only reduces the loss of valuable CH_4 with the permeate stream but allows for the application of smaller pumps and condensers on the permeate side. This enables a reduction of the energy consumption and costs and thereby a better competitiveness of the membrane based separation process.

Table 6-12: Comparison of the separation performance of POMS and MMM filled with 20 wt% AC for single gases (extrapolated values[1]), binary mixtures (1-5 vol% *n*-C_4H_{10} in feed) and a multi-component mixture (2 vol% *n*-C_4H_{10} in feed) at 20 °C and 30 bar feed pressure (average *n*-C_4H_{10} fugacity 0.33 bar)

	Selectivity *n*-C_4H_{10} / CH_4					
	Single Gas [1]		Binary Mixture			Multi-comp. Mixture
	α_0	α_p	(1 vol%)	(2 vol%)	(5 vol%)	(2 vol%)
POMS	15.6	27.8	22.6	23.1	26.8	27.8
MMM	14.6	27.4	22.2	24.1	31.6	31.5

[1] Values were estimated by the ratio of extrapolated permeances at either zero feed pressure (L_0, selectivity α_0) or an average fugacity of 0.33 bar (α_p) as found for mixtures with 2 vol% *n*-C_4H_{10} in feed under the conditions of interest.

6.2.4 Long-term Permeation of Binary Mixtures *n*-C_5H_{12} / N_2

Membrane modules for gas phase separations are usually operated for long periods without a change of material or cleaning. A long-term stability of performance is thus crucial for a successful industrial application. However, often a decrease of the membrane performance with time is reported due to the physical ageing of the polymeric material, degradation in presence of aggressive feed components or harsh conditions (temperature, pressure, pH of possible condensates) [39, 169]. In case of hybrid materials, a decrease of performance resulting for example from different thermal expansion coefficients, a delamination of polymeric chains attached to the filler surfaces under long exposure to pressure or the finite saturation limits of adsorbent materials might be possible. Although the need was stated several times, no investigations regarding the stability of the separation performance of MMMs under long-term operation are reported in literature yet [39]. In this work, the prepared MMMs filled with 20 wt% AC050 (3.5 or 1.5 μm, both saturated in iso-octane) as well as a reference POMS membrane were tested for up to 40 days under operation to evaluate the stability of the separation performance. Measurements were performed with binary mixtures of *n*-C_5H_{12} / N_2 allowing the investigation of stability under a high degree of swelling. The selection of the mixture components was determined by safety reasons. Experiments were performed at a feed pressure of 30 bar, a permeate pressure of 1.2 bar, a temperature of 20 °C and with an almost constant composition of 1.3 – 1.5 % *n*-C_5H_{12} in the feed. Although operated in a cycle, short interruptions of the pressure load for about 15 min were necessary for refilling of liquid *n*-C_5H_{12} causing slight changes of the feed mixture composition. A maximum deviation of 15 % after 5 weeks of operation was aspired.

The permeances of *n*-C_5H_{12} and N_2 over the time scale of investigation are presented in Figure 6-36 for MMMs filled with AC050-1 (d_{50} = 3.5 µm, denoted as MMM-1, black triangles) and AC050-2 (d_{50} = 1.5 µm, denoted as MMM-2, unfilled diamonds) as well as a POMS reference membrane (grey circles). Permeances were determined between stops for refilling of liquid *n*-C_5H_{12} after equilibration of the system. Results are average values of at least two measurements per type of membrane. For reasons of clarity, the error bars are not shown, but values will be reported in Table 6-13.

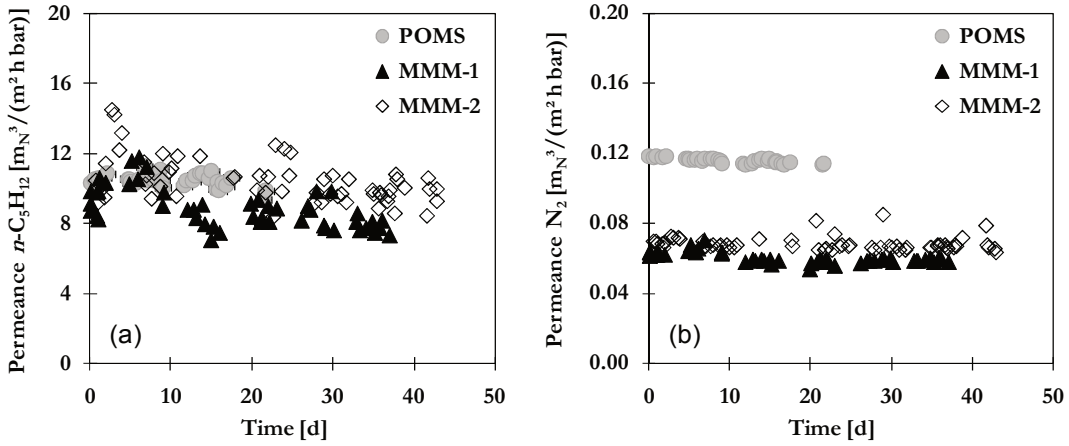

Figure 6-36: Long-term stability of permeances (a) *n*-C_5H_{12} and (b) N_2 in POMS (grey symbols), MMM-1 filled with 20 wt% AC050-1 (filled black symbols) and MMM-2 filled with 20 wt% AC050-2 (open black symbols) for binary mixtures of 1.3 – 1.5 mol% *n*-C_5H_{12} in N_2 at 30 bar and 20 °C (results are average values of at least two measurements with corresponding errors given in Table 6-13)

Apart from fluctuations mainly caused by deviations in the feed mixture composition during re-filling of liquid *n*-C_5H_{12}, a constant performance over time was observed for all membranes. The permeances of *n*-C_5H_{12} and N_2 in POMS were 10.10 (± 0.70) $m_N^3/(m^2$ h bar) and 0.11 (± 0.01) $m_N^3/(m^2$ h bar). Deviations over the 20 days of operation are 5.2 % for *n*-C_5H_{12} and 3.0 % for N_2, respectively. The presence of filler particles does not alter the stability of the polymeric POMS matrix. POMS membranes are already successfully applied on the industrial scale with a known stable performance [13, 114]. Thus, they were only tested for approximately 20 days in this work as a reference with no further significant decrease of performance expected. For MMMs, the average permeances over time were determined to 8.70 (± 0.92) $m_N^3/(m^2$ h bar) and 7.33 (± 2.18) $m_N^3/(m^2$ h bar) for *n*-C_5H_{12} and to 0.063 (± 0.003) $m_N^3/(m^2$ h bar) and 0.064 (± 0.002) $m_N^3/(m^2$ h bar) for N_2 in MMM-1 and MMM-2, respectively. The decline over time was 12.3 % and 17.7 % for *n*-C_5H_{12} and 6.7 % and 4.3 % for N_2 in MMM-1 and MMM-2, respectively. The maximum deviation was thus almost within the target range of 15 %.

Comparing the results of pure POMS and MMMs, the permeances of *n*-C_5H_{12} are within the same range whilst higher permeances of N_2 were observed for POMS. The permeation of N_2 is hindered due to its negligible adsorption affinity and its low solubility in condensed *n*-C_5H_{12} layers. In presence of the adsorbent particles, a lower degree of swelling and thus impact of an undesired co-permeation of N_2 can be expected.

The long-term stability of the separation performance of MMM-1, MMM-2 and POMS membranes is given in Figure 6-37 in terms of the *n*-C_5H_{12} / N_2 selectivity. The average selectivity over time is 137.7 (± 32.1) for MMM-1, 115.4 (± 6.8) for MMM-2 and 94.4 (± 7.8) for POMS. The corresponding deviations over time of 3.6 %, 13.7 % and 3.0 %, respectively, are all within the aspired range. The long-term stability of the MMM performance could thus be proven. In addition, the applicability of the developed MMM for the separation of higher hydrocarbons from permanent gas was demonstrated for another binary mixture.

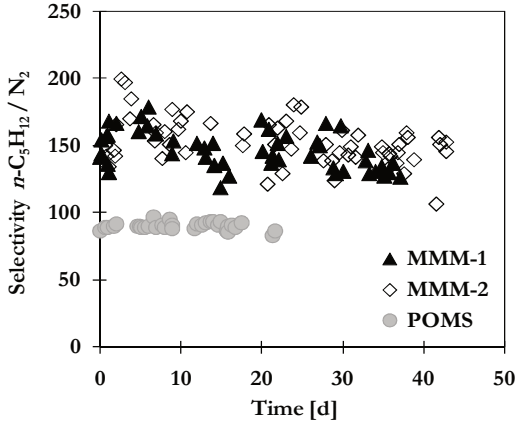

Figure 6-37: Long-term stability of the separation performance *n*-C_5H_{12} / N_2 for POMS (grey symbols), MMM-1 filled with 20 wt% AC050-1 (filled black symbols) and MMM-2 filled with 20 wt% AC050-2 (open black symbols) in binary mixtures of 1.3 – 1.5 mol% *n*-C_5H_{12} in N_2 at 30 bar and 20 °C (results are average values of at least two measurementsamples with corresponding errors given in Table 6-13)

Table 6-13 summarises the average values of the permeances *n*-C_5H_{12} and N_2 as well as the selectivity *n*-C_5H_{12} / N_2 over the investigated time scales. In addition, the corresponding errors and maximum deviations are specified. Compared to the results of single gas permeation, the permeance of N_2 is twice as high resulting from the swelling induced by *n*-C_5H_{12}. The single gas permeances of N_2 are 0.054 $m_N^3/(m^2\ h\ bar)$ for POMS, 0.033 $m_N^3/(m^2\ h\ bar)$ for MMM-1 and 0.031 $m_N^3/(m^2\ h\ bar)$ for MMM-2 at 20 °C, without any sign of pressure dependency.

Table 6-13: Long-term stability of the separation performance *n*-C_5H_{12} / N_2 in terms of average values and maximum deviations for permeances and selectivity for POMS and MMMs filled with 20 wt% AC050-1 (MMM-1) or AC050-2 (MMM-2) for binary mixtures of 1.3 – 1.5 vol% *n*-C_5H_{12} in N_2 at 30 bar and 20 °C (estimated errors are given in brackets)

Parameter	Unit	POMS	MMM-1	MMM-2
Average Values and Error				
$L_{n\text{-}C5H12}$	[$m_N^3/(m^2\ h\ bar)$]	10.10 (± 0.70)	8.70 (± 0.92)	7.33 (± 2.18)
L_{N2}	[$m_N^3/(m^2\ h\ bar)$]	0.107 (± 0.013)	0.063 (± 0.003)	0.064 (± 0.002)
Selectivity	–	94.4 (± 7.8)	137.7 (± 32.1)	115.4 (± 6.8)
Deviations		*after 20 days*	*after 37 days*	*after 42 days*
$\Delta L_{n\text{-}C5H12}$	[%]	- 5.20	- 12.30	- 17.70
ΔL_{N2}	[%]	- 2.95	- 6.70	- 4.28
Δ Selectivity	[%]	- 2.97	- 3.60	- 13.74

As previously mentioned, the refilling of liquid *n*-C_5H_{12} was followed by slight changes in the feed composition. Changes in the feed composition occur frequently in industrial applications. To ensure a stable separation performance and evaluate the impact of fluctuations in the mixture composition on the separation performance, further series of experiment were performed with varied concentrations of *n*-C_5H_{12} in the feed mixture. Again, the average fugacity of the condensable component is used as a reference for the resulting degree of swelling. Results are presented as functions of the average *n*-C_5H_{12} fugacity in Figure 6-38.

All membranes show a strong decrease of the permeances with the decreasing average *n*-C_5H_{12} fugacity. At low concentrations of *n*-C_5H_{12}, the differences between POMS and MMMs seem to diminish, especially for the permeance of *n*-C_5H_{12}. As previously discussed for binary mixtures *n*-C_4H_{10} / CH_4 (see 6.2.2.4), this implies a less effective contribution of the AC at low concentrations of the condensable components in the feed mixture. The extrapolation of N_2 permeances to zero fugacity gives values of 0.050, 0.025 and 0.024 $m_N^3/(m^2\ h\ bar)$ for POMS, MMM-1 and MMM-2. These are in good agreement with single gas results. Errors were estimated for the permeance of *n*-C_5H_{12} to 0.45, 1.06 and 1.16 for POMS, MMM-1 and MMM-2 and to 0.007, 0.005 and 0.014 for the permeance of N_2, respectively.

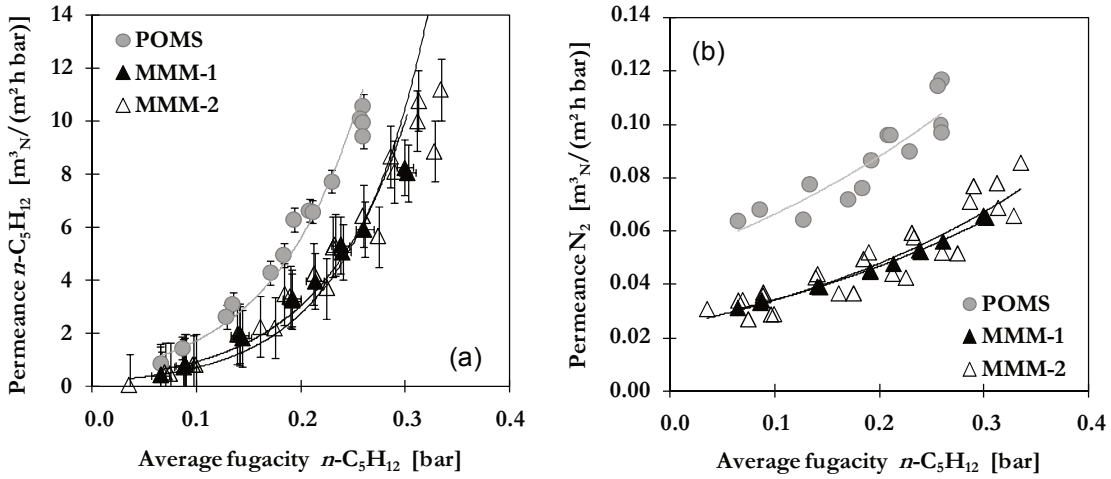

Figure 6-38: Influence of the average n-C_5H_{12} fugacity on permeances of (a) n-C_5H_{12} and (b) N_2 for POMS (grey symbols), MMM-1 filled with 20 wt% AC050-1 (filled black symbols) and MMM-2 filled with 20 wt% AC050-2 (open black symbols) in binary mixtures of 0.4 – 1.3 vol% n-C_5H_{12} in N_2 at 30 bar and 20 °C (average values of at least two measurements per membrane type, error bars are omitted for sake of clarity)

The effect of the feed composition on the selectivity n-C_5H_{12} / N_2 is summarised in Table 6-14. The greater difference between the permeance of N_2 in POMS and MMM results in a higher selectivity of the MMMs. The highest selectivity is found for each membrane at a feed concentration of 1.26 vol% n-C_5H_{12}. Values are estimated to approximately 94, 112 and 105 for POMS, MMM-1 and MMM-2, respectively. This corresponds to an improvement of 11 % for the use of MMM-2 and even up to 20 % for the MMM-1 compared to pure POMS. The selectivity declines with the decrease of the n-C_5H_{12} concentration in the feed mixture but different trends are observed for the improvement compared to pure POMS. While an almost constant improvement of around 13 % is found for MMM-2 with varying n-C_5H_{12} feed concentrations, the benefit of the MMM-1 is less pronounced at low concentrations of n-C_5H_{12}. However, the results are very sensitive and prone to error. The values given for the selectivity were calculated from average values of the permeances between refilling stops. Although having taken into account a sufficient time for equilibrating the system, an impact of the refilling stops on the volume flow rates and the feed composition cannot completely be avoided. It is assumed that the obtained values for a feed concentration of 0.75 vol% n-C_5H_{12} may be faulty due to fluctuations of the mixture composition.

Table 6-14: Selectivity *n*-C_5H_{12} / N_2 as function of the feed composition for POMS and MMM filled with 20 wt% AC050-1 or AC050-2 in binary mixtures of *n*-C_5H_{12} / N_2 at 30 bar and 20 °C

$y_{F,n\text{-}C5H12}$	$f_{m,n\text{-}C5H12}$	Selectivity *n*-C_5H_{12} / N_2			Improvement	
		POMS	MMM-1	MMM-2	MMM-1	MMM-2
[mol%]	[bar]				[%]	[%]
1.26	0.26	93.6	111.9	105.1	19.6	12.3
1.05	0.21	74.0	86.4	83.3	16.8	12.6
0.75	0.14	47.0	48.3	45.5	2.6	- 3.3
0.50	0.09	21.2	22.5	24.0	5.8	12.8
0.40	0.07	13.2	13.4	14.9	1.6	13.2
Error		*10.7*	*24.5*	*2.6*		

6.3 Evaluation of MMM Performance

The functionality of the developed MMMs for the separation of higher hydrocarbons from permanent gases has been demonstrated in the previous sections. While they allow for a much higher selectivity than state-of-art POMS membranes, their overall permeances are considerably lower. To highlight the potential of the developed MMM composed of 15 wt% POMS and 20 wt% AC050-2, a simplified process simulation was performed with Aspen Custom Modeler™ to determine the overall efficiency of separation.

A separation task similar to the natural gas processing described in Figure 2-1 has been exemplarily studied. The flow sheet of the separation task is presented in Figure 6-39. Again, a binary mixture with 5 vol% *n*-C_4H_{10} in CH_4 is used as a model mixture for the separation of higher hydrocarbons. The binary mixture enters the membrane module at 30 bar and 20 °C. The target of the process is a concentration of *n*-C_4H_{10} in the retentate stream of 1 vol%, representing for example a certain hydrocarbon dew point regulation. The permeate pressure is set to 1 bar. The hydrocarbon enriched permeate stream is recompressed and cooled to remove *n*-C_4H_{10} partly as liquid condensate while the remaining permeate stream is recycled to the process. The efficiency of the separation is assessed by the membrane area A_M, the permeate flow $\dot{V}_P$, and the required energy for the recompression P or condensation Q of the permeate stream.

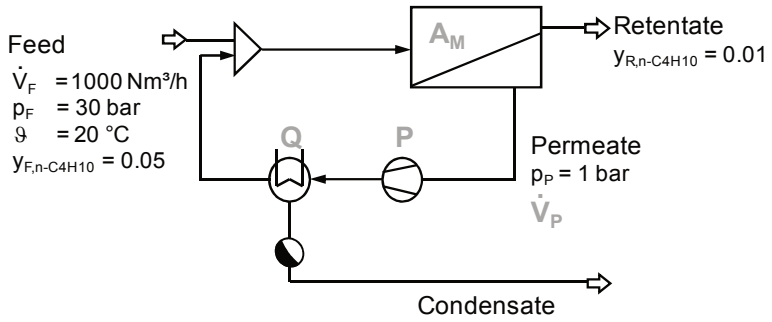

Figure 6-39: Flow sheet of a binary separation task used for a process simulation with ACM™ to demonstrate the potential of the application of developed MMMs

For reasons of simplicity, no specific module geometry is considered but only a flow channel with a parallel flow of the feed gas over a membrane surface and free permeate withdrawal. The depletion of the feed gas is calculated by solving the partial differential equations resulting from the balance equations of mass, energy and momentum between volume elements. The general model implemented in Aspen Custom Modeler™ was developed at the Helmholtz-Zentrum Geesthacht. More details can be found elsewhere in literature [113]. While the real gas behaviour and the Joule-Thomson effect are accounted for, the impacts of a concentration polarisation or of pressure drops inside the the module's flow channels or support structure are neglected. The permeances of the membranes are required as input parameters. They are calculated based on the free volume model for POMS and the derived 'pseudo free volume model' presented in chapter 6.2.2.5 for MMM. The parameters used for the calculation are summarised in Table 6-15.

Table 6-15: Parameters used for a simplified process simulation with ACM for POMS and MMM composed of 15 wt% POMS and 20 wt% AC050-2 for the separation of *n*-C_4H_{10} / CH_4 at 30 bar and 20 °C

		POMS		*MMM*	
Parameter	Unit	CH_4	*n*-C_4H_{10}	CH_4	*n*-C_4H_{10}
$L^{\infty}_{i,0}$	[$m_N^3/(m^2\ h\ bar)$]	32.4840	1.1215	0.0092	0.0053
$E_{A,i}$	[kJ/mol]	11122	- 3833	- 5910.9	- 14447.8
$m_{i,0}$	[bar^{-1}]	0	558.21	0.75	5895.01
$m_{i,T}$	[K^{-1}]	0	- 0.021	0.0025	- 0.0268

The estimated values of the required membrane area, the energy consumption for recompression and cooling as well as the energy saving potential are given in Table 6-16. The lower permeances

of the MMM result in a larger membrane area required to achieve the aspired retentate concentration of 1 vol% *n*-C_4H_{10}. Approximately 38 m² are necessary for the MMM compared to 22 m² for a POMS membrane. This greater effort is compensated by the improved selectivity of the MMM which leads to a considerable reduction of the permeate flow. This allows not only a reduction of the loss of valuable product with the permeate flow but, even more important, a significant reduction of the energy input required for recompression and condensation of the permeate stream. Compared to the common industrial state-of-art material POMS, up to 42 % of energy can be saved by application of the developed MMM composed of 15 wt% POMS and 20 wt% AC050-2. A further important step towards a better competitiveness of membrane-based separations could thus be achieved.

Table 6-16: Estimated required membrane area (in m²) and energy consumption (in kW) for POMS and a MMM composed of 15 wt% POMS and 20 wt% AC050-2 for the separation of a binary mixture of *n*-C_4H_{10} / CH_4 at 30 bar and 20 °C (flow sheet presented in Figure 6-39)

Parameter	Unit	POMS	MMM
Membrane area A_M	m²	22	38
$\dot{V}_P$	m_N^3/h	312.3	245.2
P	kW	75	58
Q	kW	- 88	- 71
Total energy consumption	kW	163	129
Energy saving potential	%	-	42

7 CONCLUSIONS

In this work, the production and applicability of thin film composite MMM based on a rubbery POMS matrix and different inorganic filler materials for the selective separation of higher hydrocarbons has been investigated and evaluated with respect to an industrial application.

In the first part of this work, a method for the reproducible production of a MMM with an improved separation performance of binary mixtures *n*-C_4H_{10} / CH_4 compared to pure polymeric POMS membranes was developed. Several compositional parameters, such as the properties of the polymeric matrix, the type of filler material, the content and particle size of the filler material, the type of solvent and the use of a gutter layer, were considered. It was shown that all parameters have to be adjusted carefully with the most important parameters being the type of the polymeric matrix, the type and content of the filler particles and the homogeneity of their dispersion. Best results were obtained with activated carbon AC050 as filler material at a content of 20 wt%. A high viscosity of the polymeric precursor solution as well as a step-wise addition and mixing with both mechanical forces and sonication were found to be beneficial to achieve a good dispersion of filler particles. The uniformity and flux could additionally be improved by casting on a gutter layer. In conclusion, the best MMM is composed of 15 wt% POMS and 20 wt% activated carbon type AC050 (d_{50} = 1.5 µm, saturated in iso-octane) casted on a porous support of PE/PAN with an additional gutter layer. The MMM could be successfully prepared in technical scale with areas up to 120 m² via suspension coating on a roll-coating machine. As far as is known, this is the largest produced area of a TFC MMM reported in literature up to date. It was thus possible to successfully overcome one of the severest limitations of the MMM concept, namely a reproducible industrial scale production.

While the addition of AC particles resulted in lower permeances or permeabilities, the selectivity *n*-C_4H_{10} / CH_4 could be increased up to 32 at a feed pressure of 30 bar, atmospheric permeate pressure, a temperature of 20 °C and a *n*-C_4H_{10} content of 5 vol-%. This corresponds to an improvement of 20 % compared to a pure POMS membrane and gives one of the highest selectivities reported in literature for a membrane-based separation of *n*-C_4H_{10} / CH_4. This

improvement highly strengthens the competitiveness of the membrane technology for the separation of higher hydrocarbons and opens up the way for further fields of application that are currently characterised by a high consumption of energy.

The second part of the work concludes detailed investigations of the separation performance of prepared MMMs. The permeation behaviour was analysed for single gases as well as binary mixtures of *n*-C_4H_{10} / CH_4 as a model mixture to represent the separation of higher hydrocarbons from permanent gas streams. The separation performance was evaluated for a variety of operating conditions, namely feed and permeate pressure, temperature and the binary mixture compositions. Most parameters affect the solution of gas components into the polymeric matrix or the adsorption on AC and thus the concentration of *n*-C_4H_{10} present inside the polymeric matrix or the porous system of AC. The average *n*-C_4H_{10} fugacity was used as an indicator for the concentration of *n*-C_4H_{10} and the resulting degree of swelling of the polymeric matrix. Both types of membranes, pure POMS and hybrid MMM, show a strong dependency of permeation on the average fugacity of *n*-C_4H_{10}. Best performance was achieved at a high average fugacity of *n*-C_4H_{10} inside the membrane as both are beneficial for the solution and adsorption of *n*-C_4H_{10}. The optimum conditions were thus identified as a high feed pressure up to 30 bar, an ambient permeate pressure, a low temperature and a high concentration of condensable *n*-C_4H_{10} inside the feed mixture.

The successful improvement of the separation performance was also proven for binary mixtures of *n*-C_5H_{12} / N_2 and for a multi-component mixture composed of hydrocarbons C_1 – C_5 and CO_2. The multi-component mixture composition was inspired by a natural gas separation task to approximate the challenges of a real application. In presence of the highly condensable *n*-C_5H_{12}, the selectivity *n*-C_4H_{10} / CH_4 could even be further improved when compared to binary mixtures of *n*-C_4H_{10} / CH_4 at the same feed concentration of *n*-C_4H_{10}. The improved separation performance of MMMs compared to pure POMS membranes can be attributed to the high adsorption affinity of higher hydrocarbons to the AC filler particles. While they facilitate the adsorption and permeation of higher hydrocarbons like *n*-C_4H_{10} or *n*-C_5H_{12}, they simultaneously impair the permeation of CH_4 due to a partial blocking of pores by a condensed layer of the higher hydrocarbons. Furthermore, the presence of filler particles is beneficial to reduce the swelling of the polymeric matrix and the associated co-permeation of CH_4.

An important requirement for an industrial application is a stable separation performance over time. Such results have not been reported in literature yet for MMMs. The developed MMM has

been tested with respect to the susceptibility of performance, e.g., by fluctuating and competing mixture compositions as well as by a long-term exposure to higher pressure. Binary mixtures of n-C_5H_{12} / N_2 with 1.3 – 1.5 mol% n-C_5H_{12} in feed at 30 bar and 20 °C have been applied for approximately 35 days of operation. A reasonably stable performance was achieved with a maximum decline of the selectivity of 14 %. The higher separation performance of MMMs was thus demonstrated for another binary mixture.

The potential of the developed MMMs has been illustrated with a simplified process simulation performed with Aspen Custom Modeler™ based on the experimental results. The lower flux of MMMs results in larger membrane areas required for the separation but the higher selectivity reduces the loss of product with the permeate stream and allows for the reduction of the energy demand for recompression and condensation of the permeate stream. Up to 42 % of energy can be saved by the application of the developed MMM composed of POMS and 20 wt% AC050 compared to the industrial state-of-art membrane material POMS.

Some key factors for the industrial application of MMMs were successfully demonstrated in this work, for example, the successful separation of multi-component mixtures, the reproducible large-scale production, the long-term stability of performance and the improved selectivity compared to conventional membranes that allow for a lower energy consumption and lower operational costs. To correctly evaluate the potential of an industrial application, the performance of the developed MMM within a membrane module has to be tested. The module production itself as well as additional transport resistances or the presence of water vapour within the module imply significant challenges. Such technical scale investigations have already been partly proven, for example, the possibility of welding the MMM material and the defect-free production of envelopes. Further investigations would include module performance tests in a pilot plant or, e.g., in by-pass to an existing membrane plant. These tests were not possible within the scope of this work but should be pursued for a complete technical and economical evaluation.

The findings and results obtained in this work demonstrate the high potential of the MMM concept to achieve a better competitiveness of membrane-based separations and to open up new fields of application. The results presented in this work can be used as a basis for further developments and implementations of the MMM technology. The MMM developed in this work is not only capable to withstand the challenges of an industrial application but does also allow an improved separation at a lower expenditure of energy. This is a promising step towards more sustainable processes.

REFERENCES

[1] Abetz, V., Brinkmann, T., Dijkstra, M., Ebert, K., Fritsch, D., Ohlrogge, K., Paul, D., Peinemann, K.-V., Pereira-Nunes, S., Scharnagl, N., Schossig, M. 2006. Developments in Membrane Research: from Material via Process Design to Industrial Application. *Adv. Eng. Mater.* 8, 5, 328–358.

[2] Adnadjevic, B., Jovanovic, J., Gajinov, S. 1997. Effect of different physiochemical properties of hydrophobic zeolites on the pervaporation properties of PDMS membranes. *Journal of Membrane Science* 136, 173–179.

[3] Ahn, J., Chung, W.-J., Pinnau, I., Song, J., Du, N., Robertson, G. P., Guiver, M. D. 2010. Gas transport behavior of mixed-matrix membranes composed of silica nanoparticles in a polymer of intrinsic microporosity (PIM-1). *Journal of Membrane Science* 346, 2, 280–287.

[4] Alpers, A. 1998. *Hochdruckpermeation mit selektiven Polymermembranen für die Separation gasförmiger Gemische*. Dissertation, Universität Hannover.

[5] Angelis, M. G. de Sarti, G. C. 2012. Gas sorption and permeation in mixed matrix membranes based on glassy polymers and silica nanoparticles. *Current Opinion in Chemical Engineering* 1, 2, 148–155.

[6] Aranguren, M., Mora, E., Macosko, C. 1997. Compounding Fumed Silicas into Polydimethylsiloxane: Bound Rubber and Final Aggregate Size. *Journal of Colloid and Interface Science* 195, 329–337.

[7] Aroon, M., Ismail, A., Matsuura, T., Montazer-Rahmati, M. 2010. Performance studies of mixed matrix membranes for gas separation: A review. *Separation and Purification Technology,* 75, 229–242.

[8] Arruebo, M., Coronas, J., Menéndez, M., Santamaría, J. 2001. Separation of hydrocarbons from natural gas using silicalite membranes. *Separation and Purification Technology* 25, 1-3, 275–286.

[9] Bae, T.-H., Long, J. R. 2013. CO2/N2 separations with mixed-matrix membranes containing Mg2(dobdc) nanocrystals. *Energy Environ. Sci.* 6, 12, 3565.

[10] Baerns, M. 2013. *Technische Chemie*. Wiley-VCH, Weinheim.

[11] Baker, R. W. 2000. *Membrane technology and applications*. McGraw-Hill professional engineering. McGraw-Hill, New York.

[12] Baker, R. W. 2002. Future Directions of Membrane Gas Separation Technology. *Industrial & Engineering Chemistry Research* 41, 6, 1393–1411.

[13] Baker, R. W. 2008. Membranes for Vapor/Gas Separation. In *Advanced membrane technology and applications*, N. N. Li, A. G. Fane, W. W. Ho and T. Matsuura, Eds. Wiley, Hoboken, N.J, 559–580.

[14] Baker, R. W., Lokhandwala, K. 2008. Natural Gas Processing with Membranes: An Overview. *Industrial & Engineering Chemistry Research* 47, 7, 2109–2121.

[15] Bakhtiari, O., Sadeghi, N. 2014. Mixed matrix membranes' gas separation performance prediction using an analytical model. *Chemical Engineering Research and Design*.
[16] Ballinas, L., Torras, C., Fierro, V., Garcia-Valls, R. 2004. Factors influencing activated carbon-polymeric composite membrane structure and performance. *Journal of Physics and Chemistry of Solids* 65, 2-3, 633–637.
[17] Barrer, R., Barrie, J., Raman, N. 1962. Solution and diffusion in silicone rubber II - Influence of fillers. *Polymer* 3, 605–614.
[18] Berkowitz, N. 1997. *Fossil hydrocarbons. Chemistry and technology*. Academic Press, San Diego.
[19] Bettermann, I., Katarzynski, D., Staudt, C. 2010. Membranverfahren zur Auftrennung von gasförmigen und flüssigen Stoffgemischen. *Analytik News*.
[20] Böhringer, B., Guerra Gonzalez, O., Eckle, I., Müller, M., Giebelhausen, J.-M., Schrage, C., Fichtner, S. 2011. Polymer-based Spherical Activated Carbons - From Adsorptive Properties to Filter Performance. *Chemie Ingenieur Technik* 83, 1-2, 53–60.
[21] Brinkmann, T., Withalm, U., Wind, J., Wolff, T. 2013. Theoretical and Experimental Investigations of Flat Sheet Membrane Module Types for High Capacity Gas Separation Applications. *Chemie Ingenieur Technik* 85, 8, 1210–1220.
[22] Bronkhorst. 2016. *General instructions digital Mass Flow / Pressure instruments laboratory style / IN-FLOW. Instruction Manual*. Document Nr.: 9.17.022V.
[23] Buhr, K. 2005. *Untersuchung neuer Membranmaterialien für Erd- und Raffineriegasanwendungen*. Diplomarbeit, Hochschule für Angewandte Wissenschaften Hamburg.
[24] Bundesministerium für Umwelt, Naturschutz und Reaktorsicherheit. 2016. *Klimaschutzplan 2050 – Klimapolitische Grundsätze und Ziele der Bundesregierung Deutschland*
[25] Bundesministerium für Umwelt, Naturschutz und Reaktorsicherheit. 2002. *Erste Allgemeine Verwaltungsvorschrift zum Bundes-Immissionsschutzgesetz. Technische Anleitung zur Reinhaltung der Luft*
[26] Burganos, V. 2010. Modeling and Simulation of Membrane Structure and Transport Properties. In *Comprehensive membrane science and engineering*, E. Drioli and L. Giorno, Eds. Elsevier Science, Amsterdam, London, 29–74.
[27] Campbell, D., Beckman, K., Calderon, C., Doolan, P., Ottosen, R., Lisensky, G. 1999. Replication and compression of bulk and surface structures with polydimethylsiloxane elastomers. *J. Chem. Ed.* 75, 4.
[28] Caro, J., Noack, M., Kölsch, P., Schäfer, R. 2000. Zeolite membranes – state of their development and perspective. *Microporous and Mesoporous Materials* 38, 1, 3–24.
[29] Chandak, M., Lin, Y., Ji, W., Higgins, R. 1997. Sorption and diffusion of VOCs in DAY zeolite and silicalite-filled PDMS membranes. *Journal of Membrane Science* 133, 231–243.
[30] Chen, B., Yang, Z., Zhu, Y., Xia, Y. 2014. Zeolitic imidazolate framework materials: recent progress in synthesis and applications. *J. Mater. Chem. A* 2, 40, 16811–16831.
[31] Cheremisinoff, N. P. 2000. *Handbook of chemical processing equipment*. Butterworth-Heinemann, Boston.
[32] Chung, T., Jiang, L., Li, Y., Kulprathipanja, S. 2007. Mixed matrix membranes (MMMs) comprising organic polymers with dispersed inorganic fillers for gas separation. *Progress in Polymer Science,* 32, 483–507.
[33] Cong, H., Radosz, M., Towler, B., Shen, Y. 2007. Polymer–inorganic nanocomposite membranes for gas separation. *Separation and Purification Technology* 55, 3, 281–291.
[34] Cussler, E. 1990. Membranes containing selective flakes. *Journal of Membrane Science* 52, 3, 275–288.
[35] DeSitter, K., Winberg, P., D'Haen, J., Dotremont, C., Leysen, R., Martens, J. A., Mullens, S., Maurer, F. H., Vankelecom, I. F. 2006. Silica filled poly(1-trimethylsilyl-1-propyne) nanocomposite membranes: Relation between the transport of gases and structural characteristics. *Journal of Membrane Science* 278, 1-2, 83–91.

[36] Diestel, L., Liu, X., Li, Y., Yang, W., Caro, J. 2013. Comparative permeation studies on three supported membranes: Pure ZIF-8, pure polymethylphenylsiloxane, and mixed matrix membranes. *Microporous and Mesoporous Materials*.
[37] Do, D. 1998. *Adsorption analysis. Equilibria and kinetics*. Imperial College Press, London.
[38] Dobrak-Van Berlo, A., Vankelecom, I. F., van der Bruggen, B. 2011. Parameters determining transport mechanisms through unfilled and silicalite filled PDMS-based membranes and dense PI membranes in solvent resistant nanofiltration: Comparison with pervaporation. *Journal of Membrane Science* 374, 1-2, 138–149.
[39] Dong, G., Li, H., Chen, V. 2013. Challenges and opportunities for mixed-matrix membranes for gas separation. *J. Mater. Chem. A* 1, 15, 4610.
[40] Dotremont, C., Brabants, B., Geeroms, K., Mewis, J., Vandecasteele, C. 1995. Sorption and diffusion of chlorinated hydrocarbons in silicalite-filled PDMS membranes. *Journal of Membrane Science* 104, 109–117.
[41] Dragomirova, R., Stöhr, M., Hecker, C., Lubenau, U., Paschek, D., Wohlrab, S. 2014. Desorption-controlled separation of natural gas alkanes by zeolite membranes. *RSC Adv* 4, 104, 59831–59834.
[42] Duval, J.-M., Folkers, B., Mulder, M., Desgrandchamps, G., Smolders, C. 1993. Adsorbent filled membranes for gas separation - Part. 1. Improvement of the gas separation properties of polymeric membranes by incorporation of microporous adsorbents. *Journal of Membrane Science* 80, 189–198.
[43] DVGW Deutscher Verein des Gas- und Wasserfaches e.V. 2000. *DVGW G 260 Arbeitsblatt: Gasbeschaffenheit* 3.
[44] Eldridge, R. B. 1993. Olefin/paraffin separation technology. A review. *Ind. Eng. Chem. Res.* 32, 10, 2208–2212.
[45] Elias, H.-G. 1997. *An introduction to polymer science*. VCH, Weinheim, Cambridge.
[46] European Commission. 2010. *Energy 2020 - A strategy for competitive, sustainable and secure energy. COM(2010)639*. Communication from the commission to the European parliament, the council, the European economic and social committee and the committee of the regions.
[47] European Commission. 2011. *A Roadmap for moving to a competitive low carbon economy in 2050. COM(2011) 112*. Communication from the commission to the European parliament, the council, the European economic and social committee and the committee of the regions.
[48] Evonik Industries AG. 2015. *Material safety data sheet. Aerosil R8200*, Hanau, Germany.
[49] Fang, S.-M., Stern, S., Frisch, H. 1975. A "free volume" model of permeation of gas and liquid mixtures through polymeric membranes. *Chemical Engineering Science* 30, 773–780.
[50] García, M. G., Marchese, J., Ochoa, N. A. 2012. High activated carbon loading mixed matrix membranes for gas separations. *Journal of Materials Science* 47, 7, 3064–3075.
[51] Goh, P., Ismail, A., Sanip, S., Ng, B., Aziz, M. 2011. Recent advances of inorganic fillers in mixed matrix membrane for gas separation. *Separation and Purification Technology* 81, 3, 243–264.
[52] Gomes, D., Nunes, S. P., Peinemann, K.-V. 2005. Membranes for gas separation based on poly(1-trimethylsilyl-1-propyne)–silica nanocomposites. *Journal of Membrane Science* 246, 1, 13–25.
[53] Grinevich, Y., Starannikova, L., Yampolskii, Y., Gringolts, M., Finkelshtein, E. 2011. Solubility controlled permeation of hydrocarbons in novel highly permeable polymers. *Journal of Membrane Science* 378, 1-2, 250–256.
[54] Hassanajili, S., Khademi, M., Keshavarz, P. 2014. Influence of various types of silica nanoparticles on permeation properties of polyurethane/silica mixed matrix membranes. *Journal of Membrane Science* 453, 369–383.

[55] Hassanajili, S., Masoudi, E., Karimi, G., Khademi, M. 2013. Mixed matrix membranes based on polyetherurethane and polyesterurethane containing silica nanoparticles for separation of CO2/CH4 gases. *Separation and Purification Technology* 116, 1–12.
[56] Haynes, W. M., Ed. 2010. *CRC Handbook of Chemistry and Physics*. Taylor & Francis Group.
[57] He, Z., Pinnau, I., Morisato, A. 2002. Nanostructured poly(4-methyl-2-pentyne)/silica hybrid membranes for gas separation. *Desalination* 146, 11–15.
[58] Henley, E. J., Seader, J. D., Roper, D. K. 2011. *Separation process principles*. Wiley, Hoboken.
[59] Hillock, A. M., Miller, S. J., Koros, W. 2008. Crosslinked mixed matrix membranes for the purification of natural gas: Effects of sieve surface modification. *Journal of Membrane Science* 314, 1-2, 193–199.
[60] Hosseini, S., Koranian, P., Gholami, A., Madaeni, S., Moghadassi, A., Sakinejad, P., Khodabakhshi, A. 2013. Fabrication of mixed matrix heterogeneous ion exchange membrane by multiwalled carbon nanotubes: Electrochemical characterization and transport properties of mono and bivalent cations. *Desalination* 329, 62–67.
[61] Hülagü, D., Kramer, V., Kraume, M. 2012. Preparation and characterization of mixed-matrix-membranes. *Czasopismo Techniczne Mechanika* 109, 5, 95–105.
[62] Humphrey, J. L., Keller, G. E. ©1997. *Separation process technology*. McGraw-Hill, New York.
[63] Hussain, M., König, A. 2012. Mixed-Matrix Membrane for Gas Separation: Polydimethylsiloxane Filled with Zeolite. *Chem. Eng. Technol.* 35, 3, 561–569.
[64] Intergovernmental Panel on Climate Change. 2014. *Global warming potential values*. https://www.ipcc.ch/pdf/assessmentreport/ar5/wg1/WG1AR5_Chapter08_FINAL.pdf
[65] Ismail, A., Goh, P., Sanip, S., Aziz, M. 2009. Transport and separation properties of carbon nanotube-mixed matrix membrane. *Separation and Purification Technology* 70, 1, 12–26.
[66] Javaid, A. 2005. Membranes for solubility-based gas separation applications. *Chemical Engineering Journal* 112, 1-3, 219–226.
[67] Jia, M., Peinemann, K.-V., Behling, R.-D. 1991. Molecular sieving effect of the zeolite-filled silicone rubber membranes in gas permeation. *Journal of Membrane Science* 57, 289–296.
[68] Jia, M., Peinemann, K.-V., Behling, R.-D. 1992. Preparation and characterization of thin-film zeolite - PDMS composite membranes. *Journal of Membrane Science* 73, 119-128.
[69] Kast, W. 1988. *Adsorption aus der Gasphase. Ingenieurwissenschaftliche Grundlagen und technische Verfahren*. VCH, Weinheim.
[70] Kattula, M., Ponnuru, K., Zhu, L., Jia, W., Lin, H., Furlani, E. P. 2015. Designing ultrathin film composite membranes: the impact of a gutter layer. *Scientific Reports* 5, 15016.
[71] Keller, J. U., Staudt, R. 2005. *Gas adsorption equilibria. Experimental methods and adsorptive isotherms*. Springer, New York.
[72] Kelman, S. D., Raharjo, R., Bielawski, C. W., Freeman, B. D. 2008. The influence of crosslinking and fumed silica nanoparticles on mixed gas transport properties of poly[1-(trimethylsilyl)-1-propyne]. *Polymer* 49, 13-14, 3029–3041.
[73] Kemp, D., Paul, D. 1974. Gas Sorption in Polymer Membranes Containing Adsorptive Fillers. *Journal of Polymer Science* 12, 485–500.
[74] Khanbabaei, G., Vasheghani-Farahani, E., Rahmatpour, A. 2012. Pure and mixed gas CH4 and n-C4H10 permeation in PDMS-fumed silica nanocomposite membranes. *Chemical Engineering Journal* 191, 369–377.
[75] Kipp, S. 2010. *Charakterisierung CO2-selektiver Membranen zur Biosgasaufbereitung*. Diplomarbeit, TUHH.
[76] Kissa, E. ©1999. *Dispersions. Characterization, testing, and measurement*. Surfactant science series 84. M. Dekker, New York.
[77] Kramer, V. 2017. *Löslichkeitsselektive Mixed Matrix Membranen zur Gaspermeation - Experimentelle Untersuchungen und Entwicklung eines Stofftransportmodells*. Dissertation, Technische Universität Berlin.

[78] Kulprathipanja, S. 2002. Mixed matrix membrane development. *Membrane Technology* 2002, 4, 9–12.
[79] Kulprathipanja, S. 2010. *Zeolites in industrial separation and catalysis*. Wiley-VCH, Weinheim.
[80] Kumar, M. V., Prasad, S. K. 2012. Influence of quenched disorder created by nanosilica network on phase transitions in tetracosane. *RSC Adv.* 2, 22, 8531.
[81] Kusworo, T., Ismail, A., Mustafa, A., Budiyono. 2010. Application of Activated Carbon Mixed Matrix Membranes for Oxygen Purification. *International Journal of Science and Engineering* 1, 1, 21–24.
[82] Le, N. L., Tang, Y. P., Chung, T. 2013. The development of high-performance 6FDA-NDA/DABA/POSS/Ultem® dual-layer hollow fibers for ethanol dehydration via pervaporation. *Journal of Membrane Science* 447, 163–176.
[83] Li, B., Xu, D., Zhang, X., Jiang, Z., Wang, Y., Ma, J., Dong, X., Wu, H. 2010. Rubbery Polymer−Inorganic Nanocomposite Membranes: Free Volume Characteristics on Separation Property. *Ind. Eng. Chem. Res* 49, 24, 12444–12451.
[84] Lin, J., Liu, Y., Yang, W., Xie, Z., Zhang, P., Li, X., Lin, H., Chen, G., Lei, Q. 2014. Structure and mechanical properties of the hybrid films of well dispersed SiO2 nanoparticle in polyimide (PI/SiO2) prepared by sol–gel process. *J Polym Res* 21, 8.
[85] Liu, C., Kulprathipanja, S., Hillock, A. M., Koros, W. J. 2008. Recent Progress in Mixed-Matrix Membranes. In *Advanced membrane technology and applications*, N. N. Li, A. G. Fane, W. W. Ho and T. Matsuura, Eds. Wiley, Hoboken, N.J, 789–819.
[86] Liu, S., Liu, G., Zhao, X., Jin, W. 2013. Hydrophobic-ZIF-71 filled PEBA mixed matrix membranes for recovery of biobutanol via pervaporation. *Journal of Membrane Science* 446, 181–188.
[87] Löffler, V., Kraume, M. 2011. Development of Mixed-Matrix Membranes for separation of gaseous hydrocarbons. In *Proceedings 18th International Conference Process Engineering and Chemical Plant Design*. Univ.-Verl. der TU, Berlin, 207–216.
[88] Lüdtke, O., Behling, R.-D. 1998. Concentration polarization in gas permeation. *Journal of Membrane Science* 146, 145–157.
[89] Mahajan, R., Burns, R., Schaeffer, M., Koros, W. 2002. Challenges in Forming Successful Mixed Matrix Membranes with Rigid Polymeric Materials. *Journal of Applied Polymer Science* 86, 881–890.
[90] Mahajan, R., Koros, W. 2000. Factors controlling successful formation of mixed-matrix gas separation materials. *Industrial & Engineering Chemistry Research* 39, 2692–2696.
[91] Mahajan, R., Zimmerman, C., Koros, W. 1999. Fundamental and Practical Aspects of Mixed Matrix Gas Separation Membranes. In *Polymer Membranes for Gas and Vapor Separation*, B. D. Freeman and I. Pinnau, Eds. ACS Symposium Series. American Chemical Society, Washington, DC, 277–286.
[92] Majeed, S., Filiz, V., Shishatskiy, S., Wind, J., Abetz, C., Abetz, V. 2012. Pyrene-POSS nanohybrid as a dispersant for carbon nanotubes in solvents of various polarities: its synthesis and application in the preparation of a composite membrane. *Nanoscale Res Lett* 7, 1, 296.
[93] Marchese, J., Anson, M., Ochoa, N., Prádanos, P., Palacio, L., Hernández, A. 2006. Morphology and structure of ABS membranes filled with two different activated carbons. *Chemical Engineering Science* 61, 16, 5448–5454.
[94] Mark, J. E., Ed. 2006. *Physical properties of polymer handbook*. Springer, New York.
[95] Melin, T. 2007. *Membranverfahren. Grundlagen der Modul- und Anlagenauslegung*. Springer, Berlin.
[96] Merkel, T. C., He, Z., Pinnau, I., Freeman, B. D., Meakin, P., Hill, A. J. 2003. Effect of Nanoparticles on Gas Sorption and Transport in Poly(1-trimethylsilyl-1-propyne). *Macromolecules* 36, 18, 6844–6855.

[97] Merkel, T. C., He, Z., Pinnau, I., Freeman, B. D., Meakin, P., Hill, A. J. 2003. Sorption and Transport in Poly(2,2-bis(trifluoromethyl)-4,5-difluoro-1,3-dioxole- co -tetrafluoroethylene) Containing Nanoscale Fumed Silica. *Macromolecules* 36, 22, 8406–8414.

[98] Mezger, T. 2010. *Das Rheologie-Handbuch. Für Anwender von Rotations- und Oszillations-Rheometern*. Farbe- und Lack-Edition. Vincentz Network, Hannover.

[99] Miller, S., Koros, W., Vu, D. 2007. Mixed matrix membrane technology: enhancing gas separations with polymer/molecular sieve composites. *Studies in Surface Science & Catalysis* 170, 1590–1596.

[100] Miller, S., Vu, D., Koros, W., Eds. 2007. *Enhancing natural gas purification with advanced polymer/molecular sieve composite membranes*. IPTC 11465.

[101] Moadebb, M., Koros, W. 1997. Gas transport properties of thin polymeric membranes in the presence of silicon dioxide particles. *Journal of Membrane Science* 125, 143–163.

[102] Moore, T., Mahajan, R., Vu, D., Koros, W. J. 2004. Hybrid membrane materials comprising organic polymers with rigid dispersed phases. *AIChE Journal* 50, 2, 311–321.

[103] Moore, T. T., Koros, W. J. 2005. Non-ideal effects in organic–inorganic materials for gas separation membranes. *Journal of Molecular Structure* 739, 1-3, 87–98.

[104] Moradihamedani, P., Ibrahim, N., Ramimoghadam, D., Yunus, W. W., Yusof, N. 2013. Polysulfone/zinc oxide nanoparticle mixed matrix membranes for CO2 /CH4 separation. *J. Appl. Polym. Sci.*, n/a.

[105] Moradihamedani, P., Ibrahim, N., Wan Yunus, W. M. Z., Yusof, N. 2014. Study of morphology and gas separation properties of polysulfone/titanium dioxide mixed matrix membranes. *Polym Eng Sci*, n/a.

[106] Mulder, M. 1996. *Basic principles of membrane technology*. Kluwer Academic, Dordrecht, Boston.

[107] Murphy, J. ©2001. *Additives for plastics handbook*. Elsevier Advanced Technology, Oxford, UK, New York, NY.

[108] Mushardt, H., Kramer, V., Hülagü, D., Brinkmann, T., Kraume, M. 2014. Development of Solubility Selective Mixed Matrix Membranes for Gas Separation. *Chemie Ingenieur Technik* 86, 1-2, 83–91.

[109] Nasir, R., Mukhtar, H., Man, Z., Mohshim, D. F. 2013. Material Advancements in Fabrication of Mixed-Matrix Membranes. *Chem. Eng. Technol.* 36, 5, 717–727.

[110] Neubauer, K., Lubenau, U., Hecker, C., Lücke, B., Paschek, D., Wohlrab, S. 2013. Abreicherung von Flüssiggas aus Erdgas mittels Zeolithmembranen. *Chemie Ingenieur Technik* 85, 5, 713–722.

[111] Nunes, S., Peinemann, K.-V., Ohlrogge, K., Alpers, A., Keller, M., Pires, A. 1999. Membranes of poly(ether imide) and nanodispersed silica. *Journal of Membrane Science* 157, 219–226.

[112] Nunes, S., Schultz, J., Peinemann, K.-V. 1996. Silicone membranes with silica nanoparticles. *J. Mat. Sci. Lett.* 15, 1139–1141.

[113] Ohlrogge, K., Ebert, K., Eds. 2006. *Membranen: Grundlagen, Verfahren und industrielle Anwendungen*. Wiley-VCH, Weinheim.

[114] Ohlrogge, K., Wind, J., Brinkmann, T. 2010. Membranes for Recovery of Volatile Organic Compounds. In *Comprehensive membrane science and engineering*, E. Drioli and L. Giorno, Eds. Elsevier Science, Amsterdam, London, 213–240.

[115] Ohlrogge, K., Wind, J., Stegger, J. 2003. *Verminderung von Emissionen mittels Membranverfahren*. Flachbodentanks: Neue Bestimmungen und Erkenntnisse für Herstellung und Betrieb, München.

[116] Pal, R. 2008. Permeation models for mixed matrix membranes. *Journal of Colloid and Interface Science* 317, 1, 191–198.

[117] Park, H., Lee, Y. 2008. Polymeric membrane materials and potential use in gas separation. In *Advanced membrane technology and applications*, N. N. Li, A. G. Fane, W. W. Ho and T. Matsuura, Eds. Wiley, Hoboken, N.J, 633–669.

[118] Paul, D. R. 2010. Fundamentals of Transport Phenomena in Polymer Membranes. In *Comprehensive membrane science and engineering*, E. Drioli and L. Giorno, Eds. Elsevier Science, Amsterdam, London.

[119] Paul, D. R., Mark, J. E. 2010. Fillers for polysiloxane ("silicone") elastomers. *Progress in Polymer Science* 35, 7, 893–901.

[120] Pedram, S., Kaghazchi, T., Ravanchi, M. T. 2014. Performance and Energy Consumption of Membrane-Distillation Hybrid Systems for Olefin-Paraffin Separation. *Chem. Eng. Technol.* 37, 4, 587–596.

[121] Pethrick, R. A. 2010. *Polymer science and technology for scientists and engineers*. Whittles Pub; Distributed in North America by John Wiley, Dunbeath, Hoboken, N.J.

[122] Petsi, A., Burganos, V. 2012. Interphase layer effects on transport in mixed matrix membranes. *Journal of Membrane Science* 421-422, 247–257.

[123] Pinnau, I., Freeman, B. D. 2004. *Advanced materials for membrane separations. Novel nanostructured polymer-inorganic hybrid membranes for vapour-gas separation*. ACS Symposium Series 876. American Chemical Society, Washington, D.C.

[124] Poling, B. E., Prausnitz, J. M., O'Connell, J. P. 2007. *The properties of gases and liquids*. McGraw-Hill, New York.

[125] Pusch, G., Rischmüller, H., Weggen, K. 1995. *Die Energierohstoffe Erdöl und Erdgas. Vorkommen, Erschliessung, Förderung*. Ernst, Berlin.

[126] Raharjo, R. 2007. *Mixed Gas Sorption and Transport Study in Solubility Selective Polymers*. Dissertation, University of Texas at Austin.

[127] Raharjo, R., Freeman, B. D., Paul, D. R., Sarti, G. C., Sanders, E. 2007. Pure and mixed gas CH4 and n-C4H10 permeability and diffusivity in poly(dimethylsiloxane). *Journal of Membrane Science* 306, 1-2, 75–92.

[128] Raharjo, R., Freeman, B. D., Sanders, E. 2007. Pure and mixed gas CH4 and n-C4H10 sorption and dilation in poly(dimethylsiloxane). *Journal of Membrane Science* 292, 1-2, 45–61.

[129] Rao, M., Sircar, S. 1993. Nanoporous carbon membranes for separation of gas mixtures by selective surface flow. *Journal of Membrane Science* 85, 253–264.

[130] Rao, M., Sircar, S. 1996. Performance and pore characterization of nanoporous carbon membranes for gas separation. *Journal of Membrane Science* 110, 1, 109–118.

[131] Rautenbach, R., Melin, T. 1997. *Membranverfahren. Grundlagen der Modul- und Anlagenauslegung ; mit 69 Tabellen*. Verfahrenstechnik. Springer, Berlin.

[132] Reid, R. C., Prausnitz, J. M., Sherwood, T. K. op. 1977. *The Properties of gases and liquids*. McGraw-Hill, New York.

[133] Rodenas, T., van Dalen, M., Serra-Crespo, P., Kapteijn, F., Gascon, J. 2013. Mixed matrix membranes based on NH2-functionalized MIL-type MOFs: Influence of structural and operational parameters on the CO2/CH4 separation performance. *Microporous and Mesoporous Materials*.

[134] Roland, E., Kleinschmit, P. 2000. Zeolites. In *Ullmann's Encyclopedia of Industrial Chemistry*, Wiley-VCH, Ed. Wiley-VCH Verlag GmbH & Co. KGaA, Weinheim, Germany.

[135] Rouquerol, J., Avnir, D., Fairbridge, C. W., Everett, D. H., Haynes, J. M., Pernicone, N., Ramsay, J. D. F., Sing, K. S. W., Unger, K. K. 1994. Recommendations for the characterization of porous solids (Technical Report). *Pure and Applied Chemistry* 66, 8.

[136] Sadeghi, Z., Omidkhah, M., Masoomi, M. 2015. The effect of particle porosity in mixed matrix membrane permeation models. *International Science Index* 9, 1, 104–109.

[137] Sattler, K. 2001. *Thermische Trennverfahren. Grundlagen, Auslegung, Apparate*. VCH, Weinheim, Chichester.

[138] Scharnagl, N., Buschatz, H. 2001. Polyacrylonitrile (PAN) membranes for ultra- and microfiltration. *Desalination* 139, 191–198.
[139] Scholes, C. A., Stevens, G. W., Kentish, S. E. 2012. Membrane gas separation applications in natural gas processing. *Fuel* 96, 15–28.
[140] Schultz, J. 1996. *Polymermembranen für die Abtrennung höherer Kohlenwasserstoff von Methan*. Dissertation, Technische Universität Hamburg-Harburg.
[141] Schulz, P., Leckebusch, V. 2013. *Nutzen statt Abfackeln von Erdölbegleitgas. Chancen und Herausforderungen für Entwicklung und Treibhausgasminderung*. Bundesministeriums für wirtschaftliche Zusammenarbeit und Entwicklung (BMZ), Hannover.
[142] Schüth, F., Sing, K. S. W., Weitkamp, J., Eds. (2002). *Handbook of porous solids*. Wiley-VCH, Weinheim.
[143] Semsarzadeh, M. A., Ghalei, B., Fardi, M., Esmaeeli, M., Vakili, E. 2014. Structural and transport properties of polydimethylsiloxane based polyurethane/silica particles mixed matrix membranes for gas separation. *Korean J. Chem. Eng.*
[144] Şen, D., Kalıpçılar, H., Yilmaz, L. 2007. Development of polycarbonate based zeolite 4A filled mixed matrix gas separation membranes. *Journal of Membrane Science* 303, 1-2, 194–203.
[145] Şerbescu, A., Saalwächter, K. 2009. Particle-induced network formation in linear PDMS filled with silica. *Polymer* 50, 23, 5434–5442.
[146] Shahid, S., Nijmeijer, K. 2014. High pressure gas separation performance of mixed-matrix polymer membranes containing mesoporous Fe(BTC). *Journal of Membrane Science* 459, 33–44.
[147] Shimekit, B., Mukhtar, H., Murugesan, T. 2011. Prediction of the relative permeability of gases in mixed matrix membranes. *Journal of Membrane Science* 373, 1-2, 152–159.
[148] Shishatskii, A., Yampolskii, Y., Peinemann, K.-V. 1996. Effects of film thickness on density and gas permeation parameters of glassy polymers. *Journal of Membrane Science* 112, 275–285.
[149] Sircar, S., Rao, M., Thaeron, C. 1999. Selective Surface Flow Membrane for Gas Separation. *Separation Science and Technology* 34, 10, 2081–2093.
[150] Stern, S., Fang, S.-M. 1972. Effect of Pressure on Gas Permeability Coefficients. A new application of "Free Volume" Theory. *Journal of Polymer Science* 10, Part A-2, 201–219.
[151] Stern, S., Shah, J., Hardy, B. J. 1987. Structure-Permeability Relationships in Silicone Polymers. *Journal of Polymer Science: Part B: Polymer Physics* 25, Part B: Polymer, 1263–1298.
[152] Stoltenberg, D., Seidel-Morgenstern, A., Enke, D. 2011. Mesoporous glass membranes as model systems to study gas diffusion through porous media. *Chem. Eng. Technol.* 34, 5, 831–836.
[153] Sun, D., Li, B.-B., Xu, Z.-L. 2013. Pervaporation of ethanol/water mixture by organophilic nano-silica filled PDMS composite membranes. *Desalination* 322, 159–166.
[154] Tantekin-Ersolmaz, S., Atalay-Oral, C., Tather, M., Erdem-Senatalar, A., Schoeman, B., Sterte, J. 2000. Effect of zeolite particle size on the performance of polymer-zeolite mixed matrix membranes. *Journal of Membrane Science* 175, 2, 285–288.
[155] Tantekin-Ersolmaz, S., Senorkyan, L., Kalaonra, N., Tather, M., Erdem-Senatalar, A. 2001. n-Pentane/i-pentane separation by using zeolite-PDMS mixed matrix membranes. *Journal of Membrane Science* 189, 59–67.
[156] Tavman, I., Aydogdu, Y., Kök, M., Turgut, A., Ezan, A. 2011. Measurement of heat capacity and thermal conductivity of HDPE/expanded graphite nanocomposites by differential scanning calorimetry. *Archives of Materials Science* 50, 1, 56–60.
[157] U.S. Energy Administration. *Natural Gas Gross Withdrawals and Production*. https://www.eia.gov/dnav/ng/ng_sum_lsum_dcu_nus_m.html. Accessed 2015.
[158] U.S. Environmental Protection Agency, Ed. 1999. *Volatile Organic Compounds (VOC) Recovery Seminar*. U.S. Environmental Protection Agency, Washington, D.C.

[159] Übler, W. 2002. *Erhöhung der thermischen Leitfähigkeit elektrisch isolierender Polymerwerkstoffe*. Dissertation, Universität Erlangen-Nürnberg.

[160] Uhlhorn, R., Keizer, K., Burggraaf, A. 1992. Gas transport and separation with ceramic membranes. Part II. Synthesis and separation properties of microporous membranes. *Journal of Membrane Science* 66, 2-3, 271–287.

[161] Valero, M., Zornoza, B., Téllez, C., Coronas, J. 2013. Mixed matrix membranes for gas separation by combination of silica MCM-41 and MOF NH2-MIL-53(Al) in glassy polymers. *Microporous and Mesoporous Materials*.

[162] van Amerongen, G. 1955. The effect of fillers on the permeability of rubber to gases. *Rubbery Chemistry & Technology* 28, 3, 821–832.

[163] Vane, L. M., Namboodiri, V. V., Bowen, T. C. 2008. Hydrophobic zeolite–silicone rubber mixed matrix membranes for ethanol–water separation: Effect of zeolite and silicone component selection on pervaporation performance. *Journal of Membrane Science* 308, 1-2, 230–241.

[164] Weigelt, F., Georgopanos, P., Shishatskiy, S., Filiz, V., Brinkmann, T., Abetz, V. 2018. Development and Characterization of Defect-Free Matrimid® Mixed-Matrix Membranes Containing Activated Carbon Particles for Gas Separation. *Polymers* 10, 1, 51.

[165] Williams, P., Koros, W. 2008. Gas Separation by Carbon Membranes. In *Advanced membrane technology and applications*, N. N. Li, A. G. Fane, W. W. Ho and T. Matsuura, Eds. Wiley, Hoboken, N.J, 599–631.

[166] Willingham, C. 1939. Separation of hydrocarbons of high molecular weight by adsorption on silica gel. *Journal of Research of the National Bureou of Standards* 22, 321–327.

[167] Wohlrab, S., Meyer, T., Stöhr, M., Hecker, C., Lubenau, U., Oßmann, A. 2011. On the performance of customized MFI membranes for the separation of n-butane from methane. *Journal of Membrane Science* 369, 1-2, 96–104.

[168] Yampolskii, Y., Pinnau, I., Freeman, B. D., Eds. 2006. *Materials science of membranes for gas and vapor separation*. Wiley & Sons, Ltd., Chichester, England, Hoboken, NJ.

[169] Yave, W., Peinemann, K.-V., Shishatskiy, S., Khotimskiy, V., Chirkova, M., Matson, S., Litvinova, E., Lecerf, N. 2007. Synthesis, Characterization, and Membrane Properties of Poly(1-trimethylgermyl-1-propyne) and Its Nanocomposite with TiO 2. *Macromolecules* 40, 25, 8991–8998.

[170] Yave, W., Shishatskiy, S., Abetz, V., Matson, S., Litvinova, E., Khotimskiy, V., Peinemann, K.-V. 2007. A Novel Poly(4-methyl-2-pentyne)/TiO2 Hybrid Nanocomposite Membrane for Natural Gas Conditioning: Butane/Methane Separation. *Macromol. Chem. Phys.* 208, 22, 2412–2418.

[171] Yilmaz, L., Süer, M., Bac, N. 1994. Gas permeation characteristics of polymer-zeolite MMM. *Journal of Membrane Science* 91, 77–86.

[172] Zeolyst International. 2006. *Material safety data sheet. CBV780 Zeolite H-SDusy Powder*, Valley Forge, USA.

[173] Zhang, C., Zhang, K., Xu, L., Labreche, Y., Kraftschik, B., Koros, W. J. 2014. Highly scalable ZIF-based mixed-matrix hollow fiber membranes for advanced hydrocarbon separations. *AIChE J.* 60, 7, 2625–2635.

[174] Zimmerman, C., Singh, A., Koros, W. 1997. Tailoring mixed matrix composite membranes for gas separations. *Journal of Membrane Science* 137, 145–154.

[175] Zornoza, B., Téllez, C., Coronas, J., Gascon, J., Kapteijn, F. 2013. Metal organic framework based mixed matrix membranes: An increasingly important field of research with a large application potential. *Microporous and Mesoporous Materials* 166, 67–78.

[176] Zulhairun, A., Ismail, A. 2014. The role of layered silicate loadings and their dispersion states on the gas separation performance of mixed matrix membrane. *Journal of Membrane Science* 468, 20–30.

APPENDIX

A Thermodynamic Equations and Properties

Equation of State

Strong deviations from ideal gas behaviour are expected for the investigated hydrocarbon components resulting from intermolecular attractions and the additional volume of gas molecules. For hydrocarbon components, the equation of state by Soave, Redlich & Kwong (SRK) as given in equation (A-1) is highly recommended [132]. It is given in equation (A-1) with p as pressure, R as gas constant, T as temperature, V_m as molar volume. The parameters a(T) and b are functions of the critical properties (see Table A–1).

$$p = \frac{R \cdot T}{V_m - b} - \frac{a(T)}{V_m \cdot (V_m + b)} \qquad \text{(A-1)}$$

Thermodynamic Property Data

Table A–1: Thermodynamic Properties of Gas and Vapour Components (data from: [1] [132], [2] [56], [3] [124])

Component	Mw [1] g/mol	T_b [1] °C	T_{crit} [1] K	c_P [2] J/(mol K)	σ_{LJ} [1] Å	ω [3]	ρ (liq.)[1] kg/m³
N_2	28.013	- 195.8	126.2	29.1	3.798	0.037	0.805
O_2	31.999	- 183.0	154.6	29.4	3.467	n/a	1.149
CO_2	44.010	- 78.5	304.2	37.1	3.941	0.225	0.777
CH_4	16.043	- 161.5	190.6	35.7	3.758	0.011	0.425
C_2H_6	30.070	- 88.7	305.4	52.5	4.443	0.099	0.548
C_3H_8	44.097	- 42.1	369.8	73.6	5.118	0.152	0.582
n-C_4H_{10}	58.124	- 0.5	425.2	140.9 (liq.)	4.687	0.200	0.579
n-C_5H_{12}	72.151	36.0	469.6	167.2 (liq.)	5.784	0.252	0.626

Vapour Pressure Estimation

The vapour pressure p_s of gas and vapour components was estimated according to the Antoine equation in (A-2) and by means of the coefficients summarised in Table A–2.

$$\ln p_s = A - \frac{B}{C + T} \qquad \textbf{(A-2)}$$

Table A–2: Antoine coefficients for the estimation of vapour pressures [132]

Component	T_{min} K	T_{max} K	T_c K	p_c bar	A mm Hg	B -	C K
N_2	54.15	90.15	126.2	33.9	14.9542	588.72	-6.60
O_2	63.15	100.15	154.6	50.5	15.4075	734.55	-6.45
CO_2	154.15	204.15	304.2	73.8	22.5898	3103.39	-0.16
CH_4	93.15	120.15	190.6	45.99	15.2243	597.84	-7.16
C_2H_6	130.15	199.15	305.4	48.83	15.6637	1511.42	-17.16
C_3H_8	164.15	249.15	369.8	42.44	15.726	1872.46	-25.16
n-C_4H_{10}	195.15	290.15	425.2	37.99	15.6782	2154.9	-34.42
n-C_5H_{12}	220.15	330.15	469.6	34.14	15.8333	2477.07	-39.94

Thermodynamics of Adsorption

Adsorption resembles a surface condensation of gas molecules on a solid surface. The equilibrium state at constant temperature is given by the adsorption isotherm. According to IUPAC, adsorption isotherms are classified into six categories [71]. A variety of mathematical descriptions based on physical or empirical correlations is available. Typical equations are given in Table A–3.

Table A–3: Equations for most common adsorption isotherms [37, 69, 71]

Adsorption Isotherm	Equation	Comment
Langmuir	$q = \frac{q_{max} b p}{1 + (bp)}$	Type I isotherm for energetically homogeneous surfaces. No interaction between adsorbed molecules. At low pressure linear (Henry), at high pressure maximum loading due to saturation of adsorption sites. Derived from mass-action kinetics.
Linear	$q = K_H \cdot p$	Linear correlation similar to Henry. No saturation. For low sorbing components with maximum loading < 25 cm^3/g.
Freundlich	$q = K \cdot p^{1/m}$	Heterogeneous surfaces with non-uniform distribution of heat of adsorption. No saturation or Henry law limit. m = 1 – 5.
Sips	$q = \frac{q_{max} (b p)^{1/n}}{1 + (bp)^{1/n}}$	No Henry law limit but finite saturation.
Brunauer-Emmett-Teller (BET)	$q = \frac{q_{max} b}{1 + (b-1)p} \cdot \frac{p}{1-p}$	For energetically homogeneous surfaces, multilayer physisorption and condensation of vapours. First layer exhibits adsorption energy, additional layers only condensation energy.
Toth	$q = \frac{q_{max} b p}{\left[1 + (bp)^t\right]^{1/t}}$	For energetically heterogeneous surfaces, monolayer physisorption of supercritical fluids. With Henry law and finite saturation limit.

Denotation: p = pressure; q = number of adsorbed species; q_{max} = maximum number of absorbed species for monolayer coverage; $\theta = q/q_{max}$ = degree of surface coverage;
b = affinity constant (Langmuir parameter; measure for strength of binding energy);
K = pre-exponential factor (temperature-dependent); m = indicator for non-linearity (Freundlich parameter; temperature-dependent); n = indicator for system heterogeneity (Sips parameter; usually > 1); t = measure for surface heterogeneity (Toth parameter; usually < 1)

Equations for MMM Permeation Models

Table A–4: Overview of Predictive Models for Effective Permeability of Mixed Matrix Membranes

Model	Equation	Conditions
Maxwell	$P_{eff} = P_c \cdot \left[\frac{2\cdot(1-\varphi_d)+(1+2\varphi_d)\cdot(P_d/P_c)}{(2+\varphi_d)+(1-\varphi_d)\cdot(P_d/P_c)} \right]$	For ideal interfaces, spherical particles, low volume fraction of filler ($\varphi_d < 0.2$). Particle shape or size distribution not considered. Explicit equation, easy to solve.
Maxwell (simplified)	$P_{eff} = P_c \cdot \left[\frac{1-\varphi_d}{1+0.5\cdot\varphi_d} \right]$	Impermeable filler particles; no interactions between filler - polymer or filler - penetrant.
Maxwell (modified)	$P_{eff} = P_c \cdot \left[\frac{2\cdot(1-\varphi_d)+(1+2\varphi_d)\cdot(P_I/P_c)}{(2+\varphi_d)+(1-\varphi_d)\cdot(P_I/P_c)} \right]$ $P_I = \frac{2\cdot(1-\varphi_s)+(1+2\varphi_s)\cdot(P_d/P_I)}{(2+\varphi_s)+(1-\varphi_s)\cdot(P_d/P_I)}$	Accounts for the influence of interfacial layer. Only valid at low to moderate filler fractions. Does not account for particle size distribution, particle shape and aggregation.
Bruggeman	$\left(\frac{P_{eff}}{P_c}\right)^{1/3} \cdot \left(\frac{P_d - P_c}{P_d - P_{eff}}\right) = (1-\varphi_d)^{-1}$	For ideal interfaces. Broader range than Maxwell but packing limit, particle size and shape not considered. Needs to be solved numerically.
Lewis & Nielson	$P_{eff} = P_c \cdot \left[\frac{1+2\varphi_d\cdot((P_c/P_d-1)/(P_c/P_d+2))}{1-((P_c/P_d-1)/(P_c/P_d+2))\cdot\varphi_d\cdot\psi} \right]$ with $\psi = 1+\left(\frac{1-\varphi_{d,max}}{\varphi_{d,max}^2}\right)\cdot\varphi_d$	For ideal interfaces. Filler fractions up to φ_{max}. Particle size and shape included in φ_{max}. Reduces to Maxwell model for $\varphi_{max} = 1$ (spherical fillers). Explicit equation, easy to solve.
Pal	$\left(\frac{P_{eff}}{P_c}\right)^{1/3} \cdot \left(\frac{P_d - P_c}{P_d - P_{eff}}\right) = \left(1-\frac{\varphi_d}{\varphi_{d,max}}\right)^{-\varphi_{d,max}}$	For ideal interfaces. Filler fractions up to φ_{max}. Particle size and shape included in φ_{max}. Reduces to Bruggeman model for $\varphi_{max} = 1$. Needs to be solved numerically.
Felske	$P_{eff} = P_c \cdot \left[\frac{2(1-\varphi_d)+(1+2\varphi_d)\cdot(\gamma_2/\gamma_1)}{(2+\varphi_d)+(1-\varphi_d)\cdot(\gamma_2/\gamma_1)} \right]$ with $\gamma_1 = (1+2\cdot\delta_I^3)-(1-\delta_I^3)\cdot(P_d/P_I)$ $\gamma_2 = (2+\delta_I^3)\cdot(P_d/P_c)-2\cdot(1-\delta_I^3)\cdot(P_I/P_c)$	For non-ideal interfaces, particles assumed as coated spheres. $\gamma_{1,2}$ are functions of permeability of 3 phases and of ratio of interphase layer to core particle.
Felske (modified)	$P_{eff} = P_c \cdot \left[\frac{1+2\cdot((\gamma_2-\gamma_1)/(\gamma_2+2\gamma_1))\cdot\varphi_d}{1-((\gamma_2-\gamma_1)/(\gamma_2+2\gamma_1))\cdot\varphi_d\cdot\psi} \right]$	Model accounts for particle size distribution, shape and aggregation via $\varphi_{d,max}$ included in ψ.

Denotation: P_{eff} = effective permeability of MMM; P_c = permeability of continuous polymeric phase; P_d = permeability of dispersed filler phase; P_I = permeability of non-ideal interfacial layer; φ_d = volume fraction of filler; φ_s = volume fraction of shell particles (filler including interfacial layer); δ_I = thickness of non-ideal interfacial layer

B Membrane Materials & Production

Polymeric Matrix

Table B-1: Viscosity of coating solutions at 27 °C and constant shear rate of 10 1/s (measured with MCR 502 by Anton Paar and a Couette cylinder DG26.7)

Sample	POMS wt%	AC wt%	Viscosity mPa s
POMS-S	5	-	0.8
POMS-S	10	-	1.3
POMS-S	20	-	2.7
POMS-S	30	-	5.0
POMS-S	40	-	10.9
POMS-S	50	-	17.5
POMS-XL	20	-	1.5
POMS-XL	20	-	7.0
MMM-AC2	30	5	8.7
MMM-AC2	30	10	11.2
MMM-AC2	30	20	32.8
MMM-AC2	30	40	132.9

Inorganic Filler Materials

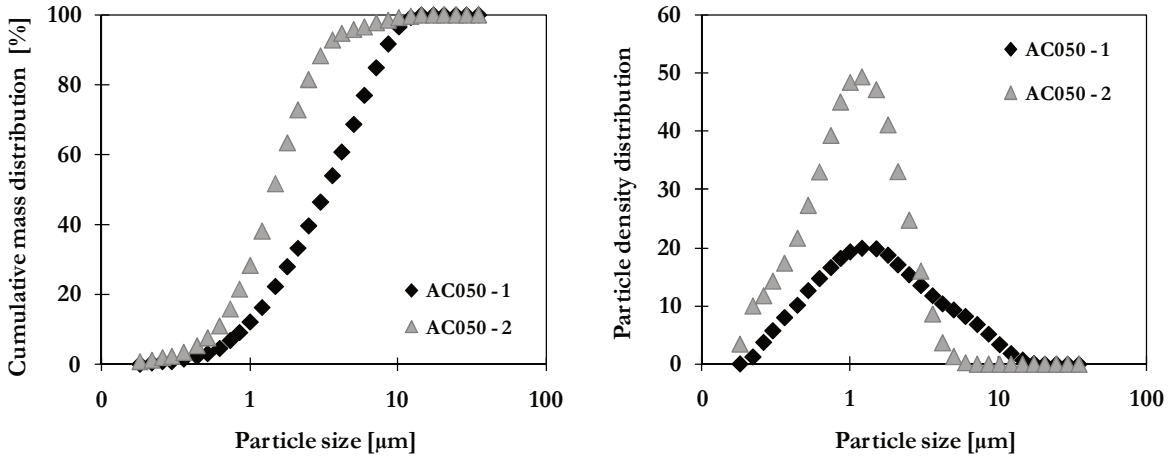

Figure B-1: Particle size distributions of AC050 sieving fractions with d_{50} = 3.5 µm (type 1, black symbols) or d_{50} = 1.5 µm (type 2, grey symbols)

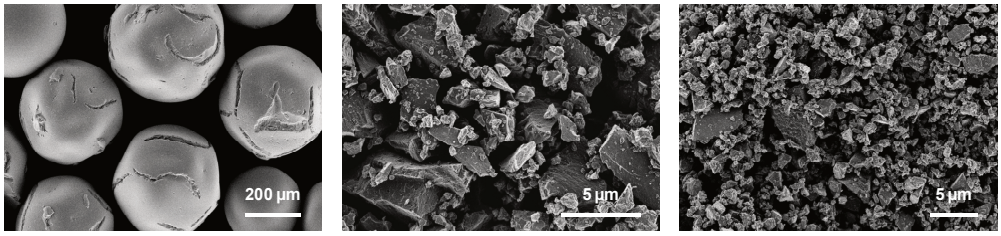

Figure B-2: SEM images of AC050 pellets (a) and sieving fractions with d_{50} = 3.5 µm (b) or d_{50} = 1.5 µm (c)

Solvents

Table B-2: Properties of applied solvents for pre-saturation of filler particles [56]

Solvent	**Formula**	**Mw** g/mol	**T_B** °C	**p_s (20°C)** bar	**ρ (20°C)** g/cm³	**Solubility in H_2O**	**$\delta^{1/2}$** $(MPa)^{1/2}$
Ethanol	C_2H_6O	46.07	78	0.058	0.79	Yes	26.2
Iso-propanol	C_3H_8O	60.10	82	0.043	0.78	Yes	23.5
Toluene	C_7H_8	92.14	111	0.029	0.87	No	18.3
Iso-octane	C_8H_{18}	114.23	99	0.052	0.69	No	14.3

[1] Hildebrandt Solubility Parameter

Membrane Production

Table B-3: Coating parameters for TFC membrane production with a roll coating machine

Parameter	**Specification**
Velocity roll	1.124 m/min or 5 – 9 U/min
Velocity support structure	0.4 – 0.46 m/min
Gap height	0.4 mm
Drying temperature	100 °C
Drying time	app. 5 min

Table B-4: Overview of prepared and investigated TFC membranes

Sample code	Support roll	GL	POMS [wt%]	Filler type	Filler [wt%]	Solvent for pre-saturation	Coated section [m]
POMS-20-S	R 12/023	no	20	none	-	-	136.0 - 140.8
POMS-20-S	R 11/020	no	20	none	-	-	125.8 – 139.5
POMS-30-S	R 11/020	no	30	none	-	-	94.4 – 101.6
POMS-30-S_GL	R 12/005	yes	30	none	-	-	62.1 – 69.0
POMS-20-XL_GL	R 13/012	yes	20	none	-	-	72.1 – 75.1
MMM-AC1_20_S(20)-E	R 10/023	no	20	AC050-1	20	Iso-octane	141.6 – 149.2
MMM-AC1_20_S(30)-E	R 11/020	no	30	AC050-1	20	Ethanol	69.6 – 75.1
MMM-AC1_10_S(30)-E_GL	R 12/005	yes	27	AC050-1	10	Ethanol	88.55 – 97.2
MMM-AC1_20_S(30)-E_GL	R 12/005	yes	28	AC050-1	20	Ethanol	50.4 – 56.8
MMM-AC1_40_S(30)-E_GL	R 12/005	yes	28	AC050-1	40	Ethanol	57.2 – 61.6
MMM-AC1_13_XL(25)-iO_Gl	R 13/005	yes	25	AC050-1	13	Iso-octane	130.1 – 134.8
MMM-AC1_13_XL(25)-E_GL	R 13/005	yes	25	AC050-1	13	Ethanol	135.0 – 138.6
MMM-AC1_20_XL(20)-iO_GL	R 13/003	yes	22	AC050-1	19	Iso-octane	213.7 – 218.1
MMM-AC1_20_XL(20)-E_GL	R 13/003	yes	22	AC050-1	19	Ethanol	210.0 – 213.6
MMM-AC1_20_XL(20)-T_GL	R 13/003	yes	22	AC050-1	19	Toluene	204.1 – 207.7
MMM-AC1_20_XL(20)-iP_GL	R 13/003	yes	22	AC050-1	19	Iso-propanol	200.5 – 203.9
MMM-AC1_15_XL(20)-E_GL	R 13/003	yes	22	AC050-1	15	Ethanol	196.7 – 193.0
MMM-AC1_25_XL(20)-E_GL	R 13/003	yes	22	AC050-1	25	Ethanol	192.9 – 189.0
MMM-AC1_20_XL(15)-iO_GL	R 13/017	yes	15	AC050-1	20	Iso-octane	109.7 – 230.8
MMM-AC1_20_XL(15)-iO_GL	R 13/018	yes	15	AC050-1	20	Iso-octane	47.3 – 112.3
MMM-AC2_10_S(30)-E_GL	R 12/005	yes	27	AC050-2	10	Ethanol	78.2 – 85.9
MMM-AC2_20_S(30)-E_GL	R 12/005	yes	27	AC050-2	20	Ethanol	72.7 – 77.7
MMM-AC2_40_S(30)-E_GL	R 12/005	yes	27	AC050-2	40	Ethanol	88.4 – 86.0
MMM-AC2_20_XL(7.5)-iO_Gl	R 13/003	yes	7.5	AC050-2	20	Iso-octane	153.5 – 156.9
MMM-AC2_20_XL(10)-iO_GL	R 13/003	yes	10	AC050-2	20	Iso-octane	157.5 – 160.8
MMM-AC2_20_XL(15)-iO_GL	R 13/003	yes	15	AC050-2	20	Iso-octane	161.5 – 163.9
MMM-AC2_20_XL(20)-iO_GL	R 13/003	yes	20	AC050-2	20	Iso-octane	166.5 – 169.3
MMM-AC2_20_XL(15)-iO_GL	R 13/017	yes	15	AC050-2	20	Iso-octane	3.0 – 109.0
MMM-AC2_20_XL(15)-iO_GL	R 13/018	yes	15	AC050-2	20	Iso-octane	113.4 – 227.5
MMM-AC3_20_XL(20)-iO_GL	R 13/012	yes	20	AC942	20	Iso-octane	68.6 – 72.0
MMM-AC4_20_XL(20)-iO_GL	R 13/012	yes	20	AC085	20	Iso-octane	64.0 – 67.1
MMM-Z_20_XL(20)-iO_GL	R 13/012	yes	20	Z	20	Iso-octane	51.5 – 53.9
MMM-CB_20_XL(20)-iO_GL	R 13/012	yes	20	CB	20	Iso-octane	56.4 – 59.8
MMM-AS_20_XL(20)-iO_GL	R 13/012	yes	20	AS	20	Iso-octane	54.0 – 56.4

Table B-5: Overview of thick film samples prepared via solution casting

Sample code	POMS content wt%	Filler type	Filler content wt%	Solvent for pre-saturation	Thickness µm	Density g/cm³
POMS-28	28	none	-	-	992	n.s.
POMS-30	30	none	-	-	794	0.962
POMS-33	33	none	-	-	1056	n.s.
MMM-18	33	AC050 -1	18	-	1284	n.s.
MMM-5-iO	32	AC050 -1	5.5	i-Octane	1287	n.s.
MMM-10-iO	35	AC050 -1	10	i-Octane	979	1.002
MMM-20-iO	31	AC050-1	18	i-Octane	n.s.	n.s.
MMM-24-iO	32	AC050 -1	24	i-Octane	1488	1.066
MMM-42-iO	30	AC050 -1	42	i-Octane	1116	1.119
MMM-57-iO	33	AC050 -1	57	i-Octane	1486	n.s.
MMM-20-E	31	AC050-1	20	Ethanol	868	n.s.
MMM-11-E	27	AC050-1	11	Ethanol	728	n.s.
MMM-18-E	31	AC050-1	18	Ethanol	n.s.	n.s.
MMM-22-E	36	AC050-1	22	Ethanol	885	n.s.
MMM-36-E	30	AC050-1	36	Ethanol	n.s.	n.s.
MMM-18-T	31	AC050-1	18	Toluene	n.s.	n.s.

C Testing Equipment

Pressure Increase Set-Up

A flow sheet of the pressure increase set-up used for single gas permeation measurements up to 1 bar is given in Figure C-1. Gas permeation leads to an increase of pressure in the permeate volume (p_P) and a decrease of pressure in feed vessel (p_F).

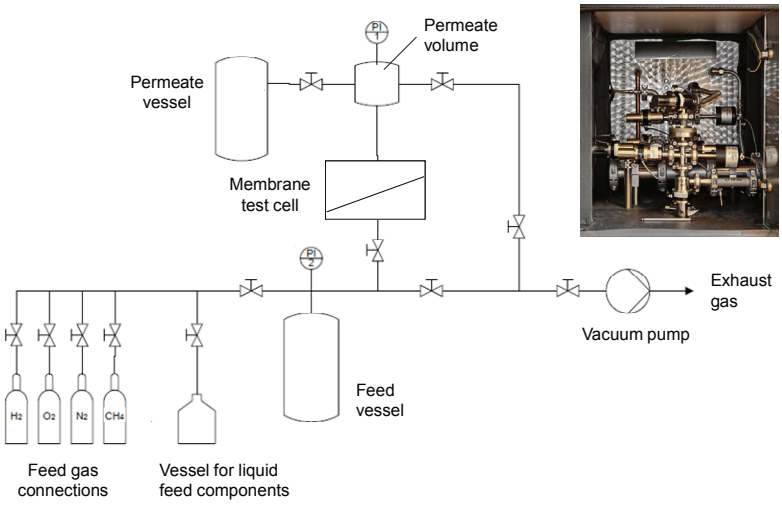

Figure C-1: Flow sheet of the pressure increase set-up for single gas measurements (p < 1 bar) [23]

Permeances were calculated from the time dependent change of pressure between feed (p_F) and permeate (p_P) according to equation (C-1) by means of the permeate flow rate $\dot{V}_P$, effective membrane area $A_{M,eff}$ and temperature T. A detailed description of the procedure and the determination of the free volume model parameters L_{i0}^{∞}, E_P, m_0 and m_T can be found elsewhere in literature [23, 75]. The effective membrane area was adjusted with a metal plate to values between 2.46 and 7.76 cm².

$$L_i = 8.07 \cdot 10^6 \cdot \frac{\dot{V}_P}{A_{M,eff} \cdot R \cdot T \cdot t} \cdot \ln\left(\frac{p_F - p_P(t_0)}{p_F - p_P(t)}\right) \quad \left[\frac{m^3}{m^2\ h\ bar}\right] \qquad \textbf{(C-1)}$$

Manual Set-Ups for Single Gas Permeation Measurements

The permeation of single gases was measured with manual set-ups depicted in Figure C-2 for N_2 / O_2 and in Figure C-3 for *n*-C_4H_{10} / CH_4 (p > 1 bar), respectively. Permeances were

calculated according to equation (C-2) by means of the permeate flow rate $\dot{V}_P$, effective membrane area $A_{M,eff}$, feed p_F and permeate p_P pressure. The effective membrane area was 36.32 cm² for measurements with N_2 / O_2 and 13.84 cm² for measurements with *n*-C_4H_{10} / CH_4, respectively.

$$L_i = \frac{\dot{V}_{P,i}}{A_{M,eff} \cdot (p_F - p_P)} \qquad \textbf{(C-2)}$$

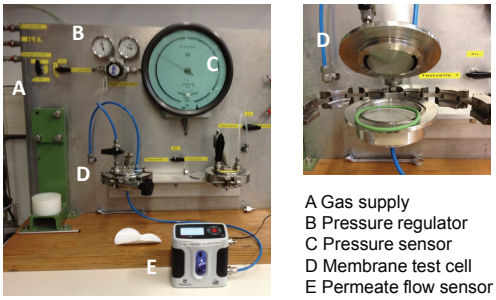

Figure C-2: Experimental set-up for single gas measurements N_2 / O_2 (p > 1 bar)

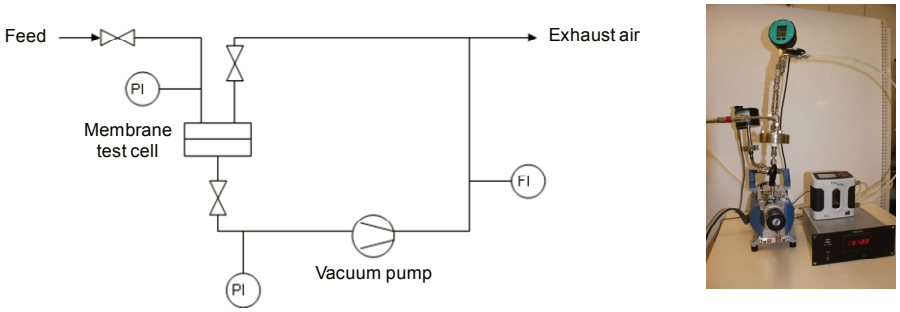

Figure C–3: Flow sheet and experimental set-up for single gas measurements *n*-C_4H_{10} / CH_4 (p > 1 bar)

Time-Lag Apparatus

A flow sheet of the time-lag apparatus used for the determination of diffusion coefficients and permeability is given in Figure C-4.

The effective diffusion coefficient $D_{eff,i}$ was calculated according to equation (C-3) by means of the time-lag θ and the thickness of the membrane film δ.

$$\theta = \frac{\delta^2}{6 \cdot D_{eff,i}} \qquad \textbf{(C-3)}$$

The permeability coefficient P_i was calculated according to equation (C-4) by means of the permeate volume flow rate $\dot{V}_P$, the thickness of the membrane film δ, the effective membrane

area $A_{M,eff}$ and the driving force in consequence of the pressure difference between feed p_F and permeate p_P pressure. The effective membrane area was 3.45 cm².

$$P_i = \frac{\dot{V}_{P,i} \cdot \delta}{A_{M,eff} \cdot (p_F - p_P)} \qquad \textbf{(C-4)}$$

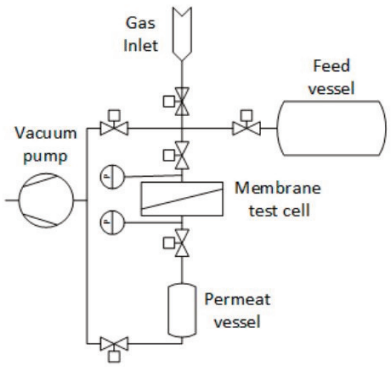

Figure C-4: Flow sheet of the time-lag apparatus [164]

Testing Facility for Mixed Gas Permeation Measurements

A detailed flow sheet of the testing facility for binary and multi-component gas mixtures is given in Figure C-5. Specifications of the components are listed in Table C-2. Permeances were calculated according to equation (C-5) by means of the permeate flow rate $\dot{V}_P$, the effective membrane area $A_{M,eff}$ and the fugacity on feed (f_F) and permeate side (f_P). The fugacity was calculated with the components partial pressures in feed and permeate and the fugacity coefficients φ_i according to the equation of state by Soave-Redlich-Kwong (see equation A-1).

$$L_i = \frac{\dot{V}_P \cdot y_{P,i}}{A_{M,eff} \cdot (f_{F,i} - f_{P,i})} \qquad \textbf{(C-5)}$$

Gas analysis was performed with a GC Varian 3400. The system was calibrated with pure gas components. Response factors, determined by normalized values of peak areas (average of at least 10 runs) to CH_4 as the reference component, are listed in Table C-1.

Table C-1: Response factors for the calibration of GC Varian 3400

Component	CO_2	CH_4	C_2H_6	C_3H_8	*n*-C_4H_{10}	*n*-C_5H_{12}
Rf binary mix	-	1.00000	-	-	1.15828	-
Rf multi-comp. mixture	0.70223	1.00000	0.63711	0.50044	0.40454	0.39393

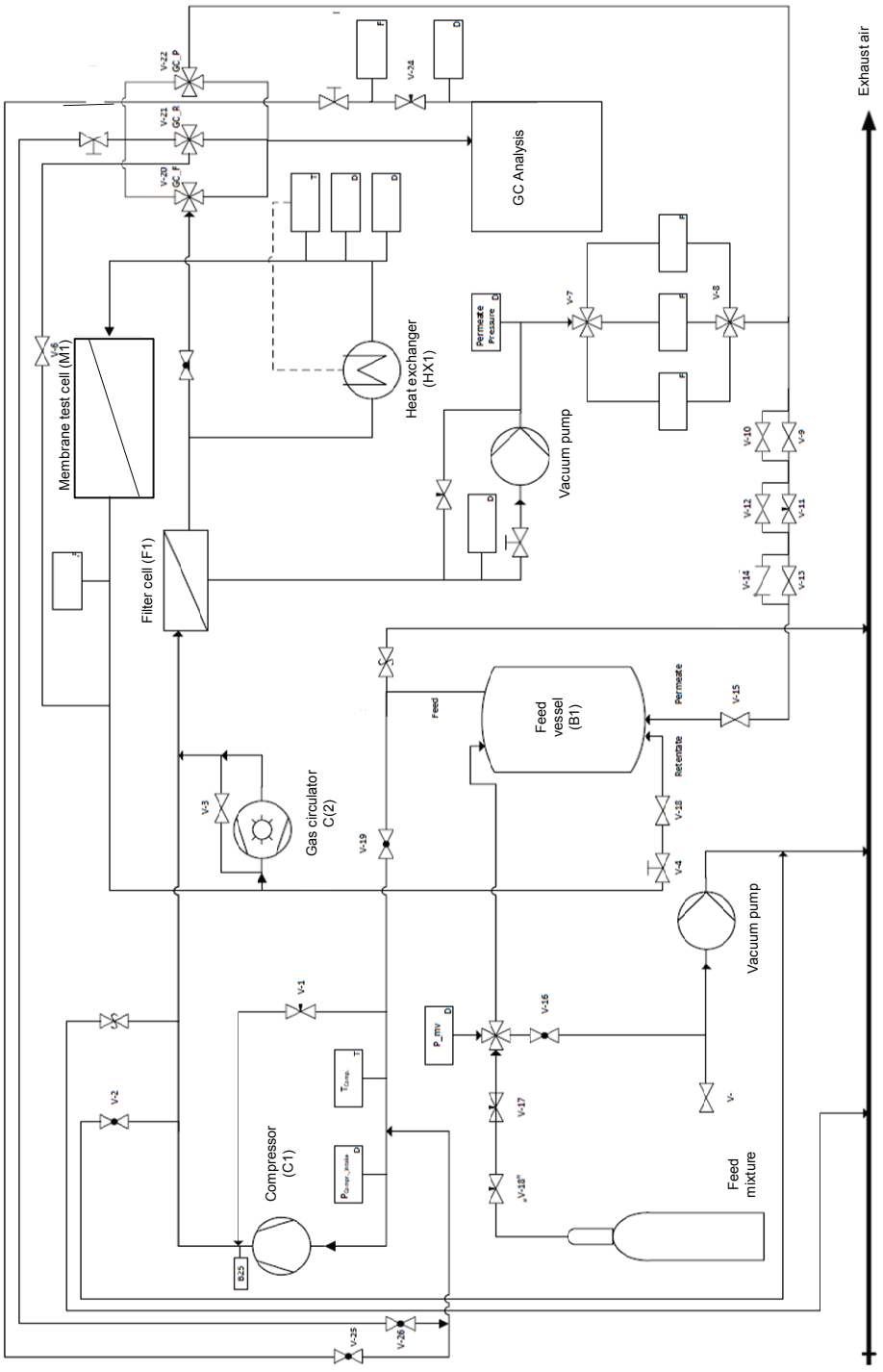

Figure C–5: Flow sheet of the testing facility for the permeation of binary and multi-component gas mixtures

Table C-2: Components of the testing facility for binary and multi-component mixtures

Component	Specifications
Membrane test cell	Stainless steel; diameter 47 mm; $A_{M,eff}$ = 0.001204 m²
Filter cell	Stainless steel, diameter 62 mm; equipped with non-woven TH 100 (Hirose Paper MFG Co., LTD, Japan)
Compressor	Haug, WTEG 60/30/16 L-ML; 3.6 kW; T_{max} = 40 °C, p_{max} = 10 / 60 bar (suction /discharge); $\dot{V}_{max}$ = 4 m³/h
Gas circulator	ASF Thomas Industries, TFK-M5 71500
Heat exchanger	Julabo, FP-45 MS
Pressure sensors Feed Permeate	Bronkhorst-Mättig Type P-512-EC, 1.2 – 60 bar Type P-501-EC, 0 – 5 bar
Flow sensors Feed Permeate	Bronkorst-Mättig Type F-113AC-HC-44-V, 40 m^3_N/h air Type F-101-D-HD-33-E; 0 – 1000 ml_N/min N_2 Type F-101-D-HC-33-V; 0 – 1 ml_N/min N_2 Type F-102-D-HC-33-V; 0 – 0.1 ml_N/min N_2 The equations and factors to convert the volume flow rates of the sensors calibrated with N_2 to the respective gas mixture are given in equation (C-9) and Table C−4, respectively.
Gas Analysis Column: Column Pressure: Column Temperature: Carrier Gas: Sample Injection: Detector:	Varian 3400 Chromosorb 107, packed metal, length 2m, diameter 1/8"; 18 psi (binary mixture) / 10 – 15 psi (multi-comp. mixture); 160 °C / 60 – 160 °C (rate 30 °C/min) (binary /multi-comp. mixture); Argon 4.6 /Helium 4.6 (binary / multi-comp. mixture); 1 µl, 120 °C TDC (200°C)

Testing Facility for Long-term Stability

A detailed flow sheet of the testing facility for long-term studies is presented in Figure C-6. Specifications of components are listed in Table C-3. Permeances were calculated according to equation (C-6) by means of the permeate flow rate $\dot{V}_P$, the effective membrane area $A_{M,eff}$, the feed (p_F) and permeate (p_P) pressure and the gas composition x_i. Fugacity coefficients φ_i were estimated according to the equation of state by Soave-Redlich-Kwong (see equation A-1).

$$L_i = \frac{\dot{V}_P \cdot x_{Pi}}{A_{M,eff} \cdot \left(p_F \cdot \varphi_{Fi} \cdot x_{Fi} - p_P \cdot \varphi_{Pi} \cdot x_{Pi}\right)} \quad \left[\frac{m^3}{m^2\ h\ bar}\right] \qquad \textbf{(C-6)}$$

Gas composition was analysed with a MTI Refinery Analyzer. The system was calibrated with N_2 (99.996 %, Linde AG) and *n*-C_5H_{12} (> 99%, Roth GmbH). Average values of peak areas of at

least 10 runs were used for calibration. Equations of calibration are given in (C-7) for N_2 and in (C-8) for *n*-C_5H_{12}.

$$x_{N2} = 0.7589 \cdot x + 0.2465 \quad \textbf{(C-7)}$$

$$x_{n-C5H12} = 0.7782 \cdot x^2 + 0.3806 \cdot x + 0.0028 \quad \textbf{(C-8)}$$

Table C-3: Components of the testing facility for long-term studies

Component	Specifications
Membrane test cell	Stainless steel; diameter 47 mm; $A_{M,eff}$ = 0.001134 m²
Filter cell	Stainless steel, diameter 62 mm; equipped with non-woven TH-100 and TH-80 (Hirose Paper MFG Co., LTD, Japan)
Mixing unit	Bronkhorst Hi-Tech, CEM type 7.01.410
Flow regulators	Bronkhorst-Mättig
Gas	Type F-201AC-FC-22-V
Liquid	T ype Liqui-Flow L1-FC-12-0
Gas circulator	ASF Thomas, type TFK-M5; controlled via frequcency converter
Heat exchanger	Julabo, type FP-45-HL (A_{eff} = 0.543 m²)
Temperature sensor	PT-100 in V2A stainless steel screws
Pressure sensors	
Cycle	Bronkhorst-Mättig, type P-512-EC, 1.2 – 60 bar
Permeate	Bronkhorst-Mättig, type P-501-EC, 0 – 5 bar
Retentate	Swagelok, analogous manometer, p_{max} = 100 bar
Flow sensors	
Cycle	Bronkorst-Mättig, type F-113AC-HC-44-V, 40 m^3_N/h air
Permeate	Bronkorst-Mättig, type F-101-D-HC-33-V; 1000 ml_N/min N_2
Bleed	Bronkorst-Mättig, type F-101-D-HC-33-V; 1000 ml_N/min N_2
GC	J&W Scientific, type ADM1000
	The equations and factors to convert the volume flow rates of the sensors calibrated with N_2 to the respective gas mixture are given in equation (C-9) and Table C−4, respectively.
Gas Analysis	MTI Refinery Analyzer; Software EZ Chrom
Columns:	Channel A: Molecular Sieve 13X / 5 Å (N_2) Channel B: PoraPlot Q /PoraPlot U Channel C: Al_2O_3 ; length 10 m, diameter 0.32 mm (*n*-C_5H_{12}) Channel D: OV-1
Column temperature:	A:90 °C, B: 100 °C; C: 80 °C; D: 90 °C
Column pressure:	A: 2.1 bar; B: 1.7 bar; C: 1.7 bar; D: 1.9 bar
Carrier gas:	A: Argon, 1 – 2 ml/min; B-D: Helium (purity 99.996 %), 0.7 – 2 ml/min
Sample time:	15 s
Detector:	TCD

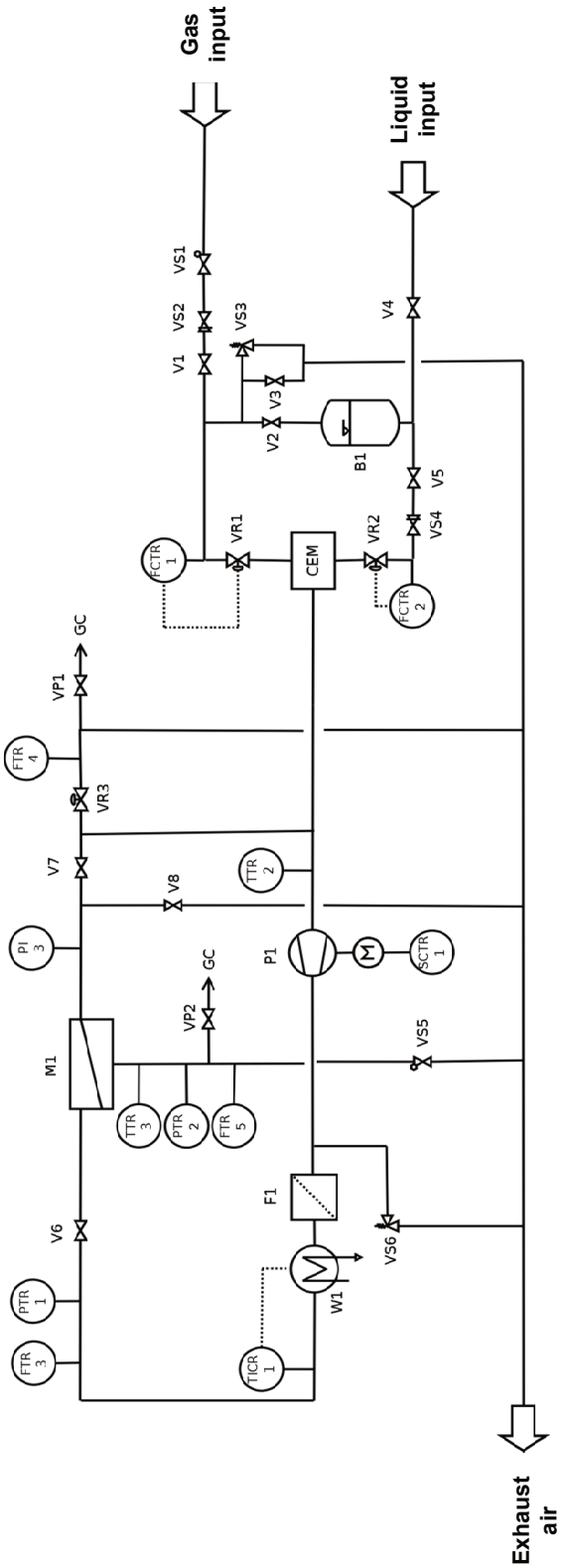

Figure C-6: Flow sheet of testing facility for long-term studies of separation performance

Gas Conversion Factors

The values of N_2 calibrated flow sensors were converted to gas mixture components using equation (C-9). The mixture conversion factor, equation (C-10), was calculated by means of volume fractions φ and gas conversion factors in Table C–4.

$$\dot{V}_{mix} = \dot{V}_{display} \cdot C_{corr,mix} \qquad \textbf{(C-9)}$$

$$\frac{1}{C_{corr,mix}} = \frac{\varphi_i}{C_{corr,i}} + \frac{\varphi_j}{C_{corr,j}} + \ldots + \frac{\varphi_n}{C_{corr,n}} \qquad \textbf{(C-10)}$$

Table C-4: Gas conversion factors [22]

Component	N_2	CO_2	CH_4	C_2H_6	C_3H_8	*n*-C_4H_{10}	*n*-C_5H_{12}
$\mathbf{C_{corr}}$	1.00	0.74	0.76	0.49	0.34	0.25	0.21

D Experimental Data

Single Gas Permeation Data

Table D-1: Single gas permeation data O_2 / N_2 for TFC membranes (mean values of n samples)

Sample code	n	ϑ	p_F	V_{N2}	V_{O2}	L_{N2}	L_{O2}	α
	[-]	[° C]	[bar]	[ml/min]		[m^3_N/(m² h bar)]		[-]
POMS-20-S	5	22.5	6.3	35.9	86.0	0.106	0.235	2.25
POMS-30-S	3	21.7	5.0	7.5	17.2	0.025	0.057	2.29
POMS-30-S_GL	17	19.6	5.1	21.0	48.5	0.062	0.142	2.30
POMS-20-XL_GL	8	21.5	5.1	18.4	41.9	0.059	0.135	2.28
MMM-AC1_20_S(20)-E	1	21.9	5.0	7.9	17.8	0.071	0.159	2.24
MMM-AC1_20_S(30)-E	2	24.8	5.1	3.6	8.0	0.012	0.026	2.28
MMM-AC1_10_S(30)-E_GL	7	20.5	5.0	29.5	68.2	0.042	0.097	2.30
MMM-AC1_20_S(30)-E_GL	7	21.2	5.0	21.9	37.3	0.023	0.054	2.29
MMM-AC1_40_S(30)-E_GL	5	18.0	5.1	12.6	29.6	0.009	0.021	2.40
MMM-AC1_20_XL(20)-iO_GL	4	20.7	5.8	9.9	23.1	0.033	0.077	2.33
MMM-AC1_20_XL(20)-E_GL	3	20.2	6.1	9.9	22.9	0.027	0.063	2.32
MMM-AC1_20_XL(20)-T_GL	1	20.5	5.2	9.5	21.9	0.031	0.072	2.32
MMM-AC1_20_XL(20)-iP_GL	1	19.9	6.1	8.8	20.3	0.029	0.067	2.32
MMM-AC2_10_S(30)-E_GL	3	19.9	5.0	6.5	15.0	0.021	0.049	2.31
MMM-AC2_20_S(30)-E_GL	3	22.2	5.1	6.7	15.2	0.022	0.050	2.27
MMM-AC2_40_S(30)-E_GL	2	18.0	5.1	11.2	11.9	0.037	0.039	1.07
MMM-AC2_20_XL(7.5)-iO_GL	6	19.1	5.1	41.9	86.9	0.1369	0.2850	2.12
MMM-AC2_20_XL(10)-iO_GL	4	20.4	5.1	14.7	33.7	0.0479	0.1104	2.30
MMM-AC2_20_XL(15)-iO_GL	11	20.6	5.0	11.05	25.2	0.0361	0.0830	2.30
MMM-AC2_20_XL(20)-iO_GL	5	18.7	5.1	6.8	15.6	0.022	0.051	2.31
MMM-AC3_20_XL(20)-iO_GL	3	19.6	5.0	10.4	23.7	0.0341	0.0782	2.29
MMM-AC4_20_XL(20)-iO_GL	4	20.7	5.1	8.1	18.5	0.0263	0.0604	2.30
MMM-Z_20_XL(20)-iO_GL	2	20.9	5.0	10.8	25.1	0.0354	0.0825	2.33
MMM-CB_20_XL(20)-iO_GL	3	19.1	5.1	13.9	31.8	0.0454	0.1030	2.27
MMM-AS_20_XL(20)-iO_GL	2	21.6	5.0	8.2	18.6	0.0269	0.0610	2.27

Table D-2: Single gas permeation data CH_4 / *n*-C_4H_{10} at 20 °C (pressure increase apparatus)

Sample	L_{CH4}	$L_{0,n\text{-}C4H10}$	P_{CH4}	$P_{n\text{-}C4H10}$	$\alpha_{CH4/n\text{-}C4H10}$
	[m^3_N/(m² h bar)]		[Barrer]		[-]
POMS-30-S_GL	0.20	3.16	283	4432	15.6
POMS-20-XL_GL	0.19	3.00	256	4070	15.9
MMM-AC1_10_S(30)-E_GL	0.19	2.74	417	6148	14.8
MMM-AC1_10_S(30)-E_GL	0.07	1.14	203	3246	16.0
MMM-AC1_10_S(30)-E_GL	0.03	0.39	138	2121	15.4
MMM-AC2_10_S(30)-E_GL	0.22	2.73	496	6082	12.3
MMM-AC2_10_S(30)-E_GL	0.09	1.16	249	3314	13.3
MMM-AC2_10_S(30)-E_GL	0.03	0.37	161	2028	12.6
MMM-AC1_20_XL(20)-iO_GL	0.11	1.47	224	3109	13.9
MMM-AC2_20_XL(15)-iO_GL	0.12	1.71			14.6
MMM-AC3_20_XL(20)-iO_GL	0.11	1.71	314	4817	15.3
MMM-AC4_20_XL(20)-iO_GL	0.10	1.60	297	4606	15.5
MMM-Z_20_XL(20)-iO_GL	0.11	1.84	257	4147	16.2
MMM-CB_20_XL(20)-iO_GL	0.14	2.35	280	4458	15.9
MMM-AS_20_XL(20)-iO_GL	0.09	1.43	281	4487	16.0

Table D-3: Single gas permeation data CH_4 / *n*-C_4H_{10} (pressure increase apparatus)

	POMS-30-S_GL				MMM-AC2_20_XL(15)-iO_GL			
ϑ	L_{CH4}	$L_{0,n\text{-}C4H10}$	$m_{n\text{-}C4H10}$	α	L_{CH4}	$L_{0,n\text{-}C4H10}$	$m_{n\text{-}C4H10}$	α
[° C]	[m^3_N/(m² h bar)]		[-]	[-]	[m^3_N/(m² h bar)]		[-]	[-]
20	0.20	3.16	1.78	15.6	0.12	1.71	1.93	14.6
30	0.24	3.12	1.16	12.9	0.13	1.65	1.27	12.3
50	0.32	2.91	0.51	9.1	0.18	1.57	0.60	8.8
70	0.40	2.64	0.26	6.6	0.23	1.46	0.31	6.5

Mixed Gas Permation Data n-C_4H_{10} / CH_4

Table D-4: Mixed gas permeation data CH_4 / *n*-C_4H_{10} for POMS membranes (mean values of n samples)

ϑ	y_F, *n*-C_4H_{10}	p_F	p_P	f_m *n*-C_4H_{10}	f_m CH_4	L CH_4	L *n*-C_4H_{10}	P CH_4	P *n*-C_4H_{10}	α CH_4/*n*-C_4H_{10}
° C	-	bar	bar	bar	bar	$m^3_N/(m^2\ h\ bar)$		Barrer		-
POMS-20-S (R10/023; n = 3)										
25	0.05	10.5	1.15	0.34	5.56	0.51	9.01	190	3393	17.8
25	0.05	19.9	1.43	0.53	9.87	0.64	12.52	242	4714	19.4
25	0.05	29.3	1.48	0.61	14.36	0.72	13.72	272	5167	19.0
25	0.05	39.5	1.44	0.63	19.01	0.79	15.31	299	5763	19.3
POMS-30-S (R11/020; n = 2)										
30	0.05	10.7	1.12	0.65	5.22	0.04	0.75	69	1190	17.3
30	0.05	20.2	1.25	0.81	9.69	0.05	1.09	87	1748	20.1
30	0.05	30.3	1.39	0.97	14.27	0.06	1.34	101	2135	21.2
30	0.05	40.6	1.50	1.09	18.75	0.07	1.61	116	2570	22.1
POMS-30_GL (R12/005; n = 4)										
30	0.05	10.6	1.21	0.35	5.45	0.33	5.45	401	6700	16.6
30	0.05	19.9	1.41	0.54	9.73	0.40	7.37	496	9076	18.2
30	0.05	29.8	1.58	0.66	14.17	0.48	8.68	596	10694	18.1
30	0.05	38.9	1.54	0.69	18.12	0.55	9.62	672	11849	17.9
POMS-20-XL_GL (R13/012; n = 2)										
22	0.05	10.3	1.23	0.31	5.31	0.28	5.54	353	7071	20.0
22	0.05	20.0	1.27	0.48	9.70	0.38	9.16	484	11689	24.2
22	0.05	29.9	1.54	0.62	14.16	0.46	11.84	581	15106	26.0
22	0.05	39.8	1.58	0.68	18.37	0.54	14.59	686	18613	27.2

Table D-5: Mixed gas permeation data CH_4 / *n*-C_4H_{10} for TFC MMM (mean values of n samples)

ϑ	$y_{F,}$ *n*-C_4H_{10}	p_F	p_P	f_m *n*-C_4H_{10}	f_m CH_4	L CH_4	L *n*-C_4H_{10}	P CH_4	P *n*-C_4H_{10}	α CH_4/*n*-C_4H_{10}
° C	-	bar	bar	bar	bar	$m^3_N/(m^2\ h\ bar)$		Barrer		-
MMM-AC1_20_S(20) (R10/023; n = 2)										
25	0.05	10.5	0.94	0.33	5.28	0.31	5.04	285	4676	16.5
25	0.05	19.8	1.38	0.53	9.64	0.38	6.99	353	6488	18.4
25	0.05	30.1	1.49	0.64	14.22	0.44	8.62	412	8001	19.5
25	0.05	39.4	1.37	0.63	18.26	0.47	8.90	435	8263	19.0
MMM-AC3_20_S(20) (R10/023; n = 2)										
25	0.05	10.2	1.00	0.32	5.15	0.35	5.91	189	3155	16.7
25	0.05	19.8	1.34	0.53	9.62	0.45	8.41	242	4489	18.5
25	0.05	30.3	1.41	0.63	14.31	0.53	10.18	283	5431	19.2
25	0.05	40.1	1.39	0.64	18.55	0.57	11.20	302	5979	19.8
MMM-AC1_20_S(30) (R11/020; n = 2)										
30	0.05	10.7	1.15	0.39	5.41	0.01	0.26	29	517	18.0
30	0.05	20.3	1.34	0.61	9.77	0.02	0.38	36	742	20.8
30	0.05	31.0	1.35	0.74	14.49	0.03	0.53	58	1034	17.7
30	0.05	40.3	1.36	0.79	18.50	0.04	0.62	79	1220	15.4
MMM-AC1_10_S(30)-E_GL (R12/005; n = 2)										
30	0.05	10.5	1.15	0.31	5.15	0.18	2.45	413	5486	13.0
30	0.05	20.5	1.33	0.51	9.79	0.23	3.72	525	8324	15.7
30	0.05	30.0	1.46	0.62	14.03	0.28	4.73	619	10589	17.0
30	0.05	40.1	1.49	0.68	18.43	0.32	5.37	712	12034	16.9
MMM-AC1_20_S(30)-E_GL (R12/005; n = 3)										
30	0.05	11.0	1.12	0.38	5.56	0.09	1.58	250	4528	18.1
30	0.05	20.6	1.31	0.59	9.93	0.11	2.13	304	6073	20.0
30	0.05	30.4	1.50	0.74	14.31	0.13	2.70	358	7714	21.6
30	0.05	40.7	1.56	0.80	18.77	0.15	3.13	432	8937	20.7
MMM-AC1_40_S(30)-E_GL (R12/005; n = 3)										
30	0.05	10.7	1.13	0.30	4.81	0.04	0.49	237	2679	11.4
30	0.05	20.8	1.31	0.47	9.84	0.06	0.63	347	3450	10.5
30	0.05	30.3	1.42	0.61	13.95	0.07	0.93	390	5131	13.2
30	0.05	40.4	1.47	0.73	18.60	0.06	1.12	322	6142	19.3

Table D-5 (continued): Mixed gas permeation data CH_4 / *n*-C_4H_{10} for TFC MMM

ϑ	$y_{F,}$ *n*-C_4H_{10}	p_F	p_P	f_m *n*-C_4H_{10}	f_m CH_4	L CH_4	L *n*-C_4H_{10}	P CH_4	P *n*-C_4H_{10}	α CH_4/*n*-C_4H_{10}
° C	-	bar	bar	bar	bar	$m^3_N/(m^2\ h\ bar)$		Barrer		-
MMM-AC2_10_S(30)-E_GL (R12/005; n = 2)										
30	0.05	10.3	1.15	0.34	5.29	0.11	2.00	454	8147	18.0
30	0.05	20.2	1.48	0.52	9.90	0.17	2.00	677	8130	13.4
30	0.05	29.7	1.62	0.69	14.09	0.17	3.14	691	12791	18.7
30	0.05	40.0	1.51	0.74	18.54	0.19	4.05	758	16493	21.7
MMM-AC2_20_S(30)-E_GL (R12/005; n = 2)										
30	0.05	10.6	1.10	0.36	5.39	0.12	1.95	542	8909	16.6
30	0.05	19.4	1.46	0.53	9.50	0.15	2.08	694	9509	13.4
30	0.05	30.1	1.56	0.72	14.24	0.17	3.34	757	15247	20.2
30	0.05	40.3	1.54	0.78	18.63	0.19	3.83	882	17518	20.0
MMM-AC1_15_XL(20)-E_GL (R13/003; n = 2)										
21	0.05	10.2	1.22	0.40	5.19	0.17	4.25	367	9360	25.6
21	0.05	20.2	1.51	0.64	9.76	0.2	6.96	530	15340	28.7
21	0.05	30.8	1.56	0.73	14.49	0.30	8.79	660	19365	28.6
21	0.05	38.9	1.55	0.72	18.29	0.30	7.15	656	15767	20.5
MMM-AC1_20_XL(20)-E_GL (R13/003; n = 2)										
22	0.05	10.5	1.25	0.38	5.30	0.12	2.88	262	6446	24.1
22	0.05	19.2	1.32	0.60	9.91	0.16	4.60	350	10313	29.0
22	0.05	29.9	1.50	0.72	14.15	0.20	6.16	445	13794	30.8
22	0.05	40.1	1.25	0.75	18.43	0.22	6.20	501	13887	27.3
MMM-AC1_25_XL(20)-E_GL (R13/003; n = 2)										
22	0.05	10.3	1.18	0.36	5.24	0.09	1.98	275	6437	23.2
22	0.05	20.3	1.51	0.60	9.83	0.11	3.37	369	10961	30.1
22	0.05	30.0	1.60	0.73	14.10	0.14	4.53	470	14724	31.6
22	0.05	40.3	1.52	0.78	18.45	0.17	5.18	542	16834	30.5
MMM-AC1_20_XL(20)-iO_GL (R13/003; n = 2)										
20	0.05	10.5	1.25	0.39	5.33	0.14	4.45	299	9479	32.4
20	0.05	20.8	1.32	0.57	10.02	0.19	5.72	399	12193	30.7
20	0.05	30.1	1.50	0.68	14.13	0.24	7.62	511	16239	31.8
20	0.05	41.2	1.25	0.66	18.88	0.25	6.96	541	14824	27.5

Table D-5 (continued): Mixed gas permeation data CH_4 / *n*-C_4H_{10} for TFC MMM

ϑ	y_F, *n*-C_4H_{10}	p_F	p_P	f_m *n*-C_4H_{10}	f_m CH_4	L CH_4	L *n*-C_4H_{10}	P CH_4	P *n*-C_4H_{10}	α CH_4/*n*-C_4H_{10}
° C	-	bar	bar	bar	bar	$m^3_N/(m^2\ h\ bar)$		Barrer		-
MMM-AC1_20_XL(20)-T_GL (R13/003; n = 2)										
20	0.05	10.1	1.31	0.36	5.23	0.15	3.61	24.8	278	6942
20	0.05	19.7	1.60	0.59	9.64	0.20	5.82	29.2	380	10917
20	0.05	30.1	1.48	0.67	14.16	0.25	7.65	31.0	471	13858
20	0.05	40.5	1.49	0.72	18.57	0.28	8.64	30.3	544	15852
MMM-AC1_20_XL(20)-iP_GL (R13/003; n = 2)										
20	0.05	10.3	1.29	0.37	5.32	0.31	3.26	24.3	300	7066
20	0.05	20.1	1.62	0.59	9.78	0.18	5.45	29.8	408	12011
20	0.05	30.3	1.60	0.69	14.27	0.23	7.20	31.5	510	15880
20	0.05	39.7	1.65	0.73	18.29	0.25	1.15	30.0	569	17652
MMM-AC2_20_XL(20)-iO_GL (R13/003; n = 2)										
20	0.05	10.6	1.30	0.38	5.41	0.11	2.66	313	7907	25.3
20	0.05	20.3	1.51	0.59	9.82	0.14	4.50	428	13361	31.2
20	0.05	30.2	1.58	0.71	14.16	0.18	5.99	541	17786	32.9
20	0.05	40.4	1.52	0.76	18.49	0.20	6.00	596	17822	29.8
MMM-AC2_20_XL(15)-iO_GL (R13/003; n = 2)										
20	0.05	10.1	1.26	0.36	5.20	0.17	4.13	284	6999	24.7
20	0.05	20.4	1.63	0.60	9.95	0.23	6.89	398	11677	29.3
20	0.05	30.2	1.62	0.70	14.20	0.29	8.81	489	14941	30.5
20	0.05	39.9	1.59	0.71	18.38	0.32	9.20	540	15598	28.9
MMM-AC2_20_XL(10)-iO_GL (R13/003; n = 2)										
20	0.05	10.4	1.27	0.37	5.36	0.28	6.74	293	6926	23.7
20	0.05	20.2	1.57	0.58	9.82	0.40	10.77	411	11059	26.9
20	0.05	30.1	1.57	0.63	14.23	0.51	13.04	524	13394	25.7
20	0.05	40.1	1.59	0.66	18.54	0.55	12.66	562	13005	23.3
MMM-AC2_20_XL(7.5)-iO_GL (R13/003; n = 2)										
20	0.05	10.3	1.39	0.36	5.35	0.45	9.98	962	21257	22.1
20	0.05	20.1	1.57	0.54	9.83	0.62	14.94	1315	31840	24.2
20	0.05	30.2	1.59	0.57	14.34	0.71	16.39	1511	34915	23.1
20	0.05	40.3	1.41	0.59	18.64	0.80	17.25	1701	36751	21.5

Table D-5 (continued): Mixed gas permeation data CH_4 / *n*-C_4H_{10} for TFC MMM

ϑ	y_F, *n*-C_4H_{10}	p_F	p_P	f_m *n*-C_4H_{10}	f_m CH_4	L CH_4	L *n*-C_4H_{10}	P CH_4	P *n*-C_4H_{10}	α CH_4/*n*-C_4H_{10}
° C	-	bar	bar	bar	bar	$m^3_N/(m^2\ h\ bar)$		Barrer		-
MMM-AC1_20_XL(15)-iO_GL (R13/017; n = 3)										
20	0.05	10.2	1.22	0.43	5.17	0.13	3.51	284	7434	26.2
20	0.05	19.7	1.62	0.70	9.49	0.20	6.52	425	13802	32.5
20	0.05	29.9	1.62	0.81	13.93	0.26	8.34	558	17651	31.5
20	0.05	40.2	1.52	0.75	18.42	0.28	12.44	599	26323	43.6
MMM-AC1_20_XL(15)-iO_GL (R13/018; n = 3)										
20	0.05	10.2	1.36	0.46	5.20	0.12	3.40	299	8231	27.6
20	0.05	20.1	1.58	0.72	9.62	0.18	5.73	440	13882	31.6
20	0.05	29.9	1.62	0.85	13.91	0.24	7.96	574	19280	33.6
20	0.05	40.3	1.58	0.86	18.31	0.26	8.85	637	21435	33.7
MMM-AC2_20_XL(15)-iO_GL (R13/017; n = 9)										
20	0.05	10.2	1.24	0.39	5.18	0.16	4.08	230	5741	25.1
20	0.05	20.1	1.46	0.62	9.72	0.25	7.48	351	10527	30.0
20	0.05	30.2	1.54	0.72	14.15	0.31	9.83	437	13835	31.6
20	0.05	39.7	1.57	0.74	18.26	0.36	10.88	502	15310	30.5
MMM-AC2_20_XL(15)-iO_GL (R13/018; n = 2)										
20	0.05	10.2	1.23	0.44	5.15	0.26	6.38	369	9019	24.9
20	0.05	20.0	1.62	0.71	9.64	0.40	11.41	566	16133	29.2
20	0.05	30.0	1.62	0.78	14.03	0.48	14.24	679	20138	30.4
20	0.05	40.3	1.63	0.81	18.44	0.52	15.14	732	21418	29.7
MMM-AC3_20_XL(20)-iO_GL (R13/012; n = 2)										
20	0.05	10.4	1.27	0.32	5.40	0.16	3.38	447	9530	21.3
20	0.05	19.8	1.27	0.48	9.64	0.20	5.00	568	14089	24.8
20	0.05	29.8	1.55	0.63	14.07	0.25	6.80	710	19166	27.0
20	0.05	39.6	1.58	0.69	18.24	0.30	8.15	844	22960	27.2
MMM-AC4_20_XL(20)-iO_GL (R13/012; n = 2)										
20	0.05	10.5	1.26	0.32	5.41	0.12	2.59	339	7465	22.0
20	0.05	20.3	1.26	0.49	9.83	0.15	3.79	436	10937	25.1
20	0.05	30.2	1.50	0.63	14.22	0.19	5.12	537	14791	27.6
20	0.05	40.2	1.60	0.71	18.50	0.22	6.12	645	17669	27.4

Table D-5 (continued): Mixed gas permeation data CH_4 / *n*-C_4H_{10} for TFC MMM

ϑ	y_F, *n*-C_4H_{10}	p_F	p_P	f_m *n*-C_4H_{10}	f_m CH_4	L CH_4	L *n*-C_4H_{10}	P CH_4	P *n*-C_4H_{10}	α CH_4/*n*-C_4H_{10}
° C	-	bar	bar	bar	bar	$m^3_N/(m^2\ h\ bar)$		Barrer		-
MMM-Z_20_XL(20)-iO_GL (R13/012; n = 2)										
20	0.05	10.9	1.25	0.33	5.60	0.18	4.19	404	9458	23.4
20	0.05	20.0	1.26	0.49	9.71	0.23	5.60	510	12655	24.8
20	0.05	29.8	1.47	0.62	14.08	0.28	7.79	633	17590	27.8
20	0.05	39.8	1.59	0.71	18.32	0.33	9.31	741	21025	28.4
MMM-CB_20_XL(20)-iO_GL (R13/012; n = 2)										
20	0.05	10.5	1.26	0.30	5.41	0.21	4.49	402	8514	21.2
20	0.05	19.7	1.25	0.48	9.55	0.27	6.57	522	12459	23.9
20	0.05	29.7	1.52	0.67	13.99	0.35	8.54	660	16201	24.6
20	0.05	39.6	1.54	0.69	24.57	0.40	11.07	768	20991	27.3
MMM-AS_20_XL(20)-iO_GL (R13/012; n = 2)										
20	0.05	10.2	1.24	0.32	5.28	0.13	2.88	408	9ß48	22.1
20	0.05	20.0	1.29	0.49	9.72	0.17	4.38	525	13770	26.2
20	0.05	30.0	1.54	0.64	14.18	0.21	5.96	661	18733	28.4
20	0.05	39.7	1.56	0.70	18.29	0.25	7.20	771	22644	29.4

Table D-6: Mixed gas permeation data CH_4 / *n*-C_4H_{10} for POMS-30_GL (mean values for n samples)

ϑ	y_F, *n*-C_4H_{10}	p_F	p_P	f_m *n*-C_4H_{10}	f_m CH_4	L CH_4	L *n*-C_4H_{10}	P CH_4	P *n*-C_4H_{10}	α CH_4/*n*-C_4H_{10}
° C	-	bar	bar	bar	bar	$m^3_N/(m^2\ h\ bar)$		Barrer		-
Variation feed pressure at 20 °C (n = 7)										
20	0.05	10.2	1.18	0.33	5.21	0.30	6.78	371	8356	22.6
20	0.05	19.9	1.29	0.51	9.68	0.40	10.26	498	12633	25.4
20	0.05	30.0	1.46	0.62	14.16	0.49	13.22	607	16287	26.8
20	0.05	39.9	1.53	0.68	18.42	0.57	14.80	701	18225	26.1
20	0.05	10.2	1.18	0.33	5.21	0.30	6.78	371	8356	22.6
Variation feed pressure at 30 °C (n = 4)										
30	0.05	10.6	1.21	0.35	5.45	0.33	5.45	401	6700	16.6
30	0.05	19.9	1.41	0.54	9.73	0.40	7.37	496	9076	18.2
30	0.05	29.8	1.58	0.66	14.17	0.48	8.68	596	10694	18.1
30	0.05	38.9	1.54	0.69	18.12	0.55	9.62	672	11849	17.9

Table D-6 (continued): Mixed gas permeation data CH_4 / *n*-C_4H_{10} for POMS-30_GL

ϑ	$y_{F,}$ *n*-C_4H_{10}	p_F	p_P	f_m *n*-C_4H_{10}	f_m CH_4	L CH_4	L *n*-C_4H_{10}	P CH_4	P *n*-C_4H_{10}	α CH_4/*n*-C_4H_{10}
° C	-	bar	bar	bar	bar	$m^3_N/(m^2\ h\ bar)$		Barrer		-
Variation feed pressure at 35 °C (n = 3)										
35	0.05	10.5	1.14	0.35	5.36	0.33	5.03	402	6195	15.4
35	0.05	20.0	1.49	0.57	9.79	0.40	6.60	491	8123	16.6
35	0.05	30.0	1.50	0.67	14.25	0.46	7.59	561	9352	16.7
35	0.05	40.6	1.54	0.70	18.96	0.49	8.14	607	10029	16.6
Variation feed composition at different feed pressure (n = 3)										
20	0.05	10.2	1.18	0.33	5.21	0.30	6.78	371	8356	22.6
20	0.05	19.9	1.29	0.51	9.68	0.40	10.26	498	12633	25.4
20	0.05	30.0	1.46	0.62	14.16	0.49	13.22	607	16287	26.8
20	0.05	39.9	1.53	0.68	18.42	0.57	14.80	701	18225	22.6
20	0.02	10.1	1.18	0.16	5.37	0.26	5.25	316	6466	20.5
20	0.02	20.1	1.19	0.25	9.98	0.31	6.80	379	8380	22.1
20	0.02	30.1	1.44	0.32	14.55	0.36	8.30	442	10207	23.1
20	0.02	40.1	1.75	0.38	19.00	0.42	9.94	513	12248	24.0
20	0.01	10.1	1.21	0.08	5.47	0.22	4.20	266	5177	19.4
20	0.01	20.1	1.23	0.12	10.17	0.24	5.24	300	6448	21.5
20	0.01	30.1	1.46	0.16	14.78	0.27	6.13	334	7554	22.6
20	0.01	40.0	1.73	0.18	19.26	0.30	6.76	375	8325	22.2
Variation temperature at 10 bar (n = 3)										
20	0.05	10.1	1.19	0.36	5.16	0.31	7.05	383	8685	22.8
30	0.05	10.4	1.22	0.37	5.32	0.34	5.55	414	6836	16.6
35	0.05	10.5	1.16	0.37	5.33	0.33	5.16	408	6356	15.6
Variation temperature at 30 bar (n = 3)										
20	0.05	30.0	1.46	0.62	14.16	0.49	13.22	607	16287	26.8
30	0.05	29.8	1.58	0.66	14.17	0.48	8.68	596	10694	18.1
35	0.05	30.0	1.50	0.67	14.25	0.46	7.59	561	9352	16.7
Variation permeate pressure (n = 3)										
20	0.05	10.0	1.19	0.38	5.10	0.31	7.31	394	9013	22.9
20	0.05	10.1	0.05	0.19	4.76	0.23	4.92	281	6060	21.6
20	0.05	10.1	0.10	0.20	4.77	0.23	5.01	285	6174	21.6
20	0.05	10.1	0.25	0.23	4.82	0.24	5.34	291	6575	22.6
20	0.05	10.1	0.50	0.27	4.90	0.24	5.87	299	7228	24.2
20	0.05	10.1	0.75	0.29	5.00	0.25	6.44	305	7933	26.0
20	0.05	10.1	1.05	0.31	5.15	0.26	6.95	315	8566	27.2

Table D-6 (continued): Mixed gas permeation data CH_4 / *n*-C_4H_{10} for POMS-30_GL

ϑ	y_F, *n*-C_4H_{10}	p_F	p_P	f_m *n*-C_4H_{10}	f_m CH_4	L CH_4	L *n*-C_4H_{10}	P CH_4	P *n*-C_4H_{10}	α CH_4/*n*-C_4H_{10}
° C	-	bar	bar	bar	bar	$m^3_N/(m^2\ h\ bar)$		Barrer		-
Variation permeate pressure (n = 3)										
20	0.05	20.0	0.05	0.32	9.29	0.31	7.34	379	9035	23.8
20	0.05	20.0	0.10	0.33	9.30	0.31	7.49	386	9230	23.9
20	0.05	20.1	0.25	0.36	9.36	0.32	7.90	392	9736	24.8
20	0.05	20.1	0.50	0.41	9.43	0.34	8.85	414	10897	26.3
20	0.05	20.0	0.75	0.44	9.50	0.35	9.57	427	11787	27.6
20	0.05	20.0	1.10	0.48	9.63	0.37	10.92	451	13446	29.8
20	0.05	30.5	0.09	0.44	13.86	0.40	9.37	491	11540	23.5
20	0.05	30.4	0.10	0.43	13.85	0.40	9.87	490	12153	24.8
20	0.05	30.2	0.25	0.46	13.78	0.41	10.32	500	12705	25.4
20	0.05	30.1	0.50	0.50	13.83	0.43	11.34	524	13973	26.7
20	0.05	30.0	0.75	0.55	13.89	0.44	12.21	542	15038	27.8
20	0.05	30.0	1.00	0.58	13.96	0.45	13.36	557	16454	29.5

Table D-7: Mixed gas permeation data CH_4 / *n*-C_4H_{10} for MMM-2_20_XL(15)-iO_GL (mean values for n samples)

ϑ	y_F, *n*-C_4H_{10}	p_F	p_P	f_m *n*-C_4H_{10}	f_m CH_4	L CH_4	L *n*-C_4H_{10}	P CH_4	P *n*-C_4H_{10}	α CH_4/*n*-C_4H_{10}
° C	-	bar	bar	bar	bar	$m^3_N/(m^2\ h\ bar)$		Barrer		-
Variation feed pressure at 20 °C (n = 9)										
20	0.05	10.2	1.24	0.39	5.18	0.16	4.08	230	5741	25.1
20	0.05	20.1	1.46	0.62	9.72	0.25	7.48	351	10527	30.0
20	0.05	30.2	1.54	0.72	14.15	0.31	9.83	437	13835	31.6
20	0.05	39.7	1.57	0.74	18.26	0.36	10.88	502	15310	30.5
Variation feed composition at different feed pressure (n = 3)										
20	0.05	10.2	1.24	0.39	5.18	0.16	4.08	230	5741	25.1
20	0.05	20.1	1.46	0.62	9.72	0.25	7.48	351	10527	30.0
20	0.05	30.2	1.54	0.72	14.15	0.31	9.83	437	13835	31.6
20	0.05	39.7	1.57	0.74	18.26	0.36	10.88	502	15310	30.5
20	0.02	10.2	1.09	0.16	5.35	0.14	2.93	204	4126	20.2
20	0.02	20.1	1.14	0.25	9.98	0.17	3.91	246	5508	22.4
20	0.02	30.1	1.41	0.33	14.55	0.20	4.91	287	6915	24.1
20	0.02	40.1	1.57	0.37	18.92	0.24	5.86	331	8249	24.9

Table D-7 (continued): Mixed gas permeation data CH_4 / *n*-C_4H_{10} for MMM-2_20_XL(15)-iO_GL

ϑ	$y_{F,}$ *n*-C_4H_{10}	p_F	p_P	f_m *n*-C_4H_{10}	f_m CH_4	L CH_4	L *n*-C_4H_{10}	P CH_4	P *n*-C_4H_{10}	α CH_4/*n*-C_4H_{10}
° C	-	bar	bar	bar	bar	$m^3_N/(m^2\ h\ bar)$		Barrer		-
Variation feed composition at different feed pressure (n = 3)										
20	0.01	10.1	1.13	0.08	5.43	0.13	2.70	189	3800	20.1
20	0.01	20.1	1.21	0.12	10.16	0.15	3.32	215	4672	21.7
20	0.01	30.1	1.45	0.16	14.78	0.17	3.83	243	5385	22.2
20	0.01	40.1	1.79	0.19	19.32	0.19	4.46	272	6278	23.1
Variation temperature (n = 2)										
15	0.05	10.2	1.30	0.38	5.26	0.16	5.02	229	7060	30.9
20	0.05	10.3	1.30	0.38	5.29	0.16	4.12	226	5800	25.7
26	0.05	10.4	1.30	0.38	5.36	0.16	3.32	225	4675	20.8
31	0.05	10.6	1.30	0.37	5.44	0.16	2.97	227	4184	18.4
35	0.05	10.7	1.31	0.37	5.50	0.17	2.67	233	3761	16.2
16	0.05	19.7	1.43	0.57	9.53	0.24	8.94	345	12586	36.5
20	0.05	20.1	1.42	0.58	9.70	0.23	6.92	326	9750	29.9
26	0.05	20.1	1.42	0.57	9.74	0.21	5.31	299	7472	25.0
30	0.05	20.3	1.42	0.58	9.88	0.21	4.39	294	6178	21.1
35	0.05	20.6	1.42	0.58	10.02	0.21	3.68	291	5174	17.8
Variation temperature (n = 2)										
16	0.05	30.7	1.54	0.70	14.34	0.33	12.01	464	16894	36.4
20	0.05	30.7	1.54	0.69	14.42	0.29	9.19	410	12931	31.6
25	0.05	30.1	1.54	0.70	14.18	0.26	7.09	370	9975	27.0
30	0.05	30.4	1.54	0.70	14.37	0.24	5.69	344	8011	23.3
35	0.05	30.7	1.54	0.71	14.54	0.24	4.66	332	6563	19.8
Variation permeate pressure (n = 3 - 4)										
20	0.05	10.1	0.05	0.21	4.76	0.14	3.00	193	4228	22.0
20	0.05	10.1	0.10	0.23	4.77	0.13	2.96	189	4167	22.1
20	0.05	10.1	0.25	0.26	4.81	0.14	3.12	192	4394	22.8
20	0.05	10.3	0.50	0.30	4.98	0.14	3.42	199	4811	24.2
20	0.05	10.1	0.75	0.32	4.98	0.11	2.63	149	3696	24.9
20	0.05	10.4	1.00	0.35	5.20	0.10	2.59	142	3643	25.5
20	0.05	10.3	1.47	0.37	5.39	0.14	3.57	198	5025	25.6
20	0.05	20.1	0.05	0.36	9.29	0.17	4.08	244	5743	23.6
20	0.05	20.2	0.10	0.37	9.32	0.18	4.19	247	5898	23.8
20	0.05	20.2	0.25	0.39	9.36	0.18	4.64	250	6531	26.1
20	0.05	20.2	0.50	0.43	9.45	0.18	4.62	252	6501	25.8
20	0.05	20.2	0.75	0.48	9.54	0.19	4.87	260	6856	26.4

Table D-7 (continued): Mixed gas permeation data CH_4 / *n*-C_4H_{10} for MMM-2_20_XL(15)-iO_GL

ϑ	$y_{F,}$ *n*-C_4H_{10}	p_F	p_P	f_m *n*-C_4H_{10}	f_m CH_4	L CH_4	L *n*-C_4H_{10}	P CH_4	P *n*-C_4H_{10}	α CH_4/*n*-C_4H_{10}
° C	-	bar	bar	bar	bar	$m^3_N/(m^2\ h\ bar)$		Barrer		-
Variation permeate pressure (n = 3 - 4)										
20	0.05	20.2	1.00	0.53	9.60	0.20	5.69	282	8011	28.4
20	0.05	20.1	1.30	0.58	9.67	0.22	6.68	309	9402	30.5
20	0.05	20.0	1.50	0.60	9.69	0.23	6.93	318	9756	30.7
20	0.05	30.3	0.06	0.47	13.70	0.24	5.95	333	8377	25.1
20	0.05	30.3	0.10	0.47	13.73	0.24	5.93	331	8346	25.3
20	0.05	30.0	0.25	0.50	13.63	0.24	6.22	337	8750	26.0
20	0.05	30.0	0.50	0.54	13.72	0.25	6.94	346	9766	28.3
20	0.05	30.1	0.75	0.58	13.85	0.24	7.40	344	10408	30.3
20	0.05	30.3	1.00	0.65	14.00	0.26	7.54	367	10606	38.9
20	0.05	30.0	1.29	0.66	14.00	0.26	8.49	371	11941	32.2
20	0.05	30.3	1.53	0.67	14.27	0.27	9.25	379	13022	34.4

Mixed Gas Permeation Data n-C_5H_{12} / N_2

Table D-8: Long-term stability of permeation N_2 / *n*-C_5H_{12} at 20 °C and 30 bar

t	$y_{F,}$ *n*-C_5H_{12}	L N_2	L *n*-C_5H_{12}	α N_2/*n*-C_5H_{12}	t	$y_{F,}$ *n*-C_5H_{12}	L N_2	L *n*-C_5H_{12}	α N_2/*n*-C_5H_{12}
d	mol %	$m^3_N/(m^2\ h\ bar)$		–	d	mol %	$m^3_N/(m^2\ h\ bar)$		–
POMS-30-S_GL (R12/005; sample 67.0 m)					*POMS-30-S_GL (R12/005; sample 77.1 m)*				
0	1.29	0.118	10.58	89.4	0	1.25	0.100	10.21	102.1
10	1.26	0.115	10.46	90.8	10	1.30	0.099	9.23	93.2
15	1.32	0.117	10.59	90.9	53	1.23	0.098	9.71	99.0
50	1.27	0.115	10.15	88.3	55	1.23	0.097	9.53	98.7
55	1.26	0.114	9.97	87.5	64	1.25	0.096	9.30	96.7
MMM-AC1_20_XL(20)_GL (R13/003; sample 214.6 m)					*MMM-AC1_20_XL(20)_GL (R13/003; sample 216.05 m)*				
0	1.56	0.063	9.23	146.5	0	1.42	0.066	8.02	120.8
10	1.46	0.060	9.86	164.3	7.5	1.39	0.065	8.45	129.1
15	1.50	0.058	7.86	135.5	8	1.44	0.066	8.24	124.7
20	1.44	0.057	8.84	155.1	8.2	1.41	0.064	7.89	123.6
35	1.53	0.060	7.09	119.2					
37	1.43	0.059	7.47	126.6					

Table D-8 (continued): Long-term stability of permeation N_2 / *n*-C_5H_{12} at 20 °C and 30 bar

T	$y_{F,}$ *n*-C_5H_{12}	L N_2	L *n*-C_5H_{12}	α N_2/*n*-C_5H_{12}	t	$y_{F,}$ *n*-C_5H_{12}	L N_2	L *n*-C_5H_{12}	α N_2/*n*-C_5H_{12}
D	mol %	$m^3_N/(m^2$ h bar)		–	d	mol %	$m^3_N/(m^2$ h bar)		–
MMM-AC2_20_XL(15)_GL (R13/017; sample 44.6 m)					*MMM-AC2_20_XL(15)_GL (R13/017; sample 99.9 m)*				
0	1.51	0.069	10.10	147.0	0	1.40	0.078	8.33	106.5
10	1.53	0.067	11.11	165.5	8	1.40	0.076	8.05	106.2
15	1.56	0.072	12.81	177.4	49	1.34	0.071	8.66	122.2
20	1.56	0.071	10.16	144.1	50	1.47	0.078	10.01	128.4
35	1.56	0.067	9.58	142.6	52	1.59	0.086	11.18	130.0
42	1.51	0.066	9.97	151.5					
92	1.55	0.066	8.93	135.4					
99	1.57	0.066	9.04	137.9					
105	1.57	0.066	8.88	135.2					

Table D-9: Mixed gas permeation data N_2 / *n*-C_5H_{12} at 20 °C and 30 bar

$y_{F,}$ *n*-C_5H_{12}	$x_{P,}$ *n*-C_5H_{12}	V_p	f_m *n*-C_5H_{12}	f_m N_2	L N_2	L *n*-C_5H_{12}	α N_2/*n*-C_5H_{12}
mol %	mol %	m^3/h	bar	bar	$m^3_N/(m^2$ h bar)		–
POMS-30-S_GL (R12/005, sample 67.0 m)							
1.29	0.21	0.0052	0.26	15.61	0.117	10.57	90.66
1.05	0.16	0.0041	0.21	15,80	0.096	6.63	69.17
0.71	0.09	0.0031	0.14	16.32	0.077	3.11	40.29
0.42	0.03	0.0022	0.07	15.81	0.064	0.84	13.15
0.52	0.05	0.0024	0.09	15.61	0.068	1.45	21.25
1.07	0.16	0.0040	0.21	15.67	0.096	6.58	68.63
1.26	0.21	0.0052	0.26	15.83	0.114	10.06	87.96
1.32	0.22	0.0048	0.26	15.16	0.111	10.54	95.17
POMS-30-S_GL (R12/005, sample 77.1 m)							
1.26	0.21	0.0044	0.26	15.73	0.100	9.93	99.7
0.99	0.15	0.0035	0.19	15.14	0.086	6.28	73.4
0.86	0.13	0.0030	0.17	16.09	0.072	4.29	60.0
0.69	0.09	0.0025	0.13	15.90	0.064	2.62	40.8
0.91	0.14	0.0032	0.18	16.27	0.076	4.96	65.4
1.12	0.18	0.0039	0.23	15.92	0.090	7.73	86.0
1.24	0.21	0.0045	0.26	16.19	0.097	9.42	97.4

Table D-9 (continued): Mixed gas permeation data N_2 / *n*-C_5H_{12} at 20 °C and 30 bar

y_F, *n*-C_5H_{12}	x_P, *n*-C_5H_{12}	V_p	f_m *n*-C_5H_{12}	f_m N_2	L N_2	L *n*-C_5H_{12}	α N_2/*n*-C_5H_{12}
mol %	mol %	m³/h	bar	bar	$m^3_N/(m^2\ h\ bar)$		–
MMM-AC1_20_XL(20)-iO_GL (R13/003, sample 216.05 m)							
1.40	0.25	0.0032	0.30	16.18	0.066	8.25	125.7
1.14	0.20	0.0024	0.24	16.08	0.053	5.31	101.0
0.95	0.15	0.0019	0.19	15.89	0.045	3.33	74.7
0.75	0.10	0.0015	0.14	15.47	0.039	1.94	49.7
0.51	0.05	0.0013	0.09	15.91	0.034	0.78	23.1
0.41	0.03	0.0011	0.07	16.32	0.031	0.41	13.4
0.50	0.05	0.0012	0.09	16.39	0.033	0.72	21.8
0.74	0.10	0.0016	0.14	16.37	0.039	1.82	46.8
0.93	0.15	0.0019	0.19	16.34	0.045	3.21	71.6
1.02	0.17	0.0021	0.21	16.43	0.048	3.96	83.3
1.14	0.20	0.0024	0.24	16.22	0.052	5.06	97.3
1.23	0.21	0.0026	0.26	16.20	0.056	5.92	105.7
1.42	0.25	0.0031	0.30	15.96	0.065	8.05	124.0
MMM-AC2_20_XL(15)-iO_GL (R13/017, sample 99.9 m)							
1.41	0.24	0.0035	0.29	15.65	0.077	8.09	105.3
1.13	0.18	0.0026	0.23	15.86	0.059	5.25	88.7
0.95	0.14	0.0022	0.19	16.11	0.052	3.38	65.1
0.74	0.10	0.0017	0.14	16.01	0.044	1.95	44.7
0.52	0.05	0.0014	0.09	16.05	0.037	0.80	21.9
0.41	0.03	0.0012	0.07	15.96	0.034	0.44	13.0
0.28	0.00	0.0010	0.04	15.87	0.030	0.04	1.38
0.43	0.03	0.0012	0.07	15,76	0.034	0.50	14.8
0.51	0.05	0.0013	0.09	16.05	0.036	0.82	23.0
0.79	0.10	0.0015	0.14	14.15	0.042	1.96	46.3
0.93	0.14	0.0020	0.19	15.72	0.049	3.46	70.3
1.14	0.19	0.0025	0.23	15.66	0.058	5.32	92.6
1.34	0.24	0.0034	0.29	16.24	0.071	8.66	122.1
1.47	0.26	0.0038	0.31	16.01	0.078	10.01	128.4
1.59	0.28	0.0042	0.34	15.88	0.086	11.18	130.6

Table D-9 (continued): Mixed gas permeation data N_2 / *n*-C_5H_{12} at 20 °C and 30 bar

y_F, *n*-C_5H_{12}	x_P, *n*-C_5H_{12}	V_p	f_m *n*-C_5H_{12}	f_m N_2	L N_2	L *n*-C_5H_{12}	α N_2/*n*-C_5H_{12}
mol %	mol %	m³/h	bar	bar	$m^3_N/(m^2\ h\ bar)$		–
MMM-AC2_20_XL(15)-iO_GL (R13/017, sample 44.6 m)							
1.75	0.278	0.0031	0.31	14.52	0.069	10.76	10.76
1.25	0.22	0.0023	0.26	15.36	0.052	6.43	6.43
1.07	0.18	0.0018	0.21	14.80	0.044	4.22	4.22
0.85	0.12	0.0014	0.16	14.94	0.036	2.26	2.26
0.57	0.06	0.0010	0.10	15.70	0.029	0.79	0.79
0.46	0.04	0.0009	0.08	15.72	0.027	0.46	0.46
0.56	0.06	0.0010	0.10	15.19	0.028	0.78	0.78
0.89	0.13	0.0015	0.18	15.97	0.036	2.20	2.20
1.11	0.18	0.0018	0.23	15.65	0.042	3.68	3.68
1.34	0.23	0.0023	0.27	15.48	0.051	5.64	5.64
1.57	0.28	0.0032	0.33	15.67	0.066	8.86	8.86

Mixed Gas Permeation Data Multi-component Mixture

Table D-10: Permeation data for the multi-component mixture (mixture composition given in Table 6–11)

ϑ	p_F	p_P	f_m *n*-C_4H_{10}	L CO_2	L CH_4	L C_2H_6	L C_3H_8	L *n*-C_4H_{10}	L *n*-C_5H_{12}	α CH_4/*n*-C_4H_{10}
° C	bar	bar	bar	$m^3_N/(m^2\ h\ bar)$						-
POMS(n = 2)										
20	10.1	1.42	0.18	1.00	0.31	1.11	2.52	7.44	39.65	23.7
20	20.0	1.43	0.26	1.40	0.46	1.74	4.17	12.48	51.12	27.3
20	30.1	1.53	0.31	1.79	0.63	2.38	5.84	17.38	64.96	27.8
20	40.1	1.84	0.35	2.23	0.83	3.16	7.93	23.75	90.65	28.9
MMM (n = 3)										
20	10.1	1.41	0.36	0.63	0.19	0.70	1.58	4.74	32.27	24.4
20	20.1	1.43	0.57	0.92	0.30	1.15	2.79	8.64	46.5	28.8
20	30.1	1.52	0.72	1.20	0.41	1.64	4.14	12.95	60.97	31.5
20	40.1	1.77	0.84	1.54	0.57	2.25	5.80	18.28	91.4	32.4

SEM Analysis

Table D-11: Thickness of the active separation layers of TFC membranes

Sample code	Support roll	Thickness [μm]
POMS-20-S	R 12/023	1.03
POMS-20-S	R 11/020	1.55
POMS-30-S	R 11/020	4.36
POMS-30-S_GL	R 12/005	3.37
POMS-20-XL_GL	R 13/012	3.49
MMM-AC1_20_S(20)-E	R 10/023	2.54
MMM-AC1_20_S(30)-E	R 11/020	5.35
MMM-AC1_10_S(30)-E_GL	R 12/005	6.13
MMM-AC1_20_S(30)-E_GL	R 12/005	7.82
MMM-AC1_40_S(30)-E_GL	R 12/005	15.07
MMM-AC1_13_XL(25)-iO_Gl	R 13/005	3.67
MMM-AC1_13_XL(25)-E_GL	R 13/005	4.02
MMM-AC1_20_XL(20)-iO_GL	R 13/003	5.83
MMM-AC1_20_XL(20)-E_GL	R 13/003	6.13
MMM-AC1_20_XL(20)-T_GL	R 13/003	5.22
MMM-AC1_20_XL(20)-iP_GL	R 13/003	6.11
MMM-AC1_20_XL(20)-iO_GL	R 13/017 / R 13/018	5.79 / 6.63
MMM-AC2_10_S(30)-E_GL	R 12/005	11.13
MMM-AC2_20_S(30)-E_GL	R 12/005	12.50
MMM-AC2_40_S(30)-E_GL	R 12/005	48.60
MMM-AC2_20_XL(7.5)-iO_Gl	R 13/003	2.00
MMM-AC2_20_XL(10)-iO_GL	R 13/003	2.81
MMM-AC2_20_XL(15)-iO_GL	R 13/017 / R 13/018	3.85 / 3.87
MMM-AC2_20_XL(20)-iO_GL	R 13/003	8.13
MMM-AC3_20_XL(20)-iO_GL	R 13/012	7.71
MMM-AC4_20_XL(20)-iO_GL	R 13/012	7.90
MMM-Z_20_XL(20)-iO_GL	R 13/012	6.18
MMM-CB_20_XL(20)-iO_GL	R 13/012	5.19
MMM-AS_20_XL(20)-iO_GL	R 13/012	8.60

Sorption Data

Table D-12: Sorption data for *n*-C_4H_{10} in POMS (thick film) at 20 °C, 30 °C and 50 °C

ϑ	p	m_{ads}	q	ϑ	p	m_{ads}	q	ϑ	p	m_{ads}	q
° C	bar	mg/g	mmol/g	° C	bar	mg/g	mmol/g	° C	bar	mg/g	mmol/g
20.5	0.03	0.00	0.00	28.9	0.33	0.00	0.00	49.1	0.03	0.00	0.00
20.1	0.09	4.24	0.07	28.9	0.45	7.64	0.13	48.9	0.11	2.27	0.04
20.1	0.23	15.99	0.28	28.9	0.68	24.73	0.43	49.0	0.29	8.34	0.14
20.0	0.33	27.77	0.48	28.9	0.86	39.72	0.68	49.0	0.41	12.41	0.21
20.1	0.38	30.71	0.53	28.9	1.18	73.80	1.27	49.0	0.50	15.58	0.27
20.1	0.39	34.09	0.59	28.9	1.33	91.90	1.58	49.0	0.51	16.01	0.28
20.1	0.58	51.85	0.89	29.0	1.54	118.31	2.04	49.0	0.74	24.81	0.43
20.1	0.73	69.39	1.19	28.9	1.74	155.90	2.68	49.0	0.90	30.85	0.53
20.1	0.87	88.75	1.53					49.0	1.02	36.21	0.62
20.1	0.97	104.65	1.80					49.0	1.03	36.63	0.63
20.1	1.16	145.55	2.50					49.0	1.23	45.75	0.79
20.0	1.32	186.36	3.21					49.0	1.39	53.20	0.92
20.0	1.45	229.17	3.94					49.0	1.50	58.35	1.00
20.0	1.57	286.48	4.93					49.0	1.63	65.61	1.13
20.0	1.72	374.75	6.45					49.0	1.79	74.05	1.27
20.0	1.85	510.74	8.79					49.0	2.01	86.45	1.49
								49.0	2.17	96.75	1.66

Table D-13: Sorption data for CH_4 in POMS (thick film) at 20 °C, 30 °C and 50 °C

ϑ	p	m_{ads}	q	ϑ	p	m_{ads}	q	ϑ	p	m_{ads}	q
° C	bar	mg/g	mmol/g	° C	bar	mg/g	mmol/g	° C	bar	mg/g	mmol/g
20.0	0.03	0.00	0.00	30.1	0.00	0.00	0.00	50.4	0.03	0.00	0.00
20.1	0.13	0.10	0.01	30.1	0.09	0.00	0.00	52.5	0.09	0.04	0.00
20.1	1.37	0.38	0.02	30.1	0.20	0.01	0.00	50.6	0.20	0.06	0.00
20.1	3.00	0.82	0.05	30.0	0.30	0.04	0.00	50.2	0.40	0.12	0.01
20.0	3.52	0.97	0.06	30.0	0.40	0.08	0.01	50.0	0.60	0.13	0.01
20.0	3.99	1.12	0.07	30.0	0.50	0.09	0.01	50.0	1.03	0.22	0.01
20.1	4.49	1.28	0.08	30.0	0.59	0.13	0.01	50.0	1.52	0.36	0.02
				30.1	0.70	0.13	0.01	50.0	2.99	0.58	0.04
				30.1	0.82	0.16	0.01	50.0	5.00	1.24	0.08
				30.0	0.91	0.19	0.01	50.0	9.98	1.94	0.12
				30.0	1.00	0.22	0.01				
				30.1	1.26	0.29	0.02				
				30.0	1.51	0.34	0.02				
				30.0	2.00	0.49	0.03				
				30.0	4.97	1.19	0.07				
				30.0	10.03	2.49	0.16				

Table D-14: Sorption coefficients and solubility selectivity for POMS and PDMS (thick films)

ϑ	S^{∞} CH_4	S^{∞} *n*-C_4H_{10}	Solubility	Δ H_s CH_4	Δ H_s *n*-C_4H_{10}
° C	$cm^3/(cm^3$ bar)		**selectivity**	kJ/mol	kJ/mol
POMS				-7.35	-39.61
20	0.45	60.21	134.3		
30	0.38	31.26	82.2		
50	0.33	12.86	38.5		
PDMS				-7.98	-76.36
20	0.44	27.16	62.5		
30	0.42	17.94	43.0		
50	0.35	3.75	10.8		

Table D-15: Sorption data of MMM detached separation layers at 30 °C

MMM 20 wt% AC050				MMM 40 wt% AC050			
p	q *n*-C4H10	p	q CH4	p	q *n*-C4H10	p	q CH4
bar	mmol/g	bar	mmol/g	bar	mmol/g	bar	mmol/g
0.00	0.000	0.00	0.032	0.03	0.000	0.03	0.180
0.18	0.128	0.06	0.045	0.04	0.138	0.15	0.203
0.30	0.221	0.25	0.042	0.05	0.293	0.30	0.237
0.46	0.364	0.50	0.049	0.10	0.399	0.51	0.311
0.58	0.471	0.75	0.041	0.20	0.507	0.66	0.429
0.92	0.794	1.00	0.046	0.30	0.582	0.90	0.490
1.00	0.884	1.30	0.051	0.49	0.659	1.25	0.507
1.25	1.188	1.70	0.066	0.49	0.737	1.53	0.513
1.47	1.512	2.01	0.073	0.74	0.949	1.75	0.499
1.73	1.983	3.01	0.097	1.00	1.196	2.02	0.530
1.98	2.572	4.94	0.117	1.24	1.440	2.52	0.539
2.16	3.139	7.54	0.140			2.75	0.548
		10.01	0.172			3.01	0.555
		12.48	0.217			3.51	0.560
		14.97	0.241			4.04	0.572
		20.09	0.241			4.51	0.575
		24.94	0.3233			5.01	0.579
		29.98	0.3676			5.44	0.572
						7.50	0.567
						9.99	0.544
						15.09	0.454
						19.89	0.310
						24.99	0.189
						30.02	0.060

Table D-16: Adsorption data for inorganic filler materials at 30 °C

	AC050		**CBV 780**		**R8200**	
p	**q CH4**	**q *n*-C4H10**	**q CH4**	**q *n*-C4H10**	**q CH4**	**q *n*-C4H10**
bar	mmol/g	mmol/g	mmol/g	mmol/g	mmol/g	mmol/g
0.001	0.001	1.655	0.002	0.095	0.0000	0.0002
0.002	0.003	2.102	0.001	0.173	0.0000	0.0005
0.003	0.004	2.340	0.001	0.241	0.0000	0.0007
0.004	0.006	2.583	0.001	0.303	0.0001	0.0009
0.005	0.007	2.742	0.001	0.360	0.0001	0.0011
0.006	0.009	2.873	0.001	0.413	0.0001	0.0014
0.007	0.010	2.984	0.002	0.462	0.0001	0.0016
0.008	0.012	3.080	0.002	0.508	0.0001	0.0018
0.009	0.013	3.164	0.002	0.551	0.0001	0.0021
0.010	0.014	3.240	0.002	0.591	0.0001	0.0023
0.011	0.016	3.308	0.003	0.630	0.0002	0.0025
0.012	0.017	3.370	0.003	0.667	0.0002	0.0027
0.013	0.019	3.427	0.003	0.702	0.0002	0.0030
0.014	0.020	3.480	0.003	0.736	0.0002	0.0032
0.015	0.021	3.529	0.003	0.768	0.0002	0.0034
0.016	0.023	3.574	0.004	0.799	0.0002	0.0037
0.017	0.024	3.617	0.004	0.828	0.0002	0.0039
0.018	0.026	3.657	0.004	0.857	0.0003	0.0041
0.019	0.027	3.695	0.004	0.885	0.0003	0.0043
0.020	0.028	3.730	0.005	0.911	0.0003	0.0046
0.021	0.030	3.764	0.005	0.937	0.0003	0.0048
0.030	0.042	4.007	0.007	1.136	0.0004	0.0068
0.040	0.056	4.197	0.009	1.308	0.0006	0.0091
0.050	0.069	4.341	0.011	1.447	0.0007	0.0114
0.060	0.083	4.455	0.014	1.563	0.0008	0.0137
0.070	0.096	4.550	0.016	1.661	0.0010	0.0159
0.08	0.101	4.630	0.018	1.747	0.0011	0.020
0.09	0.122	4.699	0.021	1.823	0.0012	0.022
0.10	0.135	4.761	0.023	1.890	0.0014	0.025
0.20	0.259	5.138	0.045	2.314	0.003	0.049
0.30	0.374	5.337	0.068	2.539	0.004	0.074
0.40	0.483	5.470	0.090	2.684	0.005	0.099
0.50	0.586	5.567	0.112	2.788	0.006	0.123
0.60	0.684	5.643	0.134	2.862	0.008	0.148

Table D-16 (continued): Adsorption data for inorganic filler materials at 30 °C

	AC050		CBV 780		R8200	
p	q CH4	q *n*-C4H10	q CH4	q *n*-C4H10	q CH4	q *n*-C4H10
bar	mmol/g	mmol/g	mmol/g	mmol/g	mmol/g	mmol/g
0.70	0.777	5.705	0.156	2.930	0.009	0.172
0.80	0.867	5.757	0.177	2.982	0.010	0.197
0.90	0.954	5.802	0.198	3.025	0.011	0.222
1.00	1.036	5.841	0.220	3.062	0.012	0.246
1.50	1.410	5.982	0.323	3.189	0.018	0.370
2.00	1.731	6.074	0.423	3.266	0.023	0.493
2.25	1.875	6.110	0.471	3.295	0.026	0.554
2.50	2.011	6.141	0.519	3.319	0.028	0.616
3.00	2.259	6.193	0.611	3.358	0.033	0.739
4.00	2.483	6.270	0.787	3.413	0.0430	0.985
5.00	3.038	6.326	0.951	3.450	0.047	1.232
10.00	4.215	6.481	3.541	1.630	0.091	2.456
15.00	4.909	6.559	2.138	3.560	0.125	3.594
30.00	5.999	6.673	3.110	3.629	0.206	4.968
45.00	6.545	6.730	3.666	3.650	0.269	4.049

Table D-17: Parameter of Toth adsorption isotherm and thermodynamic selectivity of inorganic fillers

	AC050		CBV-780		R8200	
	n-C_4H_{10}	CH_4	*n*-C_4H_{10}	CH_4	*n*-C_4H_{10}	CH_4
q_{max}	7.17	8.78	3.73	5.71	5.07	1.99
b	5428	0.165	30.65	0.04	0.048	0.007
t	0.32	0.72	0.61	1.00	5.62	0.51
α	26864		500		17	

E Error Analysis

The experimental errors were estimated based on the t-distribution which is suitable to describe the scattering for a small number of measuring data. The t-factor describes the probability with which the true value X_{true} is in the range of the chosen confidence interval for a given number of values. The error of the mean average value $\overline{X}$ is thus composed of the confidence interval p_x, the number of repeated measurements n and the empirical standard deviation s.

$$X_{true} = \overline{X} \pm t_{p_X, n-1} \cdot \frac{s}{\sqrt{n}} \qquad \text{(E–1)}$$

$$s = \sqrt{\frac{1}{n-1} \sum_{i=1}^{n} (x_i - \overline{x})^2} \qquad \text{(E–2)}$$